Unveiling the properties of the clusters in the NGC 6334 filamentary cloud, including the physics of shocked gas and accretion

INAUGURAL-DISSERTATION

zur
Erlangung des Doktorgrades
der Mathematisch-Naturwissenschaftlichen Fakultät
der Universität zu Köln

vorgelegt von

Mahya Sadaghiani
aus Teheran, Iran

Köln, 2021

Berichterstatter:
Prof. Dr. Peter Schilke
Priv. -Doz. Dr. Markus Röllig

Vorsitzender der Komission:
Prof. Dr. Joachim Saur

Tag der mündlichen Prüfung:
31 August, 2020

"Everything in the universe is within you, ask all from yourself."

Rumi

واژه به واژه،
پیشکش به مامان و بابا،
که دلشان با خداست، چشمانشان بدرقه‌ی من، و مهرشان برکت تمام زندگی‌ام

Abstract

by Mahya Sadaghiani

The process of high-mass star (M>8 $M_{\odot}$) formation out of diffuse interstellar medium is not completely understood and therefore, it marks one of the major topics in astrophysical research. High-mass stars are known to form within clusters and dense clumps with a typical size of 1 pc. The dense clumps are not distributed randomly in the molecular clouds, but they preferentially found embedded in the densest parts of filaments and filamentary-hubs that vertebrate the molecular clouds. Sensitive and high-resolution observations at (sub)-mm wavelengths have been used extensively as a tool to study the physical properties of the massive clumps and the process of mass accretion from the filaments.

This dissertation focuses on the study of the two massive protoclusters NGC 6334-I and NGC 6334-I(N), located in the nearby (at a distance of 1.3 kpc) filamentary cloud NGC 6334. In this thesis, I derive the physical properties of the clusters, study the accretion process from the cloud to the protoclusters, and characterise the properties of the shocked gas in the region. To achieve this aim, I made use of ALMA observations towards the two high-mass protoclusters, and the gas connecting them to the large-scale filament. The observations cover the spatial scales from 1800 au to 0.25 pc and are sensitive to the 3 mm continuum emission and different molecular species. The intensity maps of dense gas tracers reveal a network of filamentary structures converging at the positions of these two clusters. The analysis of the velocity fields results in mass accretion rates of 6×10^{-5} $M_{\odot}$ yr^{-1} and 4×10^{-5} $M_{\odot}$ yr^{-1} for NGC 6334-I and NGC 6334-I(N), respectively. The similar accretion rate and the proximity of these two clusters suggest that they are competing for the mass reservoir in the main filament.

The temperature map obtained for the observed region reveals a temperature gradient from the outskirts to the central regions where these two clusters are located. The coincidence of temperature minima with density peaks shows that the central regions are ideal environments for the formation of dense cores. In agreement with this finding, the ALMA continuum map at 3 mm revealed a total of 142 cores in the observed region. Using seven different machine-learning algorithms, the identified cores are grouped into four clusters: NGC 6334-E, NGC 6334-I, NGC 6334-I(N) and NGC 6334-I(NW). With these data, I studied the physical properties of the identified protoclusters such as the core mass function (CMF), the spatial distribution of cores as well as the mass segregation. The derived CMFs show an excess of high-mass objects compared to the initial mass function (IMF). I explored the effects on inaccuracies in the temperature measurements as well as unresolved multiplicity, and determined that they may affect the CMF and produce, under certain conditions, an spurious excess of massive objects. These limitations may affect the results of recently published works reporting top-heavy CMFs or an excess of massive objects. My analysis demonstrates that these effects should always be considered in this kind of studies. The clusters NGC 6334-I and NGC 6334-I(N), both harboring massive cores, show clear hints of mass segregation. The masses and separations of the cores in the clusters NGC 6334-E, NGC 6334-I and NGC 6334-I(N) are in agreement with

fragmentation being controlled by turbulence at scales of 0.1 pc. Combining our knowledge about the structure and fragmentation at different scales for the NGC 6334 region (from the large scales of the filament at a few 10 pc, down to the core scales of few thousand au), I determine that the fragmentation is a scale-dependent process controlled by turbulent pressure at large scales and regulated by thermal pressure at small scales.

The association of the clusters with HII regions and their infrared content suggest an evolutionary sequence from younger to more evolved: NGC 6334-I(N), NGC 6334-I and NGC 6334-E. Making use of this temporal evolution, I have studied possible correlations between the properties of the clusters and their evolutionary stage. I find a larger separation between the cluster members in more evolved clusters favoring the role of gas expulsion and stellar ejection. Due to the presence of filamentary structures in NGC 6334-I(N), the mass segregation in this cluster has a primordial origin, while in NGC 6334-I dynamical effects may have played a role. Finally, a top-heavy CMF in the less-evolved cluster suggests the presence of a large gas reservoir in the form of massive cores, while this reservoir is already accreted in the more evolved clusters.

The accretion process via the filamentary network possibly generates slow shocks due to the transport of material. On the other side, a large population of star-forming cores can produce high-velocity shocks due to the outflows. The SiO emission map obtained with ALMA is an ideal tracer of shocked gas and exhibits a complex morphology with a broad variety of line profiles and a large number of overlapping emission features towards the clusters NGC 6334-I and NGC 6334-I(N). In order to identify the emission features, I applied the dendrogram technique to the SiO peak intensity map. This resulted in a total 89 SiO structures with masses ranging from 0.03 to 80 $M_{\odot}$, kinetic energies from 10^{43} erg to 10^{48} erg and outflow momentum values from 0.15 $M_{\odot}$ km s^{-1} to 5300 $M_{\odot}$ km s^{-1}. As an attempt to decompose the slow shocks from the high-velocity shocks, I took advantage of spectral decomposition and wavelet analysis. The spectral decomposition separates the two types of shocks based on the width of the SiO line profile. In the present work, I adopted a threshold of 12 km s^{-1} for the decomposition. The complex wavelet analysis isolates the slow shocks based on the probability density function (PDF) of their wavelet coefficients. The decomposition analysis reveals that 30% of the shock energetics in the region are generated in slow shocks, while for the remaining 70%, outflows are responsible. The widespread emission generated by slow shocks dominates at scales $>$0.1 pc.

Zusammenfassung

by Mahya Sadaghiani

Der Entstehungsprozess von massereichen Sternen (M>8 $M_{\odot}$) aus diffusen interstellarem Medium birgt noch immer viele ungeklärte Fragen. Daher ist dieser Bereich einer der großen Themen in aktueller astrophysikalischer Forschung. Massereiche Sterne entstehen innerhalb von Sternhaufen und dichten Klumpen, die üblicherweise $\sim$1 pc groß sind. Diese dichten Klumpen sind nicht nach dem Zufallsprinzip in Molekülwolken verteilt, sondern befinden sich bevorzugt in den dichtesten Abschnitten von Filamenten und deren Knotenpunkten, welche sich wie Skelette durch Molekülwolken erstrecken. Sensitive und hochauflösende Beobachtungen bei Wellenlängen im (sub-)mm Bereich wurden ausgiebig genutzt um die physikalischen Eigenschaften dieser massereichen Klumpen und den Prozess von Massenakkretion zu untersuchen.

Diese Dissertation konzentriert sich auf die Untersuchung der beiden massiven Protocluster NGC 6334-I und NGC 6334-I(N), innerhalb der Wolke NGC 6334, welche sich in einer Entfernung von ca. 1.3 kpc zu unsere Erde befindet. In dieser Arbeit untersuche ich die physikalischen Eigenschaften dieser Cluster, sowie den Akkretionsprozess von der Wolke zu den Clustern, und analysiere die Eigenschaften des geschockten Gases. Hierzu nutzte ich ALMA Observationen beider massereicher Cluster und von Gas, welches diese mit groß-skaligeren Filamenten verbindet. Die Beobachtungen haben ein räumliche Auflösung von 1800 au bis 0.25 pc und sind sensitiv gegenüber 3 mm Kontinuumsemission und Emission verschiedener Moleküle. Karten der Strahlungsintensität von Tracern dichten Gases zeigen ein Netzwerk von Filamentstrukturen, die an beiden Cluster zusammenlaufen. Die Analyse der Geschwindigkeitsfelder ergab Massenakkretionsraten von 6×10^{-5} $M_{\odot}$ yr^{-1} und 4×10^{-5} $M_{\odot}$ yr^{-1} for NGC 6334-I and NGC 6334-I(N). Die Ähnlichkeit der Akkretionsraten und die räumliche Nähe beider Cluster deuten darauf hin, dass sie um das Massenreservoir im Haupt-Filament konkurrieren.

Die Temperaturkarte, die für die beobachtete Region bestimmt wurde, zeigt einen Temperaturgradienten von den Außenbereichen hin zur Mitte, in der sich die beiden Cluster befinden. Die Koinzidenz von Temperaturminima und maximaler Dichte deutet darauf hin, dass die zentralen Bereiche ideale Umgebungen für die Bildung dichter Kerne sind. In Übereinstimmung mit diesem Ergebnis konnten in der ALMA-Kontinuumskarte bei einer Wellenlänge von 3 mm insgesamt 142 Kerne in der beobachteten Region ermittelt werden. Mithilfe von sieben verschiedenen machine-learning Algorithmen wurden die identifizierten Kerne in vier Cluster gruppiert: NGC 6334-E, NGC 6334-I, NGC 6334-I(N) und NGC 6334-I(NW). Anhand dieser Daten untersuchte ich die physikalischen Eigenschaften der identifizierten Protocluster wie beispielsweise die Core Mass Function (CMF), die räumliche Verteilung der Kerne, sowie die Massensegregation. Die abgeleiteten CMFs zeigen einen Überschuss an Objekten mit hoher Masse im Vergleich zur, Initial Mass Function (IMF). Die Untersuchung des Einflusses von Ungenauigkeiten bei der Temperaturbestimmung sowie unaufgelöste Multiplizitäten einzelner Objekte ergab, dass diese Faktoren die CMF beeinflussen und unter bestimmten Bedingungen einen unechten Überschuss an massiven Objekten erzeugen können. Diese Einschränkungen haben auch eine Bedeutung für die Ergebnisse neu veröffentlichter Arbeiten, in denen

top-heavy CMFs oder ein Übermaß an massiven Objekten festgestellt wurden. Meine Analyse zeigt, dass diese Effekte in solchen Studien immer berücksichtigt werden sollten. Die Cluster NGC 6334-I und NGC 6334-I(N), die beide massive Kerne beherbergen, weisen deutliche Tendenzen einer Massensegregation auf. Die Massen und die Abstände der Kerne in den Clustern NGC 6334-E, NGC 6334-I und NGC 6334-I(N) deuten darauf hin, dass die Fragmentierung durch Turbulenzen in Skalen von 0.1 pc kontrolliert wird. Aufground der vorgefundenen Strukturen und der Fragmentierung in verschiedenen Größenskalen (von einigen 10 pc bis wenige tausend au) für NGC 6334 schließe ich, dass Fragmentierung ein von der Größenskala abhängiger Prozess ist: Gesteuert durch turbulenten Druck in größeren Skalen, und durch thermischen Druck in kleineren Skalen.

Die Assoziation der Cluster mit HII Regionen und ihr Infrarotgehalt legen eine Evolutionssequenz von jünger bis weiter entwickelt nahe: NGC 6334-I(N), NGC 6334-I und NGC 6334-E. Anhand dieser zeitlichen Entwicklung habe ich mögliche Korrelationen zwischen den Eigenschaften der Cluster und ihrem Evolutionsstadium untersucht. Ich fand zwischen den Objekten in weiterentwickelten Clustern eine größere räumliche Trennung, die Gasausstoß und Auswurf von Sternen begünstigt. Aufgrund des Vorhandenseins von Filamentstrukturen in NGC 6334-I(N) hat die Massensegregation in diesem Cluster einen primordialen Ursprung, während in NGC 6334-I möglicherweise dynamische Effekte eine Rolle gespielt haben. Schließlich deutet ein top-heavy CMF im weniger weit entwickelten Cluster auf ein großes Gasreservoir in Form von massiven Kernen hin, während dieses Gasreservoir in den weiter entwickelten Clustern bereits im Sternentstehungsprozess verwendet wurde.

Der Akkretionsprozess über das Filamentnetzwerk erzeugt möglicherweise langsame Schocks aufgrund des Materialtransports. Andererseits kann eine große Population sternformender Kerne aufgrund von Abflüssen (ouflows) Schocks mit hohen Geschwindigkeiten erzeugen. Die mit ALMA erhaltene SiO-Emissionskarte ist ein idealer Indikator für geschocktes Gas und weist eine komplexe Morphologie mit einer Vielzahl von linienartiger Muster und überlappender Strukturen in den Clustern NGC 6334-I und NGC 6334-I(N) auf. Um diese Merkmale zu identifizieren, habe ich eine Dendrogrammtechnik auf die SiO-Peakintensitätskarte angewendet. Diese ermittelte insgesamt 89 SiO-Strukturen mit Massen im Bereich von 0.03 $M_\odot$ nach 80 $M_\odot$ kinetische Energien von 10^{43} erg zu 10^{48} erg und Ausfluss-Impulsen von 0.15 $M_\odot$ km s^{-1} Zu 53000 $M_\odot$ km s^{-1}. Um die langsamen Schocks von den Hochgeschwindigkeitsschocks zu unterscheiden, nutzte ich die spektrale Zerlegung und die wavelet Methode. Die spektrale Zerlegung trennt die beiden Arten von Stößen basierend auf der Breite des SiO-Linienprofils. In der vorliegenden Arbeit habe ich für die Zerlegung einen Schwellenwert von 12 km s^{-1} angenommen. Die komplexe wavelet Methode isoliert die langsamen Schocks basierend auf der Wahrscheinlichkeitsdichtefunktion (PDF) ihrer wavelet Koeffizienten. Die Analyse zeigt, dass 30% der Schockenergien in der Region in Form von langsamen Schocks erzeugt werden, während für die verbleibenden 70% Abflüsse (outflows) verantwortlich sind. Die weit gestreute Emission, die durch langsame Stöße erzeugt wird, dominiert bei Skalen von $>$0.1 pc.

Contents

Chapter 1

Introduction

Stars are the most widely recognised astronomical objects in the night sky. The processes which lead to the formation of stars are one of the most fundamental open questions in astrophysics. Stars and stellar clusters are the most fundamental building blocks of galaxies. Moreover, they are responsible for the production of all heavy elements by the nuclear fusion during the successive stages of stellar evolution and supernova explosion. The dynamical, chemical and morphological structures of a galaxy is influenced by the distribution and composition of the stars in their host galaxy.

We know that stars are formed out of clouds of dust and gas which are distributed throughout the galaxies. However, star formation is a multi-scale process which involves a wide range of physical processes including self-gravity, turbulence, hydrodynamics, outflows, radiation and magnetic fields. All these processes act on different scales to cause a molecular cloud to collapse and undergo star formation. While the process of formation of isolated low-mass stars has been vastly investigated, the first stages of high-mass stars (M $> 8\ M_{\odot}$) are still poorly understood. From the observational point of view, investigating the early stages of high-mass star formation is challenging due to 1) the rarity of high-mass stars, 2) their large distances ($>$ 1 kpc), 3) their clustered birthplace and 4) their short life times. The observations presented in this work focus on the interface region between the filamentary clouds and denser substructures (i.e., embedded clusters) that lead to star formation. Investigating the physical nature of the large-scale overdensities which are the birthplace of most stars, provides us an insight into the very early stages of high-mass star formation.

1.1 Properties of the interstellar medium

The interstellar medium (ISM) is a broad name which refers to anything that exists between the stars within galaxies. The principal constituents of the ISM are baryonic matter, the electromagnetic radiation field, the gravitational filed, cosmic rays and magnetic field. The interstellar gas is mainly composed of hydrogen (70% of mass), which can be found in a neutral (HI), molecular (H_2) and ionized (HII) state. In addition, 28% of the mass is in helium and 2% in heavier elements such as oxygen, carbon and nitrogen. While the gaseous material accounts for 99% of the matter in the ISM, 1% of the mass of interstellar matter is in dust grains. The dust grains with a size of less than a micron are mainly composed of silicates and carbon compounds.

A key aspect of the ISM is that the physical conditions (e.g., density and temperature) are quite heterogeneous resulting in a variety of chemical and thermal distinct states. Therefore, the ISM is often referred to as a *multi-phase* medium. Several models have been proposed over years to describe the different ISM phases, characterized by temperatures and densities which are set by the balance between the cooling and the heating

mechanisms. As explained in the recent review by Klessen and Glover (2016), these states are:

- Warm Neutral Medium (WNM): Warm and diffuse atomic gas with kinetic temperatures in the range 5 000–8 000 K and densities of 0.01–0.1 cm^{-3} (Field, 1969).
- Cold Neutral Medium (CNM): Cold and dense atomic gas with $T \sim 100$ K and densities of ~ 30 cm^{-3} (Field, 1969).
- Hot Ionized Medium (HIM): Very hot, low-density gas which has been heated by stellar winds and blast waves from novae and supernovae. Its temperature and density are $> 10^{5.5}$ K and 0.004 cm^{-3} respectively, and is believed to fill about half of the volume of the galactic disk (McKee and Ostriker, 1977).
- Warm Ionized Medium (WIM): Hot and diffuse gaseous regions outside the localized HII regions which are photoionized by UV photons from OB stars. The WIM is a fundamental gas phase constituent of the Milky Way which accounts for 90% or more of the total ionized gas in the ISM. Its temperature ranges from about 6000 to 10 000 K and has a characteristic low density of 0.1 cm^{-3}.
- Molecular Gas (H_2): The coldest and densest phase of the ISM with temperatures of 10–20 K and densities of $10^2 - 10^8$ cm^{-3}. It is predominantly structured in cold dense giant molecular clouds (GMCs) that are gravitationally bound and harbour star formation.

In addition to the gas phase which accounts for 99% of the ISM, dust grains with a share of 1%, play a crucial role in the interstellar chemistry. They reduce the UV radiation which causes molecular dissociations and provide the sites of formation of the H_2. Moreover, dust grains further control the temperature of the ISM on one side by accounting for most of the elements which provide cooling, and on the other side by heating through electrons ejected photoelectrically from grains.

Observationally, cold and large dust grains provide two thirds of the infrared flux of our galaxy at wavelengths larger than 50 μm. The remaining one third of the IR emission is due to cooling of dust grains by the photo-absorption process.

1.2 Molecular Clouds

Among the five different phases of the ISM described in § 1.1, stars form out of the coldest and densest phase: the molecular gas. The formation of the molecular gas is mainly the result of the reactions catalyzed by dust grains and the ability of the hydrogen atom to stick to the dust grains thereby allowing recombination. The accumulation of molecular gas results in more massive and self-gravitating objects known as Giant Molecular Clouds (GMC, Sanders, Scoville, and Solomon, 1985), which are typically distributed around the mid-plane of galaxies. GMCs have characteristic masses of $10^4 - 10^6$ $M_\odot$ and sizes of about tens of parsecs (e.g., Blitz, 1993). They are often cold (10–20 K) and their average density is in the range 50–500 cm^{-3}. The main physical mechanisms responsible for the formation of GMCs are:

- **Converging flows:** Converging streams of gas which are the outcome of stellar feedback processes (e.g., supernova blast waves) that get involved in the processes of fast cooling (see e.g., Audit and Hennebelle, 2005; Bania and Lyon, 1980; McCray, 1975; Vazquez-Semadeni, Passot, and Pouquet, 1995) and then coagulate to form

large clouds. This mechanism plays a dominant role on scales up to $\sim$ 100 pc and explains the formation of Solar neighborhood clouds with masses up to 10^4 $M_\odot$.

- **Spiral-arm induced collisions:** One of the alternative scenarios for the formation of high-mass molecular clouds is the aggregation of smaller clouds. However, this process is extremely slow (>100 Myr, Blitz and Shu (1980)) in low-density environments. Therefore, spiral arms and high surface density galaxies are the proper places where collisions between small clouds become more frequent and consequently the formation time scale will be greatly reduced (see e.g., Dobbs et al., 2008; Kwan and Valdes, 1983).

- **Gravitational instability:** Single-phase infinitesimally thin gas disks become unstable and undergo fragmentation when their *Toomre* parameter Q is smaller than one. Molecular clouds are formed in gas disks as a result of gravitational instabilities (Shetty and Ostriker, 2008). The expected masses of the clouds corresponding to gas disks with moderate surface density ($< 100\ M_\odot/\mathrm{pc}^{-2}$) are higher than those of observed GMCs when the effective sound speed is 7 km s^{-1} (mean velocity dispersion for atomic medium). To better estimate the masses of molecular clouds based on this scenario, it is necessary to assume a multi-phase medium and take the turbulence dissipation into account (Dobbs, Burkert, and Pringle, 2011; Wada, Spaans, and Kim, 2000).

It is necessary to note that each mechanism acts over different spatial and time scales. The properties of the clouds are highly dependent on the mechanisms which are dominant in different time scales and environments. Observations of GMCs have been most effectively made by detecting the ^{12}CO rotational emission lines at low densities ($n \sim 10^2$ cm^{-3}). The ^{12}CO molecule is the second most abundant molecule in molecular clouds. As the H_2 molecules do not exhibit rotational transitions, the ^{12}CO molecule has been widely used to probe the characteristics of GMCs. However, it can not be used to study all densities. At densities of $n \sim 10^3$ cm^{-3}, the emissions from carbon monoxide isotopologues such as ^{13}CO and C^{18}O are optically thick and therefore serve as better tracers for dense gas. In order to trace the densest regions of GMCs, molecules with higher critical densities such as HCN are needed. Observations of various molecules help us to characterize the physical properties of the individual GMCs which are parameterized by their observed sizes, volume density and velocity dispersion. Larson (1981) identified scaling relations between the observable quantities and the physical properties of the clouds. The scaling relations are: (1) a power-law relationship between the length L of the cloud and its 3D velocity dispersion σ_v, with $\sigma_v \propto L^{0.38}$; (2) approximate virial equilibrium, with $2GM/\sigma_v^2 L \simeq 1$; and (3) a relation between the volume density n of the cloud and its length, with $n \propto L^{-1.1}$.

Observations of CO and other dense gas tracers show that the density distribution in molecular clouds is not homogeneous. Molecular clouds harbour elongated overdense regions known as *filaments* which become gravitationally unstable and fragment into clumps. Inside the clumps, compact and small structures ($\sim$ 0.1 pc) defined as *dense cores* have been found with high densities ($n > 10^4 - 10^5$ cm^{-3}), out of which single stars and multiple systems will form. In other words, to form a single star or a group of stars, molecular clouds collapse and fragment in a hierarchical way.

1.3 Filamentary structures

The presence of filamentary structures in nearby star-forming clouds has been known for quite some time (see e.g., Johnstone and Bally, 1999; Myers, 2009; Schneider and Elmegreen, 1979). However, over the past decade, the *Herschel* Space Observatory revealed the ubiquitousness of filaments and their importance in star formation (see e.g., Hill et al., 2011; Men'shchikov et al., 2010). Filaments are simply defined as elongated ISM structures with an aspect ratio of ∼5–10 that are significantly overdense with respect to their surrounding. The filaments range from about 3 to 300 pc in length and from 0.3 to 3 pc in radius (see e.g., Maddalena et al., 1986; Tatematsu et al., 1993). The differences observed in organization of the filamentary networks in different molecular clouds offer clues about the nature of the processes in play within molecular clouds. Hill et al. (2010) found that in low column density regions of the Vela C cloud, filaments are arranged in more varied directions, while in the regions with higher a column density, filaments appear more uni-directional. The formation and structure of filamentary networks can be explained by the relative influences of gravity, supersonic turbulence and the magnetic fields. When gravity dominates, the large-scale clouds first collapse along their shortest axis creating sheets and then along their second dimension producing filaments (see e.g., Burkert and Hartmann, 2004; Gómez and Vázquez-Semadeni, 2014; Shandarin and Zeldovich, 1989). However, in the scales of molecular clouds gravity is not the only dominant force. Otherwise, filamentary structures could not form in unbound atomic clouds (see e.g., Clark and Glover, 2014; Kalberla et al., 2016). Another alternative mechanism which is responsible for the filament formation is large-scale supersonic flows which compress the interstellar matter and form planar structures. Filaments can form at the intersection of two sheet-like structures (Pudritz and Kevlahan, 2013). The velocity gradient observed perpendicular to the main axis of the filaments affirms the role of supersonic flows in the formation of interstellar filaments (see e.g., Chen et al., 2014; Kirk et al., 2013a). *Planck* polarization observations show that filaments tend to be aligned along or perpendicular to the magnetic fields depending on the gas column density (Planck Collaboration, 2016). In this picture, low density filaments tend to be aligned with the magnetic fields, while dense filaments tend to be perpendicular to the field. These findings suggests that the organization of the filaments is strongly affected by the magnetic fields.

Detailed Analysis of the radial column density profiles derived for the nearby clouds of the Gould Belt using *Herschel* observations, shows that the inner widths of filaments follows a very narrow Gaussian distribution with a typical FWHM value of ∼0.1 pc (Arzoumanian et al., 2011; Koch and Rosolowsky, 2015; Palmeirim et al., 2013). Some other independent measurements of filament widths have been consistent with the "characteristic" width found by *Herschel* (see e.g., Salji et al., 2015). However, it should be pointed out that variations from the characteristic width of ∼0.1 pc sometimes exists along the main axis of the filament. Detailed analysis of the $C^{18}O$ observations towards Orion A indicates that, although the filaments have a median of 0.1 pc width, the width along the filaments vary throughout the cloud. The variation of the width is correlated with the number of substructures embedded in the filament (Suri et al., 2019). The origin of the characteristic inner width of filaments is currently a matter of debate. Assuming that filaments originate from the large-scale supersonic flows, a possible interpretation is that the characteristic width corresponds to the scale below which the turbulence become subsonic (Federrath et al., 2010; Padoan et al., 2001).

Assuming a filament as an isothermal gas cylinder, it becomes gravitationally unstable when its line-mass exceeds its critical value $M_{line,crit} \sim 2c_s^2/G$ (Ostriker, 1964). As a

result of the gravitational instability, the filament contracts radially and undergoes fragmentation along its main axis (Inutsuka and Miyama, 1997). The fragmentation process leads to the formation of dense clumps which are the birth places of (high-mass) stars. Filament intersections can also provide higher column density and generate localized mass accumulation which further triggers the star formation. Hennemann et al. (2012) found that at the locations of merged filaments in Cygnus X more massive protostellar candidates are observed compared to the rest of the cloud.

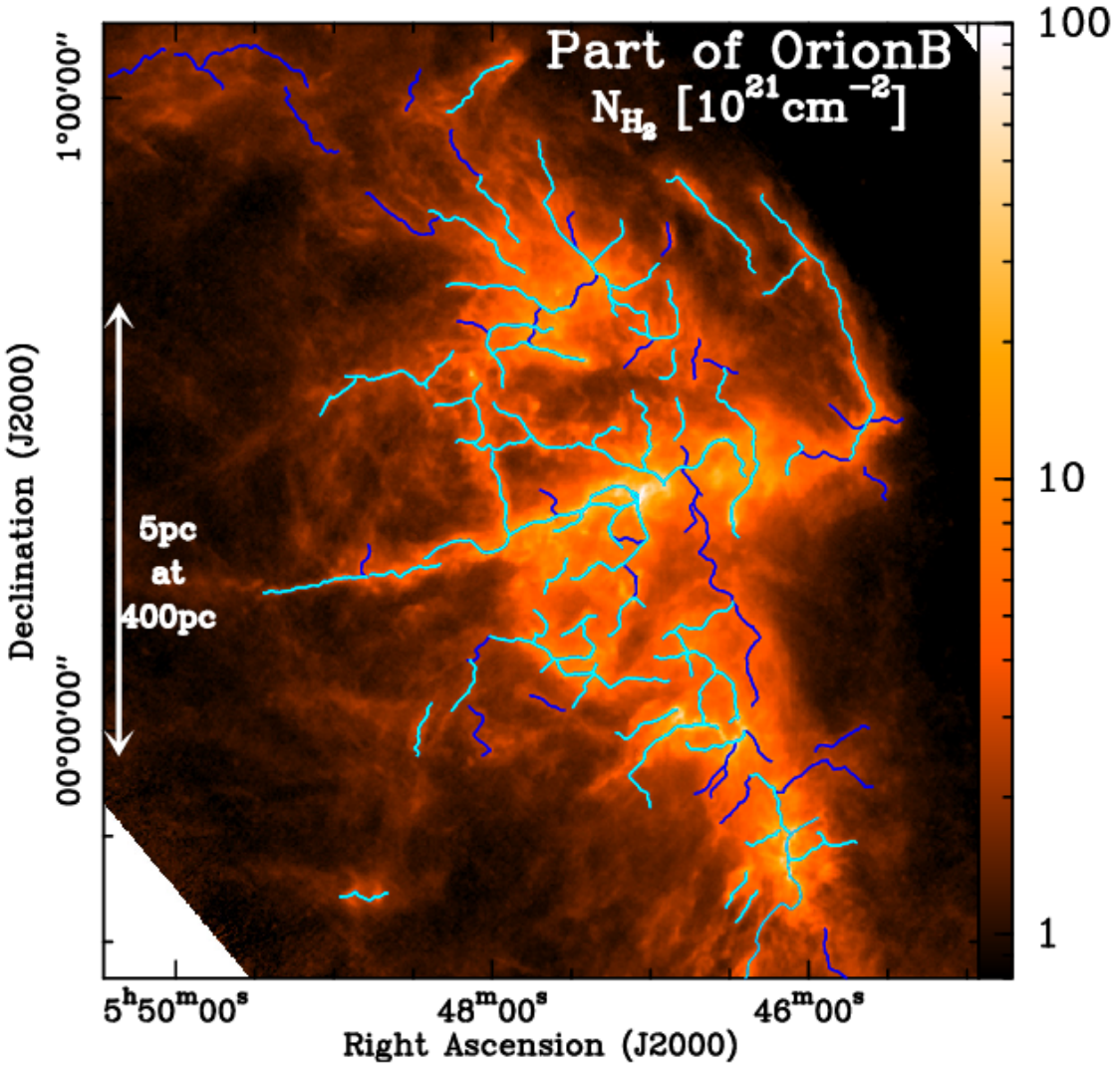

FIGURE 1.1: *Herschel* column density map of a portion of Orion B. The solid lines in color denote the filamentary structures identified using `DisPerSE` indicating the ubiquitousness of filaments in star-forming regions (Arzoumanian et al., 2018).

1.4 Cluster-forming clumps

It is thought that most of the stars do not form in isolation. Instead, they tend to form within clusters containing high-mass stars. Clumps (i.e., protoclusters) are the actual sites of clustered star formation within the filamentary molecular clouds (e.g., Bressert

et al., 2012; McKee and Ostriker, 2007; Rathborne et al., 2015; Tan et al., 2014). In this picture, star-forming clumps with gas and dust masses larger than 10^3 $M_\odot$ and H_2 densities exceeding 10^4 cm^{-3}, are believed to be the fundamental units of star formation (e.g., Lada and Lada, 2003). These structures have a typical size of 1 pc and are formed via the fragmentation of the filaments during their gravitational collapse or as a result of filament mergers. Filamentary hubs are the interplay of the colliding supersonic turbulent flows which create density enhancements (see e.g., Bonnell and Bate, 2002; Heitsch and Hartmann, 2008). As evolution proceeds, turbulence dissipates and clumps fragment to form several hundreds or thousands of cluster members. The cluster members typically present an outstanding diversity from cold dense cores to chemically rich hot molecular cores and HII regions (see e.g., Tan et al., 2014, for a review). Investigating the physical properties of the protoclusters and their environments based on observational constraints provide key knowledge leading to a better understanding of a number of fundamental problems in star formation (see e.g., Klessen et al., 2004; Lee and Hennebelle, 2016).

In Chapter 3, I discuss the statistical approaches used to derive the physical properties of protoclusters. An extensive summary is provided by Lada and Lada (2003).

1.5 Star formation

As mentioned before, stars form inside dense clumps embedded in molecular clouds. If the clumps exceed the Jeans mass, they become unstable leading to gravitational collapse. As the material falls towards the center, the density near the center of the clump increases, while the density at the edge of the clump drops. The density gradient results in a pressure gradient which slows down the collapse in the outer regions of the clump. Since the density distribution is not uniform within the clumps, the denser parts which have a low Jeans mass collapse individually and start to contract under their own gravity. This causes the clump to fragment into a number of dense condensations during the collapse phase. The first stage of collapse is isothermal as the core is optically thin and therefore is able to radiate away the heat which is produced by compression. As the collapse proceeds, the central part of the core gets sufficiently dense that the excess heat no longer radiates away and therefore breaks down isothermality. The internal energy of the central region increases until the radiation pressure balances the gravitational force and the collapse stops. At this point, the core can be referred to as a *protostar*. The protostar continues to grow by accreting material from the infalling cloud to eventually form a star. Based on the timescales over which the protostars form, one distinguishes between low- and high-mass star formation (see e.g., Tielens, 2005; Ward-Thompson and Whitworth, 2011).

1.5.1 Time scales

The timescale that would take a body to collapse under its own gravitational attraction is given by the free-fall time $t_{\rm ff}$ (Shu, Adams, and Lizano, 1987):

$$t_{\rm ff} = \sqrt{\frac{3\pi}{32G\rho}}, \tag{1.1}$$

where G is the gravitational constant and ρ is the average mass density. For interstellar density of $\sim 10^{-18}$ gr cm^{-3}, the free-fall time is $\sim 10^5$ years. Due to the gravitational contraction, the collapsing core gets smaller and releases the gravitational potential energy

in the form of heat. The time that would take a core to radiate away its total energy is defined as the Kelvin-Helmholtz timescale:

$$t_{\rm KH} = \frac{GM^2}{RL}, \tag{1.2}$$

where M, R and L denotes that mass, radius and luminosity of the star, respectively. For a Sun-like star the Kelvin-Helmholtz timescale is estimated to be $\sim 3\times10^7$ years, while it takes a value of 10^4 years for an O-type star. Up to masses $< 8\ M_\odot$ $t_{\rm KH}$ time scale exceeds the collapse time, meaning that the accretion will be completed before hydrogen nuclear burning takes over. In contrast, for massive stars $t_{\rm KH} << t_{\rm ff}$ indicating that the star begins nuclear fusion while it is still accreting more gas (Keto and Wood, 2006; Palla, Stahler, and Parigi, 1993). In this case, nuclear fusion starts during the accretion phase and the radiation pressure of the newly-born star may halt the accretion and therefore, stops the further mass growth. This problem, known as *radiation pressure* problem, makes massive star formation different from low-mass star formation. Theoretical models and observational constraints are necessary to better investigate the process of high-mass star formation.

1.5.2 Initial mass function

While the formation process of low-mass stars is reasonably well-understood, the origin of the distribution of stellar masses characterized by the so called stellar initial mass function (IMF) is still a matter of debate. The standard IMF of Kroupa (2001) adopts a three-part power-law distribution of the form $dN \propto M^{-\alpha}\, dM$ which breaks at 0.08 $M_\odot$ and 0.5 $M_\odot$:

$$\begin{aligned} \eta(m) &= m^{-\alpha} \\ \alpha &= 0.3 \text{ for } M < 0.08, \\ \alpha &= 1.3 \text{ for } 0.08 < M < 0.5, \\ \alpha &= 2.3 \text{ for } M > 0.5. \end{aligned} \tag{1.3}$$

The slope of the IMF was originally identified by (Salpeter, 1955) who found an exponent of $\alpha = 1.35$ for a log-normal distribution of stellar masses expressed as

$$\xi(m)\Delta m = \xi_0\ (\frac{m}{M_\odot})^{-1.35}\Delta(\mathrm{m}). \tag{1.4}$$

Star formation theories must be able to explain the main properties of the IMF which are the power-low slope at high masses, the break and turnovers, the predicted upper limit on the stellar masses of 150 $M_\odot$ and the universality of the shape of the IMF over a wide range of star-forming environments.

Current popular models which propose to explain the origin of IMF fall into two main categories: models that postulates that the shape of the IMF is inherited from the distribution of natal core masses and models which emphasise on the importance of accretion and dynamical interactions. According to the first category of models, the fragmentation process which is regulated by the presence of turbulence and energetics in the region form dense cores which finally evolve into stars. In this picture, there is a direct mapping between the Core Mass Function (CMF) and the IMF. The second category of models propose that the stellar masses are independent from the initial masses of natal

cores. Instead, details of the accretion process play a crucial role in determining the stellar masses. Recent numerical simulations conclude that both dynamics and nature are involved in the origin of the IMF.

If stellar masses are determined by the amount of gas in the prestellar cores, understanding the origin of the CMF is crucial for understanding the IMF. The first observational link between the CMF and the IMF was achieved by Motte, Andre, and Neri (1998) in a study of continuum dust emission in ρ-Ophiuchi molecular cloud. They find that high-mass slope of the CMF is consistent with that of the IMF. This results is confirmed by further observations towards a number of nearby star-forming clouds including Orion (Johnstone and Bally, 2006; Motte and André, 2001), Pipe nebula (Alves, Lombardi, and Lada, 2007) and Taurus (Onishi et al., 2002). In one of the most recent determination of the CMF André et al. (2010) and Könyves et al. (2010) observed more that 500 cores in the Aquila rift cloud complex using *Herschel*. This observation confirmed the conclusion of the previous studies: the observed CMF in the star-forming regions resembles the IMF but shifted to the higher masses. In the case of the extragalactic sources, the IMF constructed for a large number of clusters in the Galaxy and in the Magellanic Clouds indicates that within a 1 σ uncertainty the slopes of the derived IMFs are consistent with the Salpeter slope, suggesting a universality. Although the theoretical models of turbulent fragmentation and observations agree on the similarity of the IMF and the CMF, the picture is not so simple. To obtain an IMF which is directly inherited from the CMF, several conditions must hold. First, all observed cores must be gravitationally bound. Second, mass of the cores must remain constant. Probable mass accretion or mergers must be done in a self-similar fashion that the shape of the CMF is preserved. Third, all cores must have the same star formation efficiency. Fourth, fragmentation must be done in a self-similar fashion. Fifth, all cores must condense into stars at the same rate. Fig. 1.2 illustrates what happens when each of these conditions is violated. The observed IMF variance within extreme environments such as the Galactic center and high-mass star forming regions challenges the universality of the shape of the IMF and points out its potential dependence on the environment. Motte, Bontemps, and Louvet (2018) reported a top-heavy CMF obtained by ALMA observations towards W43-MM1 star-forming region. Additionally, the CMF of Sgr B2 obtained with ALMA observations suggest a lack of low-mass cores (Sánchez-Monge et al., 2017), similar to what has been found in the high-mass star forming region G28.34 (Zhang et al., 2015). Sensitive observations of the low-mass population of cores and multiplicity level are necessary to provide robust constraints on the star formation models which propose theoretical solutions for the IMF variance.

1.5.3 Low-mass star formation

With the general picture of star formation in mind, young stellar objects are classified into four distinct groups based on their spectral energy distribution (SED) tracing their evolutionary stages from the onset of accretion onto a protostellar core up to the main sequence (see Fig. 1.4) (André, 1994; Andre, Ward-Thompson, and Barsony, 1993; Lada, 1987).

- **Class 0:** these are the youngest objects which are heavily embedded. The SED is described by a blackbody that peaks at wavelengths > 150 μm. This emission arises from the infalling envelope. In this phase, the accretion rate is significantly high and a large amount of circumstellar dust can be found at the surrounding.

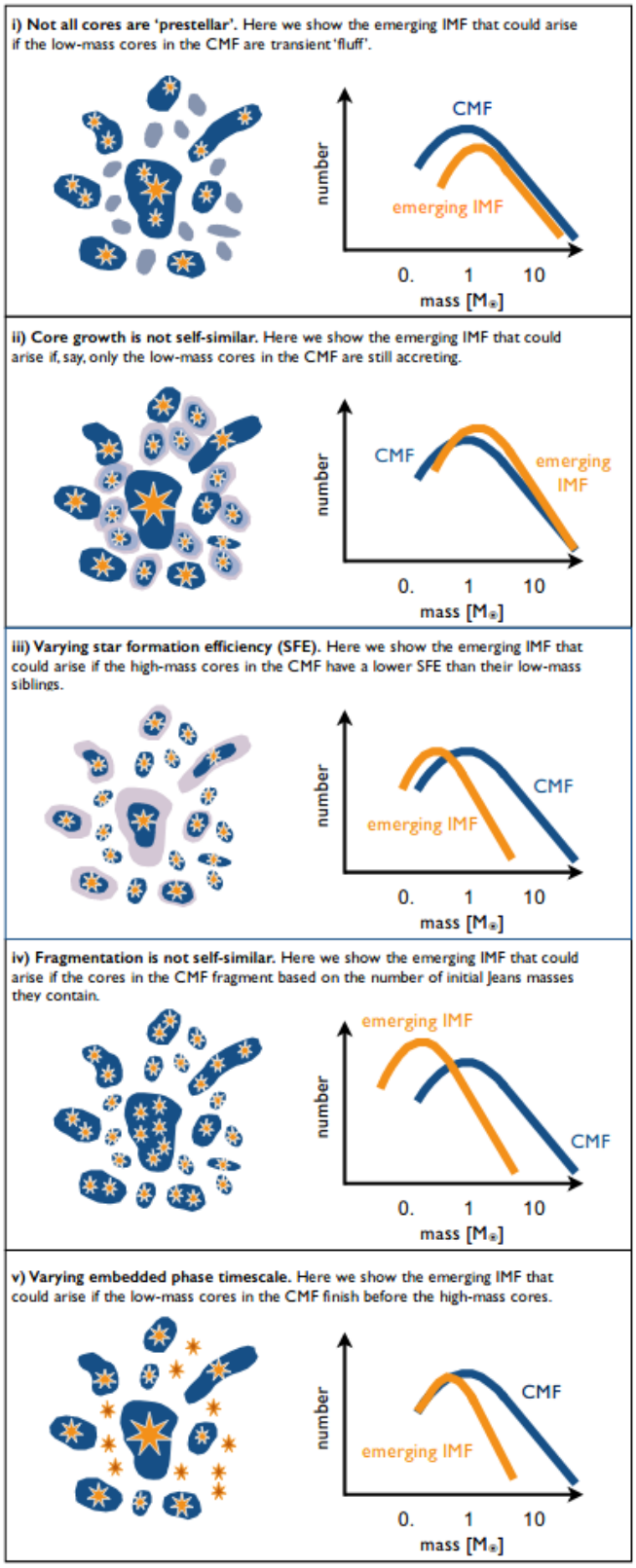

FIGURE 1.2: Schematic illustration of the results of violating the conditions necessary for the CMF to map the IMF (Offner et al., 2014).

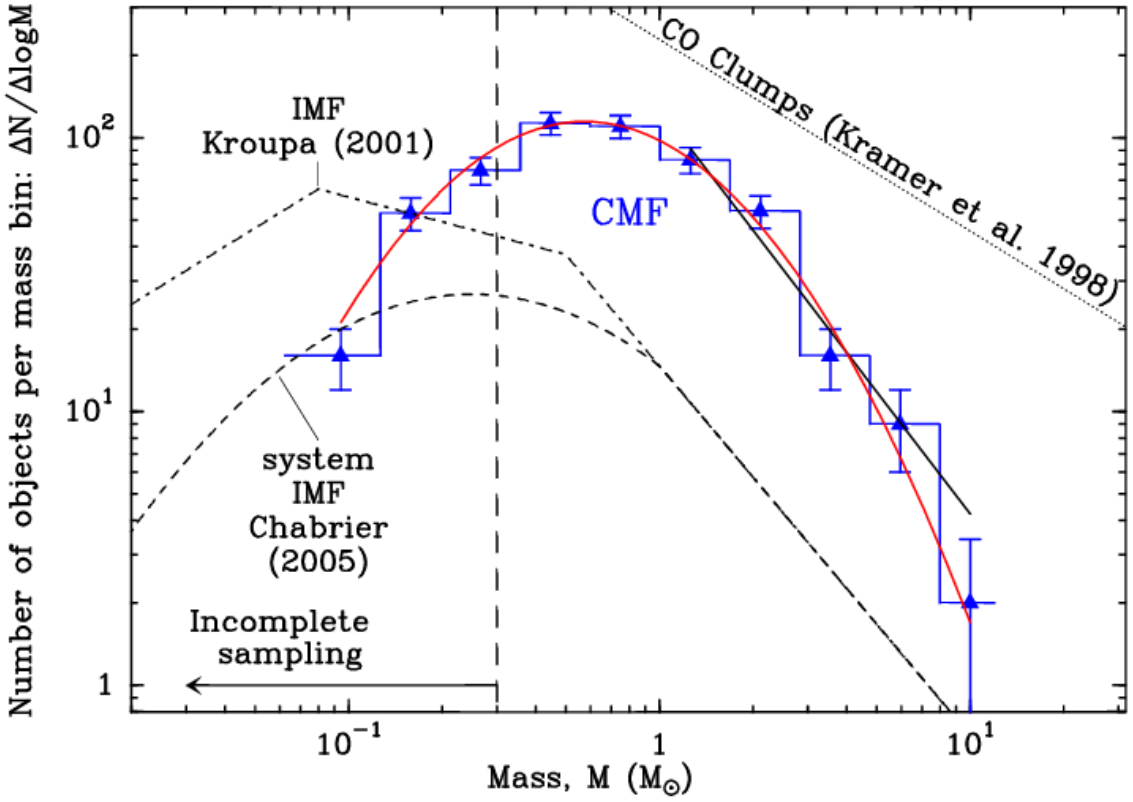

FIGURE 1.3: Differential mass function of starless cores in the Aquila main subfield in comparison with the Kroupa IMF (Könyves et al., 2010).

- **Class I:** these objects are low-mass protostars still surrounded by a remnant envelope and a massive circumstellar disk. The presence of the circumstellar envelope produces an excess of emission in the near- and mid-IR, results in a SED broader than that of a black body. The luminosity in this phase is dominated by the accretion.
- **Class II:** these objects are pre-main-sequence cores known as "classic T Tauri stars" which are visible in the optical wavelengths. At this stage, wind and outflows have swept away the outer envelope and the circumstellar disk is more exposed. The SED peaks at near-IR ($\sim 2\ \mu m$).
- **Class III:** the SED of these objects is similar to a black body, consistent with a reddened photosphere . They do not show significant excess at IR wavelengths, because they have lost almost all their circumstellar dust. Class III objects correspond roughly to "weak-lined T-Tauri stars" (WTTSs). The planet formation occurs during this stage.

1.6 Formation of massive stars

High-mass stars ($> 8M_\odot$), despite their relative low number, have a fundamental influence over the interstellar medium and galactic evolution because they are responsible of the ionization for the surrounding gas and they deposit mechanical energy first via

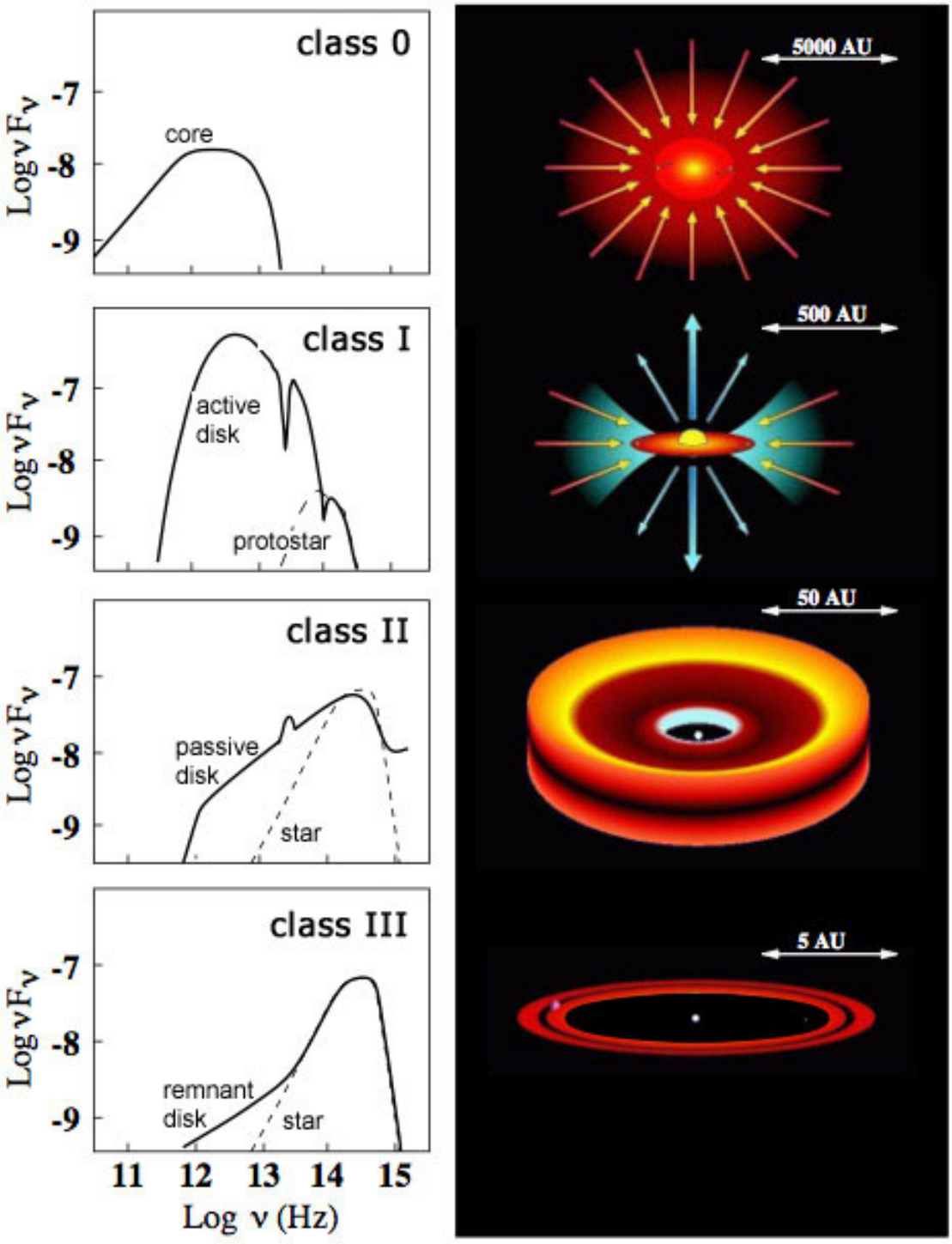

FIGURE 1.4: Stages in the evolution of a protostar. As the interstellar gas cloud begins to collapse, rotation and magnetic fields cause the formation of a disk and a polar outflow. Different stages of evolution are identified by changes in the spectrum of radiation, which is dominated in the early stages by submillimeter radiation from the gas cloud, in the intermediate stages by infrared radiation from the disk, and in the later stages by optical and infrared radiation from the newborn star (Credit: Andrea Isella, http://www.reinervogel.net/index_e.html?/YSO/YSO_e.html).

strong stellar winds and later as supernovae, enriching the interstellar medium by returning unprocessed and nuclear processed material during their whole life. Massive stars therefore condition their environment and supply it with new material available for the birth of new generations of stars, being the triggering mechanism of star formation. They also generate most of the ultraviolet ionization radiation in galaxies, and power the far-infrared luminosities through the heating of dust. The combined action of stellar winds and supernovae explosions in massive young stellar clusters lead to the formation of super-bubbles that may drive in galactic super-winds. Furthermore, massive stars are the progenitors of the most energetic phenomenon nowadays found, the gamma-ray bursts (GRBs), as they collapse as supernova explosions into black holes. However, despite the importance of high-mass stars, their formation out of diffuse interstellar medium is still not completely understood. Therefore, the process of high-mass star formation is a challenging research area that has to explain the time evolution of structures over a wide range of spatial scales: from the large molecular clouds ($\sim$10 pc) that are pervaded by filamentary structures ($\sim$1 pc), which fragment into dense clumps and condensations ($\sim$0.01–0.1 pc), to finally form stellar clusters, disks and stars ($<$1000 AU).

1.6.1 Phases of high-mass star formation

Since massive stars evolve much faster than low-mass stars, their stages of evolution are not well-classified compared to low-mass stars. The earliest evolutionary stages of high-mass stars, when the massive protostars are still embedded in the parent molecular cloud, last only about 15% of their lifetime (Churchwell, 2002). As summarized by Zinnecker and Yorke (2007), this embedded phase can be divided into three stages (see Fig. 1.5):

- **Infrared Dark Clouds (IRDCs):** They are believed to harbour the earliest phases of high-mass star formation and are identified in the late 1990s (Carey et al., 1998; Egan et al., 1998; Perault et al., 1996). They appear as dark, compact sillhouettes against strong mid-IR emission from the galactic plane due to their high extinction factor. IRDCs are typically more massive, and of a higher density, compared to the clouds from which low-mass stars form. Individual dark clouds come in wide range of sizes ranging from tens-of-parsecs to the tiny ($\sim 10^{-2}$ pc) Bok globules (e.g., Tielens, 2005). Observing the ammonia inversion transitions towards a sample of 218 IRDCs in the northern hemisphere indicated that they typically have a rotation temperature of T$<$ 20 K. The hydrogen volume densities in IRCDs are in the order of 10^5 cm^{-3} and their virial masses are between 100 and a few 100 $M_\odot$ (Chira et al., 2013).
  The galactic plane survey performed by the *Herschel* space observatory at mid-IR and sub-millimeter wavelengths provided the possibility to measure the spectral energy distribution (SED) of star-forming clouds (Molinari et al., 2010). By applying a pixel-by-pixel SED fitting method, Peretto and Fuller (2010) found that the dust temperature decreases from 20–30 K in the outer regions of an IRDC to temperatures of 8–15 K in the central regions. Temperature fluctuation play a key role in fragmentation as the local temperature minima are correlated with density peaks. Therefore, the temperature gradient found in the *Herschel* temperature maps confirms that IRDCs harbour embedded structures which are the birth-sites of massive stars.

- **Molecular hot cores:** Very compact ($<$0.1 pc) and dense condensations (n$>10^7$ cm^{-3}) which are formed in IRDCs after the cloud is heated up by newly forming stars. Hot cores have relatively high temperatures ($>$100 K) and are considered to be one of

the first evolutionary signspots of massive star formation. They exhibit a very rich chemistry in complex molecules (e.g., CH_3CN, CH_3OH, CH_3OCHO) as the heat produced by star formation warms up the dust grains and thereby evaporates the icy grain mantles into the gas phase (Ward-Thompson and Whitworth, 2011). Injection of material from the grain mantles into the gas phase also happens during the formation of low to intermediate-mass stars. When the surrounding envelope starts accreting onto the central low-mass protostar, the increased radiation output heats up the surroundings and evaporate the grain mantles. This leads to formation of sources with a rich chemistry in the central inner regions of the protostellar envelope, known as "hot corino" (see e.g., Ceccarelli et al., 2007).

- **HII regions:** These objects are defined as regions of photoionised gas which have been widely used as a signature to search for sites of ongoing high-mass star formation. Once a massive protostar reaches the hydrogen burning phase, it emits large numbers of ultraviolet photons which ionise the surrounding hydrogen gas. The resulting HII region generates strong electron free-free emission at radio wavelengths. Observations reveal that the hot (T$\approx 10^4$ K) regions of ionised hydrogen surrounding the massive protostars, are found in various shapes and sizes (see e.g., Churchwell, 2002; Kurtz, Churchwell, and Wood, 1994). Classic HII regions established around massive stars are of size in the range 1–30 pc. The compact HII regions have sizes between 0.3 pc and 3 pc and the electron density is in the range 2×10^3–3×10^5 cm^{-3}. Ultracompact HII regions (UCHII regions) are those regions with size near or under 0.1 pc and the electron density above 10^5 cm^{-3}. When a massive OB star is formed initially, it is still embedded in the remnant of its accretion envelope and the HII region around the star is extremely compact. Hydrogen burning by the OB star increases the temperature of the surrounding gas from 10 K to 10^4 K, and additionally the number density of particles increases by a factor of 4 due to the conversion of each hydrogen molecule to two electrons and two protons. This leads to rapid expansion of the HII region. The expansion is halted when the ionised region is so large that the number of recombinations within that volume is equal to the number of photo-ionisations.

1.6.2 Towards the theoretical understanding of high-mass star formation

There are two primary models proposed to explain the formation of high-mass stars: (i) monolithic collapse and core accretion (Krumholz et al., 2009; McKee and Tan, 2002; Yorke and Sonnhalter, 2002); and (ii) competitive accretion (Bonnell and Bate, 2006). These two models are based on accretion and the different initial conditions and the physical processes invoked to gather the mass of the massive star.

Monolithic core collapse model: This theory is a scaled-up version of low-mass star formation characterized by higher accretion rates. According to this scenario, all stars are formed via fragmentation of a massive clump under the combined influence of turbulence, magnetic field and gravity. This process continues down to the smallest scales forming cores. A core represents an object which gives birth to individual stars or multiple systems, and its mass determines the mass of the reservoir available to be accreted by the star. Therefore, a massive star must form out of a massive core. As shown in Fig. 1.6, the massive clump collapses monolithically and fragments into a few massive cores, rather than many low-mass objects.

According to this model, the accretion rates towards the star can reach values of 10^{-4}–10^{-3} $M_\odot$ yr^{-1}, high enough to overcome the radiation pressure and build up a massive

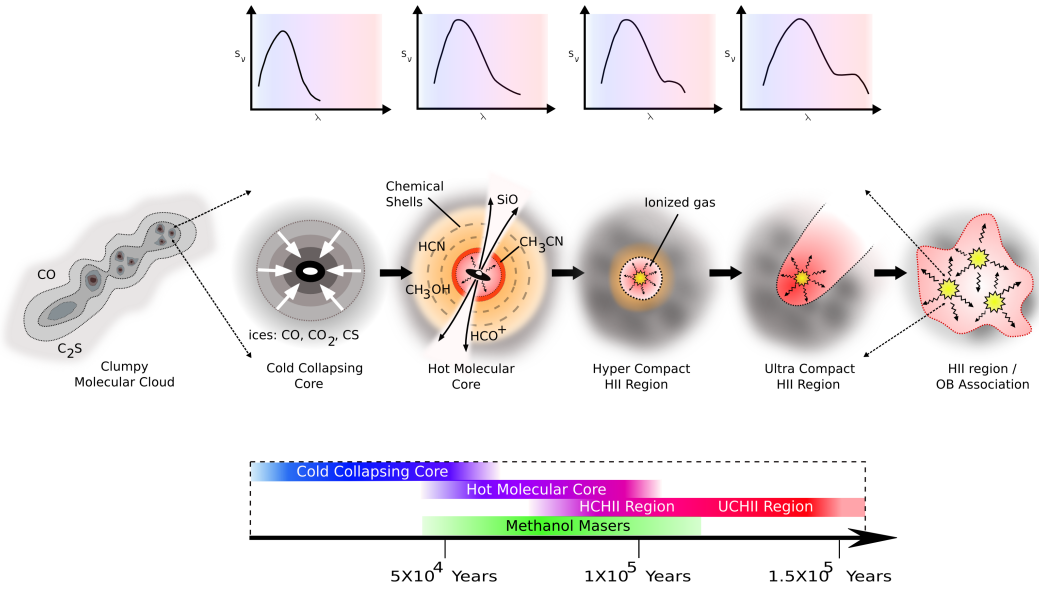

FIGURE 1.5: Observed phases in the birth and early evolution of high-mass stars. The starting point is the clumpy structure of a giant molecular cloud which begins to collapse due to gravity to form a protostar. The protostar continues to accrete mass increasing in mass until it is massive enough that the radiation emitted can ionize the surrounding gas resulting in the formation of a HII region. The HII region expands into the surrounding medium until it disperse its natal material. The top row illustrates the SED associated with each stage and the bottom row indicate the different timescales involved in each stage of evolution (Image credit: Cormac Purcell).

star in relevant time scales (Krumholz et al., 2009). This model can explain the apparent relation between the CMF and IMF. If the stars are directly formed from dense cores, there should be a one to one correspondence between the mass spectrum of stars and that of the cores. However, as mentioned in § 1.5.2, the observed variations of CMF from the canonical IMF calls this correspondence into question.

Although this scenario provides a feasible explanation for the formation of massive stars in isolation, it has exhibited incompatibility with some of the recent observations and simulations. This model claims that the density of massive clumps are high enough to become optically thick and therefore, unable to radiate the heat away. This leads to the suppression of fragmentation and the formation of super Jeans cores. However, several observations and simulations found a population of low-mass fragments rather than a massive condensations towards different star-forming regions (see e.g., Bonnell and Bate, 2006; Clark and Bonnell, 2006; Dobbs, Bonnell, and Clark, 2005; Federrath et al., 2010; Palau et al., 2013; Peters et al., 2011; Pillai et al., 2011; Smith, Longmore, and Bonnell, 2009a,b).

Competitive accretion model: This theory is based on the fact that the most massive stars form in clusters (see e.g., Clarke, Bonnell, and Hillenbrand, 2000; Lada and Lada, 2003). In this scenario, a turbulent clump undergoes fragmentation to produce condensations of gas and dust with masses around M_{Jeans} at Jeans length separations ($\sim$0.05 pc) (Larson, 1984). The role of turbulence in this picture is to drive structures into the clump,

while the fragmentation is regulated by the thermal pressure. Once the individual fragments have been formed, they fall together to form protoclusters which grow through accretion of gas and other fragments. In the hierarchical picture of fragmentation, a fraction of the total available mass in the clumps is converted into cores, and a fraction of cores is converted into stars. Since only a small fraction of the initial mass of a cloud turns into stars, this process is inefficient (Lada and Lada, 2003). Therefore, for the formation of massive stars, an additional mechanism is needed. This mechanism relies on the continued accretion onto a lower mass star due to the global infall of the material. The infall motions are the result of the overall potential well of the cluster which funnels gas from the reservoir down to the potential center. Evidences of these infall motions have been observed in different massive star-forming clumps (see e.g., André et al., 2007; Peretto, Hennebelle, and André, 2007; Pillai et al., 2011; Schneider et al., 2010). The necessary condition for competitive accretion to happen is that the cluster should be bound such that the overall potential can have a significant effect. Moreover, the gas should be free to move. If the gas is fixed due to magnetic fields, then the accretion will be limited.

As indicated by Bonnell et al. (2001), when the gas falls onto a cluster, it passes through two different regimes where the physics of accretion depends on the relative velocities between the stars and the surrounding gas:

- *Gas-dominated phase:* In this regime, the relative gas-star velocities are low. The accretion rate is dominated by the tidal lobes of each star. The star gravitationally attracts the gas which is in its tidal radius. During this stage, the low-mass stars accumulate the majority of their masses.

- *Stellar-dominated phase:* In this regime, the relative velocities between the gas and the stars are large and the accretion is determined by Bondi-Hoyle accretion. The Bondi-Hoyle accretion rate is $\dot{m}_{\rm BH}$

$$\dot{m}_{\rm BH} = 4\pi\rho\frac{(Gm)^2}{\sigma^3}\ [M_\odot\ {\rm yr}^{-1}], \tag{1.5}$$

  where ρ is the gas volume density, m is the mass of the star, G, the gravitational constant and σ, the velocity dispersion of the accreted gas. In this context, only the gas within a radius where the escape velocity is less than the relative gas-star velocity can be accreted. The mass accretion onto an individual low-mass star decreases its kinetic energy thereby sinking it deeper into the cluster potential.

The stars located closer to the center of the cluster have the privilege to accrete a larger amount of material due to the depth of the potential well at the center of the cluster. Moreover, the stars with higher initial masses have higher accretion rates and therefore are favored in the competition for accretion.

1.7 Radiative transfer

Radiative transfer deals with the interaction of radiation with the medium through which it propagates. The interaction of radiation with matter can be typically understood in terms of three processes: absorption, emission and scattering. The formal radiative transfer equation describes the differential change of specific intensity dI at a frequency ν as it passes through a medium which extends from $l = 0$ to $l = L$. Neglecting scattering, the equation is

$$\frac{dI_\nu}{dl} = -\kappa_\nu I_\nu + \varepsilon_\nu, \tag{1.6}$$

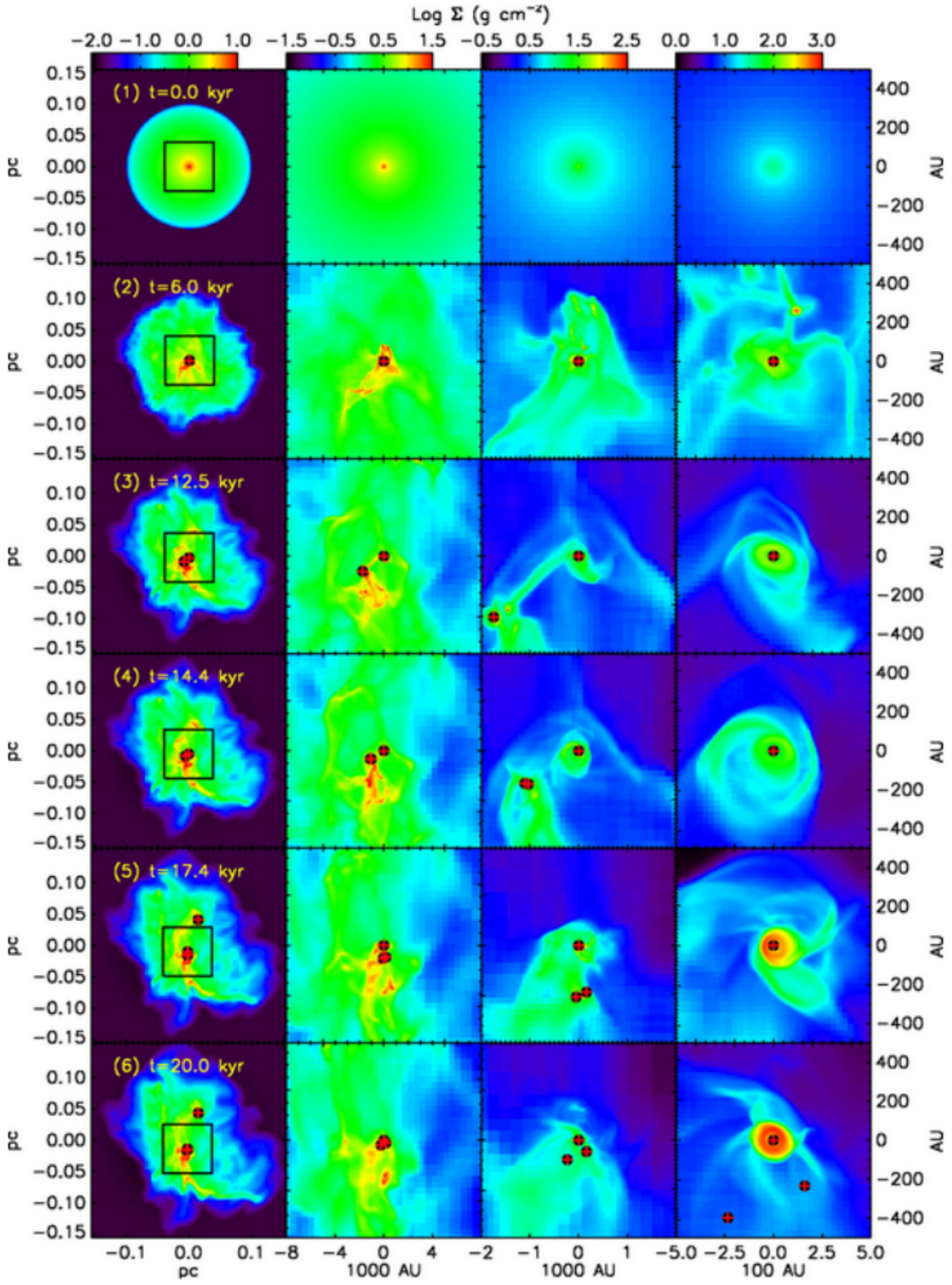

FIGURE 1.6: Monolithic collapse simulations of the column density of gas of an initial massive turbulent condensation with a diameter of 0.2 pc and mass of 100 $M_{\odot}$. From top to bottom, the rows show the evolution at increasing time. From left to right, the size of the region shown decreases by a factor of 4, from a 0.31 pc region in the left column to a 1000 au region in the right column. The black square in the first column represents the field shown in the second column. The formed stars are indicated with red plus signs inside black dots (Krumholz, Klein, and McKee, 2007).

where κ_ν is the absorption coefficient and ε_ν is the emission coefficient of the medium. The first term on the right-hand side represents the attenuation of the intensity and the second term defines the increase in intensity. If we define the optical depth as $d\tau = \kappa_\nu dl$ and the source function as $S_\nu = \frac{\varepsilon_\nu}{\kappa_\nu}$, the radiative transfer equation reduces to

$$\frac{dI_\nu}{d\tau_\nu} = -I_\nu + S_\nu. \tag{1.7}$$

In thermodynamic equilibrium the intensity is uniform ($I_\nu / d\tau_\nu = 0$) and is given by the Planck function $B_\nu(T)$. Therefore,

$$I_\nu = S_\nu = B_\nu(T) = \frac{\varepsilon_\nu}{\kappa_\nu}. \tag{1.8}$$

The general solution of the radiative transfer equation is obtained by integrating Eq. 1.7:

$$I_\nu(\tau_\nu) = I_\nu(0)e^{-\tau_\nu} + \int_0^{\tau_\nu} e^{-(\tau_\nu - \tau')} S_\nu d\tau'. \tag{1.9}$$

The first term on the right-hand side represents the attenuated emission from the source, while the second term represents the self attenuated radiation emitted by the medium.

If the medium is uniform, i.e. $\varepsilon_\nu(\tau_\nu) = \varepsilon_\nu^0$ and $S_\nu(\tau_\nu) = S_\nu^0$, the observed intensity given in Eq. 1.9 simplifies to

$$I_\nu(\tau_\nu) = I_\nu(0)e^{-\tau_\nu} + S_\nu(1 - e^{-\tau_\nu}) \approx \begin{cases} I_\nu(0)e^{-\tau_\nu}, \\ S_\nu^0(1 - e^{\tau_\nu}). \end{cases} \tag{1.10}$$

The first solution is valid if the background intensity dominates and the second one if the emission from the medium dominates. In an optically thin medium ($\tau_\nu << 1$) the second case in Eq. 1.10 represents the emission from the right through the medium

$$I_\nu(\tau_\nu) \approx S_\nu^0 \tau_\nu. \tag{1.11}$$

If the medium is optically thick ($\tau_\nu >> 1$), the emission received by the observer comes from a thin layer at the front of the medium

$$I_\nu(\tau_\nu) \approx S_\nu^0. \tag{1.12}$$

For the basics of radiative transfer, I refer the reader to (Draine, 2010; Rybicki and Lightman, 1986; Ward-Thompson and Whitworth, 2011).

1.8 An observational overview

Since Karl Jansky's first observations in 1932, improvements in technology have increased the sensitivity and angular resolution of radio telescopes significantly and extended the short wavelength limit of radio astronomy from meter to millimeter and sub-millimeter wavelengths. The pioneering efforts of the scientists in the 1950's and 1960's led to remarkable discoveries, including quasars, pulsars, radio bursts from the Sun and Jupiter, giant molecular clouds, interstellar masers and the cosmic microwave background. For over 50 years, the giant Lovell telescope at Jodrell Bank has been an internationally renowned landmark in the world of astronomy. It started operating in 1957 and with its 250-ft parabolic reflector could detect the 21-cm hydrogen line which was discovered

in 1951. In the 1970's, radio astronomers took a great step forward to develop innovative techniques such as very long baseline interferometry, millimeter wavelength spectroscopy, and fast data acquisition and signal processing crucial for the construction of steerable radio telescopes. In 1980, the very long array (VLA) with twenty-seven 25-m dishes and reconfigurable baselines in a 2D Y-shaped array was formally inaugurated. This was a great step forward in sensitivity and angular resolution. During the 1980's, the specialised hardware and algorithms for aperture synthesis imaging with high angular resolution have continued to develop. In mid-1980's, the IRAM 30m as one of the largest and most sensitive telescopes started to explore the universe at millimetre wavelengths. The Australian Telescope Compact Array (ATCA) started operating in 1987 as the premier southern hemisphere aperture synthesis telescope. The observatory at the Plateau de Bure opened a three-antenna interferometer to the world-wide scientific community in 1988. This array then evolved to a ten-antenna array and finally with the inauguration of the seventh antenna in 2014, the observatory transformed into NOEMA (NOrthern Extended Millimeter Array). The 1980's marks the beginning of millimeter and sub-millimeter astronomy as the unexplored region of the electromagnetic spectrum. As we enter the decade of the 1990's, VLBA, the GBT, the Arecibo upgrading project, and the Smithsonian Sub-Millimeter Wavelength Array are the radio telescopes which take the lead in new research initiatives. The recently-found phenomena, such as the gravitational lenses, neutron stars, and the microwave background radiation are resulting from the use of powerful new technologies. Even among the more traditional cosmic bodies, such as stars, planets, and the Sun, radio observations have led toward a much deeper understanding such as the excessive temperature of the Sun's corona and the spectacular low frequency bursts caused by violent electromagnetic activity in the atmospheres of Jupiter and the Sun.

The (sub-)millimeter wavelength astronomy has opened up new opportunities to study the chemistry and the composition of the ISM and the earliest stages of star formation. Dramatic advances in heterodyne spectroscopy of molecular clouds provided a powerful tool to investigate the kinematic details and chemistry of the ISM based on molecular line emission. Moreover, the improved sensitivity and resolution at millimeter and sub-millimeter wavelengths led to the identification of star-forming regions in dark clouds, resolving cloud fragments, protostars, and circumstellar accretion disks. While VLA has been the most widely used radio telescope in the last two decades for a wide range of frequencies from 10 MHz to 50 GHz, ALMA has provided observers with more than two orders of magnitude improvement in the sensitivity and the angular resolution compared to the existing telescopes in the millimeter wavelength range (30-300 GHz). Since the beginning of ALMA scientific observations in 2011, it has covered many important objectives from studying star and planet formation in galactic sources to targeting high-redshift galaxies with the aim of determining their composition and finally to search for the origin of life. For a review of the history of radio astronomy, I refer the reader to Arnold (2014).

This thesis particularly focuses on investigating the properties of the high-mass star-forming regions (in particular NGC 6334) using ALMA observations. The radio astronomy observations generally fall into two main categories: single-dish observations and radio interferometry. The emission which is observed towards astronomical sources via these two techniques is either continuum emission from dust and ionised gas or line emission due to the transition of electrons in different molecules. In the following sections, I elaborate on the techniques of the observations in radio astronomy and the physics of the observed emission by radio telescopes.

1.8.1 Radio astronomy

As this work is based on observing star-forming regions in the (sub-)millimeter regime, I will discuss further about the techniques of radio astronomy observations. Methods for conducting radio observations fall into two categories: single-dish observations and observations made with multiple antennas that are combined together using interferometric techniques. In the following, I present the basic considerations of radio observations made with the single-dish telescopes and the radio interferometers. For a through review, I refer to Marr, Snell, and Kurtz (2015), Perley et al. (1989), and Wilson, Rohlfs, and Huettemeister (2009).

Single-dish observations:

A single-dish telescope consists of a parabolic reflector which collects and concentrates the radiation, a mount that holds and moves the dish, a group of feeds which convert the electromagnetic waves in free space into confined waves in transmission lines, a front-end receiver which provides amplification and frequency conversion, and finally a back-end receiver which measures the amount of power and convert it to a digital signal. In simple types of observations, the power of the radiation coming from the source is measured. The collected power is related to the flux density, F_ν, of the sources using the expression

$$P = F_\nu A_{\rm eff} \Delta\nu, \tag{1.13}$$

where $A_{\rm eff}$ is the effective area of the telescope and $\Delta\nu$ is the frequency bandwidth. The power measured from the source is expressed by its equivalent temperature known as the antenna temperature T_A. To subtract the power due to the receiver noise and other sources of unwanted radiation, the single-dish telescopes observe a nearby patch of sky, known as the off-position, which contains no signal from the radio sources. By subtracting the measured voltage when the telescope points at the source ($V_{\rm on}$) from the measurement when pointed away from the source ($V_{\rm off}$), it is possible to obtain the antenna temperature. The system temperature, $T_{\rm sys}$, which represents the noise level due to different sources (e.g., components of the receiver and background radiation) is determined using a noise diode that calibrates the receiver by producing a known amount of power when the telescope points at on and off positions.

The ability of the telescope to capture the power of radiation is not constant in all directions. The sensitivity of the telescope as a function of angle relative to the pointing direction determines the telescope beam pattern, $P_{{\rm bm}(\theta,\phi)}$. For the telescopes which have a circular primary reflector, the beam pattern is axially symmetric. As shown in Fig. 1.8, the telescope has its maximum sensitivity in the direction at which the telescope is pointed. The central part of the beam, known as the main beam, is approximated as a Gaussian function of the form

$$P_{\rm main}(\theta) = exp\left[-4{\rm ln}2\left(\frac{\theta}{\theta_{\rm FWHM}}\right)^2\right], \tag{1.14}$$

where $\theta_{\rm FWHM}$ is the full width half maximum of the main beam. The angular resolution of the telescope is determined based on the main beam as

$$\theta_{\rm FWHM} = 1.022\lambda/D, \tag{1.15}$$

where λ is the wavelength of the observation and D is the diameter of the primary reflector. For a source with some angular extent on the sky, the radiation from the source is described as $I_\nu(\theta, \phi)$. For unresolved sources whose size is smaller than the main beam, the value of the normalized beam pattern integrated over the extent of the source is equal to unity. Therefore, using the measured antenna temperature, the flux density of the source can be directly measured via

$$F_\nu = \frac{2k}{A_{\rm eff}} T_{\rm A}. \tag{1.16}$$

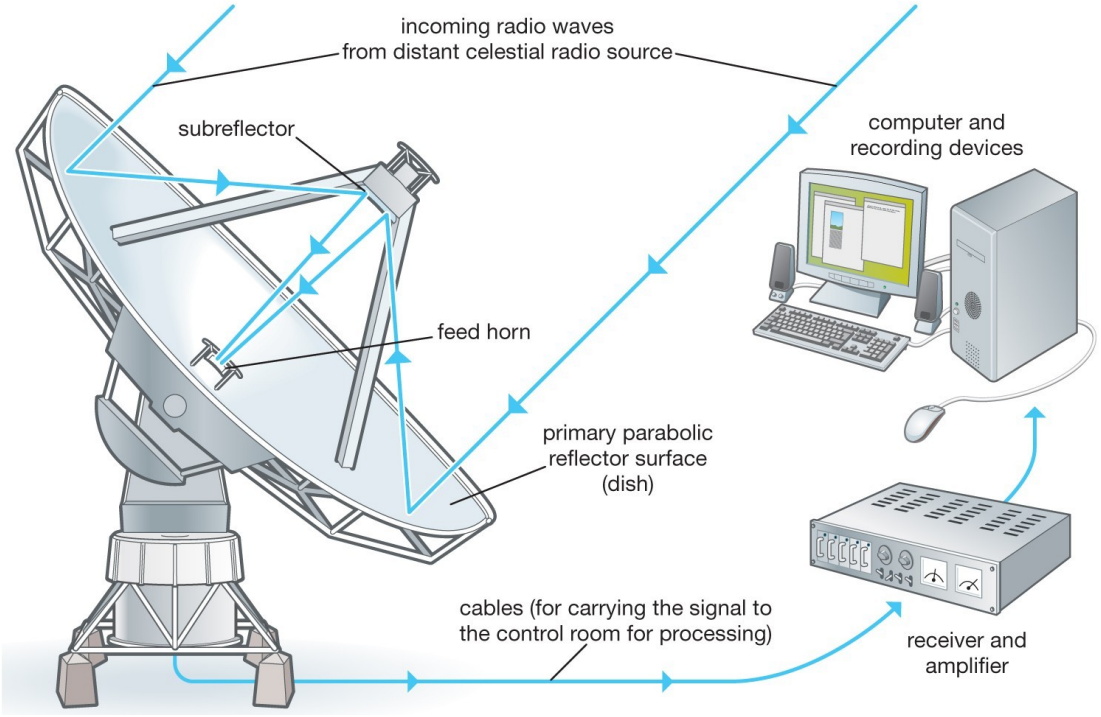

FIGURE 1.7: A prime focus radio telescope and its parts (Credit: https://www.britannica.com/science/radio-astronomy)

For a resolved source whose size is larger than the main beam, the antenna temperature is a measure of the intensity averaged over the main beam expressed as

$$< I_\nu >= \frac{2k}{A_{\rm eff}\Omega_{\rm main}} T_{\rm A}, \tag{1.17}$$

where $\Omega_{\rm main}$ denotes the solid angle of main beam.

Radio interferometry

The resolution of a single-dish telescope is limited by its collecting area. Therefore, interferometry is used as a technique to combine multiple radio antennas and synthesize a new telescope with a very large diameter. Radio interferometers consist of an array of separate single-dish telescopes and their resolution is equal to a telescope whose diameter equals the largest distance between antennas in the array (i.e., the longest baseline). For simplicity, I consider an interferometer with only two elements which are located at a distance ΔS from each other. As shown in Fig. 1.9, the radio signal from a source in

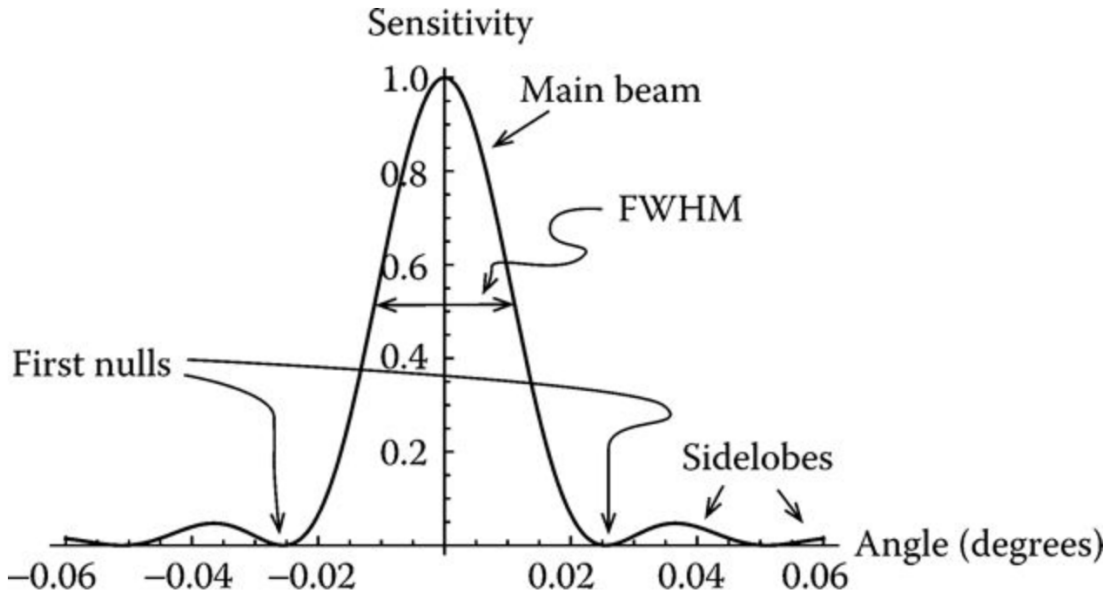

FIGURE 1.8: Beam pattern of a single-dish telescope in one dimension (credit: Marr, Snell, and Kurtz, 2015).

direction θ approaches both antennas along parallel paths. The responses of the antennas, $E_1(t)$ and $E_2(t)$, to the incoming signal have a phase difference of $\Delta\phi = 2\pi\nu\tau$ with $\tau = \Delta S/C$. Once the electric fields are sent to the correlator, they will be multiplied and averaged over time to output the detected power as

$$P_\theta =< E_1.E_2 >= \frac{E_0}{2}\cos(2\pi\nu\tau). \tag{1.18}$$

Taking the rotation of the Earth into account, we obtain the so-called *visibility* function expressed as

$$R = F_\nu \cos\left(2\pi\frac{b}{\lambda}\Delta\theta\right), \tag{1.19}$$

where F_ν is the flux density of an unresolved source and $\Delta\theta$ denotes the position shift of the source. If the science goal is an extended object, the visibility function will be the sum of the visibilities from all the infenitessimal points that make up the extended source. The intensity distribution of a 2-dimensional object relates to its visibility function via the 2-dimensional Fourier transform as

$$V = \int\int I_\nu(x,y)e^{i2\pi(b_x/\lambda)x}e^{i2\pi(b_y/\lambda)y}dxdy. \tag{1.20}$$

Therefore, the Fourier transform of the measured visibilities, as a function of baseline vectors measured in wavelengths yields the sky intensity distribution, i.e. the image of the source. Defining the u and v variables as $u = \frac{b_x}{\lambda}$ and $v = \frac{b_y}{\lambda}$, the visibility can be defined as a function which is measured in the uv-plane, while the intensity is a quantity in the xy-plane. In an array of antennas, apart from the primary beam of each element, the inferferometer as whole has a beam pattern known as the *synthesized* beam which is the Fourier transform of the points in the uv-plane for which the visibilities are measured. The Fourier transform of the points in the uv-plane yields the sensitivity pattern of the

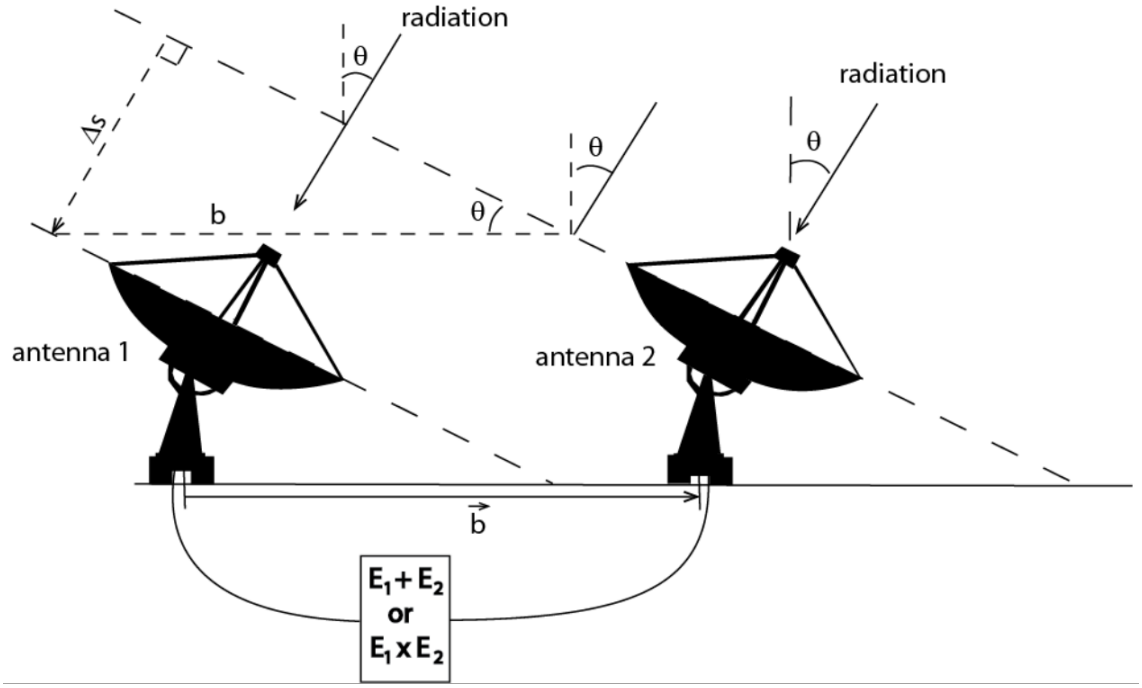

FIGURE 1.9: Observations of a point source in a direction at angle θ. The antennas are separated by a distance b. The extra path length that the wave must travel to reach antenna 1 is denoted by Δs (Marr, Snell, and Kurtz, 2015).

interferometer known as *dirty beam* (see Fig. 1.10). What is measured by an interferometer is the convolution of the true sky intensity with the beam pattern. Therefore, to obtain the final image of the radio source, it is necessary to deconvolve the true intensity of the source from the dirty beam pattern.

The distribution of visibilities (i.e., $u - v$ coverage) in interferometric observations is limited by the shortest distance between the antennas (i.e., shortest baseline). While the longest baseline defines the angular resolution of the observations, the shortest baseline determines the largest recoverable scale of the interferometer. The central hole in the sampling of the $u - v$ plane shown in left panel of Fig. 1.10 arises due to the lack of short baselines. As a result of the incomplete $u - v$ coverage, the flux at short spacing is not recovered. The solution for this problem is to combine the interferometric data with the single-dish observations. Possible methods for data combination are discussed in § 2.2.3.

1.8.2 Molecular line emission

Characterizing the chemical properties of the star-forming regions involves detecting a wide variety of chemical species and evaluating their abundances. In order for a molecule to be observed, a transition from one level to another should be facilitated by the emission or absorption of a photon. The frequency of the photon is proportional to the energy difference between the transition states. However, due to various line broadening effects, the photon that is absorbed or emitted does not have to be exactly at the frequency ν. Instead, we define a line profile $\phi(\nu)$ that describes the susceptibility of the transition to photons of frequency ν.

Molecules have rotational, vibrational and electronic energy levels as illustrated in

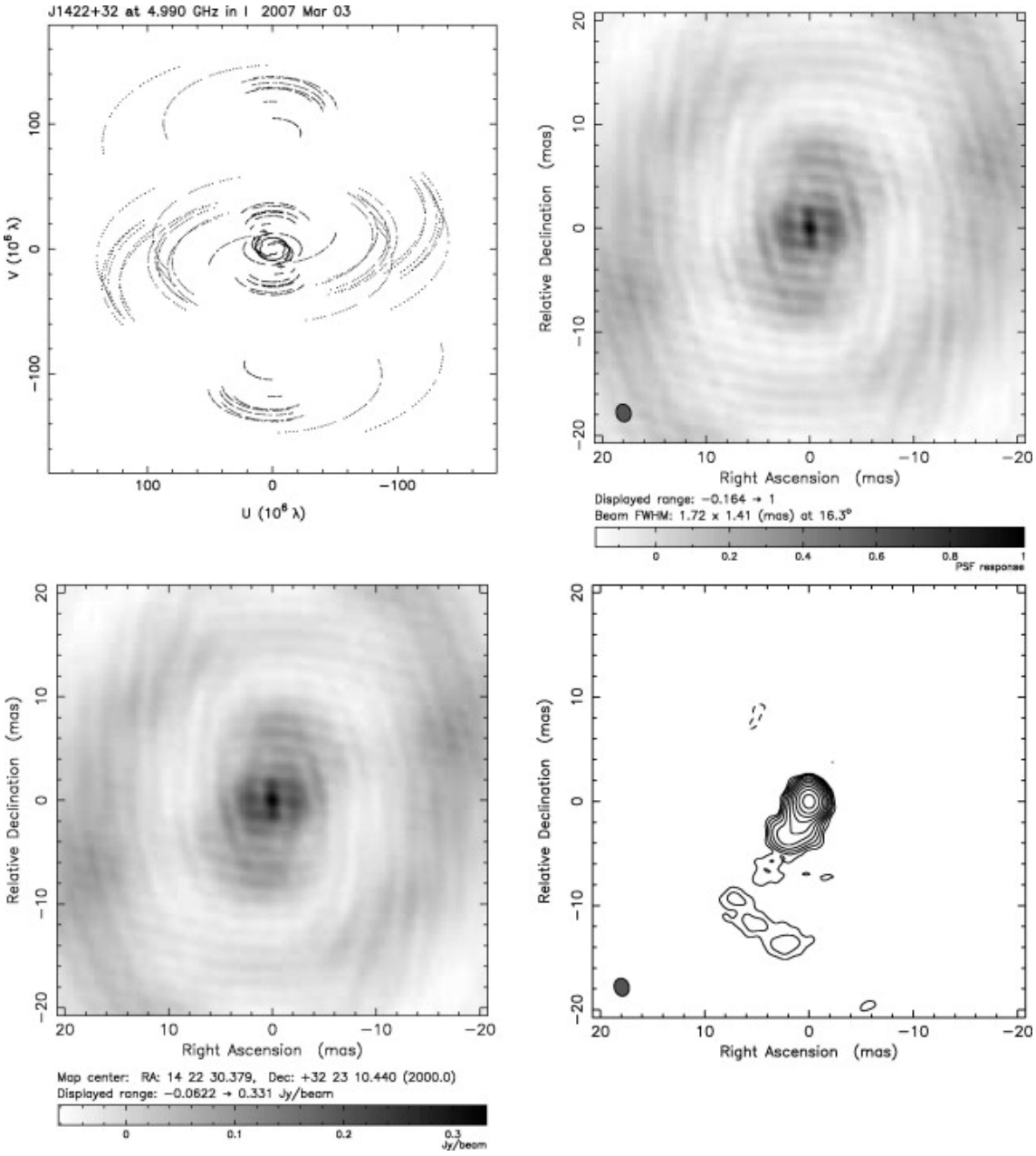

FIGURE 1.10: An example of a $u - v$ coverage (*top left*), a dirty beam (*top right*), a dirty image (*bottom left*), and a clean image resulted from the deconvolution from the dirty beam (*bottom right*) (Frey and Mosoni, 2009).

Fig. 1.11. A change in electronic energy levels require an electron to change molecular orbitals and these changes correspond to the largest energy differences and relatively high energy photons, in the optical and ultraviolet regimes. Changes in vibrational energy levels correspond to photon energies in the infrared region, while differences in rotational energy levels yield photons in the millimeter and sub-millimeter radio regimes at frequencies of ∼30–300 GHz. Due to the low temperature of the interstellar medium (10–20 K), molecules are only rotationally excited. Excitation to an upper energy level can be radiative or collisional. In both cases an electron jumps from a lower energy level to a higher one by gaining extra energy from colliding particles. Once an atom or molecule is excited to a higher level, it can then spontaneously decay to lower levels, emitting radiation. The emission is spontaneous and its rate is determined by Einstein A-coefficient, A_{ij}. During the transition of an electron from a lower energy level to a higher one, if a photon is absorbed, then an absorption line is formed. The rate is determined by B_{ij}, the Einstein coefficient for de-excitation from an upper state to a lower state. Under the LTE (local thermodynamic equilibrium) conditions, the population of each level n_i is given by the Boltzmann distribution expressed as

$$n_i = \frac{N}{Z(T)} g_i exp\left[\frac{-E_i}{(k_B T_{ex})}\right], \tag{1.21}$$

where Z is the partition function and N is the total number of atoms or molecules. In the case of collisional excitation, T_{ex} equals the kinetic temperature T_{kin}. If on the other hand the radiative excitation dominates (non-LTE), then T_{ex} equals the radiation temperature T_R.

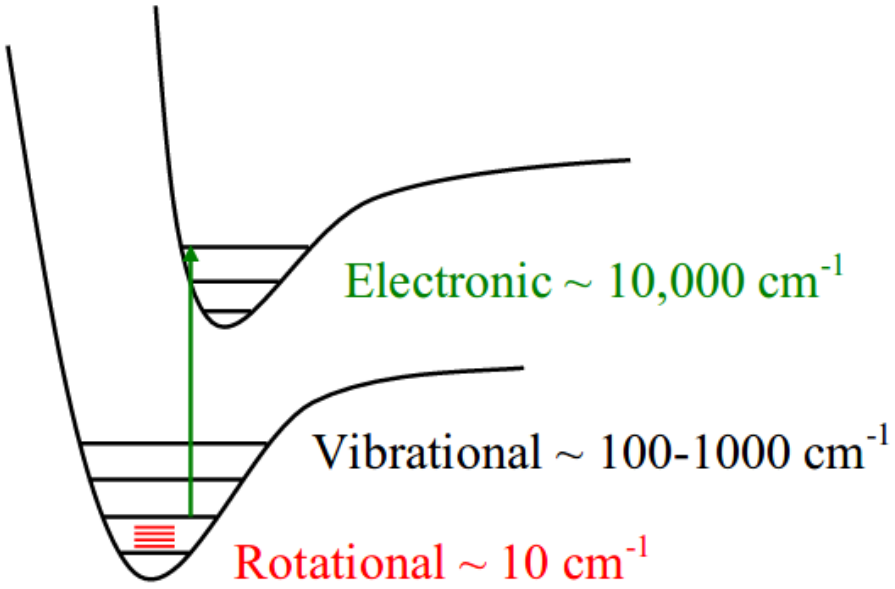

FIGURE 1.11: Energy levels of a diatomic molecule. The potential wells are individual electronic states. Within each of these wells lie vibrational and rotational levels (Credit: http://aro.as.arizona.edu/outreach/UofWashington/ARO12m_03-09-05.pdf).

In order to measure the energies of rotational levels, I focus on a simple diatomic molecule such as CO which is the strongest emitter of millimeter and sub-millimeter emission lines. A diatomic molecule has two axes which can physically rotate around.

These axes correspond to an equivalent moment of inertia defined as:

$$I = \frac{m_a m_b}{(m_a + m_b)} r^2, \tag{1.22}$$

where m_a and m_b denote the masses of the two atoms and r is the bond length of the nuclei. The moment of inertia represents the spacing between the rotational energy levels. The energies of the rotational levels are given by

$$E(J) = \frac{\hbar}{2I} J(J+1), \tag{1.23}$$

where J is the rotational quantum number. Since a photon has spin 1, and thus angular momentum conservation requires the angular momentum change to be ± 1, the transition can only takes place between levels $J \longrightarrow J-1$. The rotational spectrum is unique for each molecule and in case the lines are not blended, it is used to distinguish between different chemical species. Typical symmetric top molecules in the star-forming regions such as CH_3CN have two different moments of inertia. Therefore, their energy level is characterised by two quantum numbers J and K as

$$E(J,K) = \frac{\hbar^2}{2I_A} J(J+1) + \frac{\hbar^2}{2}\left(\frac{1}{I_A} - \frac{1}{I_B}\right) K^2, \tag{1.24}$$

where K is the projection of J onto the principal axis. As a result, the high J transitions consist of many lines exhibiting a so-called K-ladder structure. Using the relative intensities of the K-ladder lines, we can estimate the kinetic temperature. The additional degrees of freedom in polyatomic molecules, spin-orbit coupling and interaction between magnetic field and spin orbit result in further types of transitions such as torsional (e.g. CH_3OH), inversion transitions (e.g. NH_3) and hyper-fine splitting (e.g. HCN). For a detailed read, I refer to Williams and Viti (2013).

1.8.3 Thermal continuum emission

Thermal radiation is defined as the electromagnetic radiation emitted from all matter due the thermal motion of their particles. The intensity and distribution of this type of emission is governed by the temperature of the matter. Interstellar dust and gas emit thermal radiation over a broad range of wavelengths from 10 μm to 7 cm. The observed dust continuum emission is arising from the dust grains as a result of the heating by the absorbed surrounding radiation. The dust emission is often modelled as a modified black body given by

$$I_\nu = B_\nu(T_d)(1 - e^{-\tau_\nu}), \tag{1.25}$$

where τ_ν is the optical depth as a function of frequency and $B_\nu(T_d)$ is the Planck function:

$$B_\nu(T_d) = \frac{2h\nu^3}{c^2} \frac{1}{e^{h\nu/kT_d} - 1}, \tag{1.26}$$

where h is the Planck constant, k is the Boltzmann constant and c is the speed of light (see e.g. Draine, 2010; Ward-Thompson and Whitworth, 2011).

Another type of thermal continuum emission is free-free emission (i.e., bremsstrahlung) from the ionized gas. This emission is produced by an electron/proton pair when the electron is decelerated due to its interaction with the Coulomb field of the proton. As a result of the deceleration, the electron emits a photon bringing away part of its kinetic

energy. Since the assumption of local thermodynamic equilibrium is valid in the ISM, the source function of the emitting matter (i.e., HII region) is approximated to the Planck function at temperature T_0. Assuming that the HII region has a uniform temperature and the background emission is negligible, the free-free emission has an intensity given by

$$I_\nu(\tau_\nu) = B_\nu(T_0)[1 - e^{-\tau_\nu}], \tag{1.27}$$

where the optical depth, τ_ν, is a function of the electron and proton number density along the line of sight (see e.g. Draine, 2010; Tielens, 2005; Ward-Thompson and Whitworth, 2011).

To investigate the physical mechanisms that produce radio continuum emission in star-forming regions, it is necessary to determine the spectral index by fitting the spectral energy distribution (SED) of each source over a wide range of wavelengths. The spectral index measures the dependence of radiative flux density on frequency. Given a radiative flux density of S_ν at a frequency of ν, the spectral index α is given by

$$S_\nu \propto \nu^\alpha \tag{1.28}$$

The spectral index of the emission from an optically thin thermal plasma is -0.1, whereas for an optically thick plasma it is 2. Therefore, a spectral index of -0.1 to 2 at radio frequencies often indicates thermal emission, while a steep negative spectral index typically indicates synchrotron emission.

1.9 The NGC 6334 high-mass star forming complex

At a relatively nearby distance of 1.3±0.3 kpc (Chibueze et al., 2014), NGC 6334 is a high-mass star forming complex that lies in the Carina-Sagittarius arm of the Milky Way. It appears as a giant filamentary cloud with a length of 100 pc in the southern hemisphere, -9° west of the Galactic center. In the last years, NGC 6334 has been the target of multiple studies at different wavelengths from radio to X-ray bands in dust continuum emission, molecular line emission and ionized gas (see e.g. Persi and Tapia, 2008; Russeil et al., 2010, 2013). At far-infrared and (sub)millimeter wavelengths, the central part of NGC 6334, consisting of a 12 pc long filament, reveals several dense clumps with masses larger than 100 $M_\odot$. The high-mass clumps, likely pinpointing sites of active star formation, are at different stages of evolution. The five main regions which were identified in infrared images for the first time, are labelled as NGC 6334-I to NGC 6334-V. All the regions except one are associated with compact and ultra-compact HII regions that are traced by the 70 μm emission in the *Herschel* observations (Russeil et al., 2013). In addition to the five main sources, a number of dense condensations were identified along the inner part of the filament. The most prominent source among them is NGC 6334-I(N) located to the north of NGC 6334-I which was first detected at 1 mm (Cheung et al., 1978) and later at 400 μm (Gezari, 1982). At large scales, the physical properties of the whole molecular cloud such as the temperature and the column density are determined by *Herschel* observations at 150, 250, 350 and 500 μm (Russeil et al., 2013). The velocity field and dynamic status of the cloud have been studied using *APEX* observations of ^{13}CO and HCO^+ molecules. The velocity field reveals a large-scale velocity gradient (~ 0.07 km s^{-1} pc^{-1}) that is interpreted as the imprint of the original rotation of the molecular cloud (Zernickel, 2015). Moreover, the HCO^+(3–2) line emission in the central 12 pc of the filament can be modeled as a gravitationally collapsing cylinder of gas, suggesting that NGC 6334 is undergoing both, rotation and collapse (Zernickel, Schilke,

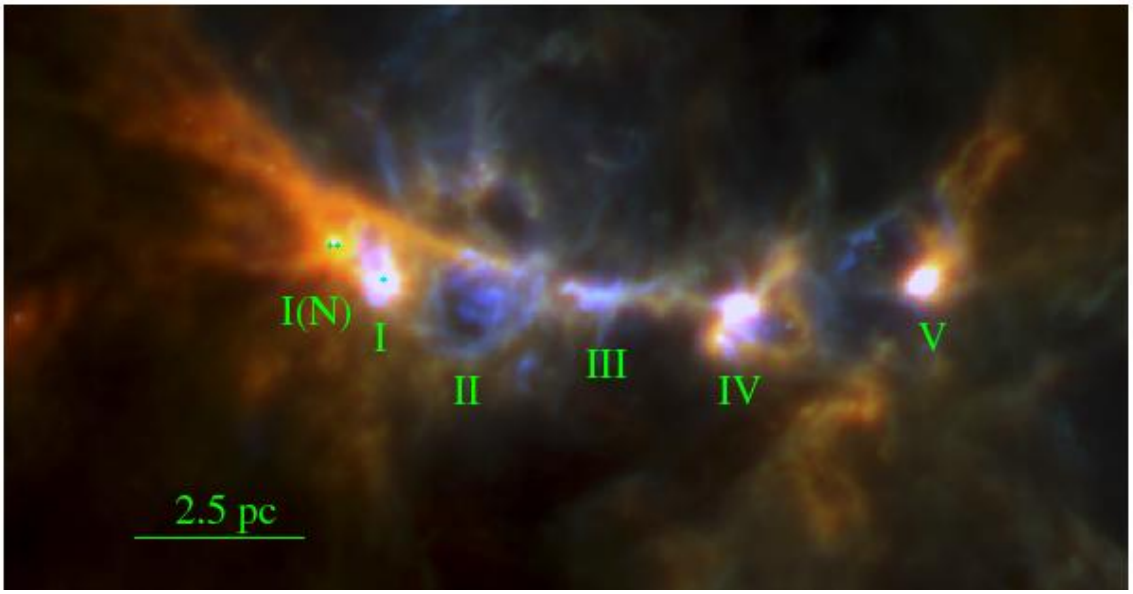

FIGURE 1.12: Three-color image of central part of NGC 6334. The positions of the active star-forming regions are highlighted via contrast enhancement (Russeil et al., 2013).

and Smith, 2013). Combining the mass distribution map with the velocity information results in a mass accretion rate of $10^{-5}\ M_{\odot}\ \mathrm{yr}^{-1}$ throughout the filament which increases up to $10^{-3}\ M_{\odot}\ \mathrm{yr}^{-1}$ towards the central 12-pc region where high-mass star formation is occurring (see e.g. Sánchez-Monge et al., 2015; Zernickel, Schilke, and Smith, 2013). The magnetic field strength studied with the Zeeman observations of OH and HI resulted in a value of $B = 200\ \mu$G for the dense clumps. Moreover, the magnetic field maps inferred from the polarimetric observations show that the mean magnetic field orientation in NGC 6334 is perpendicular to the long axis of the filament (e.g. Juárez et al., 2017; Li et al., 2006; Li et al., 2015; Zhang et al., 2014).

In the present work, I focus on the study of two of the most prominent star-forming regions in the NGC 6334 filamentary cloud: NGC 6334-I and NGC 6334-I(N). NGC 6334-I located at northern end of the inner filament, contains a cluster of stars visible in the near-infrared (Seifahrt et al., 2008; Tapia, Persi, and Roth, 1996) and a cometary ultracompact HII region (also known as NGC 6334-F; Carral et al., 2002; de Pree et al., 1995). SMA observations at 1.3 mm at $1.6''$ resolution revealed the presence of four millimeter sources in a Trapezium-like cluster (Hunter et al., 2006). Two of these sources are classified as hot cores due to their rich chemistry in complex organic molecules and high temperatures above 100 K (MM1 and MM2). In addition to the previously known sources, ALMA observations at 1.3 mm with a resolution of $0.17''$ revealed 5 new compact millimeter sources (Brogan et al., 2016). Furthermore, the observations revealed that MM1 is resolved into at least seven components within a radius of 1000 au. The second massive hot core, MM2 shows a lower level of multiplicity, being resolved into two components.

The embedded source NGC 6334-I(N), located to the north of NGC 6334-I, contains a group of Class I and Class II methanol masers (Walsh et al., 1998). SMA observations at 1.3 mm with a resolution of $2''$ revealed a bright millimeter source which is composed of four components (Brogan et al., 2009). Hunter et al. (2014) conducted new observations with the SMA and the VLA at angular resolutions of $0.5''$ which revealed a richer cluster

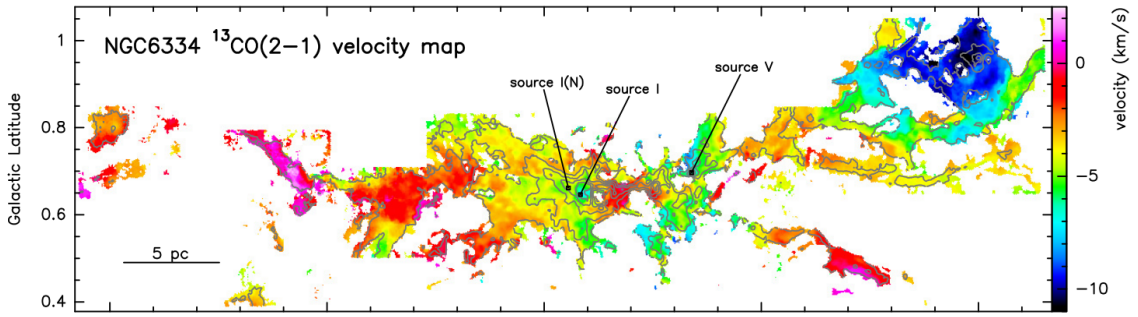

FIGURE 1.13: Velocity field as seen with the ^{13}CO (2-1) line observed with *APEX*. The filamentary structure has a general velocity gradient from east (red-shifted) to west (blue-shifted). Grey contours show the integrated intensity emission of the ^{13}CO (2–1) line (Zernickel, 2015).

with a total of 25 members. All components have spectral energy distributions (SEDs) consistent with that of dust except for one which is associated with an HII region. The detection of line emission from molecules such as CH_3CN allows to identify a number of hot cores in the central part of the cluster.

1.10 About this work

Embedded clusters (i.e., protoclusters) are the primary laboratories to constraint the physical processes of (high-mass) star formation. At the earliest stages of star formation, protoclusters are dominated by the dust content, being bright at (sub)mm wavelengths. At these stages, the interaction between the different cluster members, as well as the properties of the environment, can determine the fundamental cluster properties such as the CMF (and eventually the IMF), the spatial distribution, and the multiplicity fraction. These are essential properties that all theoretical models of (high-mass) star formation aim to reproduce (e.g. Lee and Hennebelle, 2016), and for which the observational constraints are fundamental.

In connection with the process of protocluster formation and stellar feedback, shocks are expected to be observed ubiquitously within the star-forming clusters. Feedback originated at small scales due to outflows or winds, or at larger scales due to collisions between clouds/clumps needs to be better understood in terms of cluster formation.

Finally, recent observations with the *Herschel* space observatory have shown the importance of filaments in star formation, as cores and clusters are embedded in or along filamentary structures. In the case of high-mass star formation, it is necessary to maintain a high gas accretion rate, and filamentary flow may be one method of achieving this Myers (2012). Furthermore, increasing observational evidence has shown that converging parsec-scale molecular gas filaments are likely one of the dominant modes of star cluster formation (see e.g. Galván-Madrid et al., 2013; Liu et al., 2015). However, it is crucial to establish from observations how these filaments break down on ∼5000 au scales to feed the different clusters, and the members within the clusters.

At a scale of a few hundred au, theoretical models and observational evidences lend support to the hypothesis of disk-mediated accretion towards B- and O-type stars (e.g. Beltrán and de Wit, 2016; Krumholz, Klein, and McKee, 2007; Kuiper, Yorke, and Turner,

2015). Therefore, searching for accretion disks around massive stars is of overwhelming importance for our understanding of the accretion process at small scales. To further explore the physical properties of massive protoclusters, characterising shocked gas within the clusters and studying mass accretion towards them, we have conducted high-resolution ALMA observations to image the two nearby high-mass star forming clusters NGC 6334-I and NGC 6334-I(N) as well as the gas that connecting them to the large-scale filament. This thesis is organized as follows:

- In Chapter 1, I give an overview on the star formation and present a brief introduction to radio observations towards star forming regions.
- In Chapter 2, I present our observations conducted towards the high-mass protoclusters in NGC 6334. Moreover, I describe the process of data reduction which yielded the maps and data cubes used for the scientific analysis.
- In Chapter 3, I present the detailed analysis performed on the continuum data of NGC 6334-I and -I(N) to study the physical properties of these two massive protoclusters.
- In Chapter 4, I present the physical properties of gas (e.g. temperature and column density) towards the observed region in NGC 6334. Moreover, I take advantage of the dense gas tracers to study the transport of material from the filament to the protoclusters.
- Chapter 5 focuses on characterizing the shocked gas within NGC 6334-I and NGC 6334-I(N). In this chapter, I present the methods applied to identify the SiO features across the observed region and possible ways to separate outflows from slow shocks.
- Finally, I summarise the main conclusions of this thesis in Chapter 6.

Four appendices are presented at the end of this work to complement the analysis previously described. In Appendix A, I present the catalogs of properties of the ALMA continuum sources and the observed properties of the shocked gas features in NGC 6334. In Appendix B, I present the catalog of identified SiO emission structures together with their physical and dynamical properties. In Appendix C, I briefly describe the softwares and packages used to analyse the observational data. Finally, in Appendix D, I include the additional maps to be analysed in the future works.

Chapter 2

Observations and data reduction

In this chapter, I elaborate on acquisition and preparation of the science data sets which are used in this thesis work. The majority of the analysis presented in the thesis is based on the data observed with the Atacama Large Millimeter/submillimeter Array (ALMA). Additionally, I took advantage of the IRAM 30m telescope to obtain the zero-baseline length as a auxiliary data set for the ALMA observations.

2.1 Atacama Large Millimeter/submillimeter Array (ALMA)

The Atacama Large Millimetre/submillimetre Array (ALMA), located in the Atacama Desert of Northern Chile at an altitude of over 5000 m, is the largest ground-base aperture synthesis telescope. It operates over a broad range of observing frequencies in the millimeter and submillimeter regime from 80 GHz to 950 GHz (0.31 mm–9.5 mm). The telescope is composed of 50 antennas with a size of 12 meters in the 12-m array, closely spaced 12 antennas with a size of 7 meters known as the Atacama Compact Array (ACA), and four 12 m antennas known as the Total Power (TP) array for single-dish observations. In the most compact 12-m array configurations with a maximum baseline of $\sim$160 m, the array could reach a resolution of 4.8″at 110 GHz. In the most extended configuration of the 12-m array, the maximum baseline of $\sim$16 km results in a resolution of 0.43″at 110 GHz. While the 12-m array is used for high-resolution observations, the compact array provides us with the opportunity of wide-field imaging of extended structures. The 7-m Array samples the intermediate baselines from 9 m to 32 m to recover the missing information of short *uv*-spacing. The ALMA TP array fills in the baseline coverage from 0 m to 12 m, complementing the coverage of 12-m and 7-m arrays.

The wavelength range covered by ALMA is accommodated by ten receiver bands. Each receiver band is tuned to operate in one of the atmospheric transmission windows. The front-end receiver contains a set of local oscillators and mixers which convert the observed frequency (RF) to a lower frequency (IF) which experience a smaller loss of power in the transmission line. The IF covered by the receiver changes from 4 GHz to 12 GHz. Once the voltage-based signals exit the mixer, they will be transferred to a correlator by which they are multiplied and averaged over time. Then, the correlator delivers complex fringe visibilities which result in synthesized images after calibration. The signals received by ALMA are processed by two different correlators: the 64-input correlator which is used by the 12-m array and the ACA correlator which is adopted by the 7-m array and the Total Power array. Both correlators can run simultaneously or independently. Each correlator is capable to accept eight 2 GHz bandwidth signal streams consisting of four base bands and two polarizations which results in multiple spectral windows (SPWs) within the bands. The spectral windows are composed of uniformly

spaced spectral channels whose width represent the spectral resolution once the spectral profile is deconvolved from the spectral resolution function. The spectral resolution function is given by Fourier transform of weighting function applied to the correlation function. Assuming that the data is smoothed by the Hanning weighting, the spectral resolution of the ALMA data will be two times the channel spacing. The width of the channels range between 3.8 kHz and 15.6 MHz and each data cube can have up to 3840 spectral elements.

The sensitivity of the observations is a function of the system temperature as well as the total collecting area, bandwidth and the integration time. For continuum observations, a broad spectral window with a total bandwidth of 1875 MHz centered at a specific frequency is used. While, for the line emissions the size of bandwidth is about a few tens of MHz to reach a fairly high spectral resolution.

The outstanding capabilities of the current ALMA array has led us to achieve a fundamental understanding in a wide range of scientific studies from the formation of galaxies in the early universe to the processes of star and planet formation down to solar system scales.

FIGURE 2.1: The Atacama Large Millimeter/submillimeter Array. (Credit: A. Marinkovic)

2.2 ALMA observations toward NGC 6334

The two high-mass protoclusters NGC 6334-I and NGC 6334-I(N) as well as the gas that connecting them to the large scale filament were observed with ALMA during its cycle 3 from April 2016 to September 2016, under the project number 2015.1.00230.S. We used the 12-m array consisting of 40-43 antennas and the compact array with 8-9 7m-size antennas. We covered an area of $120'' \times 120''$ around each source, using 17- and 7-pointing

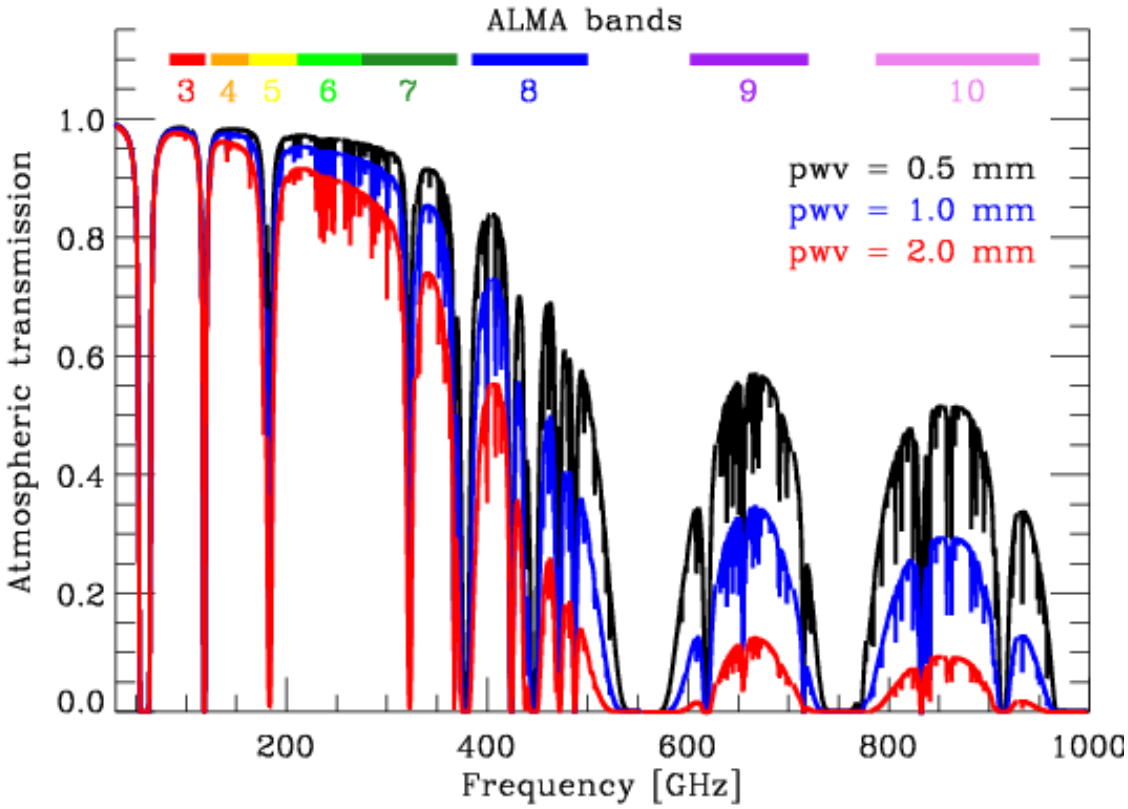

FIGURE 2.2: Atmospheric transmission at Chajnantor Plateau, the ALMA site, with different amounts of precipitable water vapor. The horizontal colored bars indicate the frequency ranges of the ALMA bands.

mosaics for the main array and ACA, respectively. The centers of the mosaics were set to α(J2000)=17$^{\rm h}$20$^{\rm m}$53$^{\rm s}$.0, δ(J2000)=−35°46′59″.0 for NGC 6334-I, and α(J2000)=17$^{\rm h}$20$^{\rm m}$54$^{\rm s}$.0, δ(J2000)=−35°45′06″.0 for NGC 6334-I(N). This coverage results in a small overlap between the two mosaics. The 12-m array provided minimum and maximum baselines of 14–626 m. This corresponds to 1.4″–25″ in angular scales with the main array at 88 GHz. The two extended and compact configurations are chosen such that the observed angular scales have overlap. Therefore, the two sets of data obtained from the main array and the compact array combined together will result in a final scale coverage from 1.4″–40″.

The ALMA correlator was configured to cover specific frequency ranges within the band 3 of ALMA. A broad spectral window with a total bandwidth of 1.875 GHz centered at a frequency of 87.6 GHz was used to be sensitive to the continuum emission. Twelve additional units with a bandwidth of 58.59 MHz and a spectral resolution of 141 kHz (or 0.4 km s^{-1}) were tuned at the frequencies of specific molecular transitions of dense gas tracers (e.g. HCN, HCO$^+$, CH_3CCH), ionized gas tracers (e.g. H42α) and shock tracers (e.g. SiO). The molecular transitions covered in our ALMA observations as well as their frequency and spectral resolution are listed in Table 2.1. Fig. 2.3 shows the amplitude versus baseline for H^{13}CO$^+$ data observed with the 12-m array and the ACA. The data obtained with the main configuration overlaps with the ACA data for baselines in range 50–66 m.

TABLE 2.1: Specifics of the ALMA observations.

Transition	Frequency GHz	Bandwidth MHz	Velocity Resolution km/s	Type of gas
$HC^{15}N$	86.054	0.141	0.492	high density gas
NH_2D	85.926	0.141	0.492	low density gas
H42α	85.688	0.141	0.494	ionised gas
CH_3CCH	85.449	0.141	0.495	high density gas
$HN^{13}C$	87.090	0.141	0.486	low density gas
SiO	86.847	0.141	0.487	shocked gas
$H^{13}CO^+$	86.754	0.141	0.488	low density gas
$H^{13}CN$	86.340	0.122	0.424	high density gas
HCO^+	89.188	0.122	0.410	low density gas
$H^{15}NC$	88.865	0.141	0.476	low density gas
HCN	88.631	0.122	0.413	high density gas
CCH	87.316	0.141	0.484	low density gas
Continuum	87.600	1875.00	106.942	–

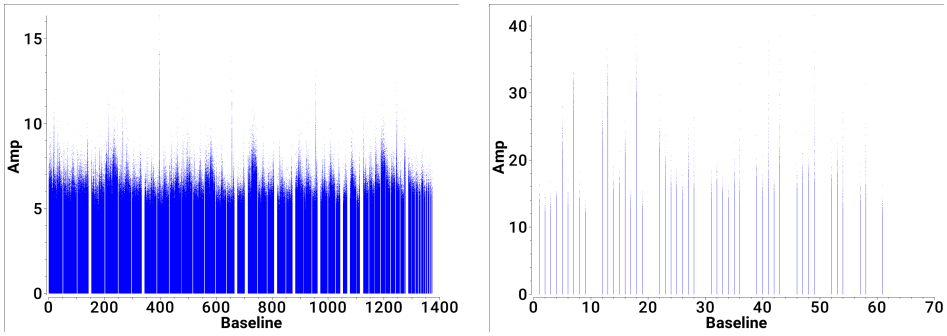

FIGURE 2.3: Amplitude (in Jy beam^{-1}) against baseline (in m) for the $H^{13}CO^+$ data obtained with the 12-m array (*left*) and the ACA (*right*). These two data sets overlap in baselines ranging from 50 to 66 m.

2.2.1 Calibration

For a variety of reasons arising either from the atmospheric effects or instrumental variations, the observed visibilities can be corrupted from their true values. Therefore, calibration is a crucial step to correct the measured visibilities and obtain the true visibilities. The calibration process includes three main steps, namely: flux calibration, gain/phase calibration and bandpass calibration. The ideal source to use as a calibrator is a bright point source for which all baselines in the interferometer measure the same amplitude and zero phase (Marr, Snell, and Kurtz, 2015).

The flux calibration is done by observing a point like source whose visibility has a known form and is relatively stable in flux density. In case of our ALMA observations, flux calibration was obtained through observations of the bright quasar J1733−1304 (with a flux of 3.63 Jy at 91.5 GHz, and spectral index of -0.53) and the planet Neptune.

Interferometric observations need to include a phase calibrator which corrects for temporal variations in the phase over the course of the observations. In a commonly employed observing procedure the flux calibrator is used to calibrate the amplitudes of

the phase calibrator. Then, the phase calibrator is used to calibrate the amplitudes and phases for the rest of the observation. It is necessary to note that the phase calibrator needs to be close to the science target in order to trace the same atmospheric variations through which the radio waves propagate when observing the scientific target. In our ALMA observations the phase was calibrated by interleaved observations of the quasar J1717−3342 (flux 0.639 Jy at 91.5 GHz, with a spectral index −0.32). The phase calibrator was observed every eight minutes. This time interval is short enough to correct for the variations in the atmosphere, and therefore, the variations in the phase of the science target can be derived by linear interpolation between consecutive observations of the phase calibrator.

When observing in spectral line mode, a bandpass calibration is also needed to correct for the frequency response across the bandpass. The bandpass calibration is accomplished by observing a bright continuum source of known spectral shape. In the case of our ALMA observations the bandpass response was obtained by observing the bright quasars J1617−5848 (flux 0.9 Jy at 103.5 GHz) and J1924−2914 (flux 5.75 Jy at 91.5 GHz).

The ALMA observations of NGC 6334 were calibrated in Common Astronomical Software Application[1] (CASA) 4.7.2 version using the calibration pipeline scripts. CASA is a data reduction suit for the processing of ALMA and VLA data. The CASA infrastructure consists of a set of tasks and tools necessary for calibration, imaging and basic analysis of a given data. CASA can be run via an IPython interface which provides flexibility to process the data via task interface or as a python script. In the following sections, I present the process of self-calibration, imaging and data combination using CASA.

Self-Calibration

After deconvolution (see § 2.2.2), the SNR (signal-to-noise ratio) and the fidelity of the map can be substantially improved. Besides incomplete *uv*-coverage, there are variety of factors such as instability of the troposphere and electronics of the antenna which degrade the quality of an interferometric image. Due to these variations the correction factors obtained by observing the calibrators will not be valid for the science target and therefore, require additional correction on shorter timescales. To eliminate the errors in phase of the visibilities, the so-called self-calibration process can be applied to the visibilities. Self-calibration is an iterative process which uses a bright source in the observed field to better calibrate the complex gains (amplitude and phase) as a function of time. As the first step, we make an initial clean map which will be used as a *model* for the following steps. The model phases are expected to be closer to the true value than the measured phases because of the cleaning process. Next, the solutions taken from the model are applied to the calibrated visibilities and the new data set is then used to make a new clean map. The new clean map serves as a new model, which is used in another round of self-calibration. The entire process is repeated over and over until the clean map no longer shows improvement.

In the case of our ALMA observations the continuum emission in source NGC 6334-I is bright enough to self-calibrate the data. Three iterations of phase-only self-calibration on the ALMA-12m data led to a considerably improved image as shown in Fig. 2.4. During the course of the ALMA observations, the gain calibrator has been observed every 8 minutes. A good choice for the time interval in the initial phase-only self-calibration is the scan length per field. Then, it has to get shorter in the following iterations in order to better track faster variations of the phases. To self-calibrate our ALMA data, the time

[1] https://casa.nrao.edu/

interval is chosen to be 180 seconds in the first iteration and decreased to 45 seconds in the final iteration. In the final continuum map the noise level is 10 times lower compared to the original map, and therefore, the faint compact sources appear to be much more pronounced (see Fig. 2.4). Fig. 2.5 shows the distribution of the intensities of each pixel in the ALMA continuum map before and after self-calibration. As presented in the figure, the width of the distribution as a measure of the noise in the map is significantly smaller in the self-calibrated continuum map.

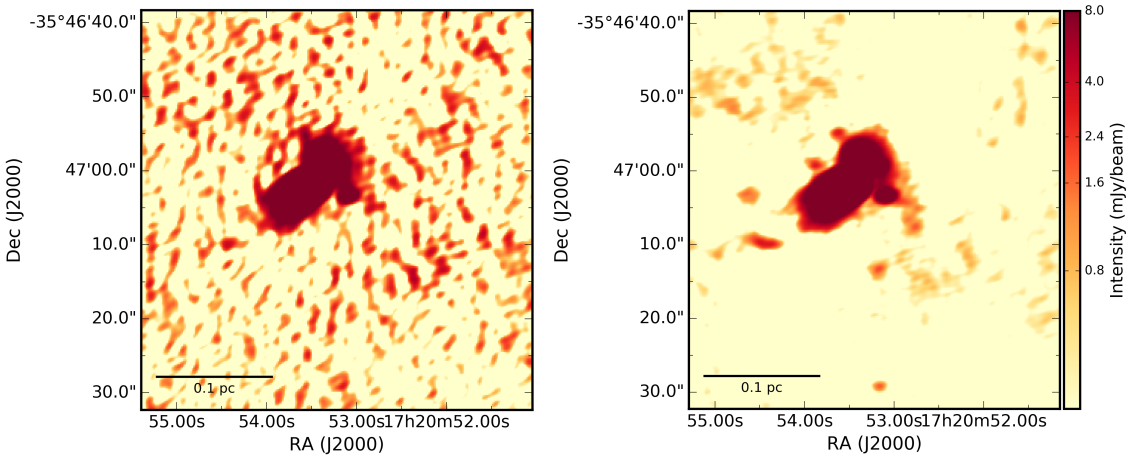

FIGURE 2.4: Progression of the self-calibration iterations. The images show, from left to right, the initial continuum image and the same field after three iterations of phase-only self-calibration.

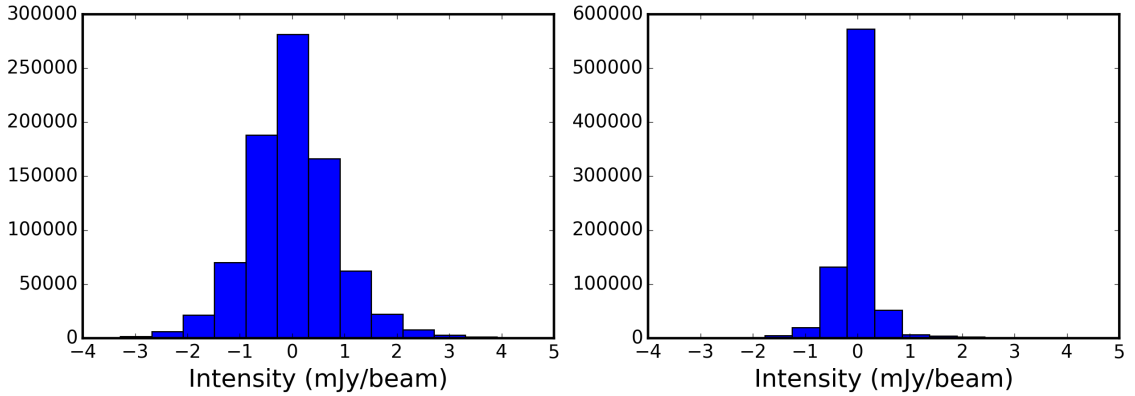

FIGURE 2.5: Distribution of intensities of each pixel in the ALMA continuum map before and after self-calibration (left to right). The width of the distribution as a measure of the noise level is significantly smaller in the self-calibrated map.

2.2.2 Construction of images and data cubes

Fourier transform of the points in the *uv*-plane results in the dirty beam of an interferometer. What we measure with an interferometer is a convolution of the true sky intensity with the dirty beam. In the course of the `CLEAN`ing process the flux density of the science

goal is deconvolved from the dirty beam. Then, it will be convolved to a new beam pattern which reflects the resolution of the observations.

After the calibration was applied to the 12-m and ACA data, the line-free channels of the broad spectral window were identified and used to create continuum images. The CLEANing process was performed with the task TCLEAN available in CASA version 4.7.2 using the multi-scale synthesis as a deconvolution algorithm. This algorithm develops an automated mask that operates in every major cycle of cleaning to identify regions of significant emission. In order to produce a mask, the multi-scale synthesis algorithm uses the residual images to identify significant peaks and then expands the mask to include emission associated with these peaks down to lower signal to noise. Compared to the other deconvolution algorithms (e.g. Högbom, Clark), the multi-scale deconvolver has a higher capability to recover a larger amount of flux especially in shorter baselines and consequently reduce the negative bowls (Offringa and Smirnov, 2017). The weighting scheme is set to Briggs with the robust parameter equal to 0.5 as a compromise between the resolution and the sensitivity. For the ALMA continuum maps, the CLEANing process has been done using 1 000 000 iterations and a threshold of 0.5 mJy. The resulting images are restored with a synthesized beam of $1.6'' \times 1.2''$ with a P.A.$= -84.2°$ (original beam size), and a circular beam of $1''$ (super-resolution image) equivalent to a linear resolution of 1300 AU. The super-resolution image is better suited to identify and distinguish continuum compact sources in crowded environments. The final continuum images have a rms noise level that varies from 0.06 mJy beam^{-1} to 0.3 mJy beam^{-1} in signal-free regions and regions close to the brightest sources, respectively. The dynamic range of the image, measured as the peak brightness in NGC 6334-I and NGC 6334-I(N) to the rms noise in the signal-free region of the 12-m image is 7 800.

In order to construct the images of line emission, the calibrated data set has been splitted into 12 subsets with each of them corresponding to one of the observed molecular transitions or spectral windows (see Table 2.1). Then, continuum subtraction has been done by applying the task uvcontsub in CASA to the line-free channels. Finally, the CLEANing process was performed with the task TCLEAN using the *auto-masking* algorithm available in CASA version 5.1. The advantage of adopting the auto-masking algorithm in the cleaning process is that the mask will be updated at the beginning of each minor cycle based on the current residual image. Therefore, the resulting image will have fewer artifacts. The number of iterations is set to 1 000 000 and a threshold of 5 mJy has been used both for the 12-m and ACA data. The final data cubes consist of 390 channels with a channel width of 0.5 km/s (141 kHz) similar to the velocity resolution of the observations. The rms noise level of each spectral channel is typically in the range 2 to 8 mJy beam^{-1}. The cubes are restored with the same synthesized beam as that of the continuum image.

2.2.3 Data combination of the ALMA 12-m and ACA data

While high-resolution interferometric observations can provide us with a detailed view of fine structures, a more compact configuration and single-dish observations are used to recover the emission of the extended structures in the observed region. Therefore, for a wide range of spatial scales multiple configurations may be needed.

The incompleteness in the *uv*-coverage results in negative bowls and spurious features around the emission components. In fact, the negative bowls are indicative of the extended emission which is filtered out in the actual high-resolution observations due to the lack of information at short spacings. Although the negative bowls can be partially eliminated during the cleaning process, recovering the missing flux is only possible when

the high-resolution data is combined with a data set with a maximum baseline in the order of the minimum baseline of the high-resolution data.

To obtain high-fidelity images of the shocked and dense gas tracers in NGC 6334, the high-resolution 12-m data is combined with the ACA data which is treated as short-spacing measurements. As shown in Fig. 2.3, the ALMA main configuration samples the spacings from 50 to 1370 m, while the ACA data covers the spacings in range 10–66 m. Therefore, these two measurement sets have a significant *uv* coverage in common. This characteristic provides improved reconstruction of the large-spatial scales in the combined image. For data combination, I adopted three different schemes which are explained below.

- **Joint deconvolution:** In this method, each of the 12-m and ACA data set is calibrated separately using the ALMA calibration pipeline. After the calibration was applied, the visibilities will be combined in the *uv*-plane using the `concat` task in CASA. The weights applied to the individual data sets are equal to 1. In the next step, the combined data set which contains both high-resolution and short spacing information is `CLEAN`ed using auto-masking as discussed in § 2.2.2. The resulting image is restored with a synthesized beam of $1.9'' \times 1.3''$ with a P.A.=-78.4°. The weighting scheme is set to Briggs with the robust parameter equal to 0.5 similar to the 12-m data cubes. The number of iterations is increased to 5 000 000 due to the larger number of points in the combined data set.

- **Feather:** This method makes use of two individually created images of the ACA and 12-m observations. Therefore, for each molecular emission line the data cubes have to created from the 12-m and ACA data sets separately. After the imaging was performed, the two images will be combined in the Fourier transform plane using the `Feather` task in CASA. Similar to the joint deconvolution method, the weights associated with both ACA and 12-m images are the same and equal to 1. The combined image is restored with a synthesized beam of $2.2'' \times 1.4''$.

- **Model-assisted cleaning:** In this method, the ACA-only image is used as a source model in the `CLEAN`ing process of the ALMA 12-m data set. This allows for a better convergence and, results in an image with fewer artifacts. In a second step, the ACA-only and the 12-m ALMA image are combined using the `FEATHER` task in CASA.

The capability of the aforementioned data combination methods can be compared based on the amount of extended emission recovered both in continuum and molecular line maps. Fig. 2.6 (left panel) shows the combined peak intensity maps of $HC^{15}N$ towards NGC 6334-I(N) created using the three aforementioned methods. In the right panel, the spectra of the marked regions in the maps are illustrated. The peak intensity, integrated intensity and the level of noise in the marked regions are listed in Table 2.2. Regarding to the values listed in the table, data combination using *Feather* results in the lowest noise level with the highest integrated intensity in comparison to the other two methods. Therefore, this approach is applied to the remaining molecular emission data sets observed with ALMA.

2.3 IRAM 30m observations towards NGC 6334

The key goal to carry out the IRAM 30m observations is to investigate the accretion process and properties of the shocked gas at scales of ∼5000 AU, i.e., the scales connecting

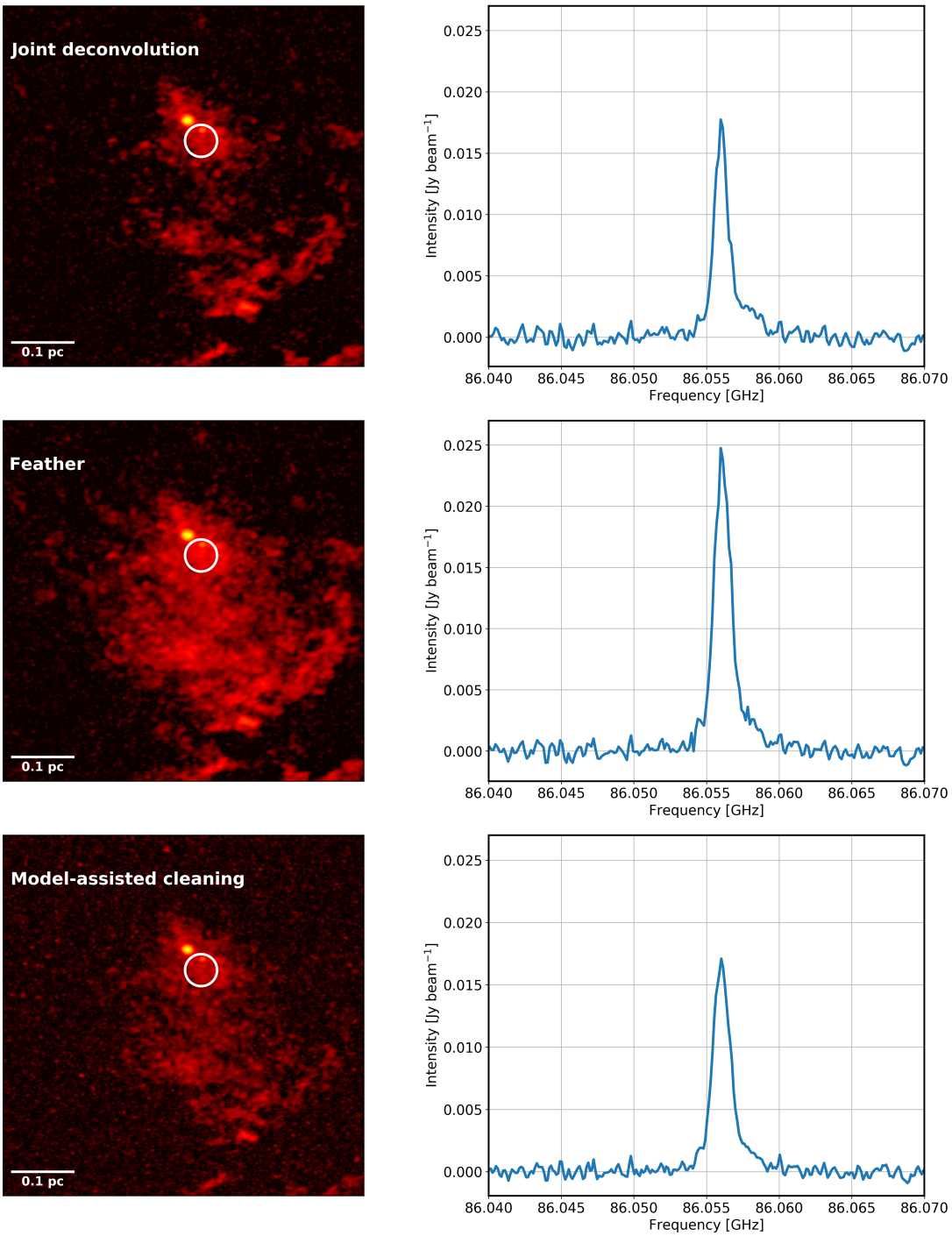

FIGURE 2.6: *(Left)*: $HC^{15}N$ peak intensity maps towards NGC 6334-I(N) created by combining the ALMA 12-m data with the ACA data using the different combination methods. *(Right)*: Spectra towards the position indicated with white circle in the peak intensity maps.

the clusters and cores to the larger-clump and filamentary cloud. The ALMA observations are adequate to resolve structures down to 1300 AU. However, due to the lack of single-dish observations, it is not possible to properly study the most diffuse and extended emission that dominates the emission in species like HCN and HCO^+ and exists

TABLE 2.2: Specifics of the data combination methods based on the position indicated towards $HC^{15}N$ peak intensity maps (see Fig. 2.6).

Method	Peak intensity [mJy beam^{-1}]	Integrated intensity [Jy beam^{-1}]	rms noise level [mJy beam^{-1}]
Joint deconvolution	17.7	2.8	4.8
Feather	24.7	3.6	2.1
Model-assisted cleaning	17.0	2.6	2.2

in the maps of complex molecules like CH_3CCH and shock tracers like SiO. Therefore, the IRAM 30m observations are conducted (i) to study the structures and distribution of dense gas, (ii) to characterize the kinematics of the accreting molecular gas filamentary structures partially seen with ALMA, and (iii) to analyse the extended shocked SiO emission, which can be associated with cloud-cloud collision events.

I made the observations on 2018 November 09–11 using the spectral line receiver EMIR at 3 mm. We used E090 with two setups to cover all the lines observed with ALMA. Our observations employed the FTS50 spectrometer to reach a spectral resolution of 0.4 km s^{-1} matching the resolution of the ALMA data. The rms of $\sim$100 mK (three times higher than ALMA observations) has been achieved in the IRAM 30m observations which ensures a good combination with the ALMA data. Using the OTF PSW observing mode, a field of view of 6.25 arcmin^2 is covered around NGC 6334-I and NGC 6334-I(N).

As the main calibrator for pointing and focus, I observed Mercury. Correction in pointing is obtained by interleaved observations of the quasar 1757-240 located close to the science target. This nearby calibrator is observed every 1.5 hour. CALW31C serves as bandpass calibrator.

The data reduction was performed with the `GILDAS/CLASS` package. The resulting images are restored with a circular beam of 29.9″. The combination with the ALMA data is done following the so-called feather method explained in § 2.2.3. Comparing the ALMA only maps with the ALMA+IRAM maps shows that for most of the observed molecular lines, $\sim$85% of the emission is already recovered with the ALMA observations. As an instance, in Fig. 2.7, I present the ALMA map of SiO emission (left panel), the ALMA+IRAM map of SiO (middle panel) and the integrated spectra extracted from both maps towards two different regions in NGC 6334-I and NGC 6334-I(N). As shown in the figure, the amount of emission which is filtered out due to the lack of zero spacing is $\sim$15%. Additionally, the IRAM+ALMA maps exhibit a higher noise level compared to the ALMA only maps (6 mJy beam^{-1} vs. 2 mJy beam^{-1}). Therefore, according to the points that most of the emission is recovered with the ALMA observations and the lower noise level of the ALMA data, the analyses presented in this thesis are performed on the ALMA data.

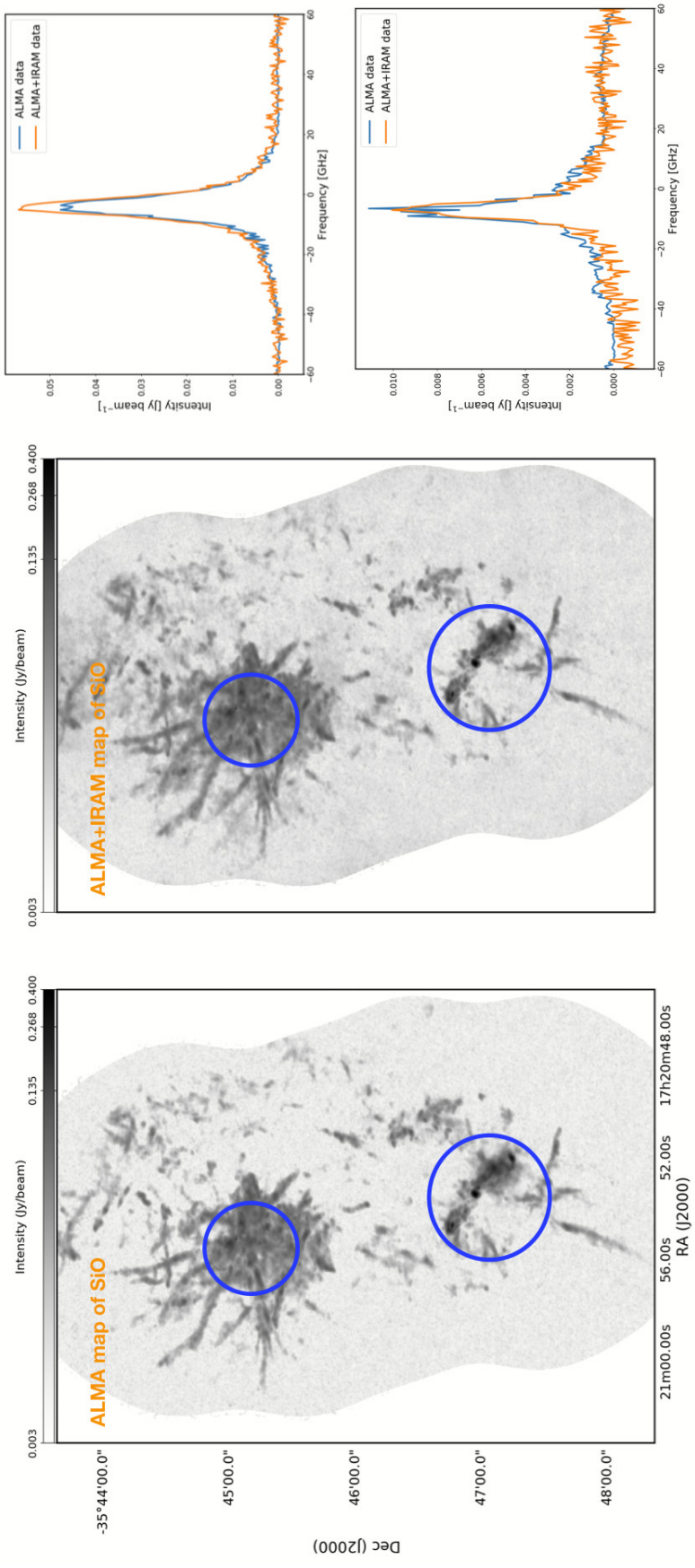

FIGURE 2.7: *Left:* SiO(2-1) peak intensity map obtained with ALMA. *Middle:* SiO(2-1) peak intensity map obtained from combined data sets of ALMA and IRAM 30m. *Right:* Spectra towards the positions indicated with blue circles in the peak intensity maps towards NGC 6334-I and NGC 6334-I(N). The blue solid line corresponds to the ALMA data, while the orange line denotes the combined ALMA+IRAM data.

Chapter 3

Physical properties of the high-mass star-forming clusters in NGC 6334

This chapter is based on Sadaghiani et al. (2020).

As I mentioned in Chapter 1, most stars including our Sun are formed within embedded clusters including high-mass stars (e.g., Bressert et al., 2012; McKee and Ostriker, 2007; Rathborne et al., 2015; Tan et al., 2014). Therefore, the embedded clusters (i.e. protoclusters) with gas and dust masses larger than 100 $M_{\odot}$ and H_2 volume densities exceeding 10^4 cm^{-3} are the fundamental units of star formation. Hence, the massive protoclusters can be used to probe the early phase of high-mass star formation.

The physical properties of the embedded clusters including the core mass function, spatial distribution of the cluster members and the level of fragmentation are affected by the radiative and mechanical feedback as well as the interaction between the cluster members. Investigating the physical nature of clusters and their environment helps us to establish an empirical foundation based on which the theoretical models and simulations can be developed (e.g.; Klessen et al., 2004; Lee and Hennebelle, 2016).

To further explore the properties of massive protoclusters, I studied the dust continuum emission towards the massive clusters in NGC 6334 with ALMA. In this chapter, I explain the detailed statistical analysis which leads to derive the physical properties of the protoclusters. In § 3.1, we illustrate the morphology of the continuum emission toward the observed region and identify the compact sources as well as their counterparts in radio, infrared and X-ray wavelengths and measure the physical properties of the identified sources. In 3.2, we study the distribution of the dense cores throughout the observed region. In § 3.3, the physical properties of the protoclusters such as the core mass function and the level of mass-segregation will be derived. In § 3.4, we discuss the implication of our findings relevant to cluster formation.

3.1 ALMA continuum map at 3 mm

The left panel of Fig. 3.1 shows the ALMA 87.6 GHz (or 3 mm) continuum emission towards NGC 6334-I and NGC 6334-I(N). The brightest source in the observed region is located towards the south and coincides with the cometary ultracompact HII region of NGC 6334-I (e.g.; Carral et al., 2002; de Pree et al., 1995). About 60″ to the north-northwest, an extended shell-like feature is identified which corresponds to the more evolved compact HII region NGC 6334-E (e.g.; Carral et al., 2002; Rodríguez et al., 2003). Nearly at the center of the shell, we detect a compact source whose location suggests that it can be responsible for the ionization of the entire shell (Carral et al., 2002).

In the north-east direction and about 100″ north of NGC 6334-I, a large population of compact sources is identified at a location of NGC 6334-I(N). The compact cores seem to

be aligned in two elongated structures. In addition to the compact sources, we detected a faint extended emission likely tracing dust filaments connecting the different cores. Finally, a number of fainter compact sources with similar intensities appear distributed over the western part of the observed region, with a larger concentration towards the north-west of NGC 6334-I(N).

3.1.1 Continuum source identification

We used the `SExtractor` package[1] (see Bertin and Arnouts, 1996), via its `python` wrapper interface `sewpy`[2], to identify and build a catalog of compact sources from our ALMA continuum image. The first step for source identification is to determine the background level. For this, the algorithm measure the mean value and standard deviation of the pixel values over a mesh grid which is defined by the user as `BACK SIZE`. In the next step, the most deviant values will be discarded and the mean and standard deviation will be computed again. This procedure will be iterated until all the pixel values of a mesh grid are within a range of mean $\pm\sigma$. Once the background level is estimated, `SExtractor` determines whether the pixel belongs to the background or to the object. Then, the area which does not belong to the background is spitted up into separate sources. The sources that have overlap in the image can not be detected separately with a single threshold. Therefore, the algorithm deblends them by searching for intensity variations based on multiple thresholds. Number of thresholds required in the deblending procedure depends on the dynamic range of the image (given by the user as `DEBLEND NTHRESH`). To take the intensity variations between the local peaks into account, a contrast parameter has been adopted which ranges from 0 to 1 (given by the user as `DEBLEND MINCOUNT`). Finally, sources must have an extension of more than a given minimum number of pixels to be included in the final catalog (defined as `DETECT MINAREA` by user). For each source, `SExtractor` determines the position, spatial extent and integrated flux. For the ALMA continuum image, I used a detection threshold of 6σ and a deblending threshold of 24σ, where σ is the rms noise. Since the noise level is not homogeneous throughout the whole map, σ is measured locally towards the different regions in the continuum map. To consider a detection as a source, it needs to have at least 5 pixels with a pixel size of $0.2''$. This threshold makes it possible to resolve the nearby sources in the crowded regions. The flux determined by `SExtractor` for each source is a summation over the counts in all pixels that belong to the source minus the background level. This value is, later on, divided by the area of the synthesized beam of the image to convert the units of the image to Jy beam^{-1}. The configuration parameters of the `SExtractor` adopted for the present work are listed in Table 3.1. To determine the geometric parameters of the objects, `SExtractor` computes the intensity-weighted moments of the pixels that form the source. A semi-major and semi-minor axis, together with a position angle are derived assuming that the sources have elliptical shapes.

In total, 185 sources are automatically identified by `SExtractor`. Due to the bright emission associated with the HII regions in NGC 6334-I and NGC 6334-E, the surrounding fields are highly affected by `CLEAN`ing artifacts. Therefore, the identified sources are visually inspected and the ones which are associated with artifacts are manually removed. The final catalog of ALMA continuum sources contains 142 objects. I list them in the order of increasing right ascension in Table A.1 and mark them in Fig. 3.1. The flux densities and peak intensities of the identified sources range from 0.1 to 2073 mJy and 0.4 to 340 mJy beam^{-1}respectively. The observed sizes (diameters) range from $0.3''$to $5.2''$,

[1]See `http://www.astromatic.net/software/sextractor`

[2]Available at `https://sewpy.readthedocs.io/en/latest/`

TABLE 3.1: Configuration parameters of the SExtractor package

Parameter	*Value*
DETECT_MINAREA	5
DETECT_THRESH	6
THRESH_TYPE	*RELATIVE*
PIXEL_SCALE	0.2
DEBLEND_MINCOUNT	0.001
DEBLEND_NTHRESH	24

corresponding to 390 au to 6760 au. In the top panels of Fig. 3.3, we show the distribution of peak intensities, flux densities and observed sizes.

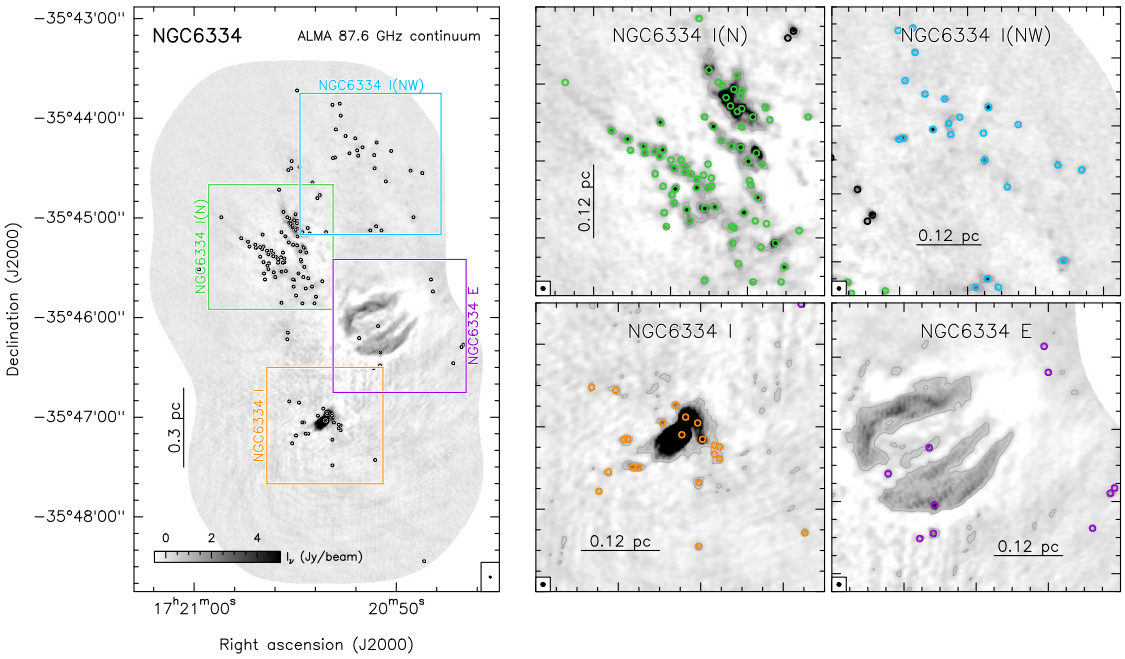

FIGURE 3.1: *Left*: ALMA 87.6 GHz continuum emission map of NGC 6334. The colored rectangles mark relevant regions studied in more detail throughout the paper. Their names, from north to south, are NGC 6334-I(NW), NGC 6334-I(N), NGC 6334-E and NGC 6334-I. *Right*: Close-up views of the four selected regions. In all panels, the circles denote the position of the compact sources identified using SExtractor (see § 3.1.1, and Table A.1). The color of the circles in the right panels indicates the association of each source with a cluster (see § 3.2.1). The synthesized beam of 1″ is shown in the bottom left or right corners of each panel.

3.1.2 Counterparts at different wavelengths

I looked for counterparts of the ALMA continuum sources (see § 3.1.1, Fig. 3.1) at different wavelengths from X-rays to radio, and also at sub-millimeter wavelengths when observed with a higher angular resolution.

To search for counterparts at infrared wavelengths, we used the IRAC/MIPSGAL

Spitzer catalog published by Willis et al. (2013). The catalog contains $>$ 700 000 sources detected at wavelengths from 3.8 μm to 24 μm toward the entire NGC 6334 filamentary cloud. Out of the near- and mid-IR detected point sources, 2283 sources are identified as young stellar object candidates based on color and magnitude criteria (Gutermuth et al., 2009). The class determination of YSOs is performed based on color criteria and the slope of the SED at mid-IR (Willis et al., 2013). The different classes of YSOs are differentiated by studying the spectral index (α; $S_\nu \propto \nu^\alpha$). In the mid-IR wavelength range, the spectral index is expected to be $\alpha \geq 0.3$ for Class I and $-0.3 > \alpha \geq -1.6$ for Class II YSOs (Lada, 1987). As a result of performing the classification schemes, $\sim$16% of the YSOs are classified as Class I and the remaining objects as Class II according to their evolutionary status. The possible contaminant objects such as background galaxies and AGNs are carefully identified an excluded from the catalog.

We determine that an ALMA source is coincident with an IRAC/*Spitzer* source if their separation is less than the distance given by the beam size of the ALMA observations and the mean full-width half-maximum of the IRAC point source, which corresponds to 2$''$. In right panel of Fig. 3.2, the ALMA sources which have IR counterparts are indicated with filled circles and we list the associations in column (3) of Table A.2. From the 142 ALMA source identified with `SExtractor` 24 sources have infrared counterparts. The comparison of out ALMA catalog with the Willis et al. (2013) catalog provides a simple diagnostics for classifying the evolutionary state of the ALMA sources. Those ALMA sources which have no infrared counterparts are assumed to be deeply embedded cores (i.e., class 0 object).

The Karl G. Jansky Very Large Array (VLA) observations in the C-band at a frequency range of 4–8 GHz and a spatial resolution of 0.17$''$–0.5$''$(220 au–650 au) has been used by Medina et al. (2018), Brogan et al. (2016) and Hunter et al. (2014) to evaluate the radio continuum content of NGC 6334. In the catalog of the radio continuum sources published by Medina et al. (2018), 83 sources have been presented over a field of view of $10^{'} \times 10^{'}$. In right panel of Fig. 3.2, we mark the location of the radio-continuum sources with star symbols. For the present work, I cross-checked the positions of the VLA continuum sources with those from our ALMA map. I consider that an ALMA source coincides with a radio-continuum source if the distance between two sources is less than the spatial extent of the sources. From the 142 ALMA sources, only 6 sources are also visible at centimeter wavelengths. Two of them are located in NGC 6334-I, two in the region of NGC 6334-I(N), and the remaining two sources are located associated with shell-like HII region NGC 6334-E. All the ALMA sources with a radio continuum counterpart except for one have positive spectral indices indicating the presence of thermal free-free radiation (Medina et al., 2018). The only remaining source with a negative spectral index (-1.7 ± 0.8) is a Class I YSO (source 5 in Table A.1). Therefore, the non-thermal emission associated with this source is likely originating from strong shocks in the region (see e.g.; Anglada, Rodríguez, and Carrasco-González, 2018; Kurtz and Hofner, 2005; Sánchez-Monge et al., 2013b). Column (2) of Table A.2 indicates whether an ALMA source is associated with a VLA counterpart.

To investigate whether an ALMA source is also detected as an X-ray source, I used the catalog of X-ray sources published by Feigelson et al. (2009). The catalog is made by analyzing a mosaic of two *Chandra X-ray observatory* images and contains $\sim$1600 faint sources. Among others, $\sim$140 X-ray sources are located towards the region observed with ALMA. The X-ray population mostly consists of low-mass pre-main-sequence stars as well as OB stars (Feigelson et al., 2009). We consider that an ALMA source is coincident with an X-ray source if their separations is less than the distance given by the source size of the ALMA source and angular resolution of the *Chandra* observations (0.5$''$). Based

on this criterion, no X-ray counterpart is found for the ALMA sources.

Finally, I compare the ALMA compact sources identified in the 1″continuum map, with millimeter compact sources identified in both NGC 6334-I and NGC 6334-I(N) at higher angular resolutions (i.e., $< 1.0''$). For NGC 6334-I, Brogan et al. (2016) found that two of our ALMA sources (numbers 43 and 44 in Table A.1) resolve into multiple components (the first into 7 and the second into 2) when observed at an angular resolution of $0.17''$. Likewise, part of the ALMA sources in the central region of NGC 6334-I(N) have been previously detected using SMA and VLA observations at the frequency range of 5 to 345 GHz (Hunter et al., 2014). The continuum emission at 230 GHz from one of the SMA sources is clearly resolved into three components. Two of these components are also visible in our ALMA super-resolution continuum map (numbers 92 and 95 in Table A.1).

In summary, out of the 142 ALMA compact sources, 6 have a radio continuum counterpart, 24 are associated with infrared emission, and 2 show both radio and infrared emission. This results in 112 sources of the total catalog only detected at millimeter wavelengths, likely tracing a cold dust population.

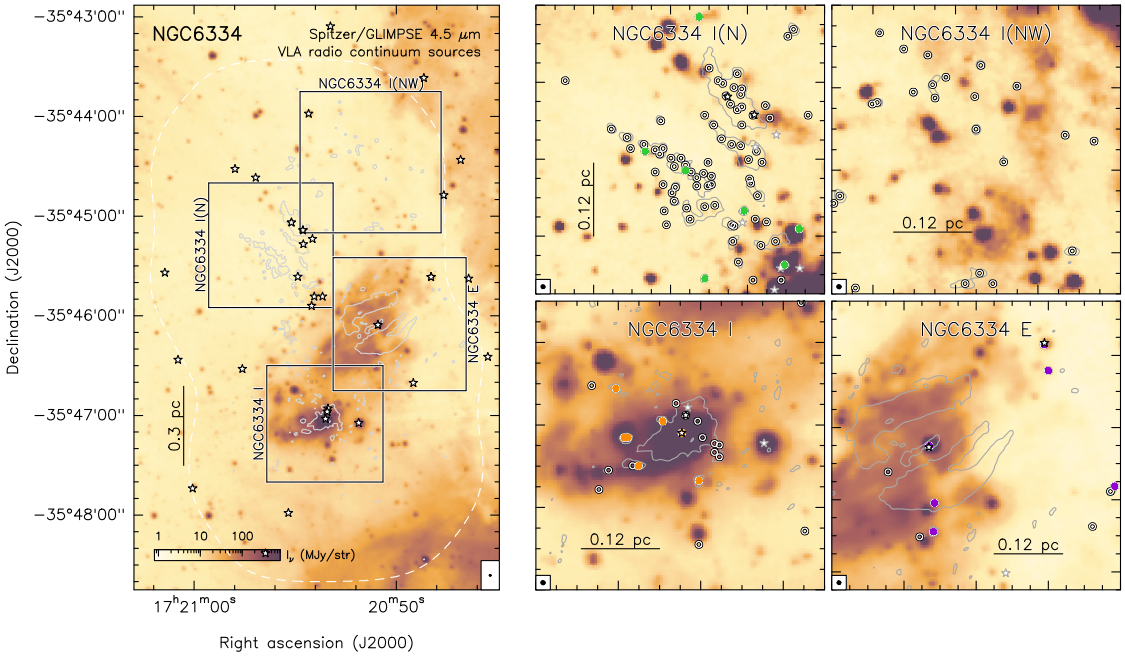

FIGURE 3.2: *Left*: *Spitzer* 4.5 ˚m in color and ALMA continuum emission at 3 mm in contour. The radio continuum sources observed with VLA at 4–8 GHz are shown as stars. *Right*: zoom-in view of the *Spitzer* image corresponding to the spatial extent of the clusters covered by ALMA. The circles indicate the position of the ALMA continuum sources at 3 mm. The filled ones correspond to the ALMA sources which are coincident with the IR sources published in IRAC/MIPSGAL *Spitzer* catalog (Willis et al., 2013). The stars indicate the position of VLA sources marked with black if associated with ALMA sources and gray if not associated.

3.1.3 Physical properties of the continuum sources

In this section, we estimate the physical properties (e.g.; mass, volume density and column density) of the identified compact sources from their ALMA 3 mm continuum emission. As mentioned in § 3.1.2, a low number of millimeter continuum sources are associated with a radio-continuum counterpart. Therefore, it is assumed that the emission at 3 mm detected with ALMA is mainly dominated by dust, with a small amount of contribution from ionized gas. The dust and gas mass for each source is determined using the equation

$$M_{\rm d+g} = \frac{S_\nu D^2}{B_\nu(T_{\rm d})\kappa_\nu}, \tag{3.1}$$

where S_ν is the integrated flux density of dust at 87.6 GHz, D is 1.3 kpc for NGC 6334 (Chibueze et al., 2014), $B_\nu(T_{\rm d})$ is the Planck function at a dust temperature $T_{\rm d}$, and κ_ν is the absorption coefficient per unit of total mass density at frequency ν. I assume optically thin emission, a gas to dust mass ratio of 100, and we adopt a dust mass opacity coefficient of 0.899 cm^2 g^{-1} at 230 GHz (Ossenkopf and Henning, 1994) corresponding to the grains with thin ice mantles. The dust opacity coefficient is extrapolated to 0.131 cm^2 g^{-1} at 87.6 GHz assuming a power-law dependence with a β power-law index of 2 (Shirley et al., 2011). For sources with radio-continuum counterparts, the contamination of ionized gas emission at 3 mm is taken into account using the fluxes at 6 GHz. I assume an spectral index of -0.1, which corresponds to optically thin emission and a spectral index of +2 for the case of optically thick emission (see e.g., Kurtz and Hofner, 2005; Panagia and Felli, 1975). By extrapolating the flux at radio wavelengths to the frequency of ALMA with the two spectral indices, I obtain a lower and upper limit to the contribution of ionized gas at 87.6 GHz. Assuming that the emission is optically thick, I find that for four ALMA sources (numbers 5, 15, 46 and 67 in Table A.1) the total observed flux could originate from the thermal free-free emission, while the flux of the other two sources is partially contaminated (35% for source 44 and 52% for source 95). The current determination of the masses for each core is done assuming a temperature of 20 K if the core is detected only in the ALMA image, 50 K if it has an infrared counterpart, and 100 K if the source has indicated a chemically-rich spectrum common of hot molecular cores in the previous high-resolution observations (see e.g., 2005; Kurtz and Hofner, 2005). For some sources I used a given specific temperature which is measured from molecular line observations (see Hunter et al., 2014). The temperatures used in the mass determination are listed in Column (4) of Table A.2.

Assuming the cores to be spheres of radius R, the volume density $n_{\rm H2}$ is determined as

$$n_{\rm H_2} = \frac{1}{\mu m_{\rm H}} \frac{M_{\rm d+g}}{(4/3)\pi R^3}, \tag{3.2}$$

where μ is the mean molecular mass per hydrogen atom (equal to 2.3), $m_{\rm H}$ is the hydrogen mass, and R is the radius of the core assumed to be the average of the minor and major axis of the source listed in Table A.1. Finally, the column density, $N_{\rm H_2}$, is determined from

$$N_{\rm H_2} = \int_{\rm line\ of\ sight} n_{\rm H_2} dl, \tag{3.3}$$

where l corresponds to the size of the core. The volume and column densities of the identified sources are listed in Table A.2. The masses of the cores in the whole observed region range from $< 1\ M_\odot$ up to a hundred $M_\odot$, with mean and median values of 8 $M_\odot$

and 4 $M_\odot$. The most massive object, with 100 $M_\odot$ is located in the vicinity of NGC 6334-I. The H_2 volume densities are in the range 10^7–10^9 cm^{-3}, with the three most massive cores having densities above 10^9 cm^{-3}. The H_2 column densities of the brightest sources are above 10^{25} cm^{-2} at the observed scales of ∼1000 au. The distribution of masses, volume densities and column densities are shown in the bottom panels of Fig. 3.3. It is necessary to note that for 90 of the cores, I have assumed a temperature of 20 K or 50 K. An error in the temperature of 10–20 K results in an error in the mass of about 40–50%. While other parameters such as the dust opacity may introduce uncertainties in the mass estimation, the temperature remains as a dominant factor when determining and comparing masses of cores that belong to the same cluster (see more details in § 3.3.2 and § 3.3.2).

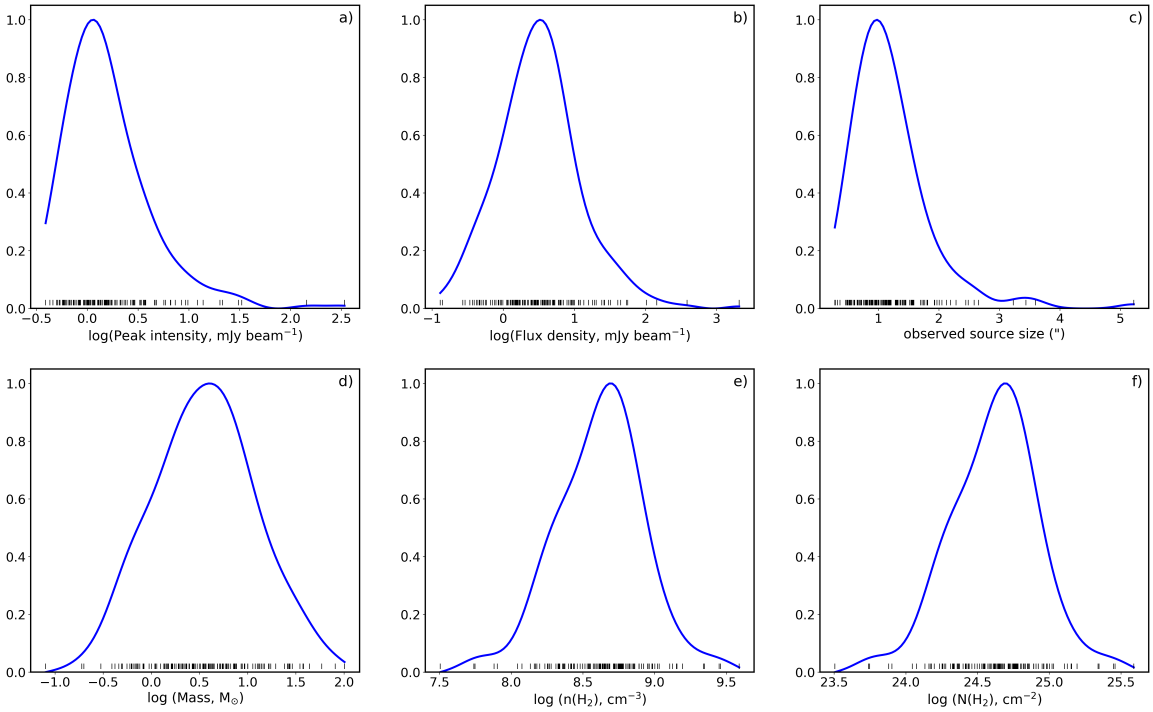

FIGURE 3.3: Distribution of (*a*) peak intensity; (b) flux density; (*c*) observed size; (*d*) dust and gas mass; (*e*) H_2 volume density; and (*f*) H_2 column density for the 142 ALMA continuum sources detected toward NGC 6334. The dark-blue solid lines correspond to the KDE (Kernel Density Estimate) built from the observed properties which are marked in the bottom of each panel, just above the x-axis.

3.2 Clusters in NGC 6334

The continuum sources identified in the ALMA map of NGC 6334 (see Fig. 3.1) are not randomly distributed over the observed region. Instead, they seem to cluster in different groups around exhibiting a fractal structure. In order to evaluate the internal structure of the observed area in NGC 6334 quantitatively, I take advantage of a measure Q. Q is a dimensionless parameter proposed by Cartwright and Whitworth (2004) which quantifies and distinguishes between the radially concentrated structures and fractal-like distributions. The Q parameter is based on construction of the minimum spanning tree (MST). The MST is a network of straight lines connecting a set of data points without closed

loops, such that the total lengths of all lines (edges) is minimum. To construct the MST for the ALMA cores in NGC 6334, I used the python package `NetworkX`[3] which is implemented based on the Kruskal's algorithm (Kruskal, 1956). The MST of the whole region is shown in the left panel of Fig. 3.8. The Q parameter is defined as the ratio of the normalized mean length of line segments in the MST, $\bar{m}$, and mean separation between the cores normalized by the cluster radius, $\bar{s}$. To calculate the value of the Q parameter, I used the equation

$$Q = \frac{\frac{\bar{m}}{\frac{\sqrt{N\pi R^2}}{(N-1)}}}{\frac{\bar{s}}{R}}, \tag{3.4}$$

where N represents the total number of the cores in a cluster and R is the radius of the cluster. The cluster radius is defined as the distance between the mean position of all the cluster members to the furthest core from this position. If $Q < 0.8$ implies fractal clustering whereas $Q > 0.8$ indicates a radial large-scale density gradient (see Cartwright and Whitworth, 2004).

The MST for the catalog of 142 ALMA continuum sources is shown in Fig. 3.8 (left panel) as black solid lines. I calculate $\bar{m}$ and $\bar{s}$ to be $7''(\sim 0.04$ pc) and $76''(\sim 0.5$ pc), respectively. Estimating a radius of $194''(\sim 1.2$ pc) for the whole region, I obtain $Q = 0.61$. This value confirms the presence of clusters in the observed region with ALMA. To estimate the uncertainty of the Q parameter, I remove 20% of the cores available in the sample randomly and repeat this process for 100 times. The outcome is the distribution of the measured values of Q. Fitting a Gaussian to this distribution results in a standard deviation $\sigma = 0.1$ which corresponds to the uncertainty of the Q parameter (see Fig. 3.4).

In the following, I present the methods which are used to identify clusters in the NGC 6334-I and NGC 6334-I(N) regions and study their properties.

3.2.1 Cluster identification

To identify the clusters of cores within the observed compact sources in our ALMA map, I took advantage of seven machine learning algorithms which search for clusters in the data points. The algorithms are available in the `Python` package `scikit-learn`[4]. As an input to the algorithms, it is necessary to indicate the coordinates of the data points as well as the number of clusters, K, to be generated. Therefore, the first step of the cluster identification is to validate the optimal number of clusters. For this, I used two different methods and I cross-validated the results. The methods are presented as follows:

- ***Silhouette* analysis:** This method is a way to determine how well each object lies within its cluster as presented by a silhouette value. In this analysis, we run one of the clustering algorithms (e.g. *K-Means*) on the whole sample of data points for different number of clusters, K. For each run, one *Silhouette* value is associated to each data point in a cluster, ranges from -1 to 1. The values displays a measure of how close each point in one cluster is to points in the neighboring clusters (Colombo et al., 2015; Kaufman and Rousseeuw, 1990; Rousseeuw, 1987). Therefore, a value of 1 indicates that the sample is far away from its neighboring cluster and very close to the cluster its assigned. Similarly, a value of -1 indicates that the point is close to its neighboring cluster than to the cluster its assigned. To select the optimal number

[3] Available at `https://networkx.github.io/`
[4] Available at `http://scikit-learn.org/stable/modules/clustering.html`

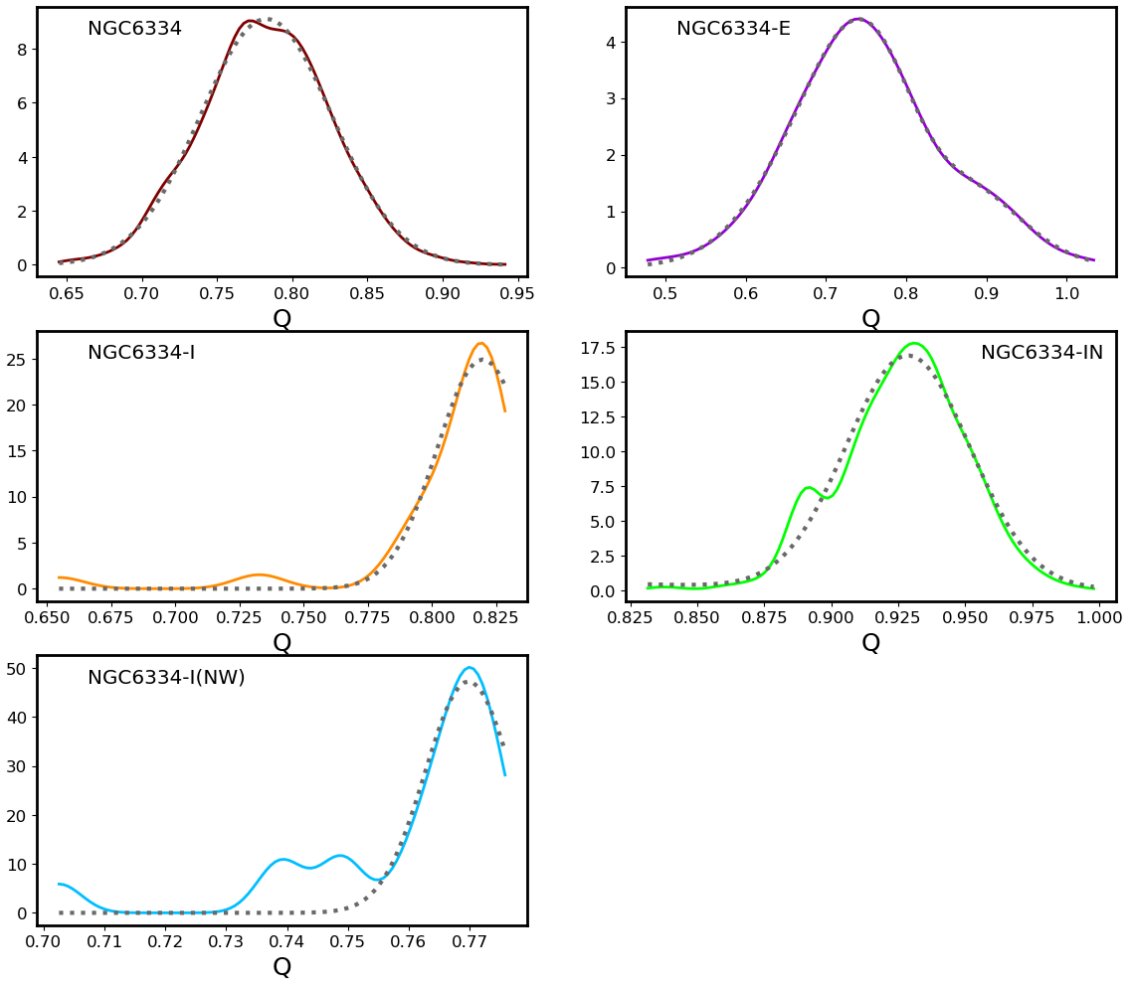

FIGURE 3.4: KDE of the values of the Q parameter generated in the iterative process of removing 20% of the cores for the whole sample and each individual cluster. In each panel, the grey dashed line denotes a Gaussian fitted to the KDEs. The width of the Gaussian is considered as the uncertainty of the Q parameter.

of clusters, one needs to calculate the average of the *Silhouette* scores for each run. The configuration which has the highest mean *Silhouette* score is the optimal one.

- **Elbow-point analysis:** In this method, similar to the *Silhouette* analysis, the *K-Means* algorithm is used to look for different number of clusters (K) in the sample (Ivezić et al., 2014; MacKay, 2002; MacQueen, 1967). For each run, we calculate the within-cluster sum of squares (WSS) which is a measure of the variability of the data points within each cluster. Therefore, a cluster that has a small WSS exhibits a more compact configuration. WSS as a function of K is always decreasing. However, there is a point where the rate of decrease shifts sharply and the line chart resembles an arm. This point is known as the elbow point and indicates the optimal number of clusters (Charrad et al., 2014).

For the present work, I performed the aforementioned analysis for a number of clusters, K, changing from 2 to 6. As shown in Figures 3.5 and 3.6, both methods results in $K = 4$ as the optimal number of clusters in the actual sample.

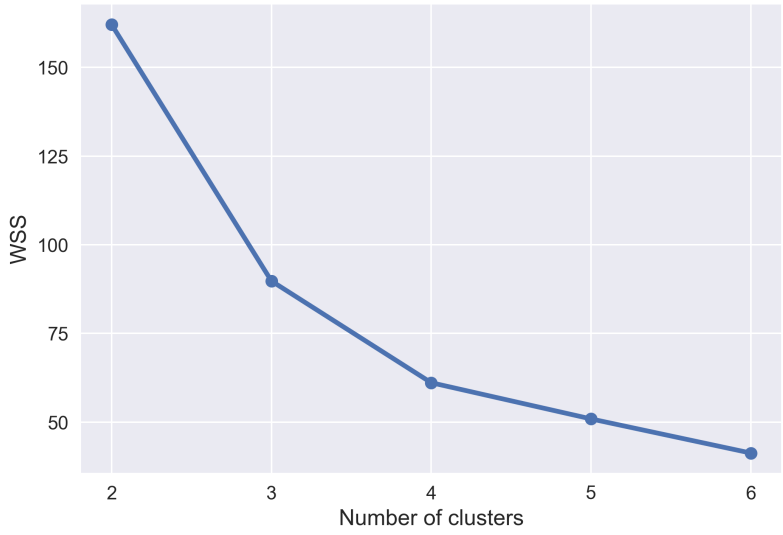

FIGURE 3.5: Sum of squared distances of data points to the center of a cluster for different number clusters. $K = 4$ is coincident with the elbow point of the function and assumed to be associated with the optimal number of clusters.

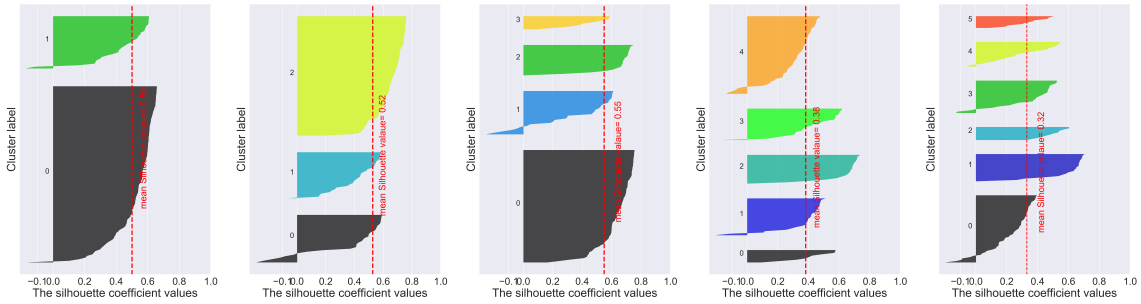

FIGURE 3.6: Silhouette values for each data point for K ranges from 2 to 6. The red dashed line denotes the average of the Silhouette values for each K. The highest mean value corresponds to $K = 4$.

Once the optimal number of clusters is validated, the next step is to apply seven different clustering algorithms to the sample of 142 ALMA compact sources and cross-validate the results. The algorithms that are used to identify clusters in the NGC 6334 observed regions are described as follows:

- **K-means**: The first step of the K-means algorithm is to initialize the cluster centroids for a given number of clusters. In the next step, the algorithm goes through each of the data points and assigns them to the cluster that is the closest. Then, the average of all the points in the cluster will be calculated and the centroids will be moved to the average locations.

- **Mean-shift**: The steps which are followed by the Mean-Shift algorithm are similar to the K-Means method. The only difference is that instead of using the number of clusters as an input, the algorithm determines the probability density function

from which the data is drawn. Then the centroids are placed at the maxima of the density function.

- **Spectral clustering**: The Spectral clustering algorithm makes use of the similarity matrix of the data to reduce the dimensionality of the space. Then, K-Means clustering is used in the low dimensional space.

- **Ward hierarchical and Agglomerative clustering**: The Ward hierarchical clustering and the Agglomerative clustering are the other two methods used to look for segmentation in the data. They try to link each data point by a distance measure to its nearest neighbour, creating a cluster. These two algorithms differ in the linkage method they use to define the proximity between any two clusters. The Agglomerative hierarchical clustering uses the Average linkage which merges the clusters based on the minimum distance between two points in two different clusters. While, the Ward linkage computes the total within-cluster sum of squares to determine the next two groups merged.

- **Gaussian mixtures**: In practice each cluster can be mathematically represented by a parametric distribution like a Gaussian. Therefore, we can assign multivariant normal distribution components to the data points. Using the Gaussian mixture model algorithm each data point will be assigned to the component which yields the highest posterior probability.

- **Birch algorithm**: The Birch algorithm operates in four phases. First, it builds a Characteristic Feature Tree for the data. In the second step, it reduces the input data to the subclusters and groups the crowded subclusters into a larger one. The branching factor limits the number of subclusters in each node. In step three, one of the other clustering algorithms (e.g. K-Means) is applied to the subclusters. The threshold gives us the flexibility to specify the diameter for clusters. After this step, the major segmentations in the data are identified. In the last step, which is a refining step, the centroids of the clusters identified in step 3 are used as reference points to find the closest data points to them and define the new clusters.

TABLE 3.2: Clustering algorithms and basic input parameters

Method	Input parameters	Metric
K-means	data points, number of clusters	distance between points
Mean-shift	data points	distance between points
Spectral clustering	data points, number of clusters, number of neighbours	graph distance
Ward hierarchical clustering	data points, number of clusters, linkage	distance between points
Agglomerative clustering	data points, number of clusters, linkage, affinity	any pairwise distance
Gaussian mixtures	data points, number of mixture components	Mahalanobis distances to centers
Birch	data points, number of clusters, threshold, branching factor	Euclidean distance between points

Figure 3.7 shows the final result obtained by applying clustering algorithms on the identified ALMA sources. The 142 objects are colored based on the cluster to which they belong. In general there is a good agreement between different methods. The southern compact sources always appear to be grouped in the region associated with NGC 6334-I (see orange circles). In all methods except for one, all the objects lying within the filamentary structures of NGC 6334-I(N) are classified in one single group (see lime circles). Only in the case of *spectral clustering* the sources which are associated with the eastern filament are classified as an independent group (see black circles). The group of objects located towards the north-west of NGC 6334-I(N) are classified in an additional cluster in

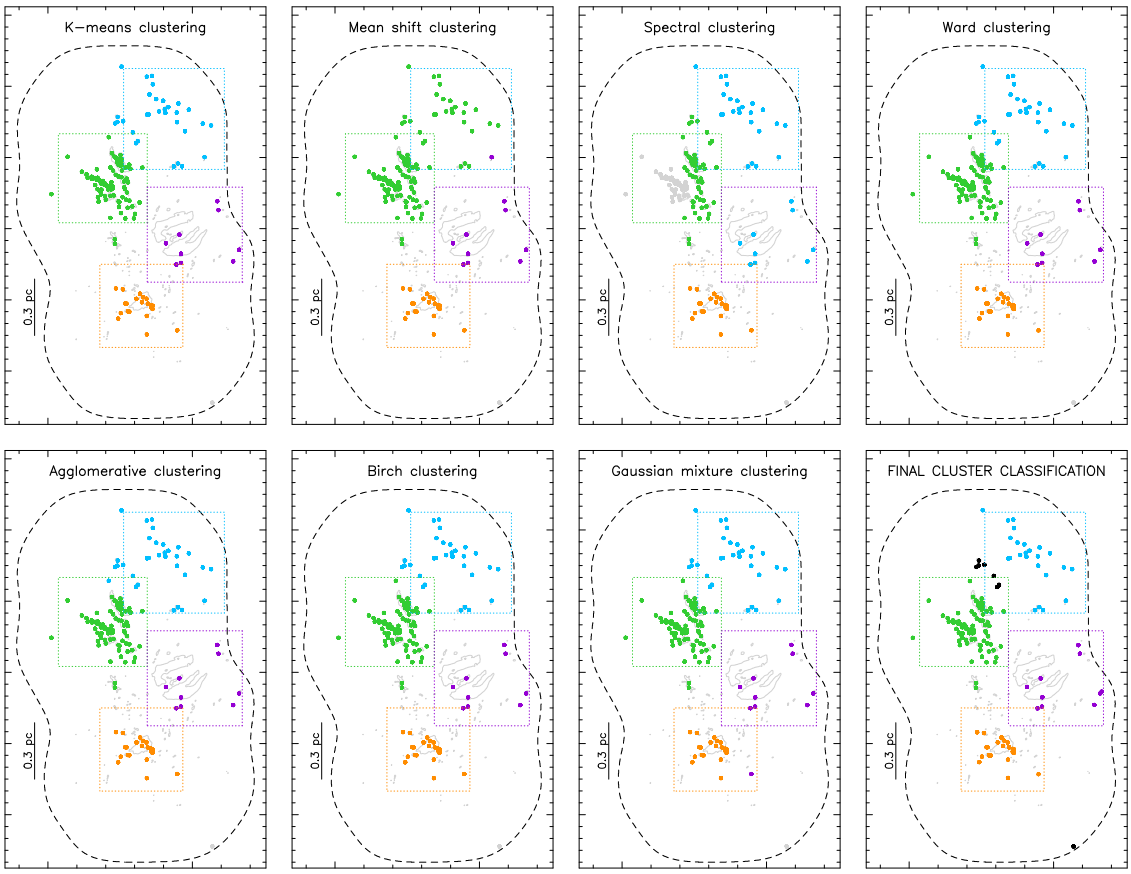

FIGURE 3.7: Each panel shows the area of NGC6334 observed with ALMA (see Fig. 3.1) and the colored circles correspond to the ALMA continuum sources detected in the region (see Table A.1). Each panel correspond to one of the seven clustering algorithms used to identify clusters in the region (see § 3.2.1). The colors of the circles depict the different clusters to which each continuum source belongs according to each algorithm. The last panel shows the final association of each source with one of the four clusters: light blue for NGC 6334-I(NW), lime for NGC 6334-I(N), violet for NGC 6334-E and orange for NGC 6334-I. The black circles in the last panel correspond to the sources not assigned to any cluster. In all panels, the rectangles mark the position of the relevant regions also marked in Fig. 3.1.

all cases (see blue circles). Finally, the sources in the vicinity of the HII region NGC 6334-E seem to form a small group with just a few members. In total I have identified four clusters of compact sources which I name: NGC 6334-E, NGC 6334-I, NGC 6334-I(N) and NGC 6334-I(NW). To specify the degree of membership for each core, I counted how many of the algorithms assign the considered core to one of the four clusters. This gives us the membership probability, or confidence level that is listed in Table A.2. The core with confidence level below 60% are excluded from the defined clusters. Based on the actual criterion, seven sources are excluded from the defined clusters. In Table 3.3, I list the numbers of members of each cluster. NGC 6334-I(N) is the most populated one with almost 80 members.

3.3 Physical properties of clusters in NGC 6334

In this section, I study the physical properties of the four main clusters, namely, NGC 6334-E, NGC 6334-I, NGC 6334-I(N) and NGC 6334-I(NW) identified in § 3.2.1. The difference between the properties of the clusters as a function of their evolutionary stage will be later discussed in § 3.4.2.

3.3.1 Internal Structure of the clusters in NGC 6334

I took advantage of the MST analysis to characterize the spatial distribution of cores in the clusters of NGC 6334. Right panels of Fig. 3.8 show the connecting segments of the MST for each one of the four main clusters identified in § 3.2.1. The length of the MST edges are used to calculate the separations from one core to its nearest neighbors, d_{nn}. Fig. 3.9 shows the Kernel Density Estimations (KDEs) of separations for unique pairs of ALMA sources in each cluster. The peak of the KDE corresponds to the characteristic separations for cores in each of the clusters. The mean and median d_{nn} as well as the peak of the KDE are listed in Table 3.3. The smallest characteristic separation between sources are found in clusters NGC 6334-E and NGC 6334-I with peak separations at about 3 000 au. The peak of the KDE for these two clusters decreases down to the resolution limit of the ALMA observations (1300 au). Thus, a higher resolution likely reveals a higher degree of fragmentation. The peak of the KDE for NGC 6334-I(N) as the most populated cluster appears at 4 500 au. Finally, the largest separations can be found in cluster NGC 6334-I(NW) with a distinct peak at 9 000 au. The results of the MST analysis is summarized in Table 3.3. The smallest difference between the mean and median separations is obtained for cluster NGC 6334-I(N) which suggests that the members of I(N) are more uniformly distributed compared to the other three clusters.

To characterize the internal structure of the clusters, I determine the Q parameter for each cluster. The radius of the clusters is defined as the distance from the geometrical center to the furthest source from this point. Making use of the results of the MST analysis and following Eq. 3.4, I obtain the values of 0.58±0.2, 0.72±,.3, 0.79±0.2 and 0.64±0.3 for NGC 6334-E, I, I(N) and I(NW) respectively. In Table 3.3 I list the radius of the four clusters as well as the values of the Q parameter. While the Q parameter for NGC 6334-E suggests the possible presence of fractal structures, the structure of the other clusters are closer to a smooth radial overdensity. However, I note that the large uncertainties of the Q parameter due to the low statistics prevent me to derive a firm conclusion from this analysis.

As a second method, I examine the two-point correlation function $\zeta(r)$ to quantify the degree of clustering of the four identified clusters. To measure $\zeta(r)$, pairs of compact sources are counted as a function of their spatial separation r. Then, this number is compared to a Poisson-distributed sample (Peebles, 1980). I used Landy-Szalay estimator to obtain the two-point correlation function as (Landy and Szalay, 1993)

$$\zeta(r) = \frac{DD(r) - 2DR(r) + RR(r)}{RR(r)}, \tag{3.5}$$

where $DD(r)$ is the observed number of source pairs with separation r, $RR(r)$ is the number of source pairs of randomly distributed points and $DR(r)$ is the number of cross-correlated observed-random pairs. The $\zeta(r) = 0$ indicates a Poisson-distributed sample, while positive and negative values of $\zeta(r) = 0$ indicate clustering and anti-clustering

respectively. Uncertainty on the two-point correlation function, σ_ζ, is estimated through the relation

$$\sigma_\zeta = \sqrt{\frac{1+\zeta(r)}{DD(r)}}. \tag{3.6}$$

To measure $\zeta(r)$, I use the `FragMent` Python/C library presented in Clarke et al. (2019)[5]. The algorithm considers the separation between each pair of sources as a single data point and convolves each data point with a Gaussian kernel. To compute the random separation distributions, the algorithm uses Monte Carlo simulation, in which it generates a given number of points, places them over the extend of each cluster and computes the distribution of separations for each pair. Due to the use of random positions, this calculation is repeated 10 000 times to obtain adequate statistics.

The two-point correlations function of each cluster are shown in Fig. 3.10. NGC 6334-E and NGC 6334-I show a systematic increase of grouping at a distance of 1500 au, close to the resolution limit. However, due to the large uncertainty in NGC 6334-E it is not possible to derive strong conclusions. The two-point correlation function in NGC 6334-I(NW) is in agreement with a random distribution by exhibiting random peaks at all separations. Finally, for NGC 6334-I(N) as the most populated cluster in NGC 6334 the uncertainties are smaller and the function indicate a significant positive peak at 4 000 au. The relative positions of the peaks of the two-point correlation function in each cluster (see Table 3.3) follows a similar trend observed for the projected separations between nearest neighbors. In this trend, the preferred length scale for NGC 6334-I(N) is shifted to larger separations compared to NGC 6334-E and NGC 6334-I.

TABLE 3.3: Cluster members, central coordinates, and distances between nearest neighbours

		Geometric cluster center		$R_{\rm cluster}$	Q	Typical separations[a] (in au)			
Cluster	#	R.A. ($^{\rm h}:^{\rm m}:^{\rm s}$)	Dec. ($^\circ:':''$)	(au)	param.	mean $d_{\rm nn}$	median $d_{\rm nn}$	peak $d_{\rm nn}$	TPCF
NGC 6334-E	10	17:20:48.97	−35:46:12.03	50 000	0.58±0.2	20 000	12 200	2 500	…
NGC 6334-I	21	17:20:53.70	−35:47:05.86	58 000	0.72±0.3	8 250	6 200	3 000	1 600
NGC 6334-I(N)	79	17:20:55.57	−35:45:22.88	82 500	0.79±0.2	5 600	4 300	4 500	4 500
NGC 6334-I(NW)	24	17:20:51.63	−35:44:23.82	83 000	0.64±0.3	11 700	9 300	8 900	…
NGC 6334	142	17:20:54.04	−35:45:30.56	252 000	0.61±0.1	9 200	5 300	5 400	–

3.3.2 Core Mass Function

In § 3.1.3 (see also Table A.2 and bottom panels of Fig. 3.3) I determined the masses and densities of the different sources detected with ALMA. The mean, median and maximum mass of the cores in each cluster of NGC 6334 are listed in Table 3.4. All clusters have a typical median mass of about 3 $M_\odot$. NGC 6334-I and NGC 6334-I(N) have a larger mean mass compared to NGC 6334-E and NGC 6334-I(NW), which suggest that forming high-mass stars is more probable in these two clusters. Most of the mass (about 66% of the total mass or 182 $M_\odot$) in NGC 6334-I is concentrated in two single cores (source 38 and 44). One of these two sources appears resolved into multiple components at sub-arcsecond resolution (see Brogan et al., 2016). By contrast, NGC 6334-I(N) appears more fragmented with the five most massive cores (source 55, 84, 87, 91 and 107) accounting only for 30% (or 213 $M_\odot$) of the total mass. Finally, the masses of the cores in

[5] Available at `https://github.com/SeamusClarke/FragMent`

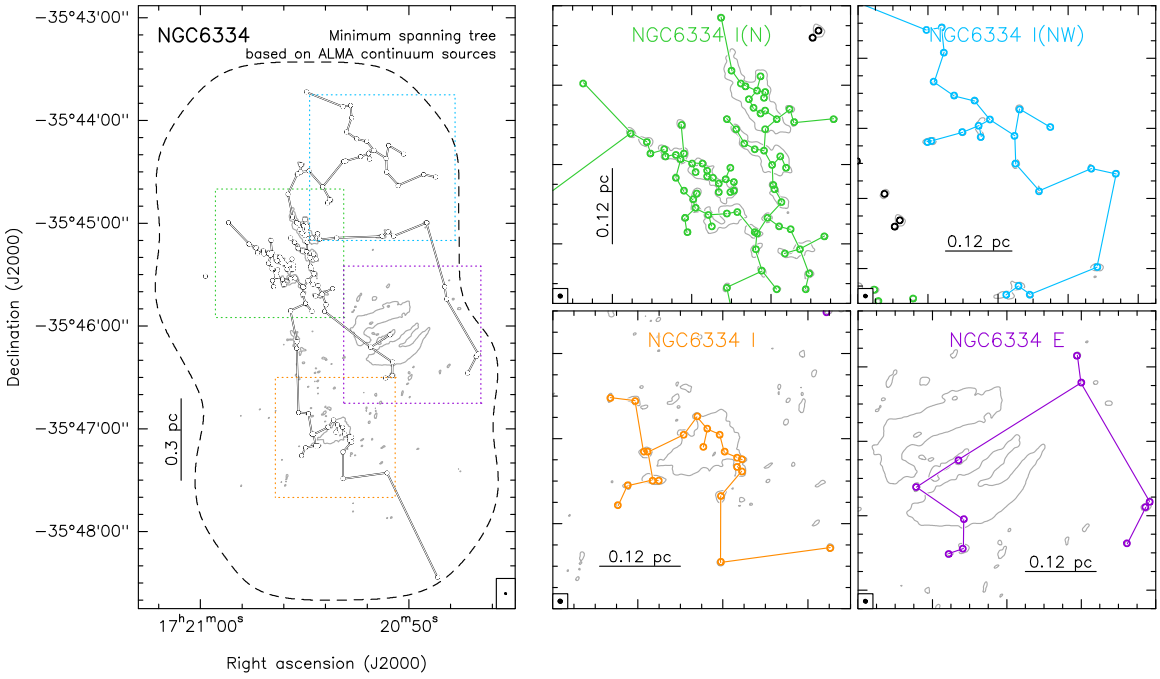

FIGURE 3.8: *Left*: Minimum spanning tree (MST) for the ALMA continuum sources. The positions of the dense cores are indicated with circles, while the lines denote the tree. The rectangles mark the positions of the relevant regions also marked in Fig. 3.1. *Right*: Minimum spanning tree for each of the four clusters identified in NGC 6334. The MSTs for each region/cluster are built considering only those members that belong to each cluster (see Table A.2). The ALMA continuum emission at 87.6 GHz is shown in grey contours. The contour level corresponds to 0.5 Jy beam^{-1}.

NGC 6334-E and NGC 6334-I(NW) suggest that they harbor mainly low/intermediate-mass fragments. However, the fidelity of the analysis performed based on mass of the cores depends on the completeness level of the core sample.

I determine the completeness level of the ALMA observations in terms of mass by generating random samples of cores with different masses and evaluate their detection probability in the ALMA continuum image. I generated 10 000 groups of masses with each group including 142 members (equal to the total number of cores identified in the whole region). The core masses are between 0.6 and 15 $M_{\odot}$ and follow the IMF $N(>M) \propto M^{-2.35}$ (see Kroupa, 2001; Salpeter, 1955). In addition to the core masses, I generate randomly 10 000 groups of temperatures which are uniformly distributed between 20 and 100 K (typical of dense cores, see e.g. Sánchez-Monge et al., 2013c). For each run, I assign each group of temperatures to the randomly generated masses. Then, for each core based on the given mass and temperature I derive the flux that would be detected at a distance of 1.3 kpc at a frequency of 88 GHz. In the last step, we compare the computed fluxes with a given threshold (defined by the noise level of the ALMA map) and measure the probability for a core with mass M to be detected by our ALMA observations. The completeness level is defined as the ratio of the number of detected sources and the total number of generated sources for any given mass. I considered a threshold of 0.3 mJy beam^{-1} for the noise-free regions and a threshold of 0.9 mJy beam^{-1} for the cores located at the vicinity of the HII region, where the dynamic range of the continuum map is high. Fig. 3.12 shows the completeness level of the ALMA sample for different

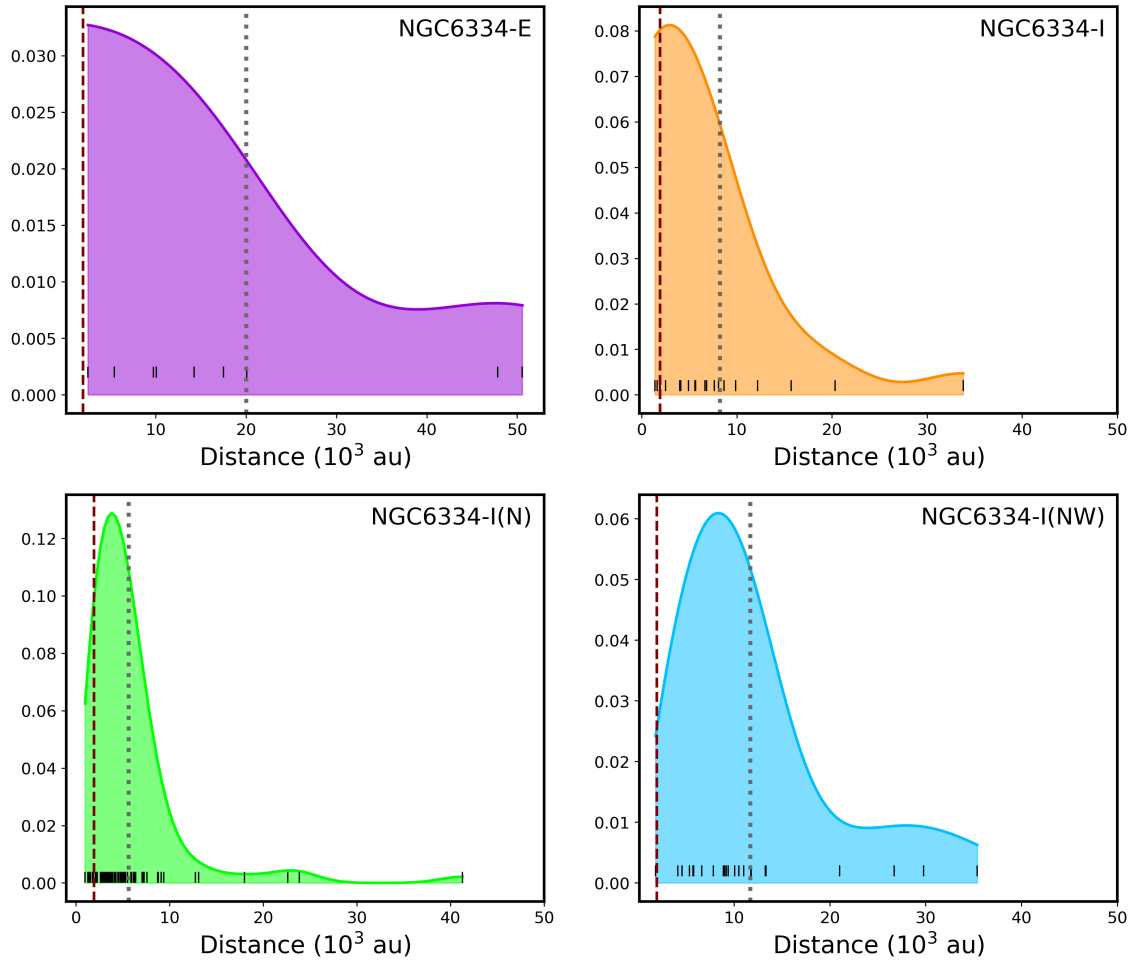

FIGURE 3.9: KDE of the projected separation between nearest neighbours for NGC 6334-E, NGC 6334-I, NGC 6334-I(N) and NGC 6334-I(NW). The red vertical dashed line shows the 1 300 au resolution limit of the ALMA observations, while the vertical grey dotted line denotes the median distance between the cores in the cluster. The short vertical lines at the bottom of the figure indicates the observed separations between members of each cluster.

masses determined based on these two thresholds. I find a completeness level of 90% for objects with masses $> 1\ M_\odot$ and $> 2\ M_\odot$ which increases up to 100% for objects with masses $> 1.5\ M_\odot$ and $> 4\ M_\odot$ for the noise-free regions and regions with high dynamic range respectively. For the present work, I consider the completeness level to be $2\ M_\odot$.

The cumulative core mass functions (CMFs) of the whole region and each individual cluster are shown in Fig. 3.11. The CMFs of the four main clusters are compared with the Kroupa initial mass function as described in Kroupa (2001), shifted to higher masses for a better comparison. Clusters NGC 6334-I and NGC 6334-I(N) indicate an excess of high-mass cores, while NGC 6334-E and NGC 6334-I(NW) seem to have a deficit of massive cores as compared with the Kroupa IMF. The excess of massive cores is also found in other high-mass star-forming regions: G28.34+0.06 (Zhang et al., 2015), Sagittarius B2 (Sánchez-Monge et al., 2017), and W43-MM1 (Motte, Bontemps, and Louvet, 2018). I fit a power-law function represented by $dN/d\ln(M) \propto M^{-\alpha}$ to the CMFs to measure the slope of the CMFs at the high-mass end. The values of α obtained for the whole sample

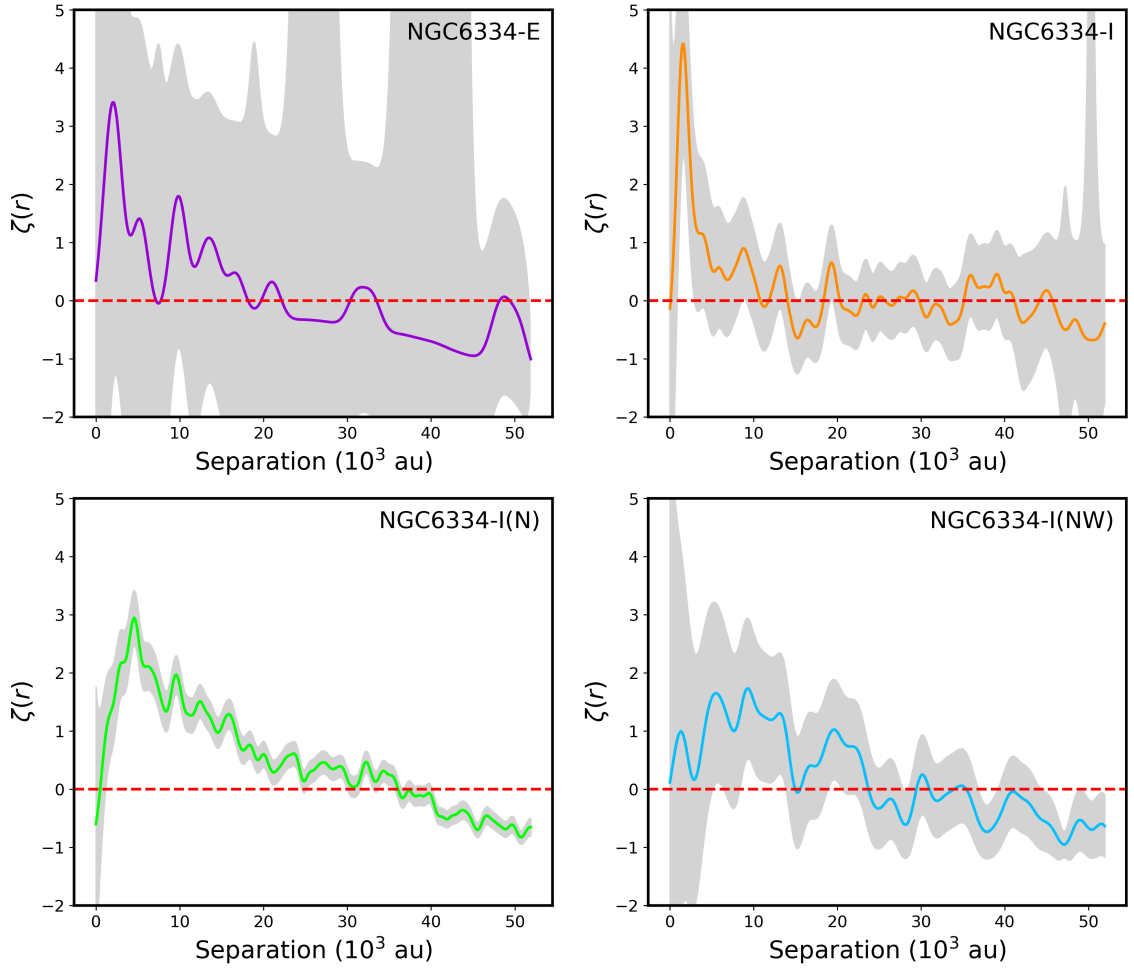

FIGURE 3.10: Two-point correlation function of ALMA continuum sources in NGC 6334-E, NGC 6334-I, NGC 6334-I(N) and NGC 6334-I(NW). The gray areas show the 1 σ confidence intervals. The dashed horizontal line, drawn at zero, indicates a random distribution.

and the four clusters are listed in Table 3.4. I find $\alpha = 1.1 \pm 0.02$ for the whole sample. For the individual clusters, estimate of α ranges from 1.1 to 3.17. The observed slope of the CMF of the whole sample is significantly shallower than the IMF. This result could challenge the widespread assumption that the shape of the IMF is inherited from the CMF and there is a one to one correspondence between these two functions. However, the measured slope can be biased towards flatter slopes due to the uncertainty in temperature measurement and resolution limit of the observations. In the following, I investigate the effect of these two factors on the CMF.

Temperature bias in the determination of the CMF

To investigate the effect of systematic errors in temperature determination on the observed CMF, I perform Monte-Carlo simulation with 100 000 runs. For each run, I randomly generate a group of temperatures which are uniformly distributed between 20 and 100 K. Then, I assign them to the observed fluxes and calculate a new mass for each core. In the last step, I build a CMF out of the newly calculated masses and fit the high-mass end of the CMF with a power-law function. I find that the slope α range from 0.7–1.46

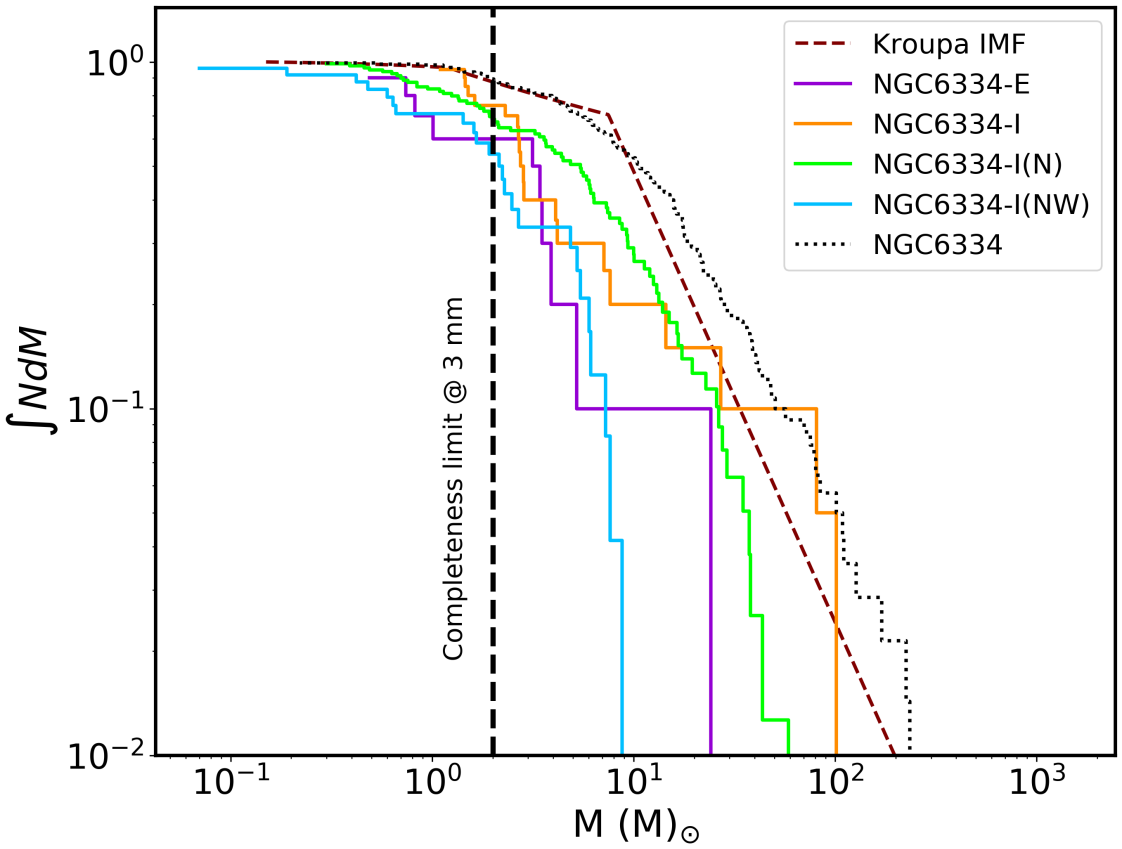

FIGURE 3.11: Cumulative core mass function of continuum sources identified in NGC 6334-E (violet), NGC 6334-I (orange), NGC 6334-I(N) (lime) and NGC 6334-I(NW) (light blue). The CMF of the whole sample is indicated with a dotted black line. The red dashed line shows the Kroupa initial mass function shifted by factor of 15 to the higher masses.

with a standard deviation of 0.10. The results of the Monte-Carlo simulation is presented in Fig. 3.13. The slopes of the most of the synthetic CMFs are flatter than the slope of -1.35, which defines the IMF. However, there are some cases with slopes consistent with the IMF. Top panel of Fig. 3.13 shows the distribution of the slopes of the synthetic CMFs. The question can be raised here is whether it can be possible to reproduce the shape of the IMF with a realistic temperature range. To answer this question, I investigate for a possible relation between temperatures and measured fluxes that would reproduce the slope of the IMF. For this, instead of assigning random temperatures to the measured fluxes, I assume that the brighter sources are associated with higher temperatures. Based on this assumption, I consider the empirical expression

$$T = T_0^{\rm obs} \left(\frac{S^{\rm obs}}{S_0^{\rm obs}} \right)^{\gamma}, \tag{3.7}$$

where $T_0^{\rm obs}$ is the minimum assumed temperature for the cores (20 K in the present work), $S^{\rm obs}$ is the observed flux density of the cores (listed in Table A.1), and $S_0^{\rm obs}$ is the minimum observed flux density (corresponding to 0.1 mJy beam^{-1} in this work). A value of $\gamma = 0.238$ results in the temperatures range from 20 K to 133 K. Using this temperature range it is possible to construct a CMF which is consistent with the IMF.

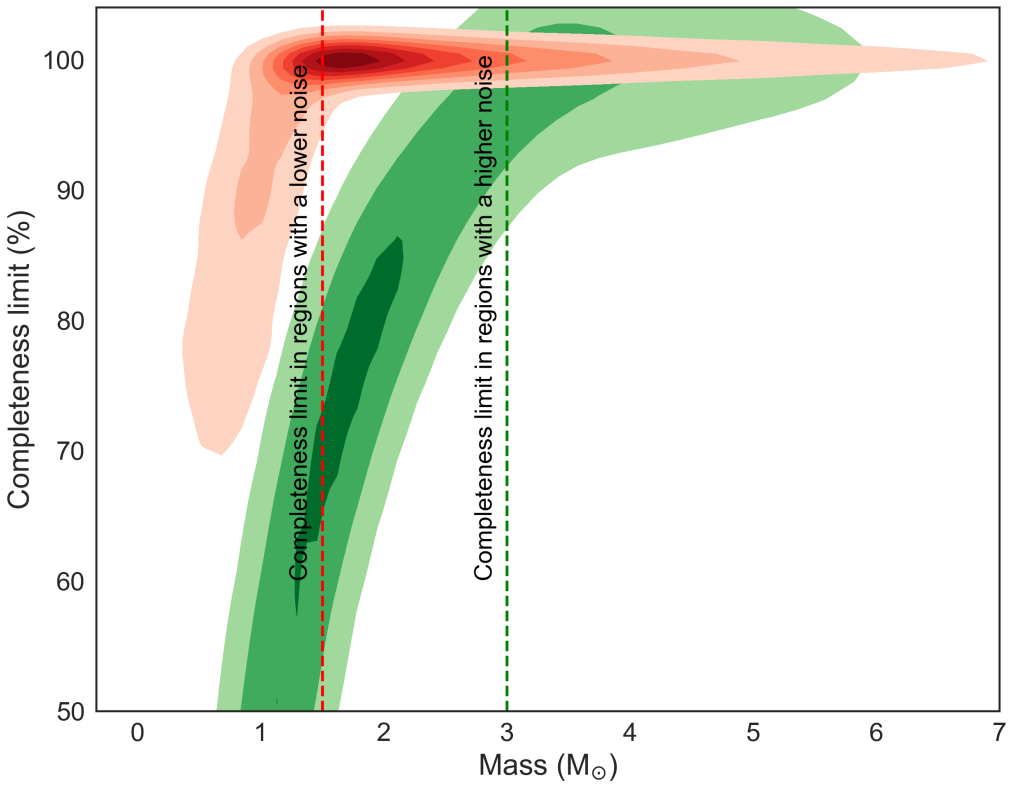

FIGURE 3.12: Completeness level of the ALMA continuum map at 3 mm as a function of mass. The KDE shown in green indicates the detection probability of the cores in the noise-free regions. The KDE illustrated in red represent the detection probability for the cores located at the vicinity of the HII regions. A completeness level of 90% is obtained for cores with masses $> 1.5\ M_\odot$ and $> 3\ M_\odot$ for the regions with a lower noise (0.3 mJy beam^{-1}) and a higher noise (0.9 mJy beam^{-1}) respectively. These completeness limits are marked with vertical dashed and dotted lines for the noise-free and noisy regions respectively.

In summary, the flatter slope found for the observed CMF as well as most of the synthetic CMFs suggest an over excess of massive cores in NGC 6334. However, the uncertainty in temperature determination can be the reason which causes the inconsistency between the CMF and the IMF. Therefore, observations of molecular line transitions such as NH_3 and CH_3CN is required to determine the temperature of each individual core accurately.

Resolution bias in the determination of the CMF

Another source of uncertainty in the determination of the CMF is related to the limited angular resolution of the observations. Previous high-resolution observations (0.17″) revealed multiplicity at the scale of a hot core within a radius of 1 000 au (Brogan et al., 2016). However, with the actual resolution of the here-presented ALMA observations (i.e., 1300 au) the small-scale fragmentation remain unresolved. The unresolved multiplicity at small scales results in overestimating the mass of the cores and therefore, biasing the CMF towards flatter slopes. In this section, I investigate if it is possible to reproduce the shape of IMF by taking all the possible fragments into account.

Each ALMA source is expected to fragments into Jeans-mass cores. Therefore, the

number of fragments for each ALMA source can be estimated by

$$N_{\rm fragments} = \frac{M_{\rm core} \times \epsilon_{\rm CFE}}{M_{\rm Jeans}}, \tag{3.8}$$

where $M_{\rm core}$ is the mass of the core (listed in Table A.2), $M_{\rm Jeans}$ is the non-thermal or turbulent Jeans mass (see Eq. (3.17) and § 3.3.6), and $\epsilon_{\rm CFE}$ is a core formation efficiency (CFE) which increases with the average density of the cores (e.g. Bontemps et al., 2010). To estimate the CFE, I consider the following empirical relation

$$\epsilon_{\rm CFE} = \epsilon_0 \times \left(\frac{n^{\rm obs}_{\rm H_2}}{n^{\rm max}_{\rm H_2}} \right)^p, \tag{3.9}$$

where $n^{\rm obs}_{\rm H_2}$ is the measured Hydrogen volume density for each core (listed in Table A.2), and $n^{\rm max}_{\rm H_2}$ is the maximum observed density. For different values of ϵ_0 and p, I determine the expected number of fragments. When the number of fragments is higher than 1, I assign to each of them a mass equal to the $M_{\rm Jeans}$. Otherwise, I consider the original mass of the core. Finally, I build a CMF including all the fragments and determine the slope of the high-mass end. I find that with $\epsilon_0 = 0.4$ and $p = 1.3$, it is possible to reproduce a CMF which mimics the IMF.

In order to evaluate the reliability of the CFEs I obtained for each ALMA core, I consider those cores of NGC 6334 that resolve into multiple components when observed at higher angular resolutions (e.g. Brogan et al., 2016; Hunter et al., 2014) and compare the predicted number of fragments with the observed one. For source 43, I estimate 2 components, consistent with the 2 fragments found by Brogan et al. (2016). For source, 44 I predict 9 components, in a good agreement with the 7 fragments detected with a resolution of 0.2″. Finally, those cores which I do not predict to resolve into further components also appear as single cores when observed at higher angular resolutions.

As discussed in the last two sections, I found a realistic range of temperature and multiplicity level that can reproduce the shape of the IMF. Therefore, the apparent variation between the CMF and the IMF can be spurious. The same statement applies to other regions where a top-heavy CMF has been reported (e.g. Motte, Bontemps, and Louvet, 2018; Sánchez-Monge et al., 2017; Zhang et al., 2015).

3.3.3 Mass Segregation

An interesting and widely-discussed aspect of the process of cluster formation is an effect called "mass-segregation" (e.g. Bonnell and Davies, 1998; Busquet et al., 2019; Chandrasekhar, 1942; Liu et al., 2015; McNamara and Sekiguchi, 1986; Plunkett et al., 2018; Spitzer, 1969; Zinnecker, McCaughrean, and Wilking, 1993). Mass segregation generally refers to a state in which the population of massive stars in a high-mass star-forming cluster are concentrated towards the center of the cluster, while the low-mass members can be found throughout the whole cluster. The physical origin of mass segregation can be explained by two alternative scenarios: primordial or dynamical. The primordial mass segregation is an intrinsic outcome of the initial condition of star formation suggested by the competitive accretion theory (Bonnell and Bate, 2006; Bonnell and Davies, 1998). Based on this theory, massive stars form preferentially in the center of the star-forming regions. In the case of dynamical mass segregation, massive stars loose their energy through two- and many-body interactions with low-mass stars and hence sink to the center of the cluster. Based on an ensemble of simulations performed by Allison et al. (2009b), dynamical segregation can happen only if clusters are born dynamically cool and fractal (with a

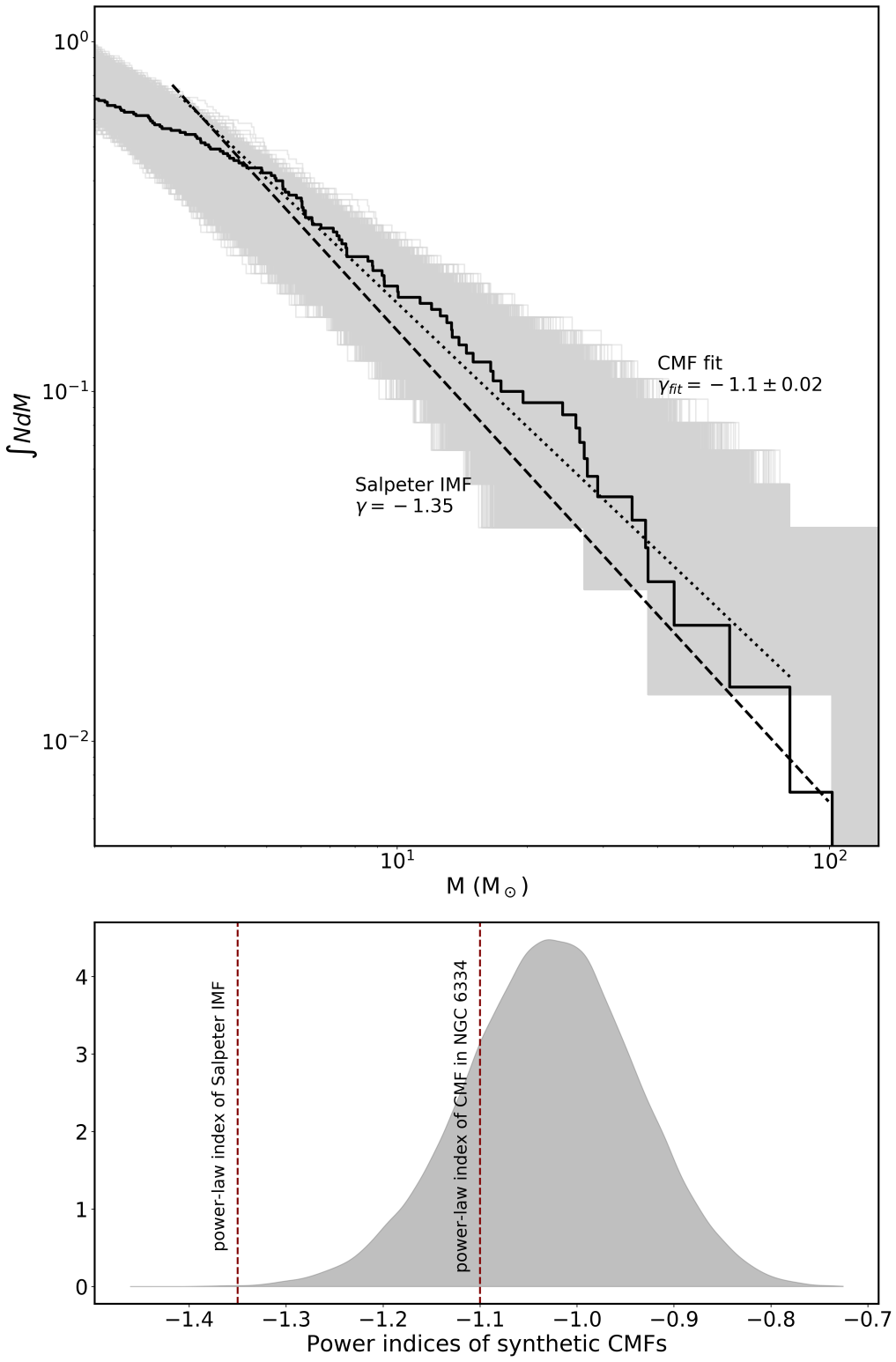

FIGURE 3.13: *Top:* NGC 6334 cumulative core mass function shown in solid black line fitted by a single power-law $dN/d\log(M) \propto M^{-1.1}$ indicated with a black dotted line. The grey area represents the synthetic CMFs for 100 000 groups of cores. The Salpeter IMF shown in black dashed line indicates a clear variation from the CMF. *bottom:* KDE of the power-law indices of the synthetic mass functions. The vertical dashed lines show the power-law index of Salpeter IMF and the power-law index of CMF in NGC 6334 region.

$Q \approx 0$). In this case, mass segregation can occur very rapidly down to a few solar masses during a short-lived state (0.5–1 Myr) after the large scale clump has collapsed (Allison et al., 2009b; Spera and Capuzzo-Dolcetta, 2017). Investigating the status and origin of mass segregation in young massive clusters is relevant for understanding the process of star formation and the dynamical evolution of the clusters.

In order to search for evidences of mass segregation in the clusters of NGC 6334, I followed three different approaches and cross checked the results. In the first method, I divide the members of each cluster into two groups of high-mass ($M > 20\ M_\odot$) and low-mass ($M < 20\ M_\odot$) cores and build individual MSTs for each group of the cores. Assuming a star formation efficiency of 30%, a compact source with a mass of $\sim 20\ M_\odot$ will form a B-type star. Therefore, the threshold considered for this analysis allows me to properly categorize the potential high-mass and low-mass stars. For a mass segregated cluster, it is expected that the subpopulation of high-mass stars is more compact as a group. For NGC 6334-I, the mean MST pathlength for the group of high-mass cores (4 700 au) is smaller than the pathlength for the low-mass cores (9 700 au), suggesting that the massive objects are located closely. In cluster NGC 6334-I(N), the mean MST pathlength for both groups of the cores are similar (6 200 au). NGC 6334-E and NGC 6334-I(NW) do not include cores with masses larger than 20 $M_\odot$. Therefore, this analysis can not be applied to these two clusters.

In a second method, I investigate the positions of the cores relative to the cluster center and the radial distribution of the mass. As mentioned before, if a cluster is mass segregated, most massive stars are preferentially towards the center. It is necessary to note that a cluster does not have a simple geometry, and thus, determining the center of a cluster is not trivial. One alternative way to define the cluster center is to assume that the central point coincides with the center of mass of the cluster. Another option is to assign the location of the most massive core as the cluster center. Finally, the center can be defined as the mean position of the cluster members (geometrical center). Since I aim at investigating the distribution of the massive cores relative to the center, all these three definitions seem to be fairly reasonable. The difference between the coordinates of the three defined centers is small in the four identified clusters, with a mean relative offset of $9.5''$. In Fig. 3.14, I plot the mass of each core against its distance to the center of the cluster. The panels of Fig. 3.14 are divided in four quadrants determined by a threshold for mass and distance from the center considered for mass segregation. The threshold considered for mass to distinguish between low-mass and high-mass cores is 20 $M_\odot$. 20% of a cluster radius is adopted to separate the inner and outer part of a cluster. The fraction of massive cores located close to the center indicates the level of mass segregation in a cluster. As shown in Fig. 3.14, 100% of the high-mass cores in NGC 6334-I are located at a distance of $<$20 000 au to the center exhibiting a clear evidence of mass segregation in this cluster. In the case of NGC 6334-I(N), 60%–80% of the high-mass cores are concentrated in the inner region while the low-mass cores are distributed uniformly in the whole region. In contrary, NGC 6334-E and NGC 6334-I(NW) do not harbour cores with masses larger than 20 $M_\odot$, and therefore, no hint of segregation is found in these two clusters.

In the last approach, I took advantage of the Λ_{MSR} parameter as introduced by Allison et al. (2009b) to quantitatively measure the degree of segregation. The Λ_{MSR} parameter compares the 2D spatial distribution of N most massive stars with a spatial distribution of N random stars based on the MST method. This approach has the advantage that it does not require any center and is independent of cluster geometry (Parker and Goodwin,

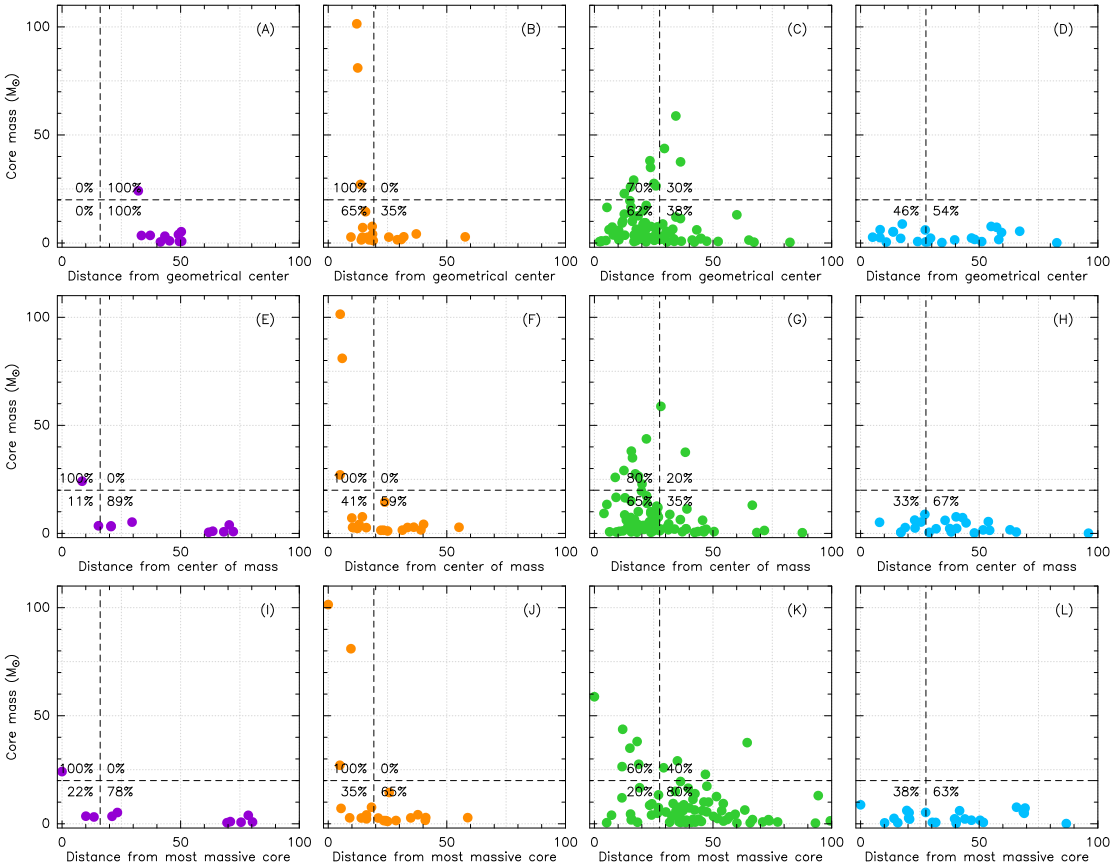

FIGURE 3.14: Mass of each core against its distance from the geometrical center of the cluster (top panels), the center of mass (middle panels), and the most massive core of each cluster (bottom panels). Each column corresponds to a cluster: NGC 6334-E (first column, in violet), NGC 6334-I (second column, in orange), NGC 6334-I(N) (third column, in green), and NGC 6334-I(NW) (fourth column, in light blue). The vertical and horizontal dashed lines divide each panel in four quadrants with a mass threshold of 20 $M_{\odot}$ and a distance threshold corresponding to one third of the cluster radius. The numbers indicate the percentage of sources (above and below the mass threshold) that are located in the inner or outer part of the cluster.

2015; Yu et al., 2017). Allison et al. (2009b) defined the mass segregation ratio ($\Lambda_{\rm MSR}$) as

$$\Lambda_{\rm MSR} = \frac{\langle l_{\rm random} \rangle}{l_{\rm massive}} \pm \frac{\sigma_{\rm random}}{\sigma_{\rm massive}}, \tag{3.10}$$

where $l_{\rm massive}$ is the mean MST length of the N most massive sources and $\langle l_{\rm random} \rangle$ is the average pathlength of the MST of N random sources in the cluster. $\sigma_{\rm massive}$ and $\sigma_{\rm random}$ represent the standard deviation associated with the average MST lengths of the massive and random stars respectively.

In practice, to determine the $\langle l_{\rm random} \rangle$, I generate 10 000 clusters with N uniformly distributed cores over an extent similar to the size of the real cluster. The individual positions of stars in a two-dimensional disk-like cluster is generated using

$$\begin{aligned} r &= (2-\alpha) R_r / 2^{1/(2-\alpha)}, \\ \phi &= 2\pi R_\phi, \\ x &= r\cos(\phi), \\ y &= r\sin(\phi), \end{aligned} \tag{3.11}$$

where R_r and R_ϕ are random numbers in range 0–1 and $\alpha = 1$. For disk of radius $R_{\rm disk}$ centered at $(X_{\rm c}, Y_{\rm c})$, the r parameter and randomly generated positions are scaled as

$$\begin{aligned} r &= R_{\rm disk}((2-\alpha) R_r / 2^{1/(2-\alpha)}), \\ x &= X_{\rm c} + r\cos(\phi), \\ y &= Y_{\rm c} + r\sin(\phi). \end{aligned} \tag{3.12}$$

$\Lambda_{\rm MSR} \approx 1$ shows that the massive sources are distributed in the same way as a uniform cluster, whereas $\Lambda_{\rm MSR} > 1$ indicates mass segregation. In contrary, $\Lambda_{\rm MSR} < 1$ implies inverse-segregation, with massive objects more widely distributed compared to a uniform cluster. In Fig. 3.16, I show the mass segregation ratio $\Lambda_{\rm MSR}$ for an increasing number of mass-ranked members $N_{\rm MST}$. NGC 6334-E exhibits an approximately flat plateau with $\Lambda_{\rm MSR}$ fluctuates around unity. This feature suggests that no clear sign of mass segregation is observed in this cluster. In contrast, NGC 6334-I indicates a very large value of the mass segregation ratio when $N_{\rm MST} = 3$. This corresponds to a mass of 20 $M_\odot$, and indicates that cores with higher masses appears more segregated. In NGC 6334-I(N), despite the fluctuations in level of segregation, there is an increase when $N_{\rm MST} = 9$, and therefore hints of segregation for cores with masses > 25 $M_\odot$. Finally, for NGC 6334-I(NW), the level of segregation exhibits no distinct deviation from a uniform behaviour around unity, suggesting no hints of segregation.

In summary, according to the results obtained using the three different methods, I find clear evidences of mass segregation in NGC 6334-I and possible evidences in NGC 6334-I(N). In NGC 6334-E and NGC 6334-I(NW), due to the lack of massive cores, no hint of segregation is found. Fig. 3.15 displays the summary of the mass segregation analysis. In this figure, I show the position of the center of mass in each cluster (cross symbol) as well as the position of the most massive member (black circle). All the mass segregated cores are indicated with filled circles. I note that the possible biases due the large uncertainties in temperature measurements and unresolved multiplicity may affect some of the results (see § 3.3.2 and § 3.3.2). Therefore, higher-angular observations together with accurate temperature determination is necessary to more precisely characterize the mass segregation.

3.3.4 Correlation between the mass segregation parameter Λ_{MSR} and the structural concentration of the clusters

As previously mentioned, analysing mass segregation in NGC 6334-I(NW) suggests that this cluster indicates no evidence of mass segregation. However, the mass segregation ratio measured for different number of cores is still not equal to 1 (see the last panel of . 3.15). To evaluate the reason that leads to this result, I investigate a possible relation between the mass segregation parameter and the concentration of the cores within a cluster. For this, I generate a sample of clusters within which the position of the cores follows a Gaussian distribution. To measure the mass segregation ratio, I compare the Gaussian clusters with a uniform cluster which has similar extent and number of cores. The concentration of members in a Gaussian cluster is defined by the width of the Gaussian σ. The larger values of σ result in a more dispersed distribution of cores. Therefore, the Gaussian clusters with a large enough σ resemble the uniform clusters.

For each value of σ, I generate 50 Gaussian clusters with each containing 70 cores. For each cluster, I run MST analysis to measure the mean MST pathlength. Then, I calculate the Λ_{MSR} parameter for each cluster, following Eq. 3.10. As the value of σ increases, it is expected that the distribution of the cores in a Gaussian cluster becomes more similar to a uniform distribution and consequently, the value of Λ_{MSR} parameter approaches to 1. In Fig. 3.17, I plot the value of Λ_{MSR} for each Gaussian cluster and the ratio of its extent and the size of the uniform cluster. As measured for the clusters in NGC 6334 (see § 3.3.1), the size of both uniform and Gaussian clusters are defined as the distance of the furthest core from the geometrical center. Fig. 3.17 indicates that the Λ_{MSR} parameter approaches to 1 as the Gaussian clusters become as dispersed as the uniform clusters (i.e., as the ratio of size of the Gaussian and uniform cluster converges to 1.). This result suggests that the Λ_{MSR} parameter does not only depend on the position of the massive cores relative to the center, but also is measure of the distribution and concentration of any number of cores in a cluster. Constant values of Λ_{MSR} slightly above 1, as found in NGC 6334-I(NW), may indicate that the cores in the cluster are not uniformly distributed. Instead, they are concentrated in different regions throughout the whole extent of the cluster. The correlation between the mass segregation ratio and the structural concentration has also been reported by de Vita, Trenti, and MacLeod (2019) in globular clusters.

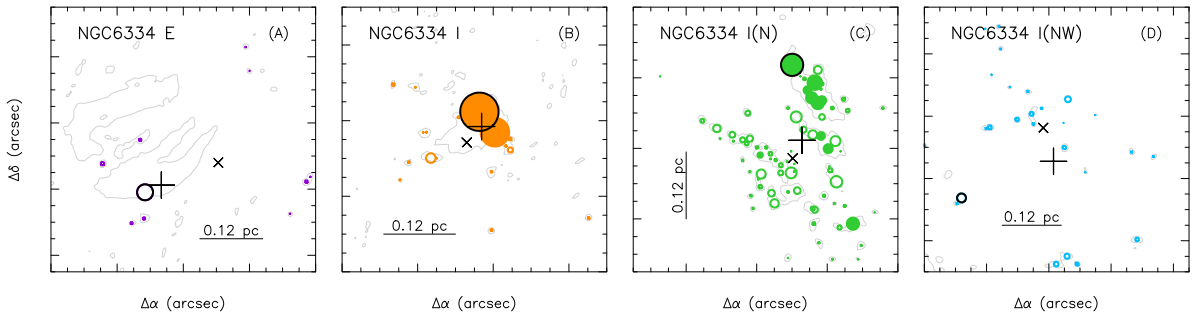

FIGURE 3.15: Distribution of the cluster members relative to the center mass marked with a plus sign. The segregated cores defined based on the mass-segregation ratio (see Fig. 3.16) are shown with filled circles. The black circle shows the position of the most massive member in each cluster. The size of the circles correspond to the mass of the cores.

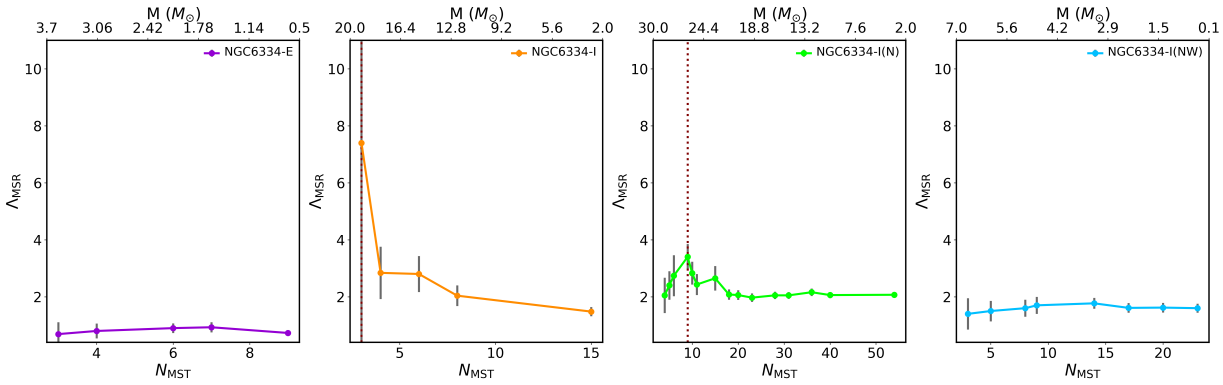

FIGURE 3.16: The evolution of Λ_{MSR} with different number of sources, N_{MST}. Each point of the figure corresponds to a specific mass range. The mass which corresponds to a sharp drop of Λ_{MSR} defines the segregation threshold. The dashed red lines show the N_{MST} at which the mass segregation picks out.

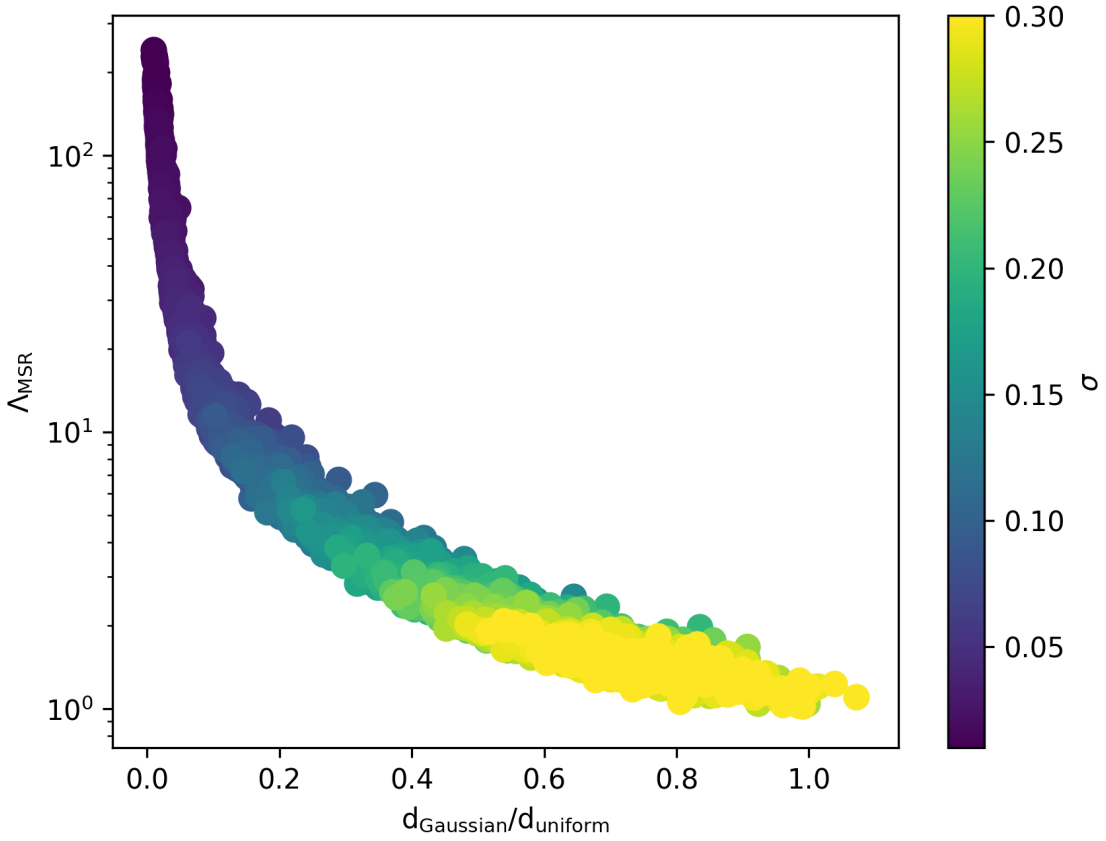

FIGURE 3.17: Mass segregation parameter Λ_{MSR} against the size ratio of a Gaussian cluster compared to a uniform cluster. Violet to yellow circles correspond to the randomly generated Gaussian clusters, each one defined by the Gaussian width σ color coded in the color bar. Extended Gaussian clusters have a distribution of cores resembling that of a uniform cluster, and thus Λ_{MSR} gets closer to 1.

TABLE 3.4: Masses, power-law index of CMFs, and mass segregation ratios for each cluster

Cluster	mean $M_{\rm core}$ ($M_\odot$)	median $M_{\rm core}$ ($M_\odot$)	Temperature (K)	n_{H_2} (cm^{-3})	$M^{\rm th}_{\rm Jeans}$ ($M_\odot$)	$M^{\rm nth}_{\rm Jeans}$ ($M_\odot$)	α-CMF [M>2 $M_\odot$]	$\Lambda_{\rm MSR}$ [M>10 $M_\odot$]
NGC 6334-E	5	3	22	3.5×10^4	1.0	20	−3.17	...
NGC 6334-I	14	3	23	4.0×10^5	1.0	20	−0.71	3.60
NGC 6334-I(N)	9	5	19	3.2×10^5	0.9	23	−0.99	2.47
NGC 6334-I(NW)	3	2	18	3.3×10^4	0.9	24	−1.32	...
NGC 6334	8	3	21	1.5×10^5	1.5	34	−1.10	2.68

3.3.5 Fragmentation Analysis

As shown in § 3.2.1, the four clusters in NGC 6334 are fragmented into a group of cores with a range of masses and densities. There is a variety of fragmentation processes which can form compact sources in proclusters. In the classic picture of star formation, cloud fragmentation takes place by balancing gravity with thermal pressure following Jeans instability. According to the turbulence regulated theory of star formation (Krumholz and McKee, 2005; McKee, 2004; Padoan et al., 1999), supersonic turbulence creates a series of local density enhancements which may become Jeans unstable and undergo gravitational collapse. In this picture, self-gravitating clumps are supported against collapse by turbulent support rather than thermal support. For this case, turbulent motions can act as a pressure that provides support against the self-gravity of the protocluster. In addition to the turbulent and thermal pressure, magnetic fields and stellar feedback are likely the two other factors which control the fragmentation process (Girart et al., 2013; Hosking and Whitworth, 2004; Padoan and Nordlund, 2002). In the following section, I investigate the effect of turbulent and thermal pressure in regulating the fragmentation process of the clusters in NGC 6334. For this, I compare the measured masses of the fragments and separations between them with those expected from thermal and turbulent Jeans instability.

3.3.6 Clump fragmentation

If the fragmentation is governed by Jeans instability, the gaseous clump with a H_2 volume density of n_{H_2} and kinetic temperature of T has a Jeans length of

$$\lambda_J = c_{\rm eff}\left(\frac{\pi}{G\rho}\right)^{1/2}\left(\frac{n_{H_2}}{10^5\ {\rm cm}^{-3}}\right)^{-1/2}, \tag{3.13}$$

where $c_{\rm eff}$ is the 'effective' sound speed, ρ is the density and G is the gravitational constant. Assuming a spherical geometry for the clump and also with the assumption that the Jeans length represents the diameter of the sphere, the Jeans mass is calculated using

$$M_J = \frac{\pi^{5/2}}{6\ G^{3/2}}\ c_{\rm eff}^3\ \rho^{-1/2}. \tag{3.14}$$

Different mechanisms of support against gravity (i.e., thermal and turbulent pressure) are taken into account through the use of effective sound speed, $c_{\rm eff}$ (see e.g. McKee, 2004). For the case of pure thermal support the effective sound speed correspond to the thermal sound speed, calculated as,

$$c_s = \sqrt{\frac{\gamma k_B T}{\mu_{H_2} m_H}}, \tag{3.15}$$

where γ is the adiabatic constant which is equal to 1 for an isothermal medium, k_B is the Boltzmann constant, T is the average temperature of the clump, μ_{H_2} is the mean molecular weight per hydrogen molecule and m_H is hydrogen mass. If we assume that the thermal pressure is dominant in the fragmentation process, the Jeans mass is written as

$$\frac{M^{th}_{Jeans}}{M_\odot} = 0.6285 \left(\frac{T}{10\ \mathrm{K}}\right)^{3/2} \left(\frac{n_{H_2}}{10^5\ \mathrm{cm^{-3}}}\right)^{-1/2}. \tag{3.16}$$

To measure the contribution of the non-thermal pressure, I calculate the non-thermal component of the lines by subtracting out the thermal velocity dispersion, i.e., $\sigma^{nth} = \sqrt{(\sigma^{obs})^2 - (\sigma^{th})^2}$, using $\sqrt{\gamma k_B T/\mu m_H}$ for the thermal velocity dispersion. To estimate the observed velocity dispersion, σ^{obs}, I use the second moment map of $HC^{15}N$ molecular line observed with ALMA over the extent of the clusters. The contribution of the thermal velocity dispersion to the total observed line width seems to be negligible (0.08 km/s) and the non-thermal component, σ^{nth}, is estimated to be 0.7 km/s. The turbulent Jeans mass is then defined as (Palau et al., 2015)

$$\frac{M^{nth}_{Jeans}}{M_\odot} = 0.8255 \left(\frac{\sigma_{1D,\,nth}}{0.188\ \mathrm{km\ s^{-1}}}\right)^{3} \left(\frac{n_{H_2}}{10^5\ \mathrm{cm^{-3}}}\right)^{-1/2}. \tag{3.17}$$

The thermal and turbulent Jeans masses estimated for each cluster are listed in Table 3.4. In case of NGC 6334-E, NGC 6334-I and NGC 6334-I(N) the mean mass of the observed core is considerably larger than the thermal Jeans mass. This suggests that the turbulent pressure plays a more crucial role compared to the thermal pressure in regulating the fragmentation process. In contrast, the mean mass of the cores in NGC 6334-I(NW) is consistent with the expected thermal Jeans mass. According to the point that NGC 6334-I(NW) harbours no massive core, this result might suggest that in low-mass star forming regions thermal motions dominate over the turbulent pressure during the fragmentation process. Turbulent fragmentation is also found in the massive star forming region G28.34-P1 (Wang et al., 2011), although other works suggest thermal Jeans fragmentation in other high-mass star forming clouds (see e.g. Palau et al., 2015).

3.3.7 Filament fragmentation

As shown in Fig. 3.1 (see also Fig. 3.18), NGC 6334-I(N) harbors two elongated filamentary-like structures which are resolved into a chain of regularly spaced cores. In this section my goal is to characterise the fragmentation in the filamentary structures and search for the relevant fragmentation scale for the filaments. For this, I focus on the southern filament shown in Fig. 3.18 which has an extent of ∼0.4 pc. While the super-resolution continuum map reveals more small-scale details, the combined 12 m with ACA image recovers more of the extended filamentary structure. Therefore, I use the combined continuum map to measure the dust mass of the filament. A commonly used model to describe the fragmentation of a self-gravitating cylinder is the so-called "sausage instability" of a gas cylinder which is first proposed by Chandrasekhar (1953) and followed by many others (see e.g. Fiege and Pudritz, 2000; Fischera and Martin, 2012; Inutsuka and Miyama,

1992; Wang et al., 2011). According to this model, the filament is gravitationally unstable against collapse if its mass per unit length (line-mass) exceeds a critical value of

$$(M/l)_{\text{th-crit}} = 2c_s^2/G = 465 \left(\frac{c_s}{1\text{km s}^{-1}}\right)^2 M_\odot \text{ pc}^{-1}. \quad (3.18)$$

To estimate the line mass of the southern filament in NGC 6334, I integrate the flux of the ALMA combined map over the extent of the filament which yields a total flux of 0.51 Jy. Then, I subtract the contribution of the cores embedded in the filament, and assume an average temperature of 26 K (based on the *Herschel* temperature map of Russeil et al. (2013)) to obtain a filament mass of 342 $M_\odot$. Considering an extent of 0.4 pc for the southern filament, the line-mass of the filament is estimated to be (M/l)=925 $M_\odot$ pc^{-1}. It is necessary to note that this value is a upper limit of the average line-mass as the inclination of the filament is neglected. For a thermally supported filament at a temperature of $T = 26$ K, the critical line-mass is $(M/l)_{\text{th-crit}}$=43 $M_\odot$ pc^{-1}. Thus, the filament is clearly supercritical and consequently undergoes gravitational collapse along its main axis. The outcome of the collapse is the formation of small fragments along the main axis of the filament as observed in NGC 6334-I(N). The "sausage instability" model predicts that if a filament fragments into a chain of core, the typical spacing between the cores is expected to be

$$\lambda_{\text{cl}} = 22\nu(4\pi G\rho_c)^{-1/2} = 1.24 \left(\frac{\sigma}{1 \text{ km s}^{-1}}\right) \left(\frac{n_c}{10^5 \text{ cm}^{-3}}\right)^{-1/2} \text{pc}. \quad (3.19)$$

In the above equation, ρ_c or n_c is the gas density at the center of the filament. The fragment mass is therefore

$$M_{\text{cl}} = (M/l)_{\text{th}-\text{crit}} \times \lambda_{\text{cl}} = 575.3 M_\odot \left(\frac{\sigma}{1 \text{ km s}^{-1}}\right)^3 \left(\frac{n_c}{10^5 \text{ cm}^{-3}}\right)^{-1/2} \quad (3.20)$$

I estimate the central density of the filament to be the average of the core density, which amounts to $n_c = 1.2 \times 10^6$ cm^{-3}. Adopting a velocity dispersion of 0.7 km/s, I calculate the typical separation of 0.2 pc and fragment mass of 59 $M_\odot$ for turbulent support. Assuming a pure thermal fragmentation yields 0.002 pc and 0.08 $M_\odot$ for the typical separation and fragment mass respectively.

Our ALMA observations of the dust continuum emission at 3 mm resolve the filament into a chain of 42 cores. The mean projected separation between the identified cores along the filament is 0.022 pc, which should be taken as a lower limit if projection effects are taken into account. The median mass of the cores embedded in the filament is 5 $M_\odot$. Comparing these two values with the expected separation and fragment mass from the thermal support suggests that turbulent motions within the filament contribute to the fragmentation process (see e.g. Seifried and Walch, 2015). In addition to the micro-scale turbulent cascades, the relative motions of the cores embedded in a filament can also contribute to the level of turbulence in a filament (see e.g, Clarke et al., 2017).

3.4 Discussion

3.4.1 Hierarchical picture of fragmentation in NGC 6334

In § 3.3.5, I investigated which process, turbulence or gravity, is controlling the fragmentation level of massive protoclusters at a scale of ∼0.1 pc. In this section, I discuss different levels of fragmentation in NGC 6334 star-forming region from the large-scale filamentary cloud with a size of a few 10 pc down to small-scale compact cores with an

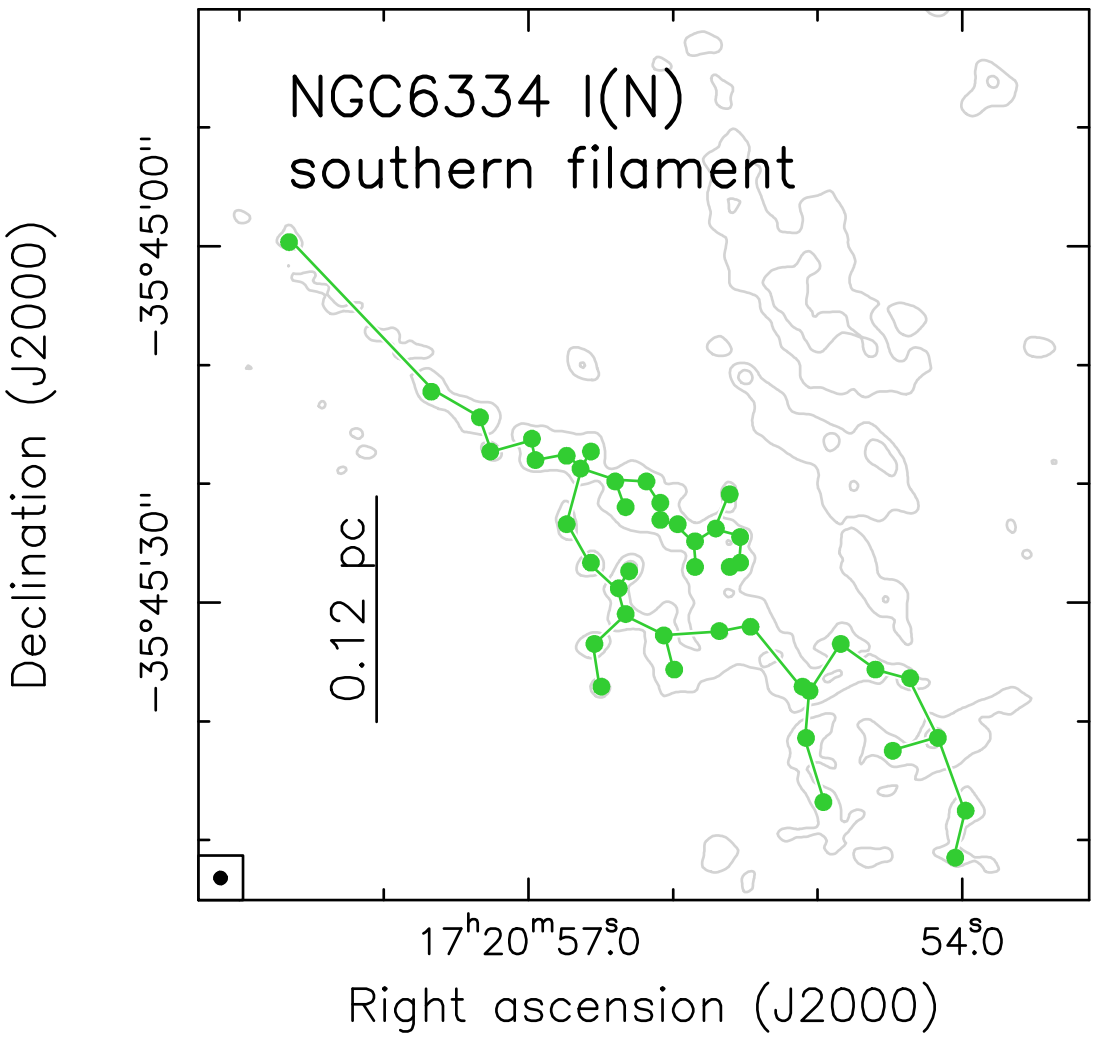

FIGURE 3.18: Close-up view of the NGC 6334-I(N) cluster. The green circles mark the positions of the sources that belong to the southern filament. The green segments correspond to the minimum spanning tree of these sources. The extent of the filament is about 0.4 pc.

extent of a few 1000 au. Fig. 3.19 displays the hierarchical structures in NGC 6334 complex. The whole molecular cloud appears as an elongated filamentary structure with an extent of about 50 pc aligned with the galactic disk (Persi and Tapia, 2008; Russeil et al., 2013; Sánchez-Monge et al., 2015). Its central part consists of a 10-pc long filament with an average density of $\sim 10^6$ cm^{-3}. Investigating the velocity field of HCO^+ towards the central part of the filament revealed a large-scale velocity gradient indicating a gravitational collapse and contraction (Zernickel, Schilke, and Smith, 2013). Simultaneously, the filament seems to be fragmenting into a number of star-forming clumps with sizes of 1 pc and masses of a few hundred $M_\odot$. The clumps which have been identified in *Herschel* observations at sub-millimeter wavelengths harbour a few tens of compact sources with a typical separation of a few ten/hundred thousands au.

The second level of fragmentation is found towards the massive protoclusters at a scale of $\sim$0.1 pc. As detected in our ALMA observations at millimeter wavelengths, the four identified protoclusters are fragmented into a number of smaller dense cores with sizes of a few hundred to a few thousands au. MST analysis shows that the frequency of nearest neighbor separations of the cores increases down to the resolution limit of the observations. The mean typical separation of the cores (3 700 au) is consistent with the turbulent Jeans length. Particularly in NGC 6334-I(N), in addition to the compact cores, I find two elongated filamentary-like structures with an extent of about 82 000 au and width of 19 000 au. This suggests that small-scale filaments can appear as substructure in massive clumps connecting the scales between the clumps and cores.

The smallest scale of fragmentation is found within the massive cores in the observed region. Observations at sub-arcsecond angular resolution (Brogan et al., 2016; Hunter et al., 2014) reveal that some of the cores (e.g. sources 43 and 44) divided into multiple components at a scale of a few hundred au. The further fragmentation of the dense cores is in agreement with the numerical simulations which predict that core fragmentation at scales between 500–5 000 au is an efficient formation mechanism of bound clusters (Offner et al., 2010). To investigate the mechanism which regulate the fragmentation in small scale, I consider the hot core in NGC 6334-I (source 42) which is resolved into at least seven components (Brogan et al., 2016). MST analysis on the observed components in these hot cores results in a typical projected distance of 620 au between the fragments. The observed typical distance is in agreement with the thermal Jeans length which is estimated to be 412 au. This point suggests that fragmentation at small scales seems to be controlled mainly by thermal support, while at clump scales, non-thermal pressure is dominant.

Thermal Jeans fragmentation at small scales is found in other regions (Beuther et al., 2018; Liu, 2019; Palau et al., 2015, 2018; Pokhrel et al., 2018). Palau et al. (2015) has combined interferometric and single-dish data of 19 nearby massive dense cores to study the active mechanisms controlling their fragmentation level at a scale of $\sim$20 000 au. They found that the observed number and measured masses of fragments are in agreement with the case of pure thermal Jeans fragmentation on small scales such as the protostellar objects ($\sim$15 au). However, the thermal motions are least efficient in providing support on larger scales such as the whole cloud ($\sim$10 pc). This trend is in agreement with our ALMA observations at the clump and core scales and confirms the role of non-thermal support on increasing the efficiency of formation at the scales of a clump. A more recent study by Palau et al. (2018) towards the Orion Molecular Cloud 1 South (OMC-1S) also suggested that the fragmentation at the earliest stages and within spatial scales of $\sim$1 100 au is following a thermal process.

In conclusion, multi-scale analysis of fragmentation in NGC 6334 indicates that fragmentation is a scale-dependent process which is regulated by non-thermal pressure at the

first two levels of hierarchy, from the large-scale cloud to the massive clumps and from the clumps to the compact cores. However, at small scales where the compacts fragment into low-mass components, thermal pressure plays a more crucial role.

3.4.2 Correlation between the time evolution and properties of the clusters

As discussed in § 3.2.1, ALMA observations towards NGC 6334 revealed the presence of four well-identified clusters: NGC 6334-E, NGC 6334-I, NGC 6334-I(N) and NGC 6334-I(NW). In § 3.3, I determined the different physical properties of the each cluster such as separations between the members, distribution of masses between the members and mass segregation. In the following, I investigate if the different properties may be correlated with a different evolutionary stage of each cluster.

The physical association of protoclusters with HII regions or cold dust objects is related to their evolutionary stage. The younger embedded clusters are more associated with dust, while the most evolved ones are located within HII regions (2005; Kurtz and Hofner, 2005). Based on this criterion, NGC 6334-E with a well-developed HII region is classified as the most evolved of the four clusters. The evolutionary order is followed by NGC 6334-I which is associated with an UC HII region (see Kurtz, 2000; Peters et al., 2011, for classification of HII regions). In a younger stage, we can find NGC 6334-I(N) as the HII region identified within this cluster is still compact and embedded. Finally, NGC 6334-I(NW) harbors dust cores only with presence of no HII regions. The absence of the HII region in NGC 6334-I(NW) indicates that this cluster is either at its early stage of evolution or no massive star is forming in it. If the later case is true, the cluster can not be clearly classified in an evolutionary stage. As a complementary criterion for classifying the clusters based on their evolutionary stage, I consider their infrared stellar content. The ratio of mm sources per young stellar objects provides a simple diagnostic for the evolutionary stage of each cluster. Based on this, NGC 6334-E with 2 mm sources per young stellar object, and NGC 6334-I with 3 mm sources per young stellar object are the most evolved clusters. NGC 6334-I(N) with 4 mm sources per young stellar object follows NGC 6334-I. NGC 6334-I(NW) with 2 mm sources per young stellar objects does not follow the expected evolutionary trend. This point can be another evidence which suggest that NGC 6334-I(NW) is a relatively evolved cluster with no massive star. In summary, I can classify the identified clusters from more evolved to less evolved in the following order: NGC 6334-E and NGC 6334-I as the most evolved, followed by NGC 6334-I(N) as the youngest.

I make use of the evolutionary classification of the clusters to investigate how the physical properties of the clusters change with the evolutionary stage. In particular, I focus on the variation of typical separations between cluster members and the internal structure of the clusters, mass distribution in the clusters and presence of mass segregation effects. Comparing the mean and median distances between cluster members derived from the MST analysis indicates an increasing separation as the cluster evolves (excluding NGC 6334-I(NW) from the comparison). The observed trend is consistent with the expected expansion of clusters due to the gas expulsion and stellar ejection in their later evolutionary stages (Pfalzner and Kaczmarek, 2013). A comparison of the KDEs of the nearest neighbour distances in each cluster (see Fig. 3.9) shows that the cluster members are widely distributed in NGC 6334-E and NGC 6334-I, while the cluster members in NGC 6334-I(N) are more closely located with respect to each other. It is necessary to note that the observed cores in NGC 6334-E may not be related to the original cluster. Instead, they can be a new population of cores that has recently formed as a result of the expansion of the HII region.

The internal structure of the clusters is quantitatively evaluated based on the Q parameter (see § 3.2). In spite of the large uncertainties due to the low statistics in two of the clusters, I find that the Q parameter for NGC 6334-I, NGC 6334-I(N) and NGC 6334-I(NW) has a value close to 0.8 suggesting that these clusters centrally concentrated with a radial density gradient. In contrast, NGC 6334-E with a low value of Q parameter seems to be substructured. According to the observations conducted towards a sample of 16 open clusters in different evolutionary stages, less evolved clusters tend to exhibit fractal patterns, while the older clusters have distributed their stars in centrally concentrated structures (Sánchez and Alfaro, 2010). A similar results is reported in the simulations of the early evolution of clustering in a turbulent environment (Maschberger et al., 2010). The simulations show that a sub-structured cluster with a Q value of $\sim$0.5 evolves into a radially concentrated system with a $Q > 1.1$ after a certain number of free-fall times. Therefore, the Q parameter does not seem to be a fixed property. Instead, it seems to be a measure of evolution. However, due to large uncertainty in the measurements of the Q parameter, I can not confirm the observed trend in my sample of four clusters. Therefore, better statistics in the observed clusters as well as observations of other clusters in NGC 6334 complex is required to provide more reliable constrains in the relation of the Q parameter with the evolutionary stage of star-forming clusters still embedded in large amounts of gas and dust.

Regarding mass segregation, I find hints of segregation for clusters NGC 6334-I and NGC 6334-(N), with the former one showing stronger evidences as a more evolved cluster. The difference between the level of segregation in these two clusters suggest a possible dynamical origin for mass segregation (Allison et al., 2009a). Based on N-body simulations performed by Allison et al. (2009a), the dynamical segregation in young clusters can be possible only if they are born in a cool and clumpy distribution. Comparing the observed evidences with the results of the N-body simulations, it is possible to speculate that NGC 6334-I(NW) will be segregated in a later stage of its evolution, while NGC 6334-E has lost the hints of segregation. To better address the origin of mass segregation, it is also necessary to estimate the dynamical time scales for the clusters. I follow Eq. 1.1 to estimate the free-fall time for the clusters. The relaxation time scale is determined as $t_{\rm relax} = \frac{N}{6\log(N)} \frac{1}{\sqrt{G\rho}}$, where N is the number of cluster members. The free-fall time scale for NGC 6334-I and NGC 6334-I(N) ($\sim 10^5$ yr) is one order of magnitude smaller than the relaxation time scale ($\sim 10^6$ yr). This point call the scenario of dynamical mass segregation into question. Moreover, the presence of prominent filamentary structures in NGC 6334-I(N) is a sign of primordial segregation, since the dynamical evolution of the cluster should have dispersed substructures like filaments.

Finally, the CMFs of the different clusters show a steeper slope for most evolved cluster NGC 6334-E compared to the younger clusters NGC 6334-I and NGC 6334-I(N), indicating a deficit of high-mass cores in this cluster. Since massive cores are assumed to be the gas reservoir of a cluster, the lack of high-mass cores suggests that NGC 6334-E may have already exhausted or accreted the gas and dust mass. However, one has to note that in addition to the low statistics for cluster NGC 6334-E, the members of the cluster could present the second generation of the cores with lower masses.

The analysis presented in this chapter constitute the first step towards a comprehensive study of a larger sample of high-mass (proto)clusters. Increasing the number of studied regions in NGC 6334 compiles a larger catalog of clusters in different evolutionary stages, while at the same time ensuring that the dispersion of initial conditions is reduced because all of them formed within the same molecular cloud. Thus, such a study will provide statistically reliable results of the cluster properties and its relation with the

evolutionary stage.

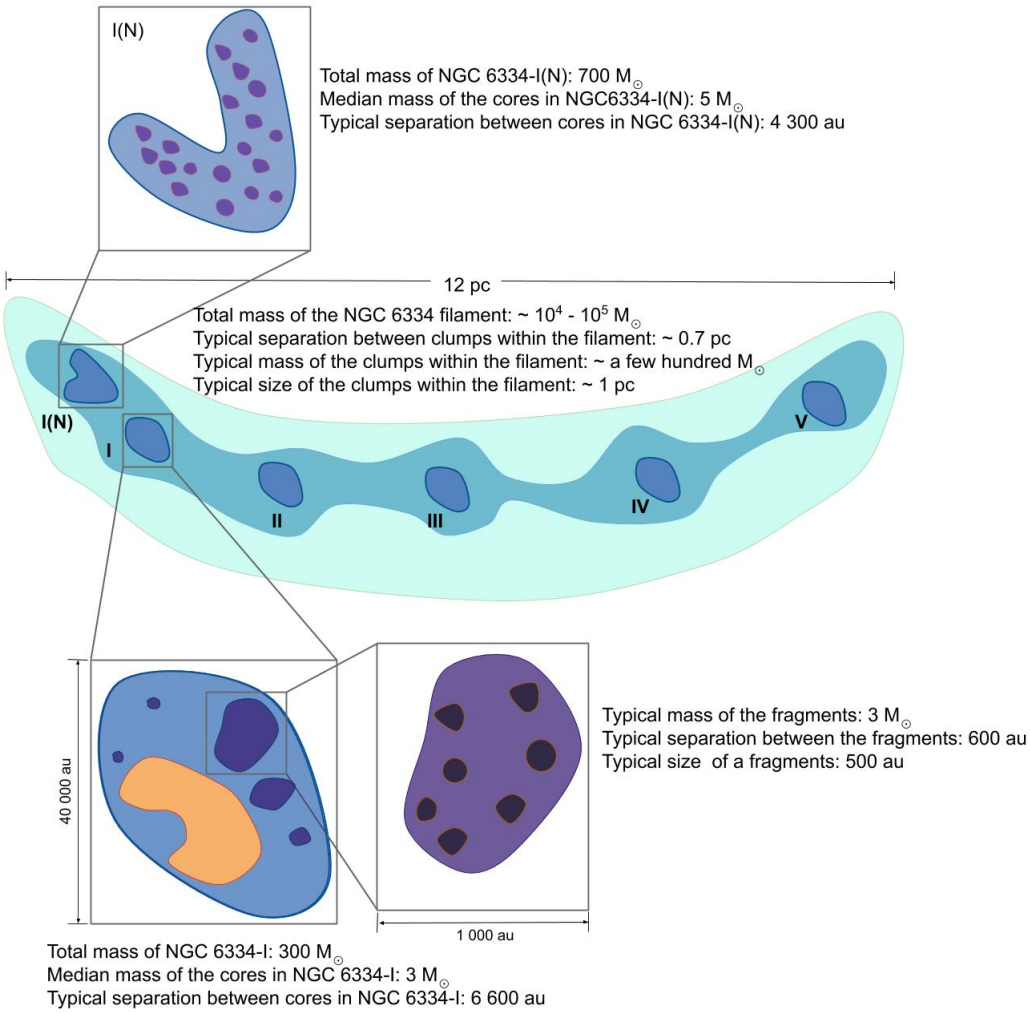

FIGURE 3.19: Schematic view of the central part of the NGC 6334 filamentary cloud. The distribution is based on *Herschel* observations by Russeil et al. (2013). The horizontal and vertical orientations correspond to the Galactic longitude and latitude coordinates. The sketch displays the hierarchical fragmentation seen in the cloud from the scale of the filament down to the scale of individual dense cores and protostars. The colors are scaled based on the density (from light blue to black). In this color scheme, the lighter colors (e.g. blue) correspond to the lower densities, while the darker colors (e.g. violet and black) represent the dense regions. The ionized gas is shown with orange. The values of masses and sizes are based on the observations presented in this work and from the literature (Brogan et al., 2016; Hunter et al., 2014).

Chapter 4

Kinematics of dense gas in NGC 6334

Recent observations in the (sub-)mm and IR regimes have shown the crucial role of filaments in star formation as clusters and cores are embedded in filamentary structures. For the formation of massive stars in a clustered environment, maintaining a high accretion rate is a possible solution to the radiation pressure problem. Increasing observational evidences have shown that the filamentary flows to the clusters and finally to the cores are one of the methods of achieving a high accretion rate. Numerical simulations also highlight the role of filaments as gas mass reservoirs which undergo global collapse and consequently transport material from large scales to their center of gravitational potential wells, where the clusters and cores are located. The filamentary gas flow is not only limited to parsec scales, but also it takes place on the ∼5000 au scales. At smaller scales, these filaments break into substructures which connect the clusters to the large-scale cloud. These substructures can be considered as accretion channels that feed different members of protoclusters. Determining the velocity fields of filaments over different scales is crucial to characterise the accretion process based on observational data. To accomplish this, large scale observations (a few tens of pc) must be linked with high spatial resolution on cluster scales (a few thousands au). In § 4.1, I elaborate on the large-scale APEX observations towards NGC 6334 presented in Zernickel (2015). In § 4.2, I focus on the kinematics of dense gas in the central part of the filament over a scale of 10 pc. In § 4.3, I study the kinematics of accretion on intermediate scales using the velocity fields of the dense gas observed with ALMA and APEX. In § 4.4, I measure the accretion rates of the filaments identified in the central part of the cloud. Finally, in § 4.6, I discuss the implication of my findings as relevant to accretion process.

4.1 Gas flows over large scales

In order to investigate the velocity field and mass flows in large scales, Zernickel (2015) obtained a ^{13}CO (2-1) APEX map of the whole filamentary structure of NGC 6334 over 60 pc. ^{13}CO is a proper tracer for diffuse gas and therefore, it can be used to probe the accretion toward the dense part of the filament from its diffuse surrounding. Fig. 4.1 demonstrates the first three moment maps of ^{13}CO. The central part of the filament exhibits higher integrated intensity with several peaks coinciding with the sites of massive star formation. The velocity field reveals systematic motions from the eastern and western parts of the map towards the main filament. The observed velocity gradient spans a range of ∼5 km s^{-1} in both directions with respect to the systemic velocity. Concentrating on the scale of the whole filament, a large velocity gradient along the filament from blueshifted velocities (~ -9 km s^{-1}) to redshifted velocities ($\sim +2$ km s^{-1}) is observed, spanning a range of 11 km s^{-1}. The velocity dispersion map has its highest value σ=3 km s^{-1} at the location of the sources NGC 6334-I and NGC 6334-I(N). Although the

observed gradient in the velocity field map likely traces the accretion of diffuse gas towards the densest part of the filament, a velocity analysis based only on the moment maps could be misleading in some aspects. First, the mean velocity is deviated by multiple velocity components along the line of sight. Secondly, the threshold which is chosen to subtract the noise, might filter out the weak components. Therefore, it is necessary to decompose the spectral information by Gaussian fitting. I took advantage of the BTS algorithm (see § C.1 for more details) to fit an arbitrary number of Gaussian components to each pixel in the spectral line cubes. The fits are done fully automatically with an assumption for the smoothing length, noise level and χ^2 limit. Selecting a low value for the smoothing length allowed me to fit the velocity components which are closely located. As the output, BTS returns the amplitude, centroid velocity and dispersion of each component. The linewidth can be then obtained from the velocity dispersion using FWHM=$\sqrt{8\ln(2)}\sigma \approx 2.355\sigma$. In the ^{13}CO data cube, 39% of the pixels are fitted with a single component, 60% with two components and only 1% with 3 components. Left and right panels of Fig. 4.2 show the velocity maps of the first and the second component respectively. Similar to the observed trend in the first order moment map of ^{13}CO, the velocity field of the first component reveals a velocity gradient of 10 km s^{-1} across the length of the whole filament ($\sim$60 pc) tracing, most likely, the original rotation of the molecular cloud (Zernickel, 2015). Moreover, a velocity gradient of a 4 km s^{-1} is observed towards the central and densest part of the filament. The second velocity component is mainly observed towards the dense filament, while the diffuse surrounding is fitted with one single component in most pixels. The large-scale velocity gradient is also clearly appreciated in the velocity field of the second component. Moreover, jumps from blue-shifted to red-shifted velocities are observed towards the two ends of the main filament.

4.2 Kinematics in the central part of the filament

Analysis of the velocity field of the dense gas over a scale of $\sim$60 pc reveals large-scale infall motions and rotation. In this section, I study the kinematics of dense gas in the central part of NGC 6334, where the high-mass star-forming clumps are located. Zernickel, Schilke, and Smith (2013) used APEX to map the dense central part of the NGC 6334 filamentary cloud in HCO$^+$ (3-2) emission line. Fig. 4.3 shows the first three moment maps of HCO$^+$ (3-2). The integrated intensity map reveals six peaks which coincide with the star-forming clumps embedded in the filament: NGC 6334-I(N) and NGC 6334-I to V. As shown in the first order moment map, the highest velocity (+2 km s^{-1}) is found at the position of source NGC 6334-II. A velocity gradient of 2 km s^{-1} is observed towards NGC 6334-I and NGC 6334-I(N). Perpendicular to the main filament, two subfilaments exhibits longitudinal gradient at α(J2000)=17^{h}19^{m}30^s.0 and α(J2000)=17^{h}19^{m}20^s.0. The velocity dispersion map has it highest value $\sigma = 3.5$ km s^{-1} at the positions of the massive clumps. It then decreases to 0.2 km s^{-1} in the outskirt of the central filament. The peak velocity map of of HCO$^+$ (3-2) is obtained by fitting the spectra extracted from each pixel of the data cube using the BTS algorithm. 95% of the pixels available in the cube are fitted with one single Gaussian component. As shown in Fig. 4.4, the highest velocity gradient ($\sim$4 km s^{-1}) is found towards NGC 6334-I, NGC 6334-I(N) and NGC 6334-V as the most massive clumps in the filament. This value drops to $\sim$2 km s^{-1} towards the remaining clumps which are less massive.

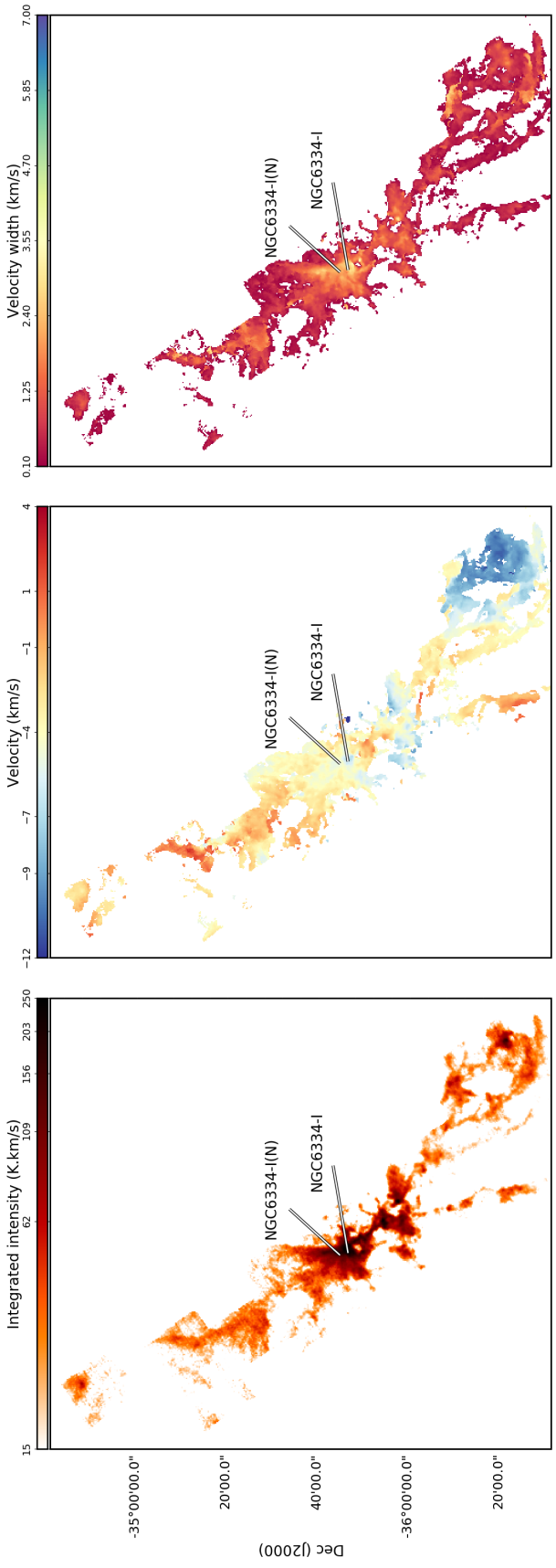

FIGURE 4.1: Spectral moments of ^{13}CO (2-1) molecule in NGC 6334. *Left:* Integrated intensity in units of Jy beam^{-1} kms^{-1}. *Middle:* Centroid velocity in km s^{-1}. *Right:* FWHM of central line in km s^{-1}.

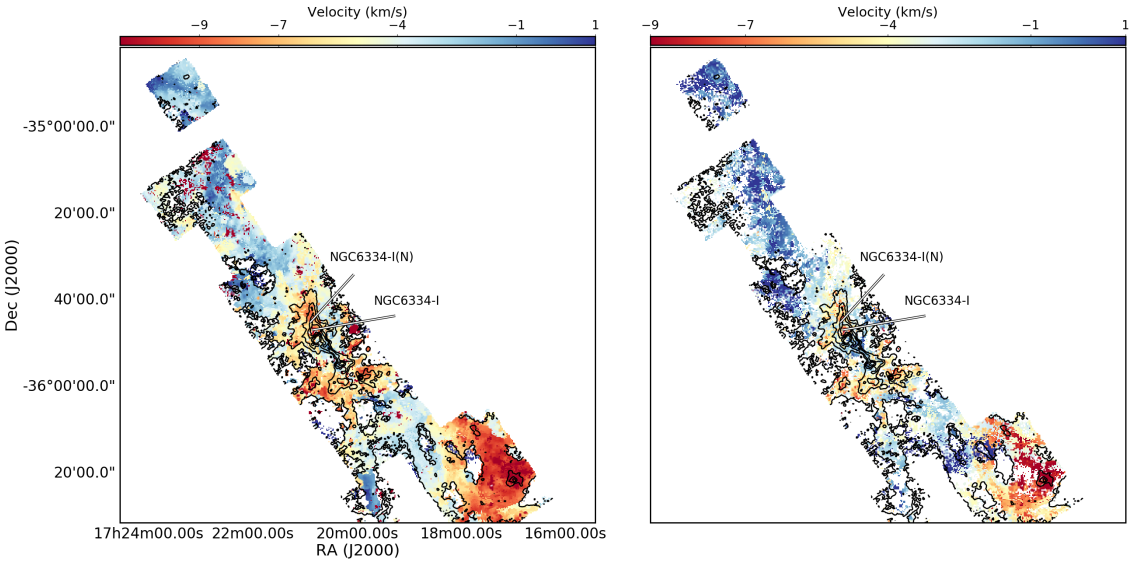

FIGURE 4.2: Velocity maps of the first and second component of ^{13}CO molecular emission obtained by spectral decomposition using the BTS algorithm. The zeroth-order moment map of ^{13}CO is overlaid in black contours.

4.3 Gas flow over cluster scales

Infall motions over scales of a few tens of pc is revealed by analysing the velocity fields in different clouds (e.g. Peretto et al., 2013; Wang et al., 2011; Zhang et al., 2015). However, to efficiently investigate high-mass star formation in filaments, it is necessary to resolve filamentary structures down to the scales of a few 0.1 pc. Such high spatial resolution observations towards massive filaments allow us to combine kinematic information from spectral lines with dust continuum emission and investigate the connection of the massive protoclusters with the environment in filaments.

With the aim of investigating the infall motions towards massive protoclusters embedded in filaments, Zernickel (2015) conducted APEX observations of HCO^+(4-3) and HCN(4-3) lines towards NGC 6334-I and NGC 6334-I(N). Fig. 4.5 shows the integrated intensity (left panel), velocity centroid (middle panel) and linewidth (right panel) maps for HCO^+(4-3) molecular line. As seen in the left panel of Fig. 4.5, HCO^+(4-3) shows an extended emission distributed across all the surveyed area revealing a set of filamentary extensions coming from different directions to converge into the central protoclusters NGC 6334-I and NGC 6334-I(N), where the significant intensity enhancements are observed. For clarity, the relevant structures seen in the map are marked with dotted lines and named as filaments one to six. The middle panel in Fig. 4.5 shows the velocity field as determined from the first-order moment analysis. I find a clear velocity gradient of $\sim$3 km s^{-1} along the filaments 3, 4 and 5 towards NGC 6334-I. The velocity map along the three remaining filaments does not exhibit a clear gradient, with most of the emission at systemic velocities (-4 km s^{-1}). However, a slight velocity enhancement at the center of NGC 6334-I(N) compared to the surrounding likely reveals a small gradient due to infall motions. The right panel of Fig. 4.5, shows the velocity dispersion as determined from the second-order moment analysis. The extended emission has a constant, relatively narrow linewidth of $\sim$1.5–2 km s^{-1}, which increases towards the central parts

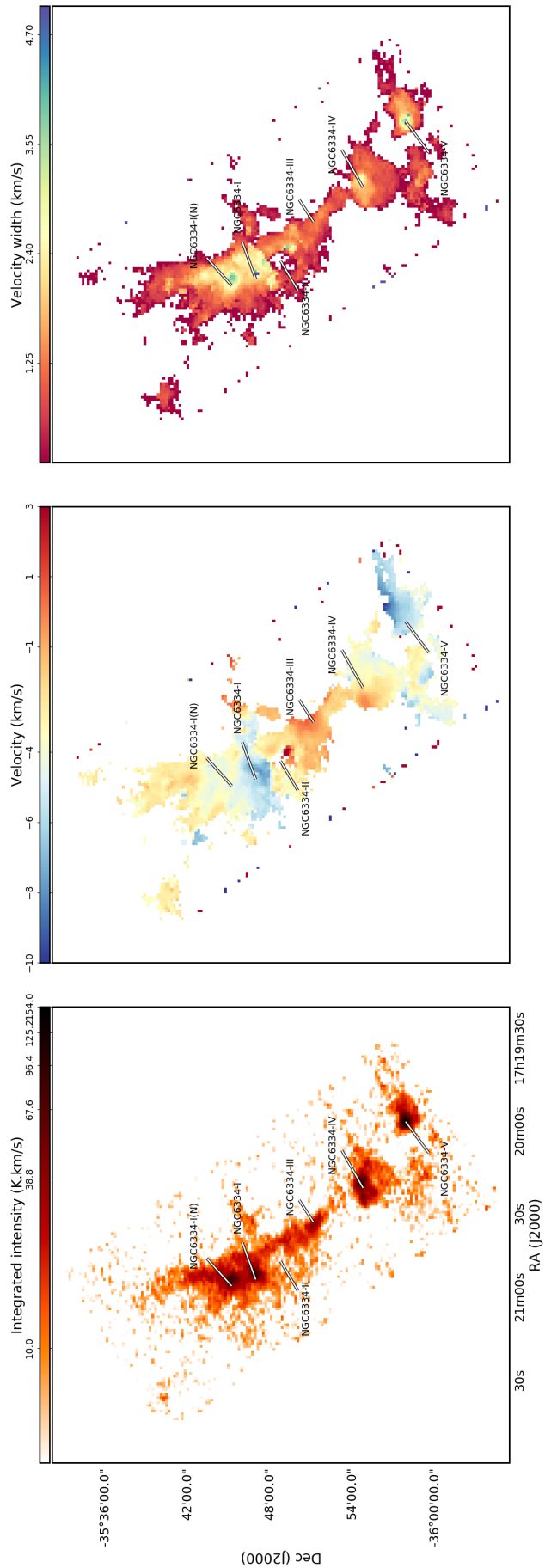

FIGURE 4.3: Spectral moments of HCO^+ (3-2) molecule in NGC 6334. *Left:* Integrated intensity in units of Jy beam^{-1} kms^{-1}. *Middle:* Centroid velocity in km s^{-1}. *Right:* FWHM of central line in km s^{-1}.

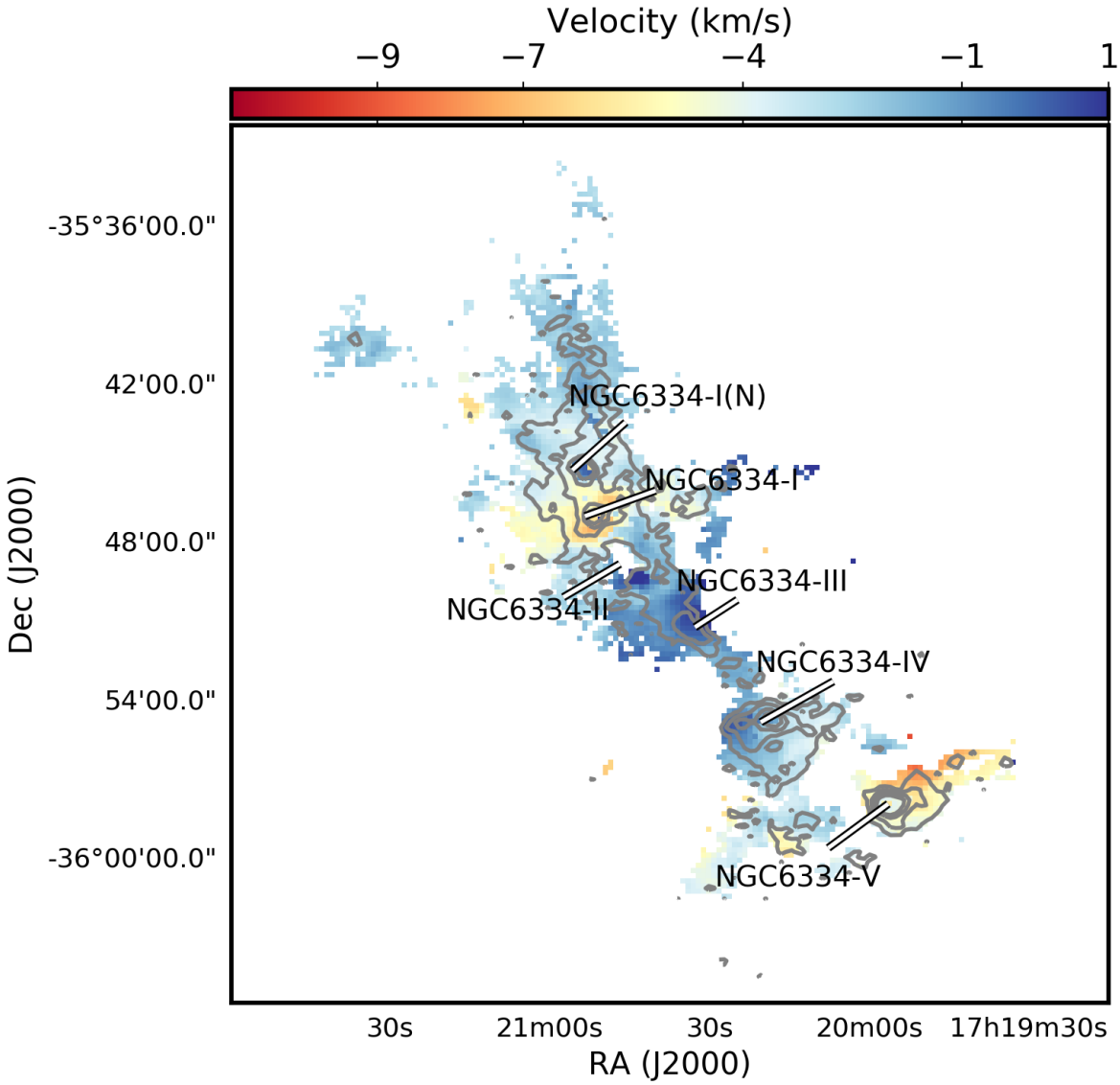

FIGURE 4.4: Peak velocity map of HCO^+ (3-2) molecular emission obtained by spectral decomposition using the BTS algorithm. The zeroth-order moment map of HCO^+ (3-2) is overlaid in gray contours.

of NGC 6334-I and NGC 6334-I(N), reaching a maximum value of 5 km s^{-1}. These large linewidths are likely the consequence of the complex kinematics in the inner regions of the two protolcusters (i.e., infall together with rotation, expansion and oscillation along the line of sight) which are not resolved by the actual resolution of APEX observations.

Although evidences of infall motions towards the massive protoclusters NGC 6334-I and NGC 6334-I(N) are seen in the first-order moment map of HCO^+(4-3), the centroid velocities in this map are not reliable when there are multiple velocity components. Therefore, similar to § 4.1, I applied the BTS algorithm to the HCO^+(4-3) data cube to decompose the different velocity components. 56% of the pixels in the HCO^+(4-3) data cube are fitted with two Gaussian components, while the rest exhibit only a single component. In Fig. 4.6, I show the peak velocity map of the first component which is the

most intense component. As shown in the figure, the observed velocity gradients in the first-order moment map are clearly appreciated here. Moreover, a velocity gradient of 3 km s^{-1} from different directions towards NGC 6334-I(N) is revealed which likely confirms the existence of gas flows along the filaments towards the central hub.

Although single dish observations with APEX resolve velocity gradients when moving outwards from the two massive protoclusters, high-resolution observations are necessary to more accurately investigate the morphology and dynamics of filamentary networks and their role in the accretion process. To reach enough resolution for this study, we took advantage of the ALMA observations. Using ALMA, we imaged the two massive protoclusters NGC 6334-I and NGC 6334-I(N) as well as the filamentary substructures which connect the clusters to the main filament, reaching a resolution of 1300 au. In the following sections, I elaborate on the kinematics of dense gas observed with ALMA. Moreover, I connect the observed velocity trend with the filamentary network visible in the dust continuum emission to obtain the accretion rate along the filaments.

4.3.1 Molecular dense gas observations with ALMA: moment maps

As mentioned previously, we conducted high dynamic range observations of dense gas tracers such as HCN, HCO^+, HNC and their isotopologues with ALMA to study the velocity field and the mass flows towards the two massive protoclusters NGC 6334-I and NGC 6334-I(N). Among the observed tracers, I restrict my analysis to $H^{13}CO^+$, $HC^{15}N$, $H^{13}CN$, and $HN^{13}C$ which are optically thin and therefore, well suited for analysing the kinematics of accretion.

$H^{13}CO^+$

Fig. 4.7 shows the first three moment maps of $H^{13}CO^+$. The zeroth-order moment map shows two lumps of integrated emission in the central regions of the two clusters. Moreover, two prominent spiral features are found pointing towards the north-east and north-west. These two features converge at the position of source NGC 6334-I, likely tracing the gas connecting this cluster to the main filament. NGC 6334-I(N) is surrounded by faint extensions of gas towards the north-east, north-west and south-west directions. However, the emission features towards NGC 6334-I(N) look more bulky and less extended compared to NGC 6334-I. The velocity map (first-order moment) reveals a small velocity gradient, spanning a range of $\sim$3 km s^{-1} in the north-east, south-west and north-west directions of source NGC 6334-I. The velocity gradient likely traces the systematic motions on small scales. In contrast, the velocity field in the region of NGC 6334-I(N) reveals no clear gradient. The velocity dispersion map exhibits two pronounced peaks with values of 28 km s^{-1} and 21 km s^{-1} close to the position of the massive hot core in NGC 6334-I. These high values are likely caused by ejection of material due to the presence of an outflow associated with the hot core (see § 5.1). Apart from these two peaks, the velocity dispersion map looks coherent with velocity widths varying from 0.3 km s^{-1} to 2 km s^{-1}.

$HC^{15}N$

In Fig. 4.8, I present the spectral moment maps of $HC^{15}N$. The distribution of the dense molecular gas traced by $HC^{15}N$ is highly non-uniform and shows significant substructures. The $HC^{15}N$ emission appears to be more compact compared to $H^{13}CO^+$ and consists of two main clumpy structures associated with NGC 6334-I and NGC 6334-I(N). The faint extended structures of dense gas are not visible in the moment zero map suggesting

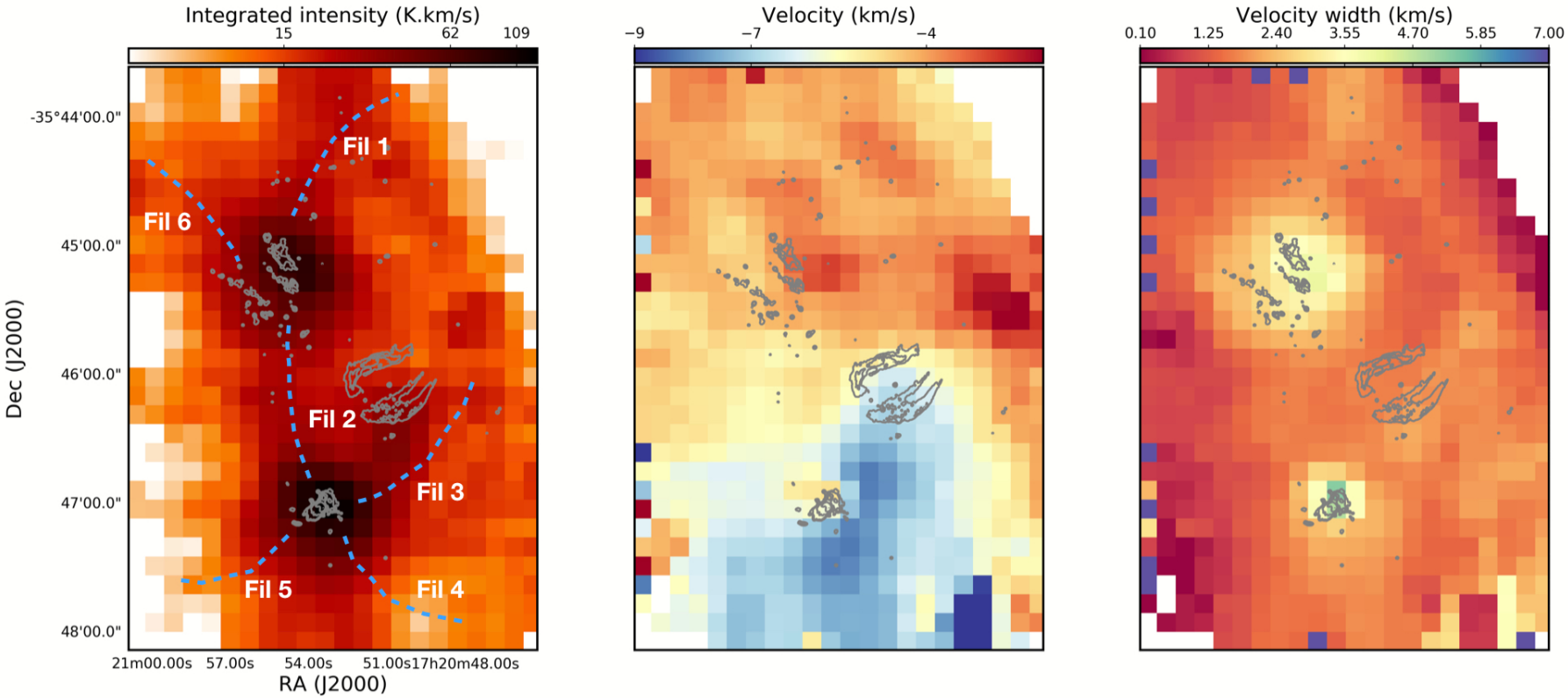

FIGURE 4.5: Spectral moments of HCO^+(4–3) molecule in NGC 6334. *Left:* Integrated intensity in units of Jy beam^{-1} kms^{-1}. *Middle:* Centroid velocity in km s^{-1}. *Right:* FWHM of central line in km s^{-1}. Dashed lines denote the relevant structures found in the integrated intensity map. The ALMA continuum map at 3 mm is overlaid in gray contours.

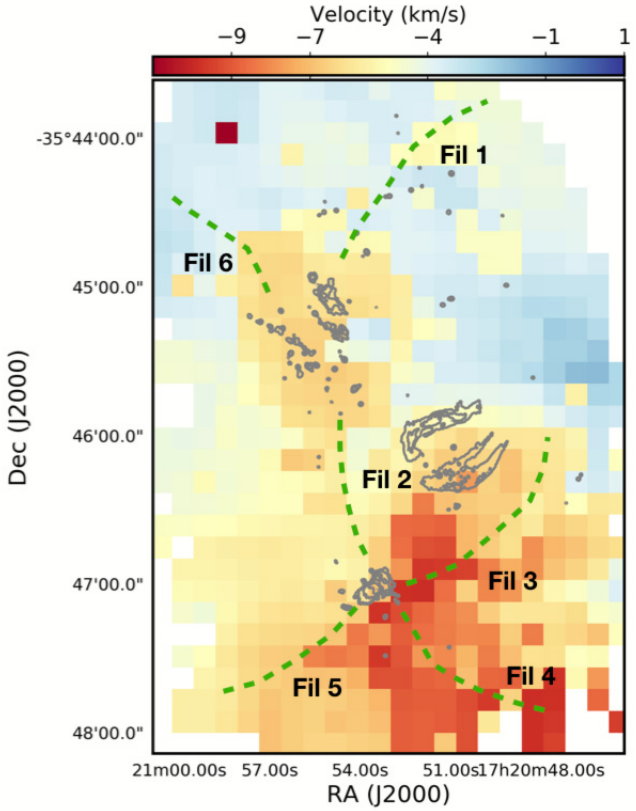

FIGURE 4.6: Velocity map of the first component of HCO^+(4–3) molecular emission obtained by spectral decomposition using the BTS algorithm. Green dashed lines denote the relevant structures found in the integrated intensity map (see Fig. 4.5). The ALMA continuum map at 3 mm is shown in gray contours.

that $HC^{15}N$ is less abundant and it is absent at the vicinity of the dense central regions. The first order moment map shows three extended structures elongated in the south-west, north-east and north-west directions converging at the center of NGC 6334-I. All the structures exhibits a high velocity gradient, spanning a range of $\sim$ 30 km s^{-1}. The velocity dispersion map shows two prominent peaks with a value of $\sim$ 45 km s^{-1}, one at the position of the hot core in NGC 6334-I(N) and the other at the center of NGC 6334-I. Both the high red-shifted velocity and the broad line profile can be the result of the energetic outflows associated with star forming activities. Except for these two peaks, the velocity width changes smoothly between 0.3 and 1.5 km s^{-1} throughout the whole map.

$H^{13}CN$

The first three moment maps obtained for $H^{13}CN$ line are presented in Fig. 4.9. The integrated intensity map of $H^{13}CN$ resembles the $H^{13}CO^+$ emission, with three faint extended structures converging to the position of NGC 6334-I. The emission structure in NGC 6334-I(N) looks more clumpy with a short extension towards the south-east. The map of velocity field reveals a velocity gradient of $\sim$10 km s^{-1} along the extensions from the center of NGC 6334-I towards south and north-west. Towards the northern direction of NGC 6334-I, the velocity map demonstrates a smaller gradient of $\sim$5 km s^{-1}. Similar to the $H^{13}CO^+$ and $HC^{15}N$ lines, the velocity dispersion map has the highest value of

σ =32 km s^{-1} at the center of NGC 6334-I. Additionally, the dispersion map shows several enhancements coinciding the position of ALMA compact sources in NGC 6334-I(N).

HN^{13}C

The first three moment maps of HN^{13}C are shown in Fig. 4.10. The integrated intensity map exhibits a long filamentary-like structure towards the south-west of source NGC 6334-I. Moreover, the two small extensions towards the south-east and north-east are appreciated in the map. The HN^{13}C emission in NGC 6334-I(N) looks clumpy. However, small extensions towards the north-east, south-west and northern directions are visible in the map. Compared to the other three dense gas tracers presented in this section, the HN^{13}C emission appears to be fainter and more diffuse. The velocity field has its highest value of 40 km s^{-1} at the center of source NGC 6334-I. Along the extensions converging at the position of NGC 6334-I, a velocity gradient of σ =3 km s^{-1} is found. In contrast, the velocity map towards NGC 6334-I(N) shows no clear gradient and velocity variations between -6 km s^{-1} and -3 km s^{-1} randomly throughout the cluster. Similar to the other three tracers, the velocity dispersion map has its highest value at the positions of the hot cores in NGC 6334-I and NGC 6334-I(N). Apart from these two prominent peaks, the velocity dispersion fluctuates smoothly between 0.3 km s^{-1} and 1.5 km s^{-1}. As previously mentioned, high red-shift in the velocity and the extreme broadening of the line width towards the positions of the hot cores in these two protoclusters can be due to the presence of energetic outflows which are ejecting the material with a high velocity.

In summary, the intensity maps of the selected dense gas tracers reveal three extended structures of gas converging at the position of NGC 6334-I, with one of them connecting NGC 6334-I to NGC 6334-I(N). Although the distribution of dense gas towards NGC 6334-I(N) is more clumpy and less extended, three faint and small-scale extensions are appreciated in the maps. The velocity maps reveal a velocity gradient of $\sim$3 km s^{-1} along the observed elongated structures. The observed velocity gradient together with the morphology of the emission likely trace the accretion channels which transport material from the large scale filament to the denser regions of the protoclusters. However, in order to better constraint the small-scale motions and the kinematics of accretion, it is necessary to investigate the velocity field of different components individually and look for possible correlations with the velocity fields at large scales.

4.3.2 Filament identification

In order to investigate how the observed protoclusters with ALMA are connected to the large-scale filamentary cloud, I took advantage of the large-scale continuum map of the NGC 6334 filamentary cloud observed with the ArTéMiS camera on the APEX telescope (André et al., 2016). The ArTéMiS map covers the central part of the NGC 6334 filamentary cloud over a scale of $\sim$10 pc with a resolution of 8$''$ corresponding to 0.07 pc at a distance of 1.7 kpc. In Fig. 4.11, I show the ArTéMiS continuum map at 350 μm with the ALMA continuum emission overlaid in contours. As shown in the figure, the ArTéMiS continuum map exhibits significant intensity enhancements at the positions of NGC 6334-I and NGC 6334-I(N). Moreover, it reveals a network of filamentary substructures at scales of a few 0.1 pc that are converging towards the most massive objects forming in the filamentary cloud, i.e. NGC 6334-I and NGC 6334-I(N). The filamentary substructures shown in green dotted lines connect these two clusters to the main filament located towards the western direction. The identification of the filaments has been done

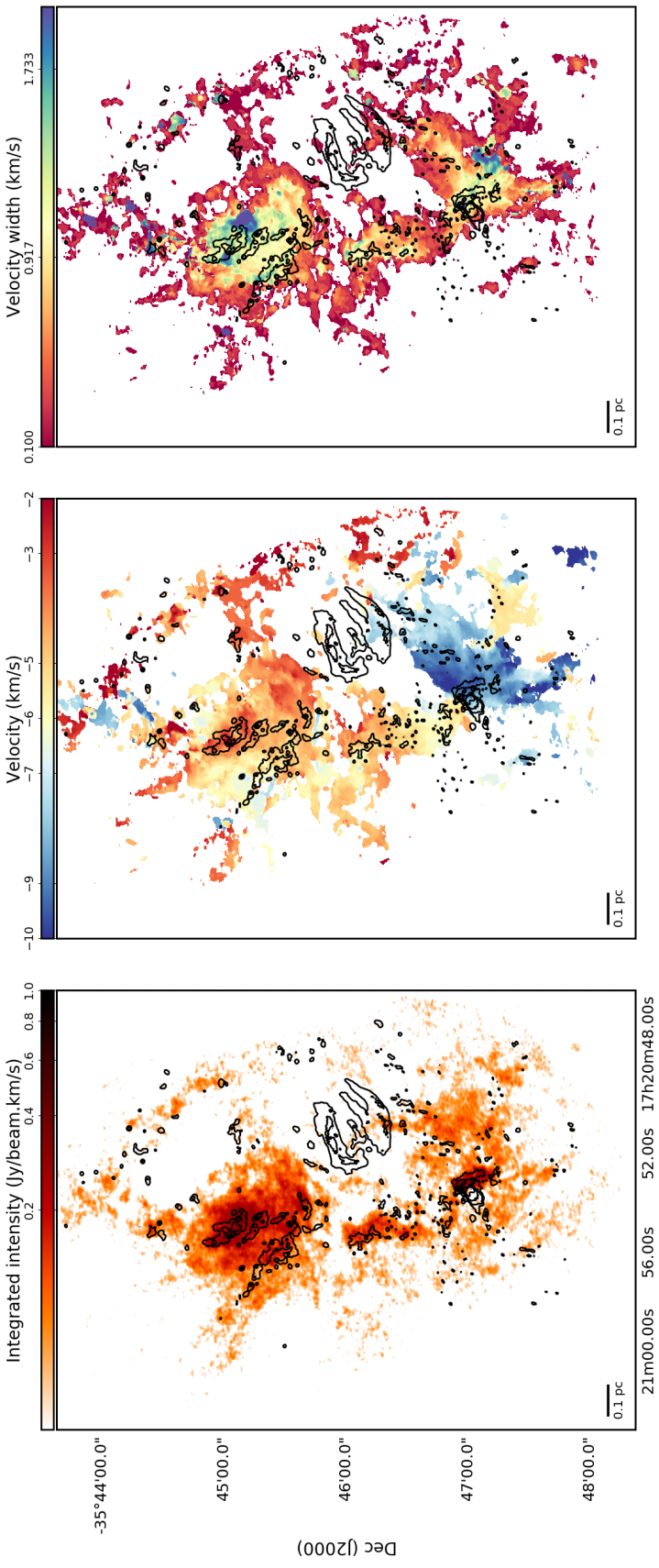

FIGURE 4.7: Spectral moments of $H^{13}CO^+$ molecule in NGC 6334. *Left:* Integrated intensity in units of Jy beam^{-1} kms^{-1}. *Middle:* Centroid velocity in km s^{-1}. *Right:* FWHM of central line in km s^{-1}. ALMA continuum map at 88 GHz is shown in black contours.

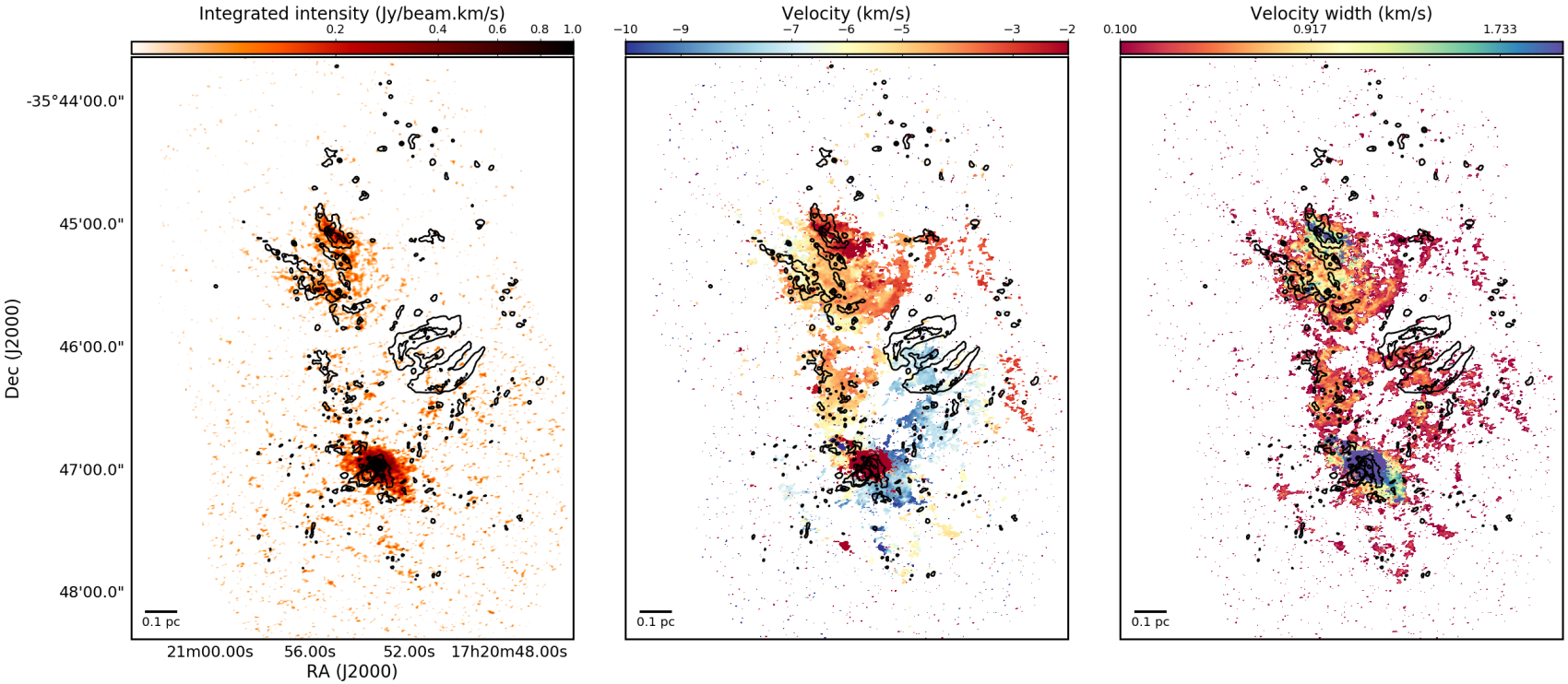

FIGURE 4.8: Spectral moments of $HC^{15}N$ molecule in NGC 6334. *Left:* Integrated intensity in units of Jy beam^{-1} kms^{-1}. *Middle:* Centroid velocity in km s^{-1}. *Right:* FWHM of central line in km s^{-1}. ALMA continuum map at 88 GHz is shown in black contours.

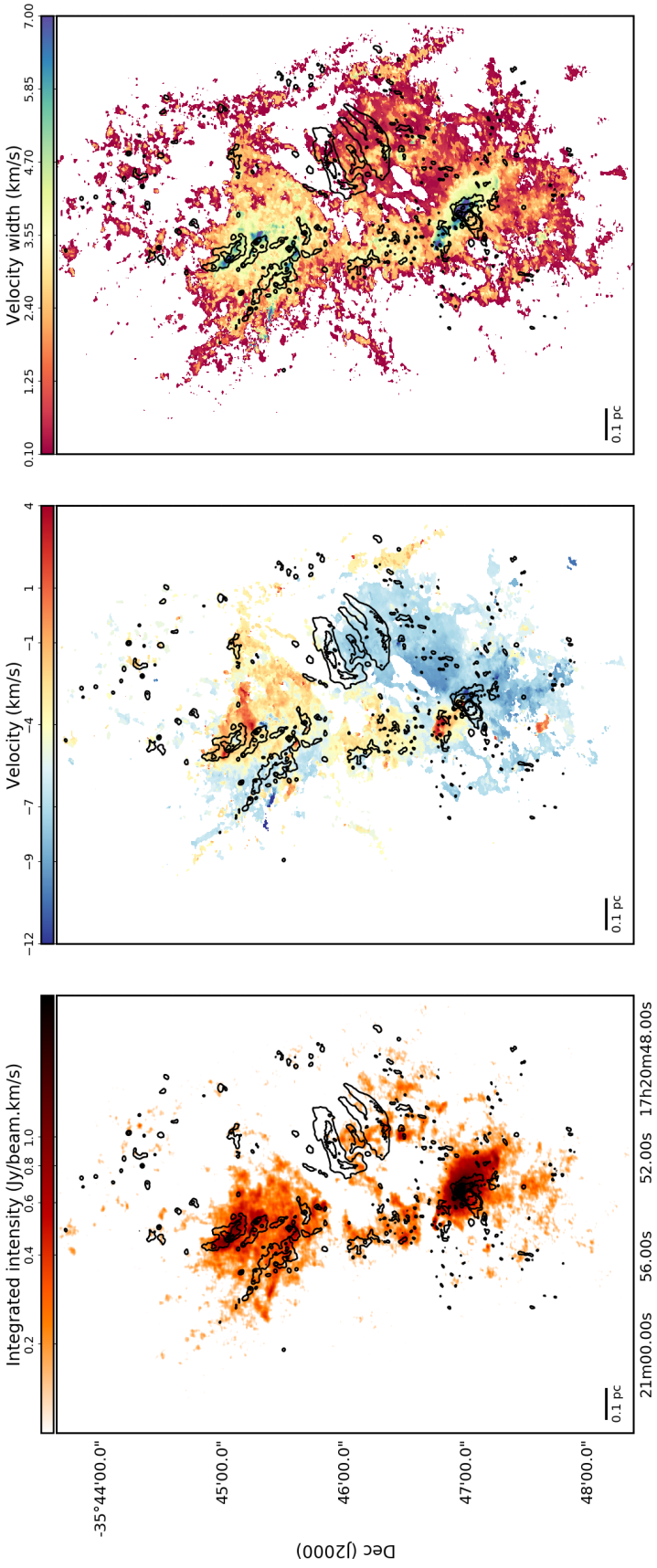

FIGURE 4.9: Spectral moments of $H^{13}CN$ molecule in NGC 6334. *Left:* Integrated intensity in units of Jy beam^{-1} kms^{-1}. *Middle:* Centroid velocity in km s^{-1}. *Right:* FWHM of central line in km s^{-1}. ALMA continuum map at 88 GHz is shown in black contours.

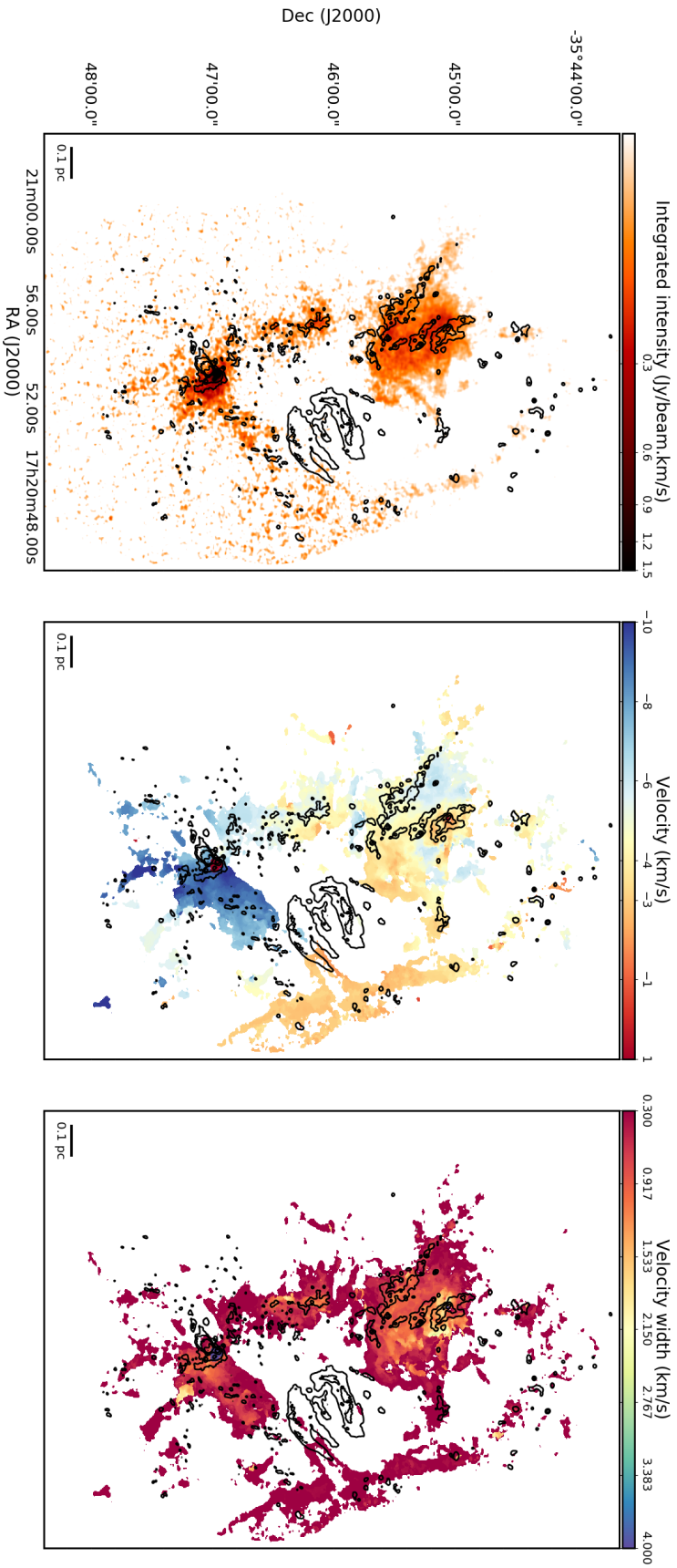

FIGURE 4.10: Spectral moments of $HN^{13}C$ molecule in NGC 6334. *Left:* Integrated intensity in units of Jy beam^{-1} kms^{-1}. *Middle:* Centroid velocity in km s^{-1}. *Right:* FWHM of central line in km s^{-1}. ALMA continuum map at 88 GHz is shown in black contours.

tracing their dust continuum emission, starting at a position close to the protoclusters and following the intensity ridge outwards by visual inspection. Using the ArTéMiS map, I identified eight arms or filamentary structures in total with three converging towards NGC 6334-I(N), one connecting source NGC 6334-I to NGC 6334-I(N), three converging toward NGC 6334-I and finally one connecting the cores in NGC 6334-I(NW) to the main filament. The identified filaments coincide with the elongated structures appearing in the moment maps of the ALMA dense gas tracers (see § 4.3.1). The consistency between the structures observed in the dust continuum emission and molecular line emission, together with the correlation of the trends observed in the APEX and ALMA maps provide an observational evidence for the existence of accretion channels and their crucial role in feeding the clusters.

4.4 Filament kinematics and mass accretion rates

Comparing the identified filaments in the ArTéMiS map with the moment maps obtained for the ALMA dense gas tracers shows that all the intermediate-scale filaments found in the ArTéMiS continuum map are clearly detected in the ALMA moments map. The observed velocity gradients of a few km s^{-1} along the filamentary structures confirm the existence of accretion channels which transport material from the main filament to the clusters. The analysis of the velocity structure of each filament has been done using the $H^{13}CO^+$ and $H^{13}CN$ data cubes, excluding the arm F8 which is not directly connected to NGC 6334-I(N). The peak velocity map of the transitions of these two molecules (see Fig. 4.12) reveals a velocity gradient between the one end of the arms to the other connected to clusters. The Gaussian fits of each spectrum obtained using the `BTS` algorithm provide the possibility to derive the velocity and linewidth of each component and more accurately explore the possible variations with distance along the filament. A more detailed study of the velocity structure is obtained by constructing the position-velocity (hereafter PV) diagrams along the filaments. The PV diagrams are obtained with the python routine `pvextractor`[1] which generates PV diagrams along any user-defined path in a position-position-velocity data cube. In the PV diagrams I average over 25 pixels (corresponding to one beam, or 1300 au) in the direction perpendicular to the filament to increase the signal to noise. Fig. 4.13 shows the PV diagrams along the identified filaments for the $H^{13}CO^+$ line. Most of the filaments are described by two velocity components, with the exception of filament F5, for which I consider a single velocity component. For all the filaments, I see a velocity gradient in all four species. In Table 4.1, I list the velocity gradients of the nine filaments obtained based on the pv-cuts of the $H^{13}CO^+$ data cube. The velocity structure of each filament is consistent between different molecular species, suggesting similar kinematic properties. I determine an average velocity gradient of roughly 15 km s^{-1} pc^{-1}. Arm F4 reaches the highest value of 32 km s^{-1} pc^{-1}, which together with its short length, suggest that F4 is a filament oriented close to the line of sight. The gradients in all filaments is positive, meaning that they go from blue to red-shifted velocities when moving outward from the two clusters. It is necessary to note that the observed velocity gradients might be biased due to the projection effect, as the filaments are 3D structures with some curvature.

Using the derived velocity gradients and mass of each filament, I evaluated the accretion rate of the filaments. In order to measure the masses of the filaments, I took advantage of the ArTéMiS dust continuum emission at 350 μm (André et al., 2016). Along each filament, I defined a polygon that delineates the 50% contour level with respect to the 3σ

[1] Available at `https://pvextractor.readthedocs.io/en/latest/`

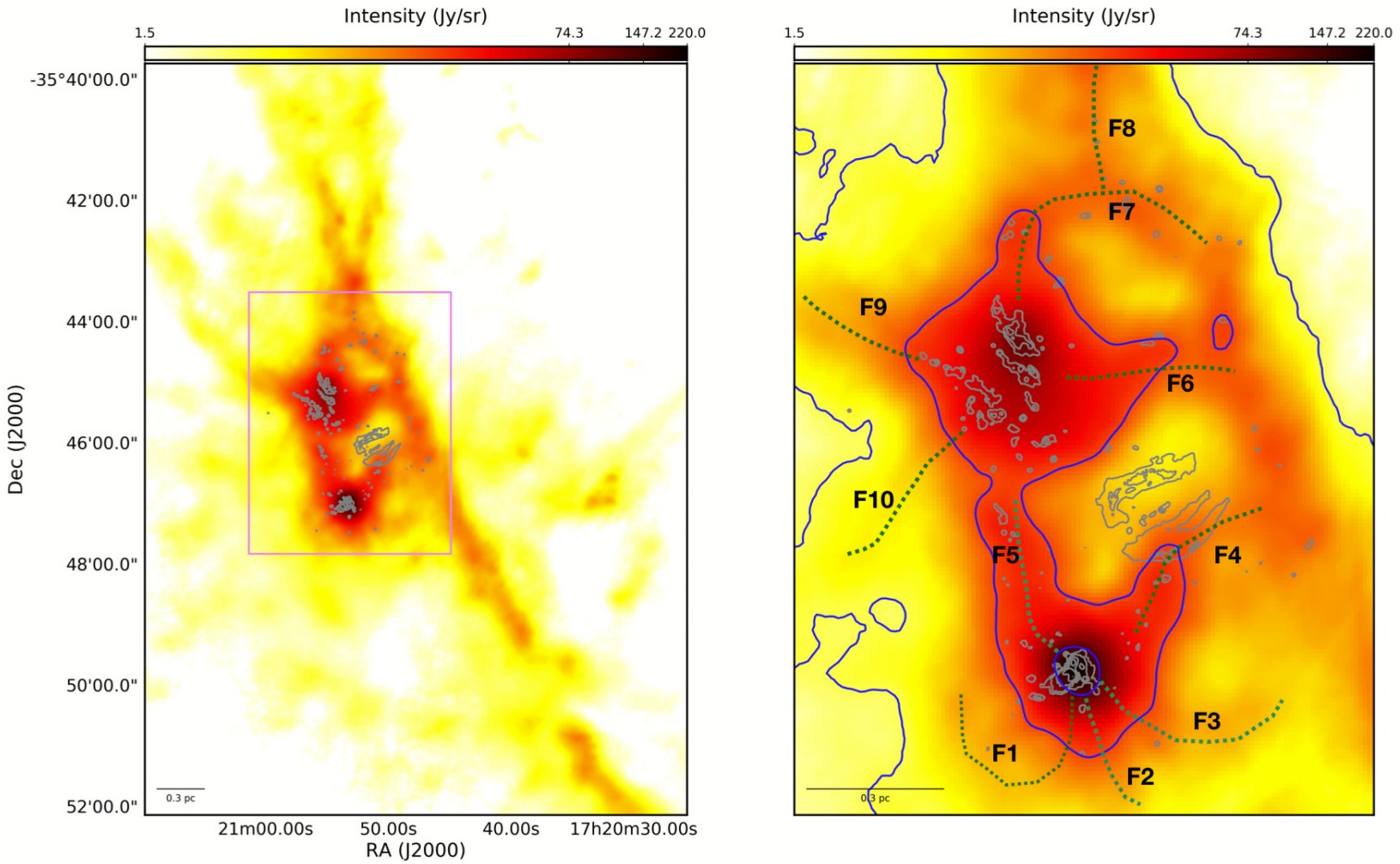

FIGURE 4.11: *Left:* ArTéMiS 350 μm dust continuum map of the central part of the NGC 6334 filamentary cloud. *Right:* Close-up view of NGC 6334-I and NGC 6334-I(N) marked with a rectangle in the left panel. The green dotted lines trace the path of the filaments identified in the ArTéMiS continuum map. The ALMA continuum map at 3 mm is shown with grey contours. Overlaid in blue contour is the ArTéMiS dust continuum map.

contour level. These polygons are used to determine the flux of each filament. I assumed optically thin emission, a gas to dust mass ratio of 100, and a dust opacity coefficient of 0.899 cm^2 at 230 GHz (Ossenkopf and Henning, 1994). Adopting a dust temperature of 20 K, I derived masses of the filaments in the range 10–40 $M_\odot$(see Table 4.1). According to Kirk et al. (2013b), the filamentary accretion rate implied by a velocity gradient can be estimated using a simple cylindrical model. In this model, a filamentary structure resembles a cylinder which has a mass of M, length of L, radius r, an inclination to the plane of the sky of angle α, and motions of velocities $V_\parallel$. The accretion rate, $\dot{M}$, along the filament onto the central cluster is derived as

$$\dot{M} = V_\parallel \times \frac{M}{L}. \tag{4.1}$$

Considering an inclination α between the filament and plane of the sky, the observed parameters are given by

$$L_{\rm obs} = L\cos(\alpha) \quad \text{and} \quad V_{\parallel,\rm obs} = V_\parallel \sin(\alpha). \tag{4.2}$$

Therefore, the mass accretion rate is modified to

$$\dot{M} = \frac{\nabla V_{\parallel,\rm obs}.M}{\tan(\alpha)}. \tag{4.3}$$

For the calculation of mass accretion rate, I assumed a projection angle α of 45°. The mass accretion rates along the filaments of NGC 6334 are between 1.2–30.7$\times10^{-4}$ $M_\odot$ yr^{-1} at the scales of 0.4–0.8 pc (see Table 4.1), thus in the order of the rates usually found in star-forming filaments at larger scales of ∼1 pc (e.g. Lu et al., 2018; Peretto et al., 2013; Treviño-Morales et al., 2019). This results in a total of 0.1–3 $M_\odot$ accreted on to the central cluster in about 1 kyr.

TABLE 4.1: Kinematic and physical properties of the filaments in NGC 6334.

		Filament parameters			
ID	Velocity gradient (km s^{-1} pc^{-1})	Mass ($M_\odot$)	L (pc)	M/L ($M_\odot$ pc^{-1})	$\dot{M}$ ($10^{-4}M_\odot$yr^{-1})
F1	+11.1	10.4	0.5	5.2	1.2
F2	+15.8	13.6	0.8	17.0	2.2
F3	+9.5	16.4	0.4	41	1.6
F4	+31.7	38.1	0.4	95.2	30.7
F5	+6.3	39.6	0.4	94	2.5
F6	+11.1	36.0	0.3	120	4.1
F7	+11.1	33.9	0.6	57	3.8
F9	+15.8	17.0	0.4	42.5	2.7
F10	+21.2	9.6	0.5	19.2	2.1

4.5 Temperature and column density maps

In order to probe the temperature and column density of the dense gas in NGC 6334 we observed the CH_3CCH (J=6-5) molecular transition towards the two massive protoclusters NGC 6334-I and NGC 6334-I(N) as well as the gas connecting them to the large-scale filament.

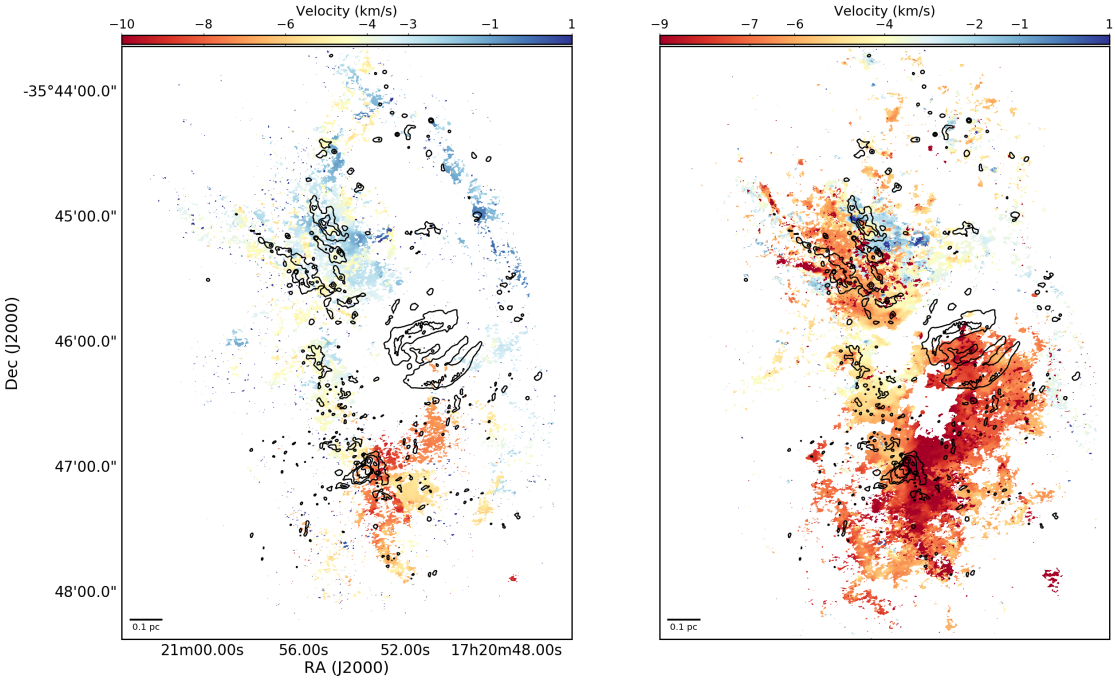

FIGURE 4.12: Peak velocity map of $H^{13}CO^+$ (*left panel*) and $H^{13}CN$ (*right panel*). The emission below 5σ is masked out. The ALMA continuum map is shown in black contours.

CH_3CCH, also known as methylacetylene, is a symmetric top molecule with a carbon chain at its backbone whose rotational energy levels are given by $E = hBJ(J+1) + h(A-B)K^2$. Radiative transitions between the K-ladders are forbidden, so that the relative populations of the K-ladders depend primarily on the kinetic temperature of the colliding particles. Therefore, each K component of a given rotational transition represents a different excitation energy, i.e. temperature, which increases with K. The low K components occur in fairly narrow frequency ranges so that they can be observed simultaneously. Since CH_3CCH has a lower dipole moment (0.78 D) is more easily thermalized and therefore, well suited as a temperature probe.

In order to measure the kinetic temperature and column density of the gas throughout the observed region in NGC 6334, I fitted the K components of the CH_3CCH molecular transition simultaneously using `XCLASS` (see § C.2). The CH_3CCH emission towards the observed region exhibits a complex morphology and the spectra change drastically between pixels. Therefore, using a fixed set of initial values for all the pixels of the CH_3CCH data cube does not lead to a reliable fit. As a solution to this problem, I extracted the spectra of all the pixels in the first step. In the second step, I estimated the velocity offset and the velocity width of the brightest component using the signal processing package of `scipy` (`scipy.signal`). Using the estimated values for the centroid velocity and velocity width, I generated an individual `molfit` file for each corresponding pixel. The initial values of temperature and column density are fixed for all the pixels. In order to validate the initial values used for temperature and column density, I generated synthetic spectra using these two values and compared the results with the observed spectra. The values which resulted in a better-matched synthetic spectrum are chosen as initial values. Fig. 4.14 shows the rotational temperature (T_{rot}) and column density (N_{CH_3CCH}) maps of CH_3CCH towards the whole observed area with ALMA. Both maps are masked with CH_3CCH peak intensity map to remove the pixels with no emission. As shown in the

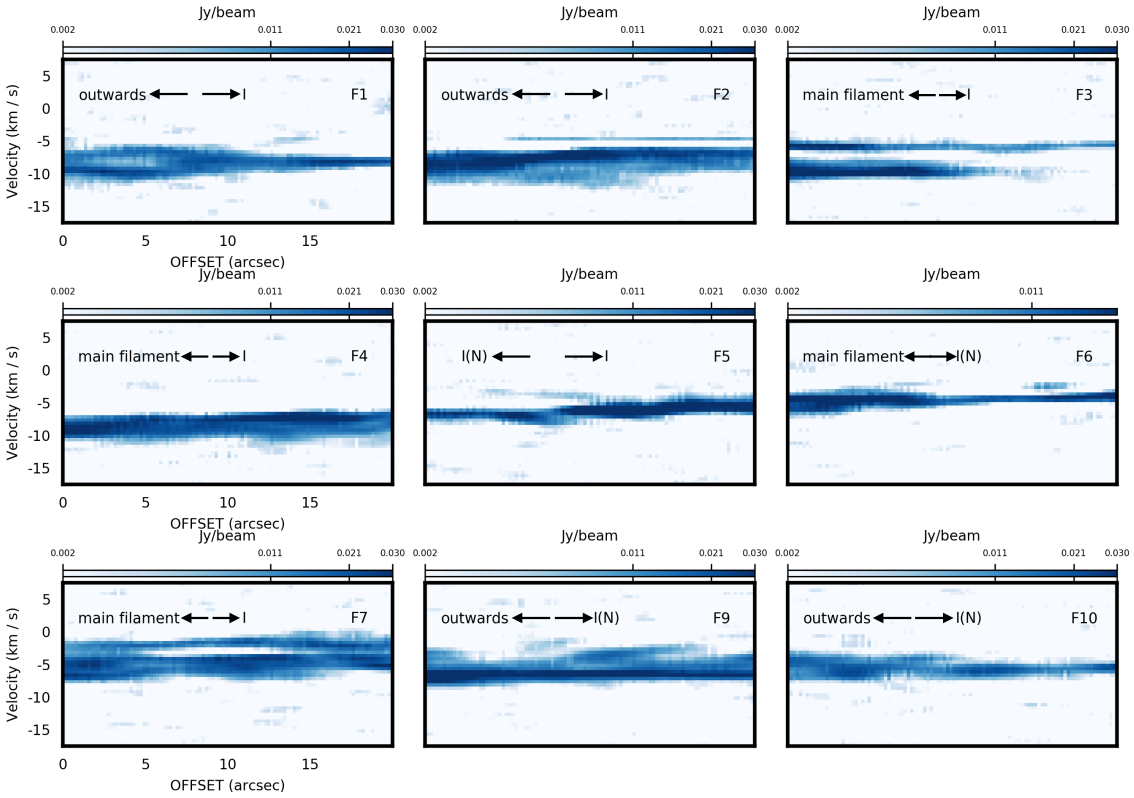

FIGURE 4.13: Position velocity cut along each identified filament in $H^{13}CO^+$ (see Fig. 4.11). The measured velocity gradient changes in range 6–32 km s^{-1} pc^{-1} (see Table 4.1). The arrows show the paths of the filaments.

figure, the rotational temperature varies between 14 and 20 K in the central regions of the map where the protoclusters are located. Despite the consistent low temperatures in the central regions, the highest temperatures (∼70 K) are found towards the positions of the hot cores in NGC 6334-I and NGC 6334-I(N) as well as the shell-like HII region NGC 6334-E. As it gets closer to the outskirt of the clusters, the rotational temperature increases by 30 to 40 K, resulting in a temperature gradient from the edge to the center. Therefore, the striking feature of the gas temperature map reveals the non-isothermal nature of dense clumps. This trend is in agreement with the non-isothermality observed in IRDCs (Peretto and Fuller, 2010). The picture we can draw from the observed temperature gradient suggests that massive clumps in the filaments form from warm molecular gas with a temperature of ∼30 K, which cool down efficiently to 10–20 K. In the central regions of the observed area, the column density has a value around $\sim 10^{15}$ cm^{-2} , while in the outer regions it drops to a few 10^{14} cm^{-2}. Comparison of the temperature and column density maps shows that the local temperature minima are correlated with density peaks. This correlation confirms the role of temperature fluctuation in fragmentation of protoclusters in their early stage of evolution (Bate, 2009; Krumholz et al., 2010).

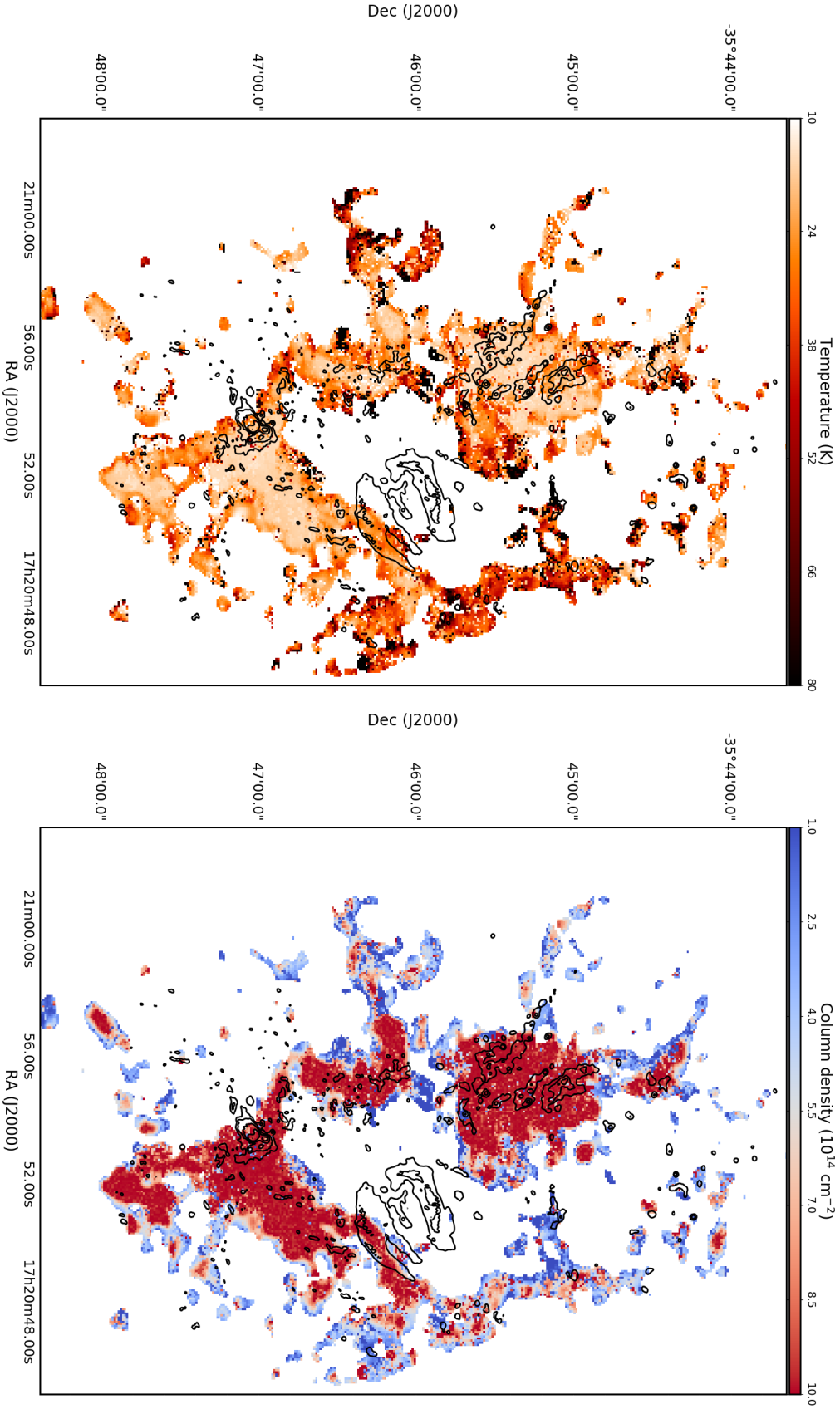

FIGURE 4.14: *Left:* Rotational temperature map of CH_3CCH (units in K). *Right:* Column density map of CH_3CCH units in cm^{-2}). Overlaid in contours is the ALMA continuum map at 3 mm.

4.6 Discussion

The analysis of transitions of different molecular species together with the dust continuum emission revealed a network of filaments in NGC 6334 converging towards the two massive protoclusters NGC 6334-I and NGC 6334-I(N). This finding indicates that filaments serve as highly efficient routes for feeding material into hubs where there is ongoing clustered star formation. Considering the five filaments that feed each protocluster, I determine a total mass accretion rate of 4×10^{-3} $M_\odot$ yr^{-1} and 1.5×10^{-3} $M_\odot$ yr^{-1} for NGC 6334-I and NGC 6334-I(N) respectively. It is necessary to note that the measured values should be taken as a lower limit if projection effects are taken into account. Compared to other star-forming regions, the mass accretion rates measured along the filaments of NGC 6334 are larger by one order of magnitude than those seen in Mon R2 (10^{-4} $M_\odot$ yr^{-1}, Treviño-Morales et al., 2019) and Serpens (1–3×10^{-4} $M_\odot$ yr^{-1}, Kirk et al., 2013b) and by two orders of magnitude that those measured in SDC 13 (2–5×10^{-5} $M_\odot$ yr^{-1}, Peretto et al., 2014), Perseus (1–4×10^{-5} $M_\odot$ yr^{-1}, Hacar, Tafalla, and Alves, 2017) and Orion (6×10^{-5} $M_\odot$ yr^{-1}, Hacar et al., 2017). Sgr B2(N) as a clump which may evolve to a super cluster, reveals a total accretion rate of 0.16 $M_\odot$ yr^{-1} (Schwörer et al., 2019) which is larger by two orders of magnitude than the rates found in NGC 6334.

The total accretion rate obtained for NGC 6334-I(N) is similar to the one measured for NGC 6334-I. Since NGC 6334-I is a more evolved cluster with a hypercompact HII region, a higher accretion rate is expected for NGC 6334-I(N). The similar accretion rates could be due to the fact that NGC 6334-I is more massive including a relatively large amount of ionised gas. The similar mass accretion rate of both clusters and their proximity (0.5 pc) suggest that they are competing for the mass contained in the filament. Therefore, it is possible to speculate that competitive accretion is not only an alternative scenario for mass accretion inside a cluster, but also it is an accretion mechanism which may take place over larger scales between the clusters embedded in a filament. In a scaled-up version of the competitive accretion scenario, protoclusters can be considered as the centers of the potential and the main filament is the large reservoir of material. The filamentary substructures converging towards the clusters have roles as the accretion channels which funnel gas down to the center of the potential. Since the competitive accretion model is based on the inefficiency of the fragmentation process, it is possible to speculate that the inefficient fragmentation in the NGC 6334 filamentary cloud resulted in a large reservoir of gas from which the protoclusters embedded in this cloud including NGC 6334-I and NGC 6334-I(N) can accrete mass. Assuming a dust mass of $\sim$300 $M_\odot$ for NGC 6334-I and $\sim$700 $M_\odot$ for NGC 6334-I(N), the actual accretion rates obtained for these two clusters suggest a timescale of about 70 kyr and 0.4 Myr for the formation of NGC 6334-I and NGC 6334-I(N), respectively. This timescale is one order of magnitude smaller than the free-fall timescale ($\sim10^5$ yr) for the case of NGC 6334-I, suggesting a dynamically young system.

Chapter 5

Properties of shocked gas in NGC 6334

Shock waves are common phenomena in star-forming regions. Shocks occur due to supersonic compressive motions of material in the surrounding medium. Since shock waves propagate faster than the characteristic sound speed, the medium ahead of the shock can not dynamically respond to the upcoming material until it strikes. The shock will then compress, heat, and accelerate the medium. The heated material cools through the emission of photons, further compressing the medium (Tielens, 2005). There are two types of interstellar shocks: non-magnetic shocks (termed as J shocks by (Draine, 1980)), and shocks in magnetized, weakly ionised plasmas (termed as C shocks by (Draine, 1980)). In cold gas where the sound speed is considered negligible and with no magnetic field, a pressure disturbance create a shock wave, a thermodynamically irreversible transition in which the energy of the bulk flow is transformed into the random thermal motions of particles. The gas properties such as temperature, density and flow velocity suffer an incontinuous jump from their preshock to their postshock values in a shock front smaller than one mean free path. Such a shock occurs in ionised or neutral atomic gas, or at high velocities (v_s >50 km/s). The three Rankine-Hugoniot jump conditions can be used to describe the relationship between the states on both sides of a shock wave based on conservation of mass, momentum and energy. In contrast to J shocks, the C shocks arise in a magnetised medium consisting of neutral species mixed with a small population of ions. The neutral species interact with the magnetised fluid through ion-neutral collisions, which produce dynamical friction and heating of the neutral fluid. In such a shock, the shock front is much thicker than the cooling length scale and the temperature is set by the balance between heating and cooling. In the case of C shocks, we have to solve the conservation equations instead of using the jump conditions. C shocks occur in gas that has a low degree of ionisation ($x \leq 10^{-6}$), a high density and molecular fraction (10^2–10^4 cm^{-3}), at least a moderate B field, and low shock velocities. In a magnetised medium which consists of neutral and ion species, each of these fluids can sustain short wavelength waves. For the neutrals, these waves propagate with the sound speed, while the ionised fluid propagate at the Alfvén speed of the ions. Therefore, the resulting compressional wave travels slower than the Alfvén speed, but faster than the sound speed. As this wave propagates, accelerates the ions in the upstream gas in a smooth and continuous fashion. The drifting ions heat up the neutral species through collisions over a relatively long time scale. As a result, the density and temperature will vary continuously. Now, when the ion fraction increases, the C-shock thickness decreases and the heating rate increases, and so eventually the shock will develop into the J-type.

To probe the shocked gas in star-forming regions, SiO molecular emission has been extensively used as an ideal tracer (see e.g. Gibb, Wyrowski, and Mundy, 2004; Martin-Pintado, Bachiller, and Fuente, 1992; Schilke et al., 1997). In contrast to CO molecular

emission which appears to be contaminated by the surrounding infalling gas, SiO is a reliable shock tracer observed principally in outflows associated with regions of star formation. In the preshock phase, the silicon-bearing material is locked up in the dust grains in the form of silicates (e.g. May et al., 2000). As shock waves propagate through the surrounding medium, the grains are charged and undergo collisions with the neutral species from the gas phase (e.g. Flower and Pineau des Forêts, 2003). Consequently, the silicon present in the grain mantles will be released in the gas phase. Once silicon is in the gas phase through the sputtering, it can react with molecular oxygen or a hydroxyl radical to form SiO (e.g. Schilke et al., 1997). In the postshock region, SiO is depleted from the gas phase due to conversion in SiO_2 or adsorption on to the grain surface (e.g. Gusdorf et al., 2008a).

In young embedded clusters, most of the shock waves are thought to be driven by molecular outflows associated with star-forming activities. Outflows develop as a result of momentum conservation during the collapse of a rotating core and are signposts of the early stage of star formation. Molecular outflows have a collimated structure and show broad line profiles with linewidths of few tens of km s^{-1}. Another form of feedback which generates shock waves in star-forming regions is the stellar winds that are distinguished from the bipolar outflows by being less collimated and indicating the non-symmetric spherical shapes. In more evolved stellar clusters, the strongest shocks in the ISM are produced by supernovae. In the adiabatic phase of their evolution, supernova remnants drive shocks into the ISM with velocities of up to about 100 km/s (see e.g. Dopita, Mathewson, and Ford, 1977; McKee and Ostriker, 1977). In addition to the shocks associated with stellar feedback and star formation, recent observations towards the G035.39-00.33 infrared dark cloud (Jiménez-Serra et al., 2010), W43-MM1 ridge (Louvet et al., 2016) and NGC 6334-V protocluster (Aghababaei et al. in prep) reveal the detection of widespread SiO emission with narrow line profiles (Δv ~0.8–7 km/s). These slow shocks are the results of cloud-cloud collision events or collisions of gas inflows (Jiménez-Serra et al., 2010; Nguyen Luong et al., 2011; Nguyen-Lu'o'ng et al., 2013; Sanhueza et al., 2013). Dynamical scenarios of star formation suggest that cloud formation generates colliding flows that transport mass from large-scale structures (e.g. molecular clouds and filaments) to small scales (Hartmann, Ballesteros-Paredes, and Heitsch, 2012; Smith et al., 2013; Vázquez-Semadeni et al., 2005). At the interface of colliding flows, density enhancement and formation of slow shocks are expected.

In this chapter, I present the results of the analysis of shocked gas towards the high-mass protoclusters NGC 6334-I and NGC 6334-I(N). In § 5.1, I describe the peak intensity and moment maps of SiO molecular emission. § 5.2 presents the results of line fitting which leads to filtering the noise in the SiO data cube. In § 5.3, I explain the methods applied to the SiO peak intensity map to identify the emission structures. In § 5.4, I present the maps of dynamical properties of the observed SiO emission. § 5.5 focuses on the decomposition of low- and high-velocity shocks. Finally, the results are discussed in § 5.6.

5.1 Maps of SiO (2-1) molecular emission

In the left panel of Fig. 5.1, I show the peak intensity map of SiO (2-1) towards the whole observed area with ALMA. The emission is dominated by bright features distributed over the whole surveyed region. In the region of NGC 6334-I, the emission is dominated by a bipolar object likely tracing an outflow associated with one of the compact sources in this cluster. This prominent feature is surrounded by several faint elongated emission

structures pointing at different directions. The SiO emission towards NGC 6334-I(N) reveals a complex network of collimated structures extending up to a distance of ∼0.2 pc which are pointing in different directions. Finally, a number of faint, more compact emission features appear to the west and north-west of NGC 6334-I(N). The close-up views of these two regions are shown in the middle panel of Fig. 5.1. The SiO emission in both regions exhibit a wide variety of line profiles, from very broad to narrower lines peaking at the ambient cluster velocity $v_{LSR} \sim -5$ km/s (see the right panel of Fig. 5.1).

In Fig. 5.2 and Fig. 5.3, I present the spectral moment maps of SiO (i.e., the integrated SiO (2-1) intensity map, centroid velocity map, and line FWHM map) for NGC 6334-I and NGC 6334-I(N) respectively. The positions of the ALMA continuum sources are marked with white circles on the integrated intensity map of these two regions. Both NGC 6334-I and NGC 6334-I(N) show a wide range of features. In NGC 6334-I, the peak in integrated intensity map corresponds to the red-shifted lobe of the possible outflow candidate. In contrast, the distribution of intensity in NGC 6334-I(N) is more homogeneous and exhibits no significant enhancement. The highest velocity of the centroid velocity map in NGC 6334-I at v∼+32 km/s coincides with the peak position in the integrated intensity map. The lowest velocity is found towards the blue-shifted lobe of the bipolar polar object at v∼-13 km/s. The observed velocity gradient along the two lobes (∼35 km s^{-1}), together with its morphology, its association with source 44 of the ALMA continuum image (see Table A.1), and the spectra exhibited by this object suggests the presence of an outflow in this region. The second velocity peak in NGC 6334-I is at the position of the elongated structure towards the south of the prominent bipolar outflow at a velocity of v∼10 km s^{-1}. Similarly, this SiO feature also exhibits a velocity gradient along its main axis likely suggesting the presence of another outflow. Apart from these two features, the velocity map looks smooth all over the cluster showing a velocity close to the ambient velocity of NGC 6334-I (v∼-5 km s^{-1}). Similar to NGC 6334-I, the velocity map in NGC 6334-I(N) looks smooth with four pronounced peaks. The position of the peak with the highest velocity (∼ 50 km s^{-1}) is coincident with continuum source 95 (see Table A.1). The SiO (2-1) linewidths in NGC 6334-I vary between 0.2 and 70 km s^{-1}. The peak of the linewidth is coincident with source 44. Along the bipolar object, the linewidth changes from 18 to 32 km s^{-1}. The rest of the velocity dispersion map looks smooth showing a linewidth of ∼2 km s^{-1}. In NGC 6334-I(N), the linewidth ranges from 0.5 km s^{-1} up to 45 km s^{-1}. The maximum linewidth corresponds to the position of source 95. Moreover, there are two collimated structures with a width of ∼13 km s^{-1}. Similar to NGC 6334-I, the linewidth distribution throughout the cluster is quite smooth showing a typical linewidth of 1.5 km s^{-1}.

5.2 Gaussian fitting

The spectra of SiO (2-1) emission throughout the whole surveyed area seem to be composed of multiple components, and the linewidth of the emission changes drastically between different pixels of the SiO data cube. In order to have a more quantitative idea of the properties of the spectra, I fitted each pixel of the SiO data cube individually using the `BTS` algorithm (see more details in § C.1). To obtain more robust results, I only consider emission features with an intensity above 5σ. Among the fitted spectra, 75% are composed of one single component, 19% of two components, 4.2% of three and finally 1.8% of the pixels are fitted with 4 to 6 components. As mentioned in § C.1, `BTS` returns the intensity, velocity and linewidth of each component as output. By obtaining the number of components of each individual pixel together with the properties of each

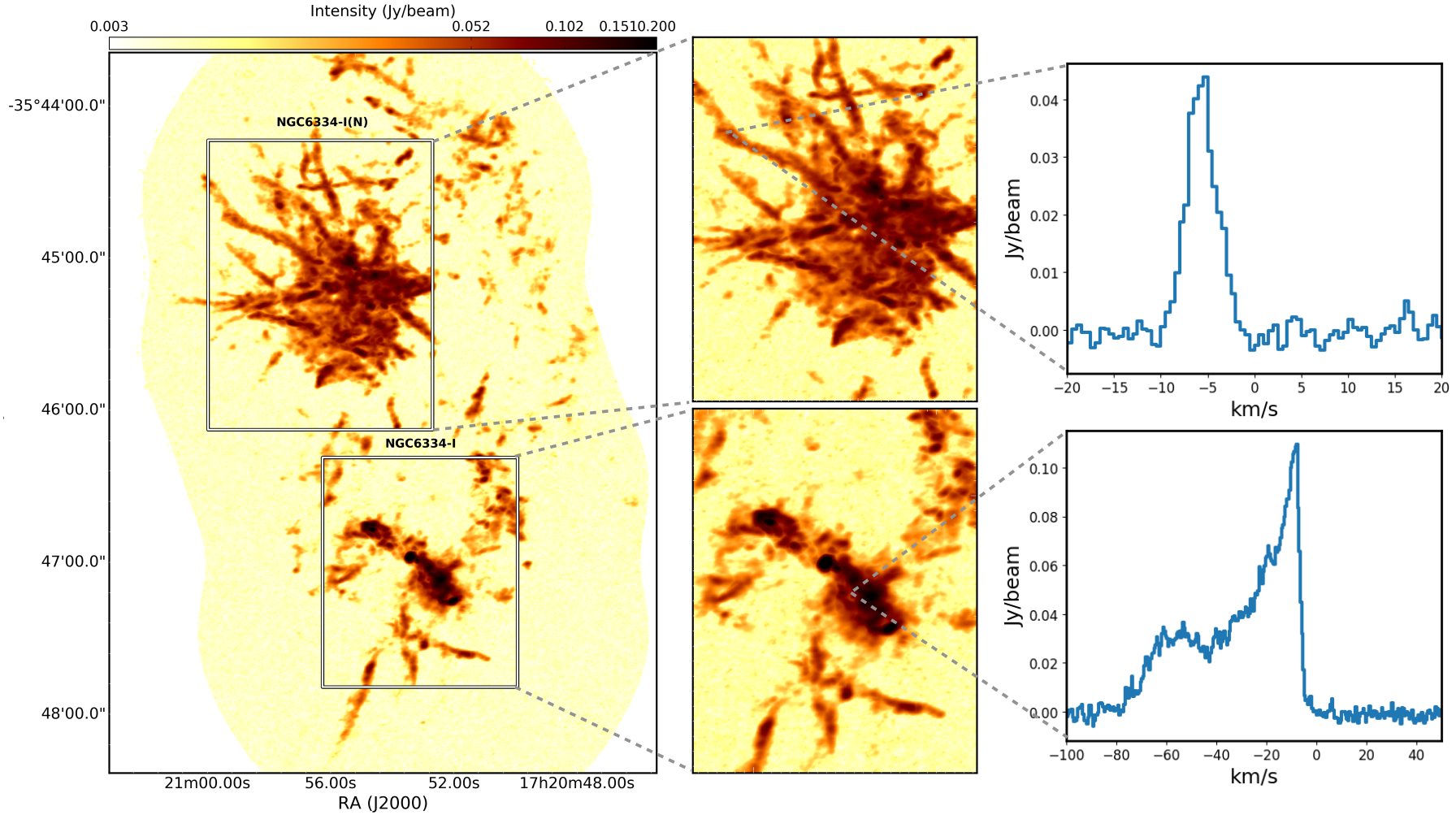

FIGURE 5.1: *Left:* ALMA SiO (2-1) peak intensity map towards NGC 6334-I and NGC 6334-I(N). *Middle:* Close-up views of the two regions makred with rectangles in the left panel. *Right:* SiO spectra towards selected positions. The regions exhibits a variety of line profiles from wide red/blue-shifted associated with outflows to narrow lines associated with low-velocity shocks.

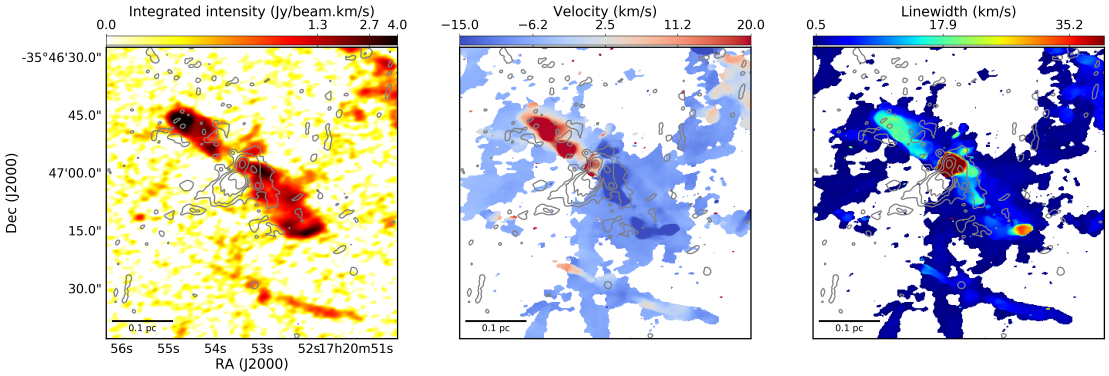

FIGURE 5.2: Spectral moments in NGC 6334-I. *Left:* Integrated intensity in units of Jy beam^{-1} kms^{-1}. *Middle:* Centroid velocity in km s^{-1}. *Right:* FWHM of central line in km s^{-1}.

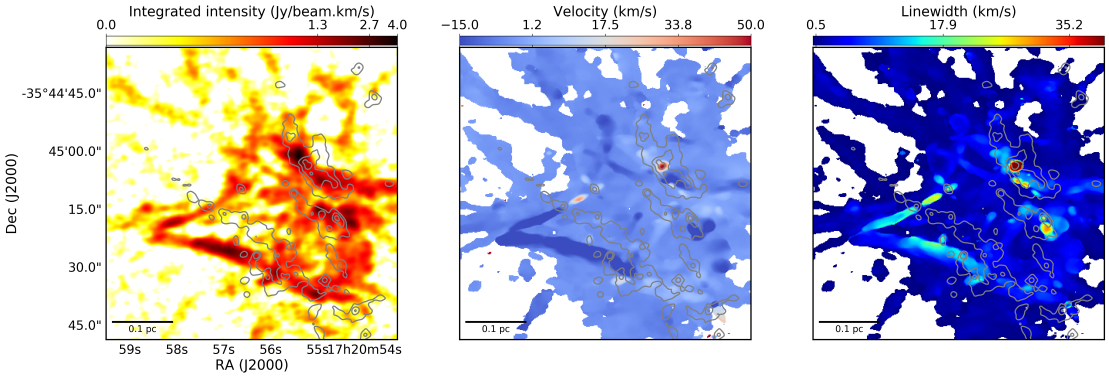

FIGURE 5.3: Spectral moments in NGC 6334-I(N). *Left:* Integrated intensity in units of Jy beam^{-1} kms^{-1}. *Middle:* Centroid velocity in km s^{-1}. *Right:* FWHM of central line in km s^{-1}.

component, it is possible to reconstruct a *synthetic* SiO data cube in which noise is filtered out. To probe the precision of the best-fit parameters, I measure the ratio of the fitted and original spectrum for each pixel. In Fig. 5.6 and Fig. 5.7, I show two selected channels of the original SiO data cube with a relatively large amount of emission, same channels of the synthetic data cube and map of the ratio of these two channels towards NGC 6334-I and NGC 6334-I(N) respectively. The ratio of the original and synthetic spectra for 85% of the pixels throughout the whole map is larger than 0.8 showing the reliability of the best-fit parameters. As shown in the middle panel of Fig. 5.8, all the emission structures present in the original data cube are successfully reconstructed in the synthetic data cube. Therefore, the synthetic data cube can be used for further analysis.

5.3 Structure Identification

As shown in the left panel of Fig. 5.1, the peak intensity map of SiO (2-1) exhibits numerous shock structures throughout the whole surveyed area which are overlapping in many positions. Therefore, disentangling distinct SiO emission structures in such an overcrowded region is a challenging task. Some algorithms were developed to find emission structures in data cubes and two-dimensional maps of star-forming regions. Amongst the commonly used structure identification algorithms such as `getfilaments`

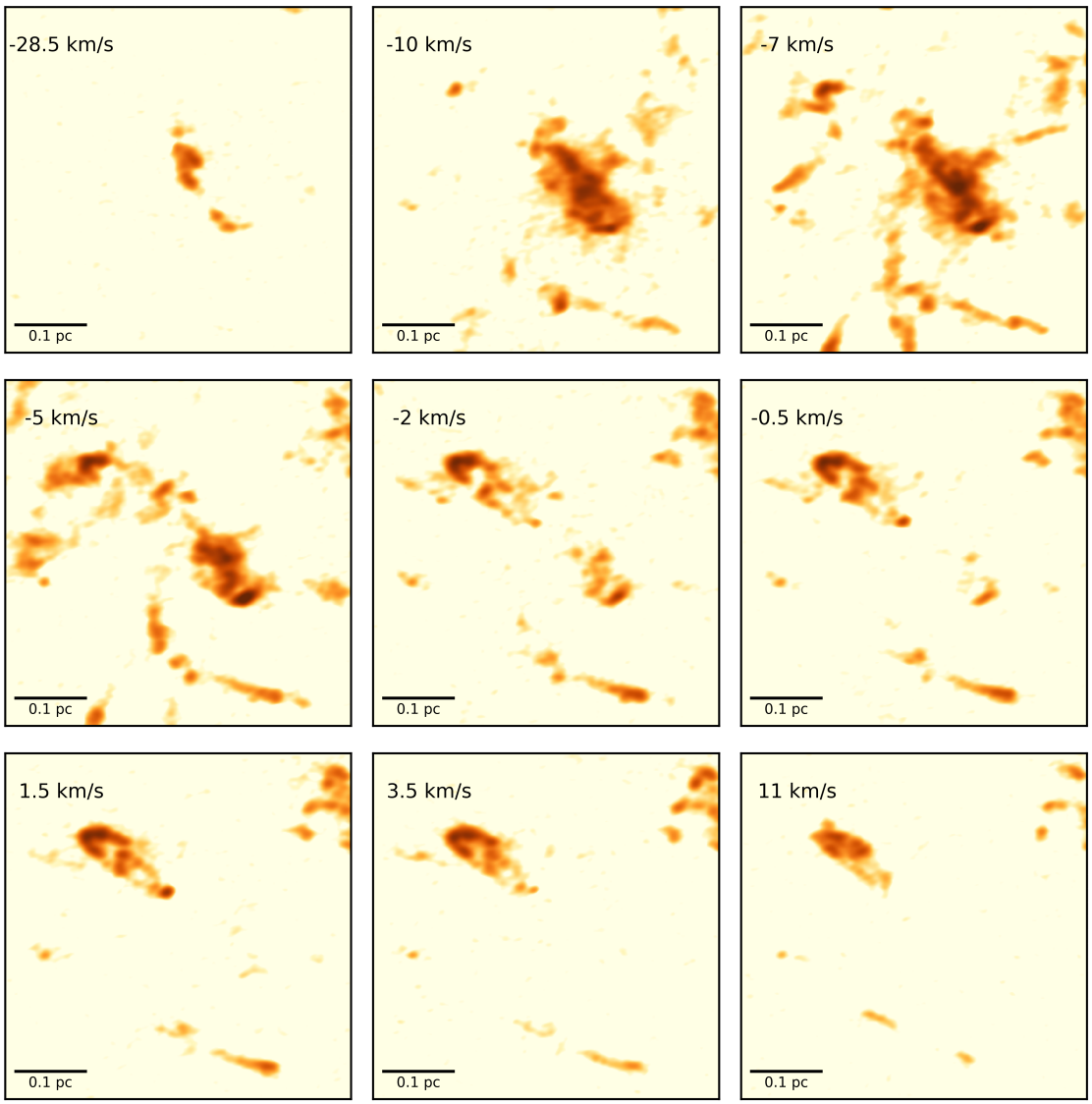

FIGURE 5.4: SiO channel map towards NGC 6334-I. The map is shown for the velocities from -28 km s^{-1} to 11 km s^{-1}.

(Men'shchikov, 2013), `FIVE` (Hacar et al., 2013) or `getsource`, I applied Discrete Persistent Structures Extractor (`DisPerSE`) (Sousbie, Pichon, and Kawahara, 2011) and `Astrodendro` to identify shock structures in the 2D peak intensity map of SiO and in 3D using the position-position-velocity information of the SiO data cube towards NGC 6334. In the following, I present the details of the structure identification using these two methods.

5.3.1 Discrete Persistent Structures Extractor (DisPerSE)

`DisPerSE` is an algorithm developed to identify topological features such as peaks, voids and in particular filamentary structures in 2D and 3D data sets. The framework of `DisPerSE` is based on two mathematical pillars: (i) the "Discrete Morse Theory" (Forman, 2002) for identification of the topological features, and (ii) the "persistent homology" (Edelsbrunner, Letscher, and Zomorodian, 2000) to deal with the noise in the data. The Morse theory looks at singularity structures of the density field $f(x)$. It leads to the translation of the spatial distribution and connection between maxima, minima and saddle

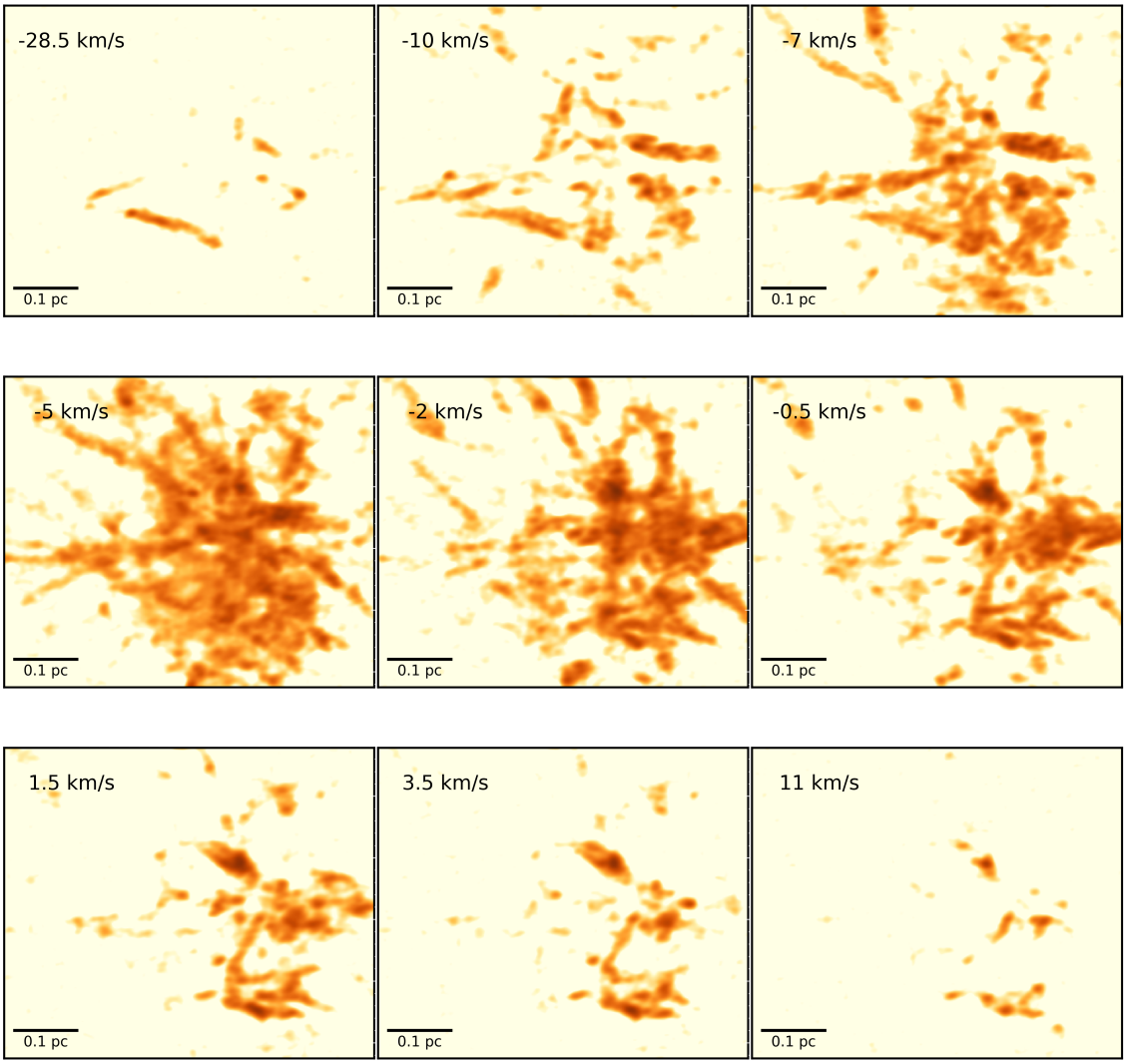

FIGURE 5.5: SiO channel map towards NGC 6334-I(N). The map is shown for the velocities from -28 km s^{-1} to 11 km s^{-1}.

points in the density fields into a geometric segmentation of space known as *Morse-Smale Complex (MSC)*. Based on the Morse theory, filaments are identified with the ascending or descending manifolds. Since the observation data sets include a specific amount of noise, the topological persistence is used to identify the observed features based on their significance. Persistence is defined as the difference of two values between two critical points (i.e., minima or maxima of the density fields) that are connected. Therefore, removing the pairs of points with a low persistence level, leads to a map with the most prominent structures.

So far, the `DisPerSE` algorithm has been extensively used to extract filamentary structures of star-forming clouds in other works (see e.g. André et al., 2016; Arzoumanian et al., 2011; Schneider et al., 2012; Suri et al., 2019). As the SiO features appear as elongated filamentary-like structures in our ALMA map (mainly towards the source NGC 6334-I(N), `DisPerSE` is an alternative for an automated structure identification. `mse` is the main function of `DisPerSE` which calculates the MSC of a given data set. The persistence level

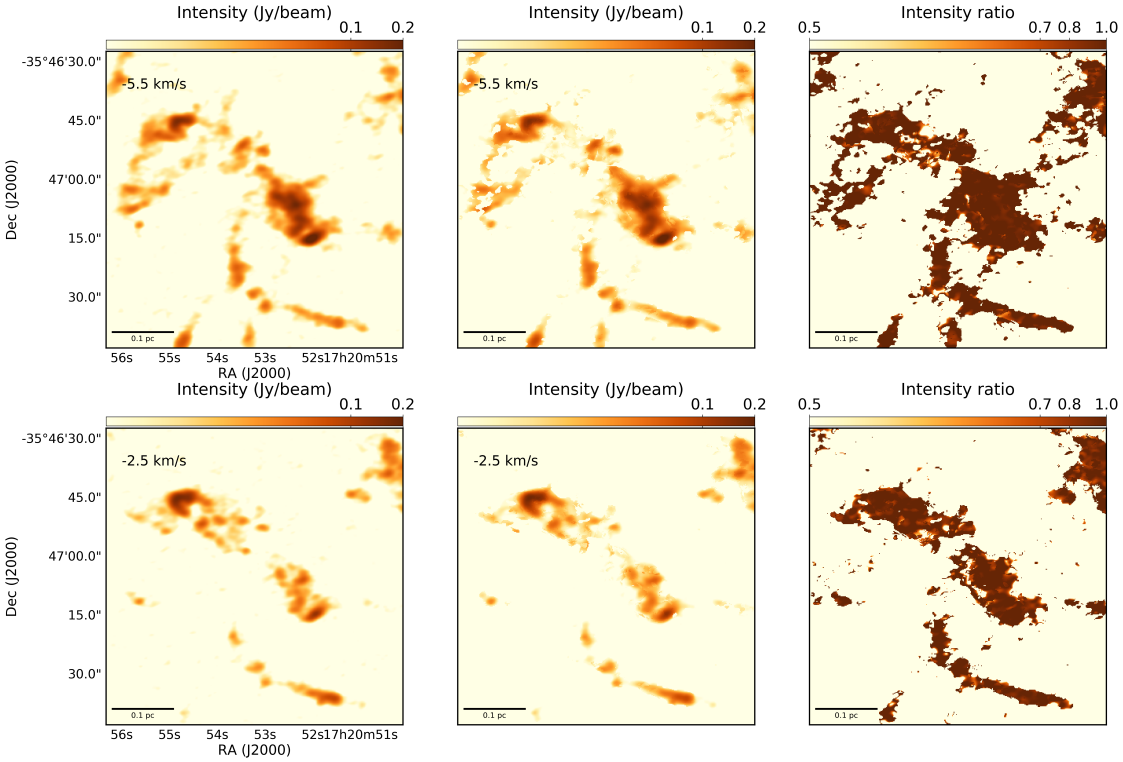

FIGURE 5.6: *Left:* Intensity map of two selected channels from the original SiO data cube toward NGC 6334-I. *Middle:* Intensity map of same channels from the synthetic data cube obtained by Gaussian fitting using BTS. *Right:* Ratio of the corresponding intensities of the selected channels from the original and synthetic data cube. Most pixel values are close to 1, indicating the reliability of the best-fit parameters.

is given as an input to the `mse` function. This can be set through two different ways. One option is to set it interactively using a persistence diagram. The other option is to directly introduce the value of the threshold as a priori to the algorithm. To define the persistence level interactively, one has to check the persistence diagram where all the critical point pairs are plotted. An example of a persistence diagram is shown in Fig. 5.9. On this diagram, each dot represents a persistence pair of critical points. The y-axis is the persistence of the pair (i.e. the value difference between the two, interpreted as contrast of the topological feature it represents with respect to its background). The x-axis represents the lowest density value of a pair. The pink dash-dot line denotes the persistence threshold. The points above the threshold correspond to the structures which are more pronounced compared to the background. The user can drag the line to his desired point.

To run `DisPerSE` on a given FITS file, the following command line in used in the first step:

```
> mse fitsFile.fits -interactive -upSkl,
```

where `upSkl` is a function that identify the filaments by connecting maxima to saddle points. Running this command generates two different files: (i) a `.MSC` file which includes all the mse information, and (ii) a `.NDSkl` file or the so-called *skeleton file* where the information of filaments after the application of the persistence threshold is stored. In the second step, the `skelconv` needs to be run on the `.NDSkl` file obtained in the first step to extract information of the identified filaments and write it in a FITS or an ASCII file:

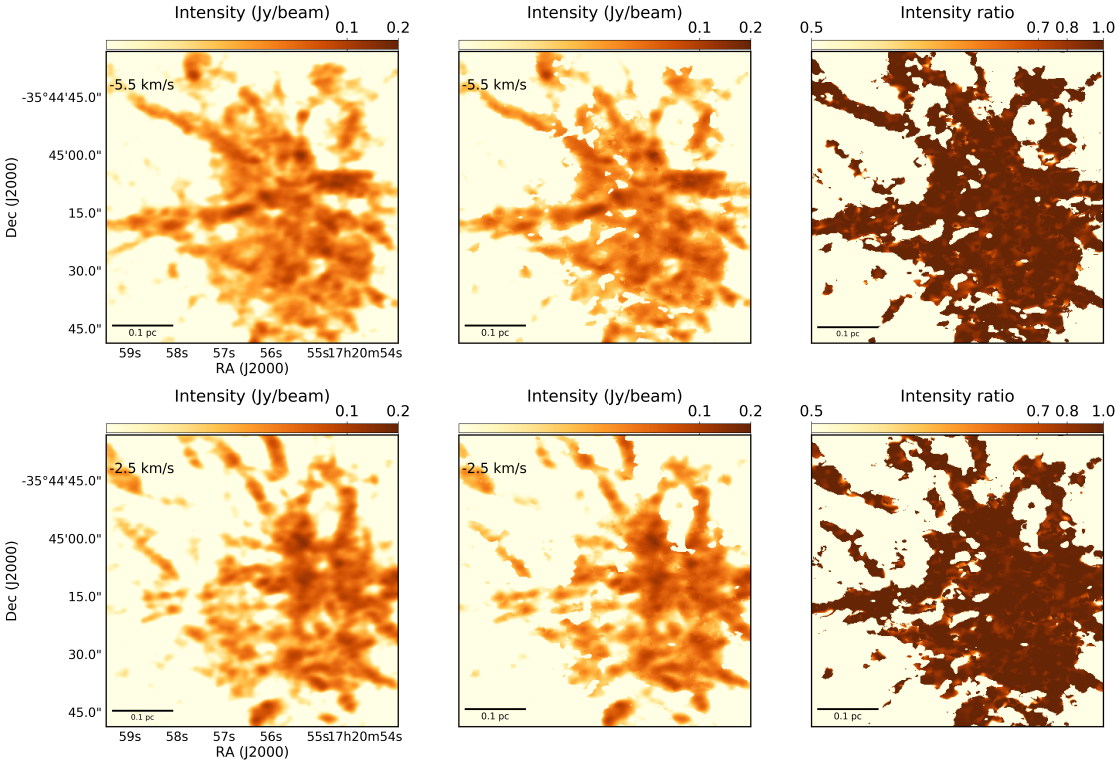

FIGURE 5.7: *Left:* Intensity map of two selected channels from the original SiO data cube toward NGC 6334-I(N). *Middle:* Intensity map of same channels from the synthetic data cube obtained by Gaussian fitting using BTS. *Right:* Ratio of the corresponding intensities of the selected channels from the original and synthetic data cube. Most pixel values are close to 1, indicating the reliability of the best-fit parameters.

```
> skelconv skeletonfile.NDSkl -breakdown -smooth 6
-trimBelow 4e+20 -assemble 70 -toFITS
```

The `skelconv` can be followed by several user-defined parameters which further adjust the procedure of filament identification. One parameter is the scale which represents the number of pixels over which the filament is smoothed (i.e., the `smooth` parameter). The second parameter is the detection threshold which removes the features associated with noise or cleaning artifacts (i.e., the `trimBelow` parameter). Finally, the last parameter defines the minimum angle between two features necessary to be identified as two distinct filaments (i.e., the `assemble` parameter). If two filaments form an angle smaller than this threshold, they will be merged into a single longer filament.

To identify the SiO features in 2D towards NGC 6334-I and NGC 6334-I(N), I applied `DisPerSE` on the SiO peak intensity map produced out of the SiO synthetic data cube. For identification of structures in 3D, `DisPerSE` is applied to the SiO synthetic data cube. The SiO peak intensity map and data cube are convolved to a larger beam with a size of $4.04'' \times 2.8''$ in order not to be biased with small-scale substructures. Based on the distribution of the critical point pairs in the persistence diagram, I used a persistence threshold of 4×10^{-7}. Since the peak intensity map is noise-free, the detection threshold possesses a value in the order of the persistence threshold. While most of the observed structures seem to be collimated, I set the `assemble` parameter to 118 degrees to connect smaller features together to form a larger structure. A total of 124 SiO emission structures in 2D and 200 structures in 3D are automatically identified by `DisPerSE`. The identified features

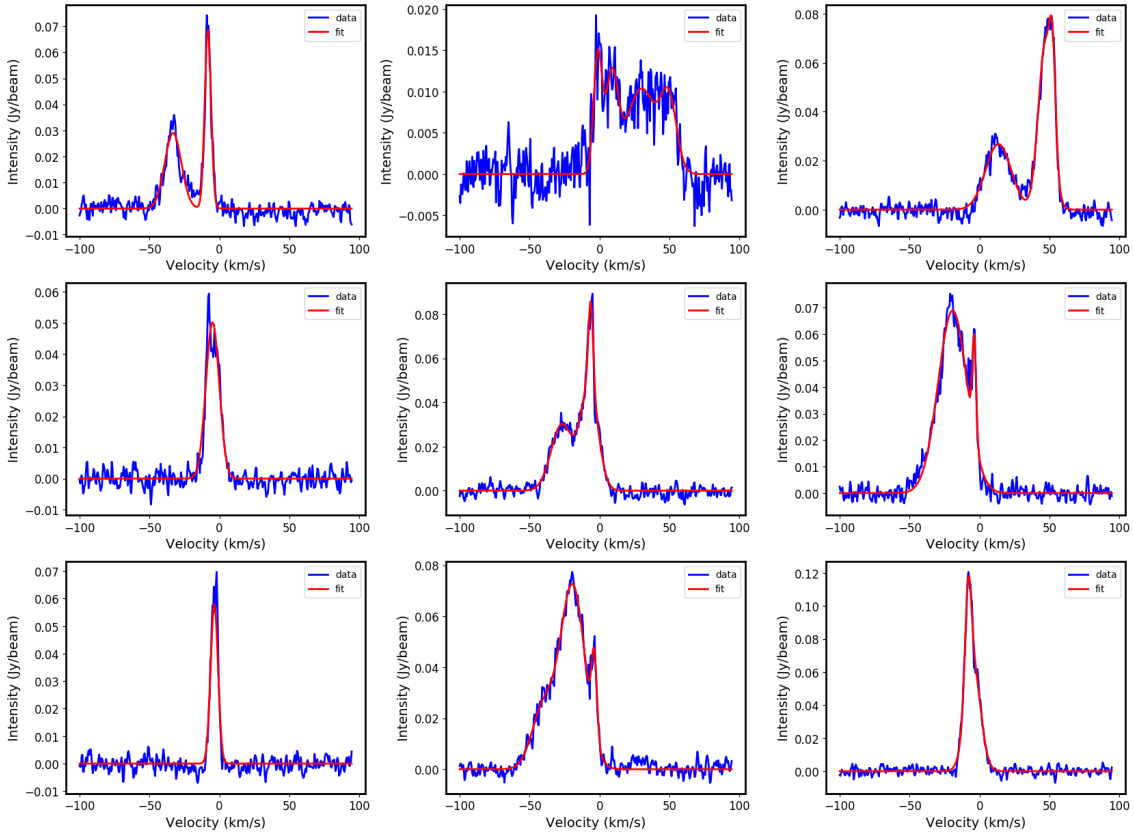

FIGURE 5.8: Example SiO spectra extracted from different pixels throughout the observed region (blue solid line) and corresponding fitted spectra (red solid line) obtained with BTS.

within the whole surveyed area are shown in the left panels of Figs. 5.10 and 5.11 in 2D and 3D respectively. As previously mentioned, `DisPerSE` identifies features by deriving gradients within each grid cell and connecting maxima and saddle points with each other. In case of our ALMA SiO map, the identification of critical points led to the extraction of features that are essentially not related to the underlying physical structure. In some structures such as the bipolar outflow in NGC 6334-I, single features are identified as several distinct structures due the variation of intensity throughout the feature. Moreover, the overlap of features resulted in an artificial network of structures in NGC 6334-I(N) which connects the overlapping features. It is necessary to note that the SiO features do not have a simple geometry. Although, by using the results from `DisPerSE` it is possible to obtain a rough estimation of the length of each feature, an accurate determination of the spatial extent of each feature particularly in crowded regions is not possible. Moreover, analysing the physical and dynamical properties of the SiO emission structures based on the `DisPerSE` results does not lead to a reliable outcome.

5.3.2 Dendrogram

The dendrogram technique is a segmentation method represented by a structure tree which looks for hierarchical structures in a given data set. It is presented first by Houlahan and Scalo (1992). A dendrogram is composed of two types of structures: branches, which are structures that split into multiple sub-structures, and leaves, which are structures that have no substructure. The term *trunk* refers to a structure that has no parent

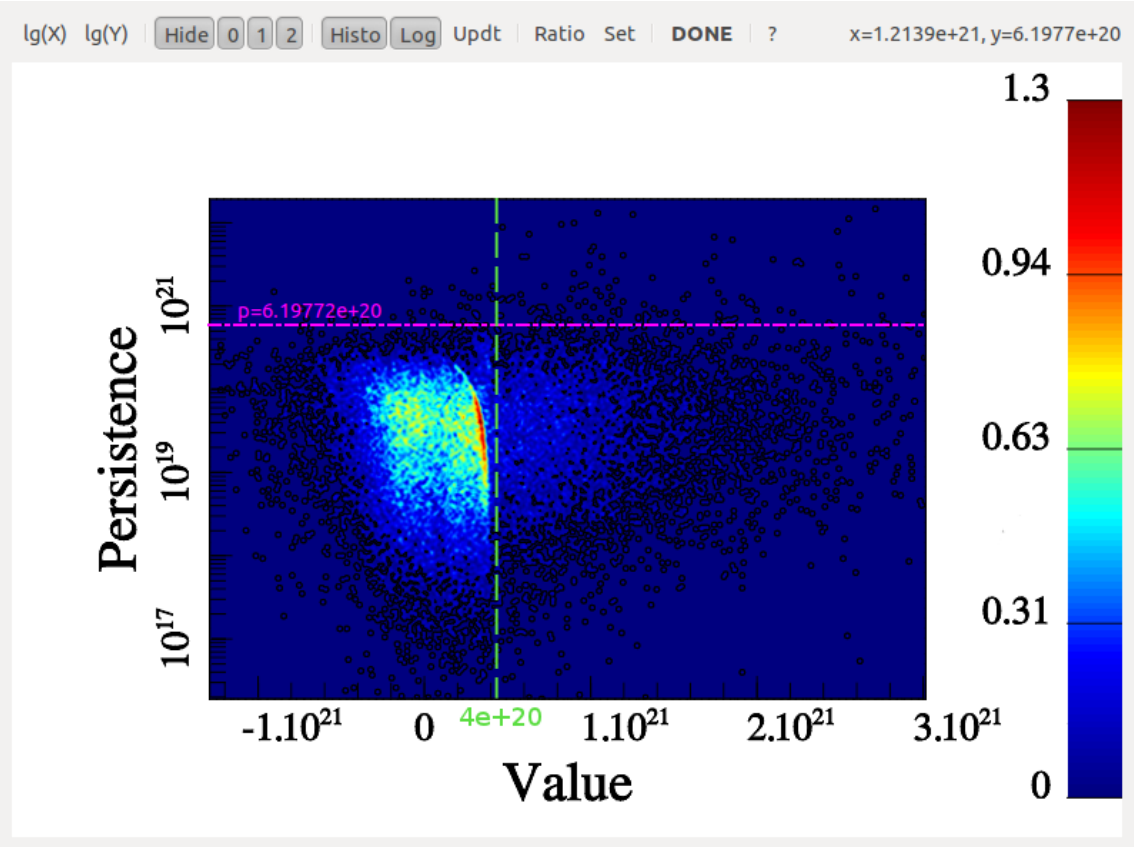

FIGURE 5.9: Persistence diagram. Image taken from http://www2.iap.fr/users/sousbie/web/html/index55a0.html?category/Quick-start

structure. The left panel of Fig. 5.12 shows a schematic view of a two-dimensional map which includes a hierarchical structure. The equivalent dendrogram representation is shown in the right panel. Thinking of a dendrogram in the framework of graph theory, the leaves which are representing the local maxima are denoted as the vertices of the graph. The branches that connect two leaves are equivalent to the edges of the graph. A dendrogram can be further described as a weighted graph, in which each edge is associated with a non-negative value w_{ij}, representing the *strength* of each connection. In a graph of a dendrogram of a hierarchical object, all pairs of vertices are connected with every other pairs resulting in the weights to be always positive. Therefore, we can assume that each leaf represents a structure in a certain level of hierarchy. Since the aim of generating a dendrogram is to characterise the relation between sub-structures, the resulting graph has no self-loop.

In the framework of astrophysics, the original concept of dengrogram has been generalized to three dimensional data cubes which include molecular line emissions (Rosolowsky et al., 2008). Applications of this method for characterising the hierarchical structures in different molecular clouds are presented, among others, by Colombo et al. (2015), Goodman et al. (2009), and Storm et al. (2014). Using this method it is possible to disentangle overlapping features by using two-dimensional position-position (PP) intensity maps or the three-dimensional position-position-velocity (PPV) information of a data cube. The structures of a dendrogram in a PP or a PPV cube are determined by the local maxima in the data. The local maxima which we refer to as leaves are distinct regions containing

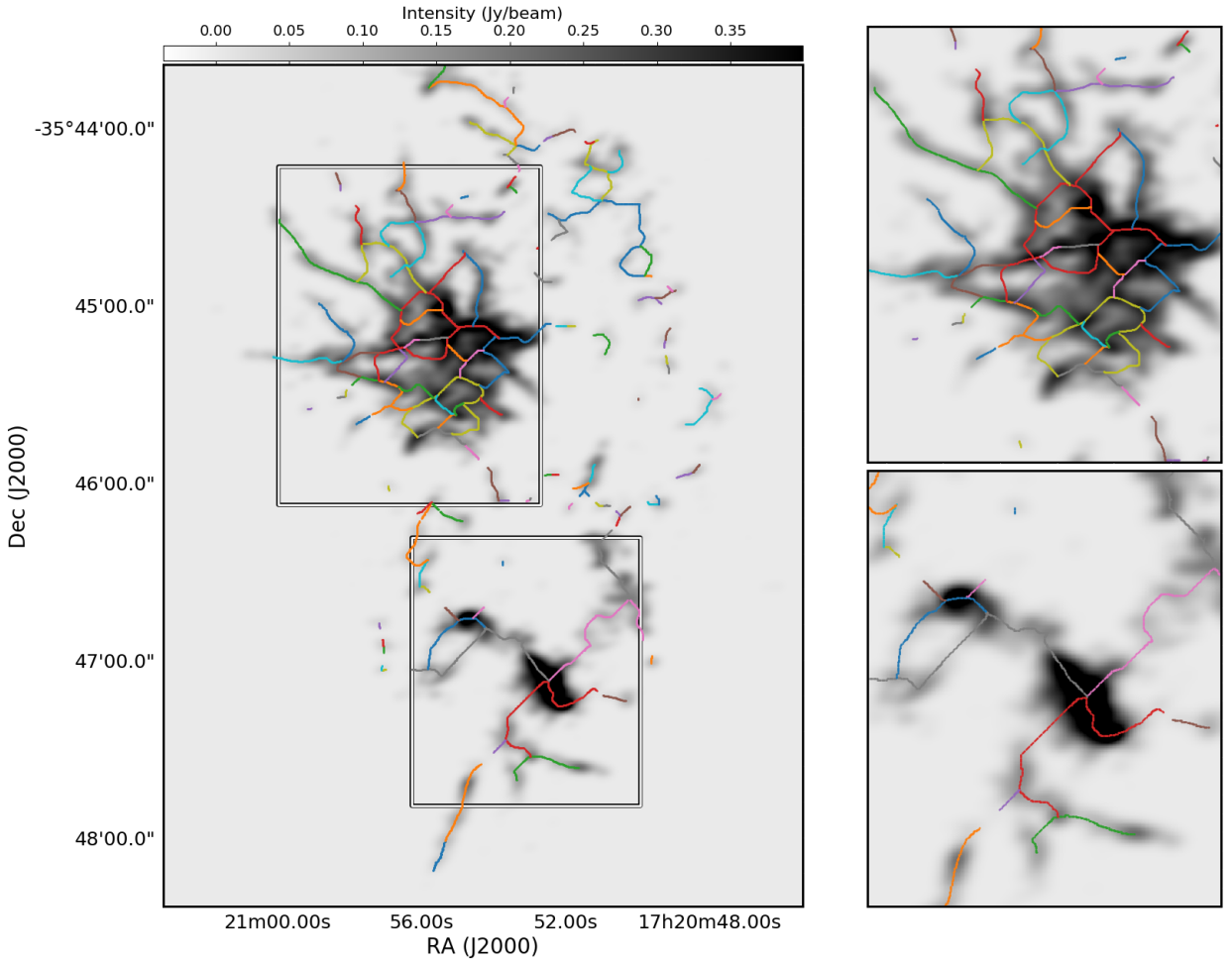

FIGURE 5.10: *Left:* SiO emission structures identified towards NGC 6334-I and NGC 6334-IN in 2D. Grey scale shows the SiO peak intensity emission, while the colored segments indicates the structures identified with `DisPerSE`. *Right:* Close-up view of the two regions marked with rectangles in the left panel.

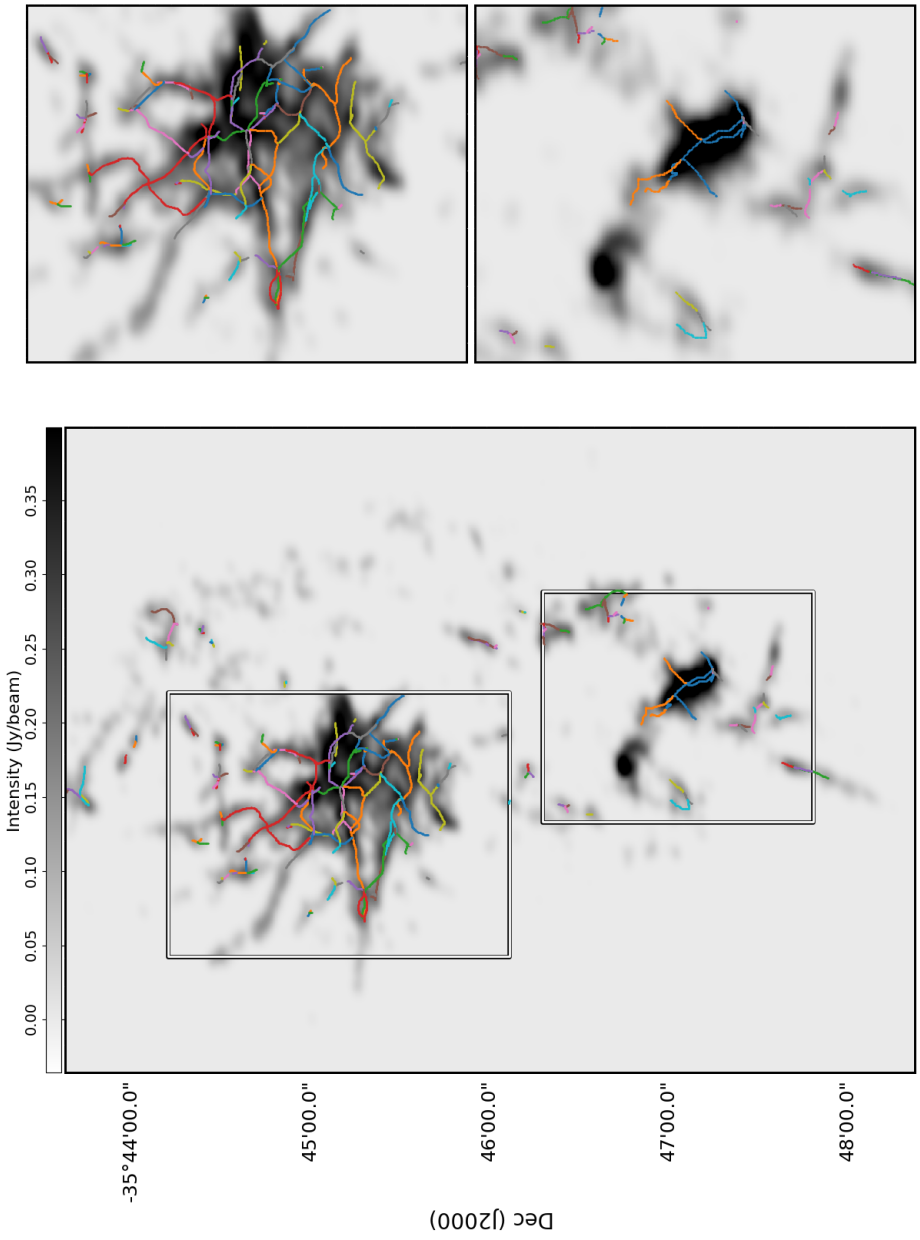

FIGURE 5.11: *Left:* SiO emission structures identified towards NGC 6334-I and NGC 6334-IN in 3D. Grey scale shows the SiO peak intensity emission, while the colored segments indicates the structures identified with `DisPerSE`. *Right:* Close-up view of the two regions marked with rectangles in the left panel.

no data value larger than the local maximum. Then, the leaves are represented by isosurfaces with a size of $D_{\rm max} \times D_{\rm max} \times V_{\rm max}$ in case of three-dimensional data cubes and by contours with a size of $D_{\rm max} \times D_{\rm max}$ in two-dimensional maps. To suppress the spurious structures created by noise fluctuations, it is possible to eliminate the structures whose volume is smaller than a certain threshold defined based on the number of pixels or their peaks that are smaller than a certain brightness temperature. Moreover, if the difference between two local maxima are smaller than a certain threshold in terms of intensity, the corresponding leaves will be merged into one single structure.

To identify SiO features automatically using dendrogram, I took advantage of the `python` package `Astrodendro`[1] which is implemented based on the algorithm presented in Rosolowsky et al. (2008). As mentioned before, the outcome of the dendrogram analysis depends on three main parameters which are defined by the user:

- `min_value`: the minimum value of the peak in a local maximum to consider in a data set.
- `min_delta`: the difference of the peak flux in a leaf and the value at which it is being merged into the tree. This parameters determines if the leaf is significant enough to be considered as an independent structure.
- `min_npix`: the minimum number of pixels for a leaf to be considered as an independent entity.

The noise level of the data is a limiting factor in structure identification that results in masking the low-amplitude variations in emission structures. Therefore, in the present work, I applied the dendrogram analysis to the synthetic peak intensity map of SiO. The `min_delta` and `min_value` for the SiO peak intensity map is determined using the sigma clipping method to be 0.7 Jy/beam. The minimum number of pixels necessary to consider an identified structure as an independent entity is 200 pixels which is seven times that of the beam size (28 pixels). The flux determined by the dendrogram corresponds to the counts of all pixels above the threshold. The observed geometric parameters (i.e., shape and size) of the structures are computed from the intensity-weighted moments of the pixels that form the structure. The sizes of the semi-major and semi-minor axis, together with the position angle, are derived assuming that the structures can be described by ellipses.

A total of 150 structures are automatically identified in the dendrogram analysis. After visual inspection, I excluded manually the low-level structures (i.e. trunks and branches) which correspond to a group of structures instead of a single entity. The final catalog of ALMA SiO emission structures contains 89 objects. I list them in the order of increasing right ascension in Table B.1, and marked them with contours in Fig. 5.14. The integrated fluxes of the identified structures range from 4 to 560 Jy. The observed sizes (diameters) range from $2''$ to $11''$ corresponding to 2 600 au and 143 000 au. In the first two panels of Fig. 5.15, I show the distribution of integrated fluxes and observed sizes.

5.4 Maps of dynamical properties

In the following section, I calculate the column density, mass and dynamical properties (i.e., momentum and kinetic energy) of the SiO emission on a pixel by pixel basis.

Although the critical density of the SiO (2-1) transition is high at typical conditions of

[1] Available at `https://dendrograms.readthedocs.io/en/stable/`

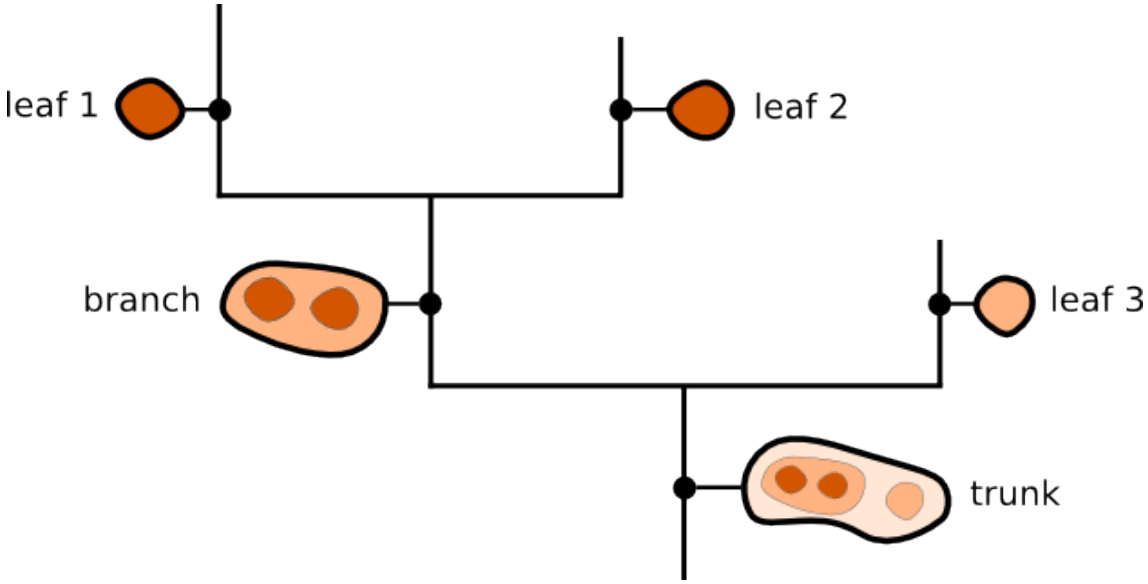

FIGURE 5.12: Schematic figure of a dendrogram.

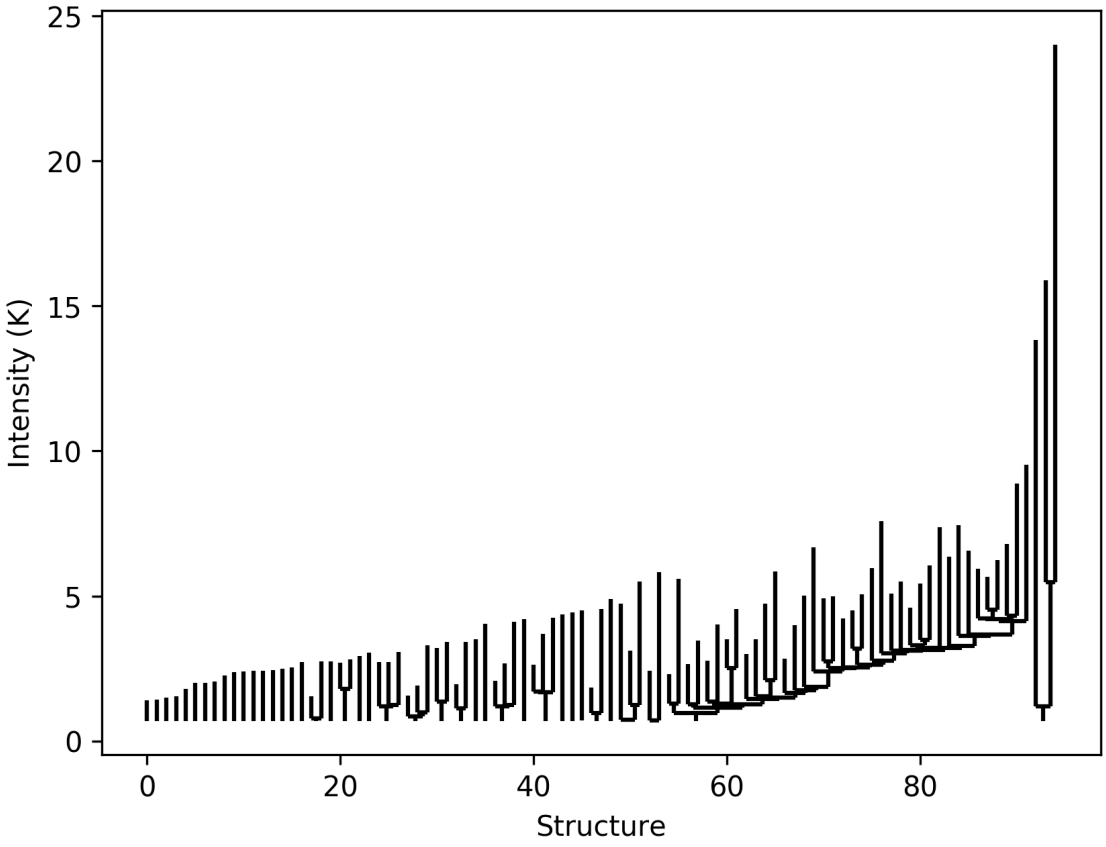

FIGURE 5.13: Dendrogram for emission structures in the SiO peak intensity map.

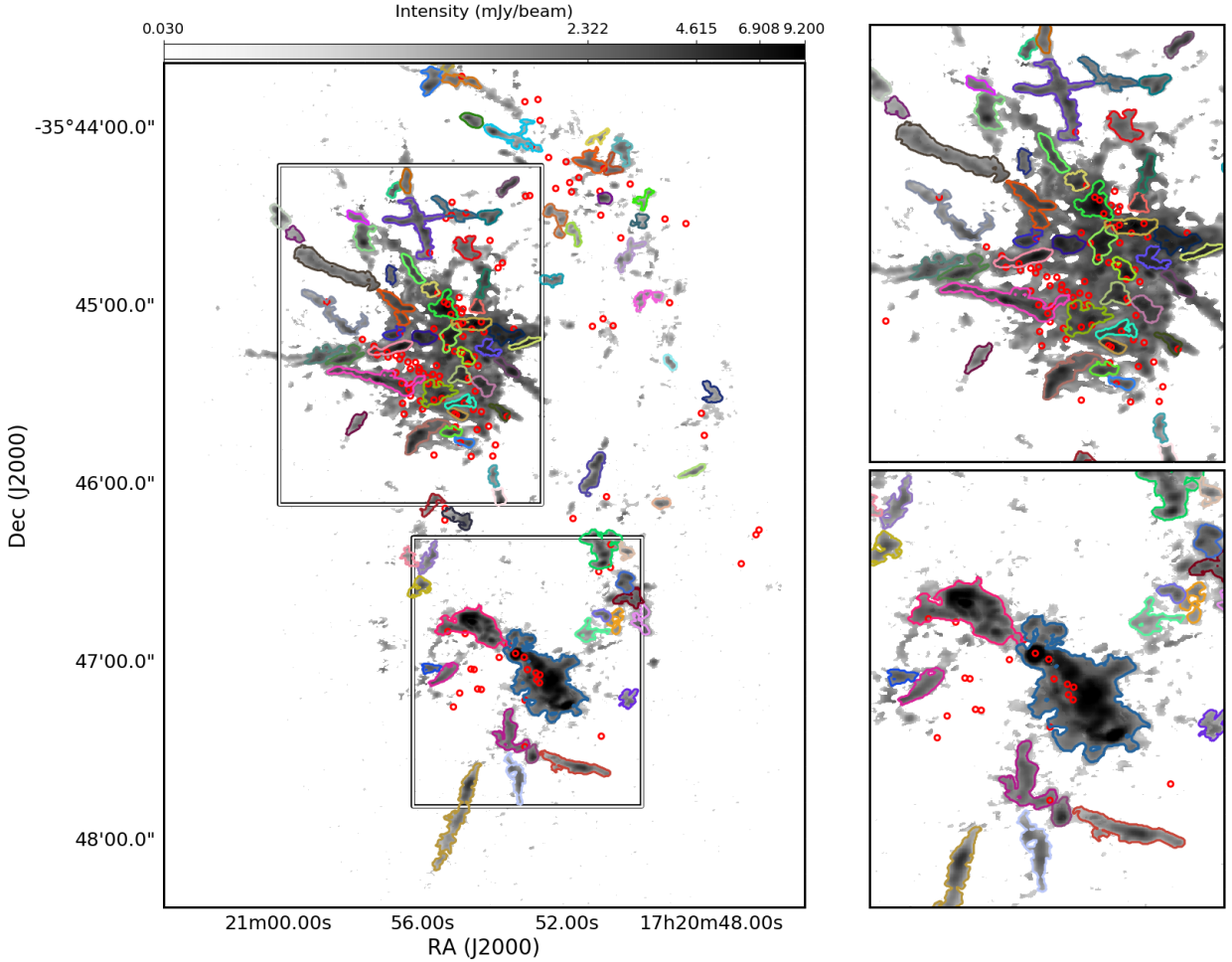

FIGURE 5.14: *Left:* Structures identified in the clusters NGC 6334-I and NGC 6334-I(N). Grey scale shows the SiO peak intensity emission, while the colored contours indicate the SiO emission structures identified with the dendrogram. Red circles denote the position of compact sources identified using SExtractor (see § 3.1.1). *Right:* Close-up view of the two regions marked with rectangles in the left panel.

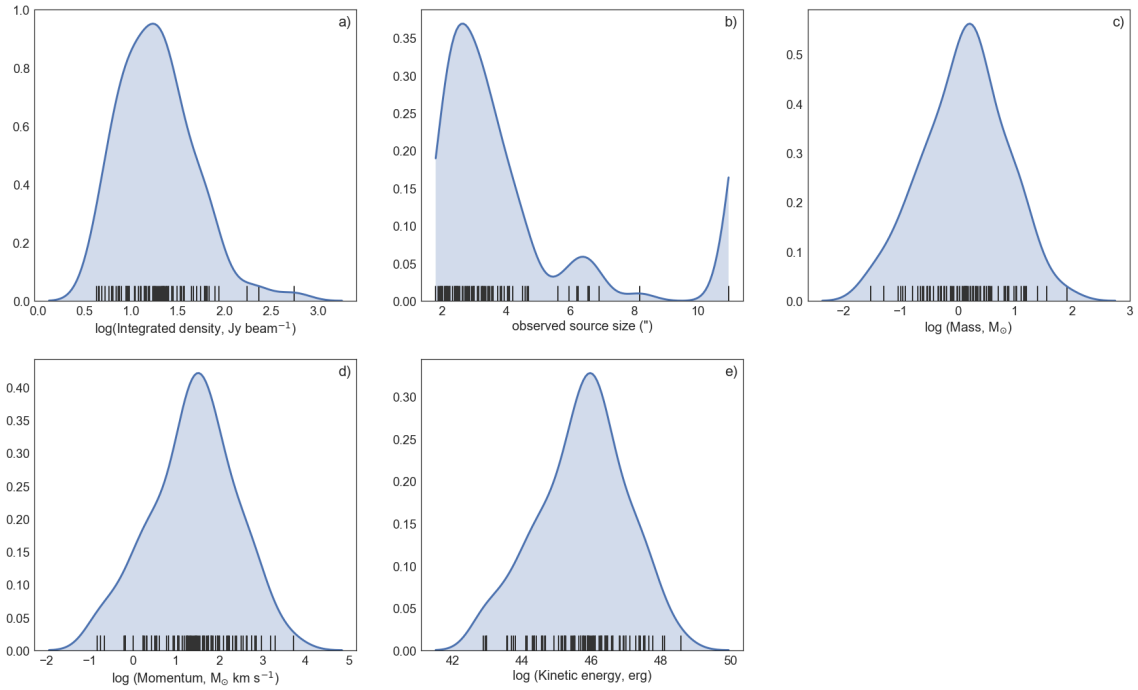

FIGURE 5.15: Distribution of *(a)* integrated intensity; *(b)* observed sizes; *(c)* mass; *(d)* momentum; *(e)* kinetic energy for the 89 SiO emission structures identified towards NGC 6334. The blue solid lines correspond to the KDE built from measured properties which are marked in the bottom of each panel, just above the x-axis.

shocks, it is a commonly used approach to derive the SiO column density assuming LTE condition (e.g. Csengeri et al., 2016; Nguyen-Lu'o'ng et al., 2013; Sánchez-Monge et al., 2013a). Assuming optically thin, LTE emission, the total column density of SiO (2-1) is estimated by

$$N_{\rm tot} = \frac{3k^2}{4\pi^3 h\nu^2}\frac{1}{S\mu^2}T_{\rm ex}e^{\frac{E_u}{kT_{ex}}}\int T_{mb}dv\frac{\tau}{1-e^{-\tau}} \approx 1.8\times10^{12}\int T_{mb}dv\ [{\rm cm}^{-2}], \tag{5.1}$$

where $S = 2$ is the statistical weight, $\mu = 3.1$ Debye is the electric dipole moments, $\nu = 86.85$ GHz. The assumed excitation temperature is 10 K for the LTE calculations (e.g. Csengeri et al., 2016). The integral $\int T_{\rm mb}$ is over the velocity channels and is given by the main-beam temperature in that channels multiplied by the channel width. I assume a SiO abundance relative to H_2 of $X_{\rm SiO}$=10^{-8}, which can vary by several orders of magnitude between 10^{-12} to 10^{-7} (e.g. Bachiller and Pérez Gutiérrez, 1997; Codella et al., 2005; Garay et al., 1998; Gerner et al., 2014; Nisini et al., 2007). The mass within each velocity channel in each pixel is then calculated as

$$M_{\rm v,pixel} = \mu_{\rm H_2} m_{\rm H} N_{\rm H_2} A_{\rm pixel}, \tag{5.2}$$

where $m_{\rm H}$ is the mean of a hydrogen atom, $\mu_{\rm H_2}$ is the mean molecular weight per hydrogen atom, $A_{\rm pixel}$ is the area of each pixel. The total mass of each SiO emission structure identified using dendrogram (see § 5.3.2) is obtained by summing $M_{\rm v,\ pixel}$ over all velocity and spatial pixels encompassing the structure. The calculated masses are listed in column (6) of Table B.1. The maps of SiO column density and mass are shown in Fig. 5.16. The velocities of integration are assumed to be symmetrical about the centroid

velocities obtained by the Gaussian fitting for each pixel. To determine the lower band of integration, I select the lowest velocity as $v_{\rm min} = v_c - 3\sigma_{\rm v}$, where $\sigma_{\rm v}$ is the linewidth. Since I adopt a symmetrical velocity limits, the upper bound of integration is defined as $v_{\rm min} = v_c + 3\sigma$. The momentum and kinetic energy in each pixel are calculated as

$$P_{\rm v,\ pixel} = M_{\rm v,\ pixel} \times \Delta v \tag{5.3}$$

and

$$E_{\rm v,\ pixel} = (1/2) M_{\rm v,\ pixel} \times \Delta v^2, \tag{5.4}$$

respectively, where Δv is the difference between the lower and upper bound of integration for each pixel. The total momentum ($P_{\rm tot}$) and kinetic energy ($E_{\rm tot}$) of each SiO emission structure are then calculated by summing over the same pixels as for the mass, and are listed in columns (7) and (8) of Table B.1, respectively. The masses of the identified structures range from 0.03 $M_\odot$ to 80 $M_\odot$, their kinetic energy from 10^{43} erg to 10^{48} erg and their momentum from 0.15 $M_\odot$ km s^{-1} to 5300 $M_\odot$ km s^{-1}. The last three panels of Fig. 5.15 show the distribution of mass, kinetic energy and momentum of the identified structures. In Fig 5.17, I present the momentum and energy of each pixel throughout the whole observed area.

5.5 Separation of low-velocity shocks from fast shocks

In this section, I present two different methods to isolate the widespread diffuse SiO emission associated with low-velocity shocks. The first method is a spectral analysis performed on the SiO data cube. The second method is a wavelet-based technique performed on the SiO peak intensity map. Once the low- and high-velocity shocks are disentangled, it is possible to estimate the contribution of each to the total observed emission. Furthermore, we can better constraint the mechanisms generating shocks at different scales.

5.5.1 Spectral decomposition

I have investigated the distribution of the SiO emission close to the systemic velocities of the protoclusters whose line profile is fitted by a narrow Gaussian. As shown in Figs. 5.2 and 5.3, the SiO emission map towards NGC 6334-I and NGC 6334-I(N) exhibits a complex morphology with a network of collimated structures combined with slow shocks in different regions. Moreover, in some cases the SiO emission from the high-velocity gas is along the line of sight, indicating a narrow Gaussian profile. Therefore, separating the contribution of outflows from the low-velocity shocks associated with colliding flows is a critical task. As an exercise for the decomposition of these two types of emission, I took advantage of the results of the Gaussian fitting explained in § 5.2. As mentioned in this section, each individual pixel of the SiO data cube is fitted with a single, double or multiple Gaussian profiles. According to the results obtained from the fitting procedure, I classify the observed spectra into four groups based on their number of components and the centroid velocity of each component:

1. Single or multiple asymmetric broad components overlapping with a Gaussian narrow component
2. A broad component with little/no narrow emission
3. Narrow component adjunct to broad emission with no overlap

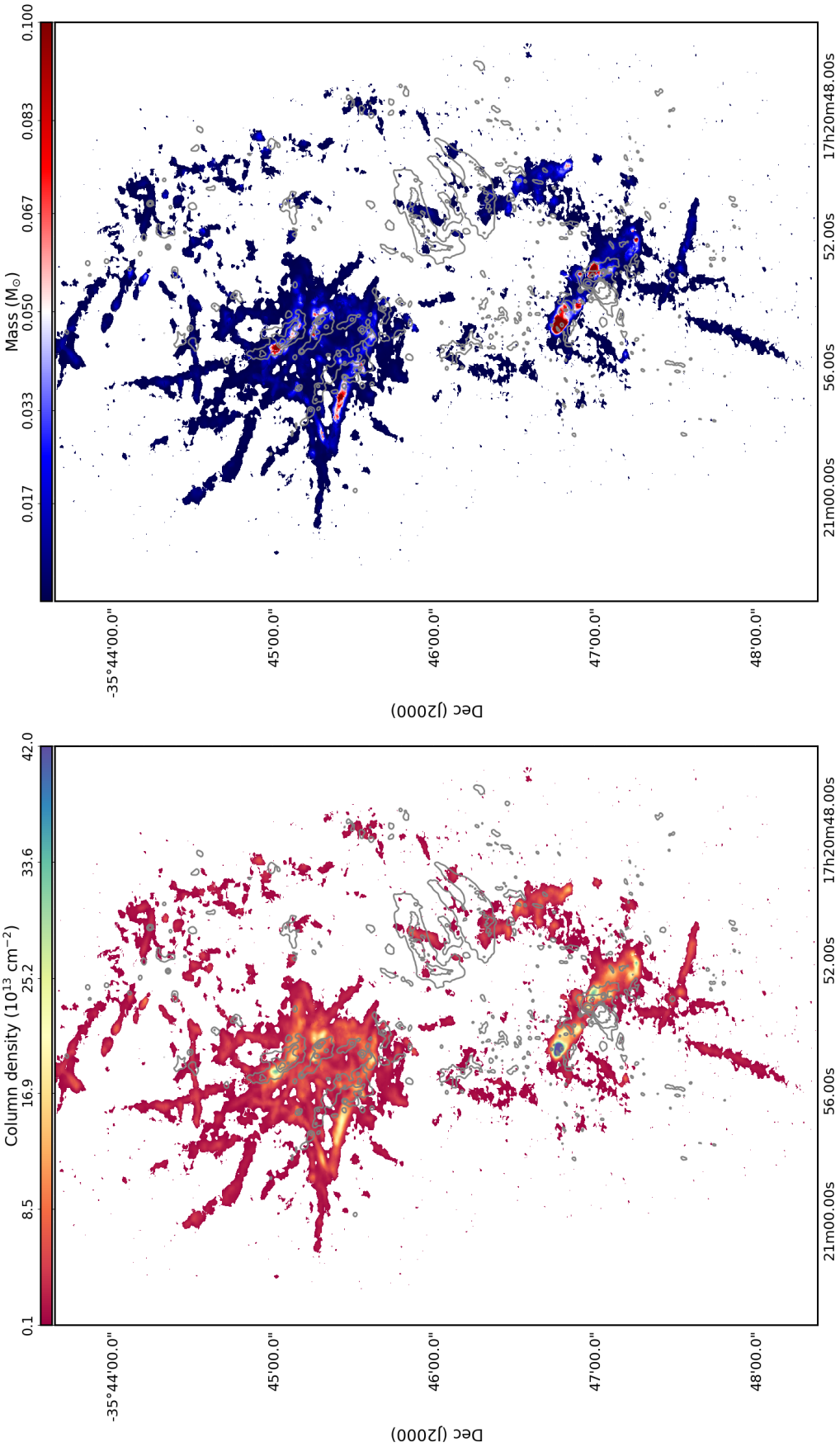

FIGURE 5.16: *Left:* Column density map of SiO for the whole observed area calculated following Eq. 5.1. *Right:* Calculated mass within each pixel over the whole observed area following Eq. 5.2. ALMA continuum map at 3 mm is overlaid in gray contours.

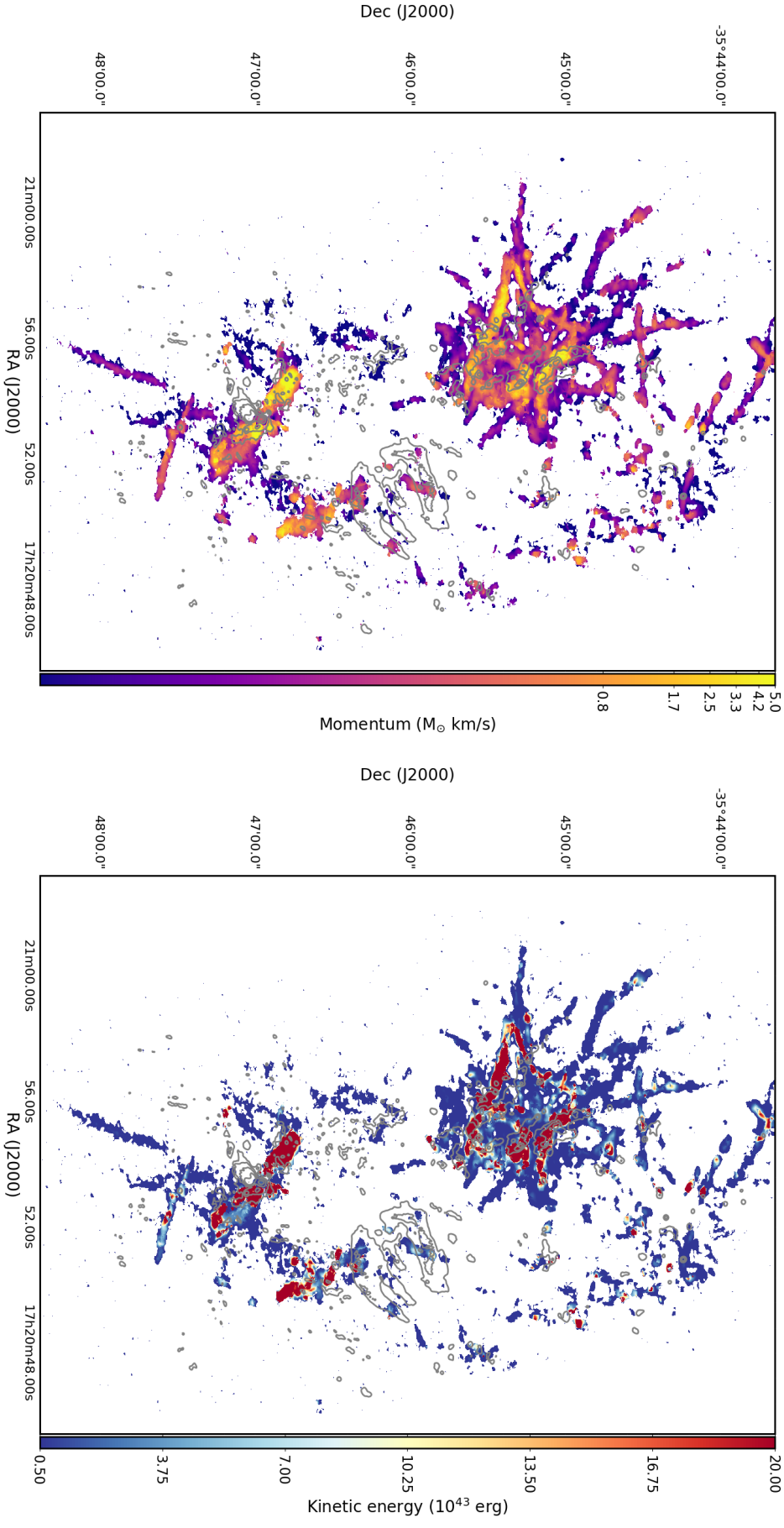

FIGURE 5.17: *Left*: Map of momentum calculated following Eq. 5.3. *Right*: Map of kinetic energy calculated following Eq. 5.4. ALMA continuum map at 3 mm is overlaid in gray contours.

4. Narrow emission with no broad emission at the vicinity

According to the 1D shock models (e.g. Anderl et al., 2013; Gusdorf et al., 2008a), a typical profile of SiO associated with high-velocity shocks is composed of a broad and a narrow component exhibiting a highly asymmetric profile. This profile explains the first case which is the most typical case in our SiO data cube. The shock models predict the narrow profile to be shifted by tens of km s^{-1} from the systemic velocity. However, due to the projection effects, the velocity shift of the narrow component can be significantly decreased. Therefore, the narrow component becomes less visible and the SiO profile looks either broad and symmetric or slightly asymmetric with the narrow component partially visible. This explains the profiles of the second case. Outflows as a continuous process have the capability to replenish the decelerated SiO in outskirts of outflow cavities. In this case, we expect to observe a narrow Gaussian profile in the vicinity of a broad component consistent with case 3 (Duarte-Cabral et al., 2014). Consequently, the first three cases are associated with outflows generated during the star formation activities. The remaining case with a narrow symmetric profile at systemic velocities is the one which can be associated with slow-shocks generated by collision of gas flows or cloud-cloud collision events. To subtract the contribution from a broad outflow profile, in the first step, I selected all the pixels where the fitted spectra has only one component. By doing so, I removed the contribution of the first and the third case. In the second step, it is necessary to apply a threshold to the linewidth of the spectra with a single component. This leads to removing the contribution of the pixels with a broad line profile (i.e., case 2). However, there is no clear definition to distinguish the high-velocity component from a narrow Gaussian profile commonly observed at the systemic velocity. Various definitions so far have been used in the literature. Nguyen-Lu'o'ng et al. (2013) refer to a broad component with a linewidth >25 km s^{-1}, while other studies are more conservative. Jiménez-Serra et al. (2010) refer to a low-velocity component with linewidths up to 3 km s^{-1}, and consider as a high-velocity component linewidths between 4–7 km s^{-1}. In W43-MM1 ridge, Louvet et al. (2016) report that the velocity of the low-velocity shock components changes in the range 7 to 12 km s^{-1}. In the present study, I adopt a threshold of 12 km s^{-1} for the linewidth to statistically disentangle the low- and high-velocity components. As a result of decomposition, I end up with a data cube for broad components and a data cube for narrow components. Figs. 5.18 and 5.20 show the moment maps of the broad components towards NGC 6334-I and NGC 6334-I(N) respectively. On average, I find 5 km s^{-1} linewidth for the low-velocity component centered at the ambient velocity in both clusters. The high-velocity component is fitted on average with 19 km s^{-1} towards NGC 6334-I(N) as a younger cluster and it decreases to 17 km s^{-1} towards NGC 6334-I as a more evolved cluster.
Fig. 5.22 represents the KDE of the linewidths of the narrow and broad components. The maximum linewidth for the broad component is found to be 70 km s^{-1} with a mean of 19 km s^{-1} towards the entire observed region with ALMA. The broad line profiles suggest an ongoing star formation with significant high-velocity gas likely associated with the outflows emanating from hot cores and young protostars.

The linewidths of narrow components change between 1.1–11.9 km s^{-1} with a mean of 4.8 km s^{-1} towards the whole observed region. As a comparison, the average linewidth for the low-velocity regime is a factor of at most 4 larger than that found by Jiménez-Serra et al. (2010) for spatially extended SiO emission, but is comparable to the findings of Louvet et al. (2016) towards the W43-MM1 ridge and Csengeri et al. (2016) in the infrared-quite clumps captured in the ATLASGAL survey.

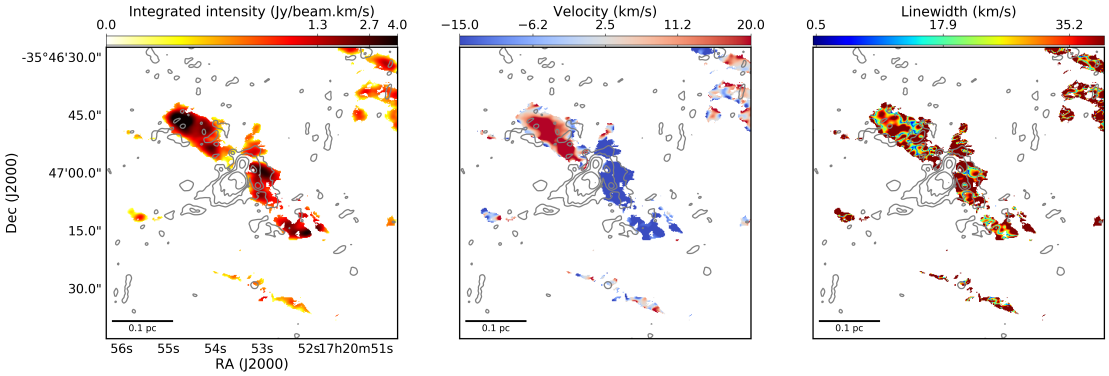

FIGURE 5.18: Spectral moments of broad component in NGC 6334-I. *Left:* Integrated intensity in units of Jy beam^{-1} kms^{-1}. *Middle:* Centroid velocity in km s^{-1}. *Right:* FWHM of central line in km s^{-1}. ALMA continuum map at 3 mm is overlaid in gray contours.

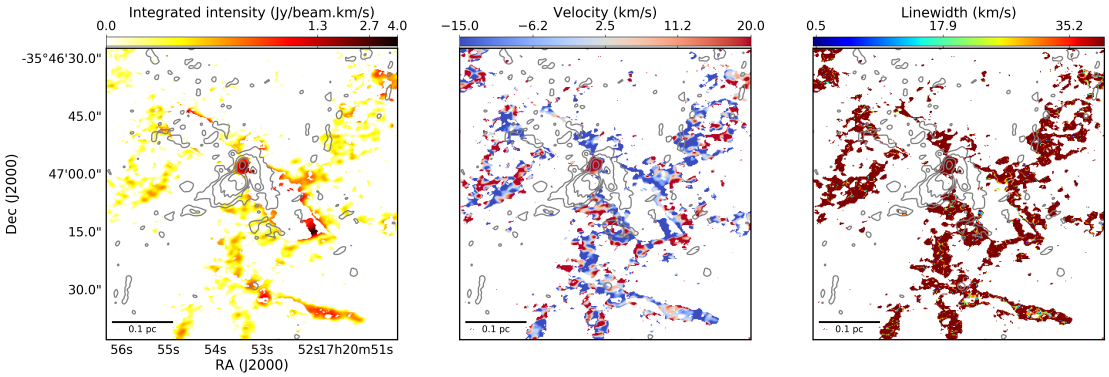

FIGURE 5.19: Spectral moments of narrow component in NGC 6334-I. *Left:* Integrated intensity in units of Jy beam^{-1} kms^{-1}. *Middle:* Centroid velocity in km s^{-1}. *Right:* FWHM of central line in km s^{-1}. ALMA continuum map at 3 mm is overlaid in gray contours.

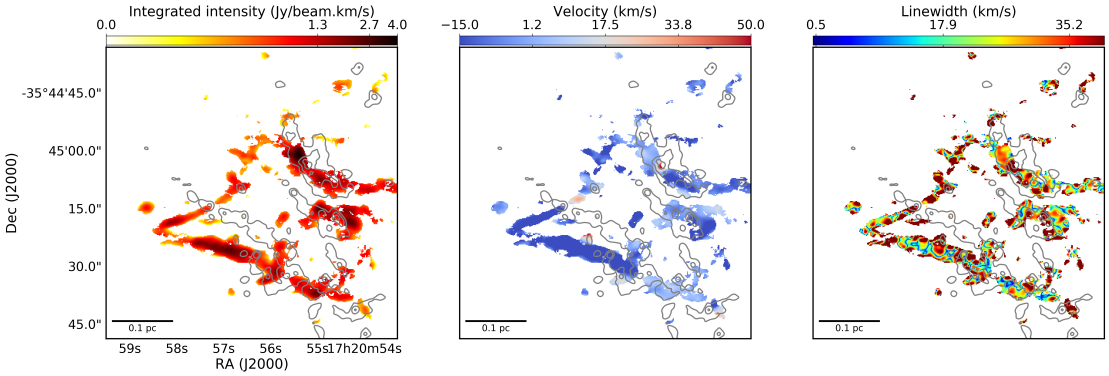

FIGURE 5.20: Spectral moments of broad component in NGC 6334-I(N). *Left:* Integrated intensity in units of Jy beam^{-1} kms^{-1}. *Middle:* Centroid velocity in km s^{-1}. *Right:* FWHM of central line in km s^{-1}. ALMA continuum map at 3 mm is overlaid in gray contours.

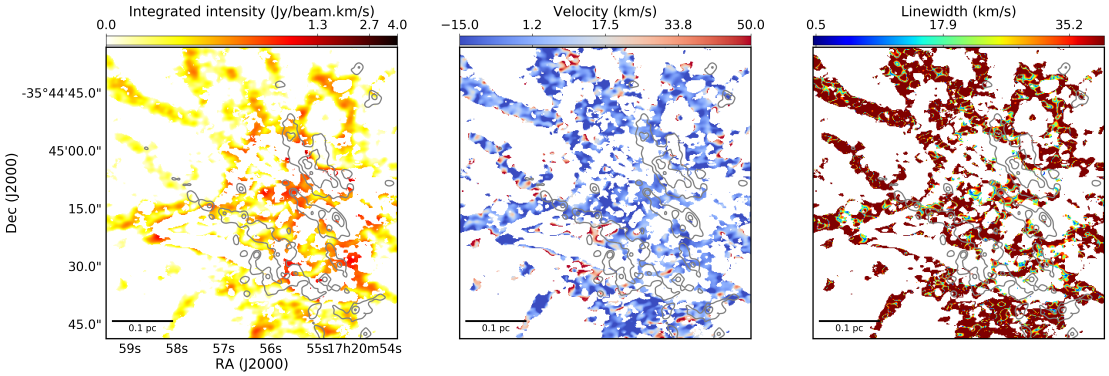

FIGURE 5.21: Spectral moments of narrow component in NGC 6334-I(N). *Left:* Integrated intensity in units of Jy beam^{-1} kms^{-1}. *Middle:* Centroid velocity in km s^{-1}. *Right:* FWHM of central line in km s^{-1}. ALMA continuum map at 3 mm is overlaid in gray contours.

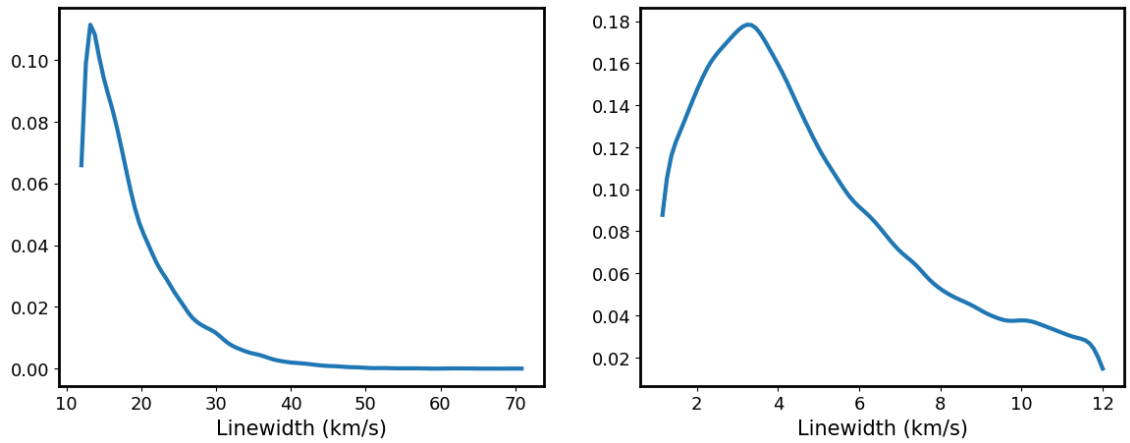

FIGURE 5.22: Distribution of the linewidth for the broad (*left*) and narrow (*right*) components.

5.5.2 Complex wavelet decomposition

Real world data and signals frequently exhibit slowly changing trends or oscillations punctuated with transients. On the other hand, images have smooth regions disrupted by the edges and changes in contrast. These changes are usually the most interesting part of the data in terms of information they provide. In astrophysical contexts, detailed statistical analysis of interstellar maps is fundamental to characterise the physical processes dominating at different scales and their link to the star formation activity. In the mid-1980s, the Fourier power spectrum (Crovisier and Dickey, 1983; Green, 1993; Miville-Deschênes et al., 2003) was introduced as a tool for morphological analysis of ISM signals. Although the Fourier power spectrum is useful to describe the intensity distribution of a map, it is not able to present the local intensity fluctuations as a function of spatial scales. The reason is that the Fourier transform represents the data as the sum of sines which are not localized in time or space. These sine waves oscillate forever and consequently all the local information associated with the intensity fluctuations are lost. As a solution to this problem, Robitaille, Joncas, and Miville-Deschênes (2014) introduced the `MnGSeg`[2] algorithm which is a wavelet-based method. This method provides us with the possibility

[2]Available at `https://github.com/jfrob27/pywavan`

to not only gain information on the spatial frequency content of the signal, but also on the localized intensity fluctuations as a function of the spatial scales.

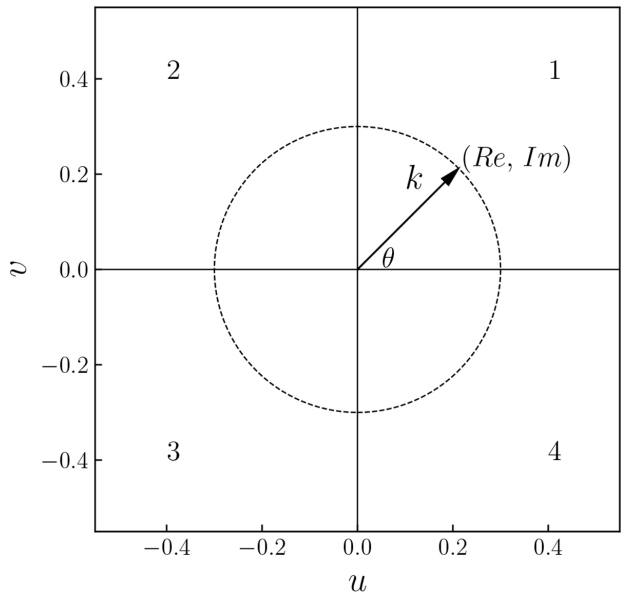

FIGURE 5.23: Schematic representation of 2D Fourier space, where u and v are the two dimensions, k is the wave number and θ is the azimuthal angle.

Wavelet is a rapidly decaying wave-like oscillation that has zero mean and exists for a finite duration. To compute the wavelet transform, the function $f(x)$ is convolded with 'daughter' wavelets which are generated from dilation and translation of a 'mother' wavelet $\psi(x)$:

$$\tilde{f}(l,x) = \frac{1}{l}\int_{-\infty}^{+\infty} f(x')\psi^*(\frac{x'-x}{l})dx', \tag{5.5}$$

where l represents the scale factor which controls the dilation of the functions and ψ^* is the complex conjugate of ψ. The function $\tilde{f}(l,x)$ represents the wavelet transform of $f(x)$ which is a function of position x and spatial scale l. Based on shape and size, wavelets are classified into different groups. Among others, the Morlet wavelet is the best wavelet function for reproducing the Fourier power spectrum (Kirby, 2005). The Morlet wavelet consists of a plane wave modulated by a Gaussian. It is defined in the Fourier space as:

$$\hat{\psi}(k) = e^{-[(u-|k_0|cos\theta)^2+(v-|k_0|sin\theta)^2]/2}, \tag{5.6}$$

where k_0 is set to 5.336 to ensure the zero mean value of the wavelet function. θ denotes the azimuthal angle is a 2D Fourier space shown in Fig. 5.23. By integrating over θ it is possible to estimate the power spectrum of an image:

$$P^W(l,x) = \frac{\delta\theta}{N_\theta}\sum_{j=0}^{N_\theta-1} \mid \tilde{f}(l,x,\theta_j) \mid^2, \tag{5.7}$$

where $\tilde{f}(l,x,\theta_j)$ are the Morlet wavelet coefficients for map $f(x)$ and $N_\theta = \Delta\theta/\delta\theta$ is the number of directions sampled over the range $\Delta\theta$. The dependency of the Morlet wavelet power spectrum on both position and spatial scale provides us with a more detailed information on the intensity fluctuation compared to the Fourier power spectrum. Averaging

the power spectrum over all positions x results in the global wavelet power spectrum, $P^W(l)$, defined as

$$P^W(l) = \frac{1}{N_x} \sum_x P^W(l, x), \tag{5.8}$$

where N_x is the number of pixels in the map. In order to compare the global wavelet power spectrum with the Fourier power spectrum, it is necessary to convert the spatial scale l to the Fourier spatial frequency using $k = \mid k_0 \mid / l$.

Non-Gaussian segmentation and image reconstruction

Nguyen-Lu'o'ng et al. (2013) showed that it is possible to disentangle the scale-dependent intensity fluctuations from the random components whose properties are not spatially correlated across the scales. This can be done by analysing the PDFs of the wavelet coefficient. While small wavelet coefficients represent the scale-free structures, the large ones are considered to be associated with scale-dependent fluctuations. The PDF distribution of wavelet coefficients for scale-dependent intensity fluctuations look pretty non-Gaussian, while for the case of random components the PDF resembles a Gaussian distribution. Therefore, by setting a threshold on the PDF distribution of wavelet coefficients it is possible to isolate the scale-dependent fluctuations which contribute to the non-Gaussianity of the PDF distribution. To perform this analysis, the `MnGSeg` algorithm samples every spatial scale as a function of the azimuthal direction. Assuming Φ is the threshold for separating the non-Gaussian terms from the Gaussian terms, and L_Φ the function indicator, the threshold Φ is estimated using

$$\sigma^2_{l,\theta}(\Phi) = \frac{1}{N_{l,\theta}(\Phi)} \sum_x L_\Phi(\mid \tilde{f}_{l,\theta}(x) \mid) \mid \tilde{f}_{l,\theta}(x) \mid^2, \tag{5.9}$$

where

$$L_\Phi(\mid \tilde{f}_{l,\theta}(x) \mid) = \begin{cases} 1, & \text{if } \mid \tilde{f}_{l,\theta}(x) \mid < \Phi \\ 0, & \text{else.} \end{cases} \tag{5.10}$$

and

$$N_{l,\theta} = \sum_x L_\Phi(\mid \tilde{f}_{l,\theta}(x) \mid) \mid . \tag{5.11}$$

The iterative calculations result in an optimal value of Φ which allows to separate the scale-free components from scale-dependent fluctuations. As a result of decomposition, two sets of wavelet coefficients are obtained, the Gaussian set $\tilde{f}^G(l, \theta)(x)$ and the non-Gaussian set, which is also called the coherent set, $\tilde{f}^C(l, \theta)(x)$. Using Eq. 5.7, the power spectrum of each set can be calculated. The total power spectrum which is equivalent to the Fourier power spectrum is the linear combination of the two sets.

As demonstrated by Robitaille, Joncas, and Miville-Deschênes (2014), the wavelet coefficients can be used to reconstruct the signal. The reconstruction formula is

$$f(x) = C_\delta \sum_l \sum_{j=0}^{N_\theta - 1} l \tilde{f}(l, x, \theta_j) + \mu_0, \tag{5.12}$$

where C_δ is a correction factor and μ_0 is the mean value of the original map. Due to linearity of wavelet transforms, images corresponding to each set of wavelet coefficients

(i.e., Gaussian and coherent) can be reconstructed using

$$f^G(x) = \sum_l \sum_{j=0}^{N_\theta - 1} l\tilde{f}^G(l, x, \theta_j) \tag{5.13}$$

and

$$f^C(x) = \sum_l \sum_{j=0}^{N_\theta - 1} l\tilde{f}^C(l, x, \theta_j) \tag{5.14}$$

Application on SiO peak intensity map

In order to separate the SiO emission produced by outflows and star formation activity from the widespread diffuse emission associated with colliding flows (i.e., slow shocks), I applied the `MnGSeg` technique to the SiO peak intensity map obtained with ALMA. In case of the SiO peak intensity map, the scale-dependent intensity fluctuations which are represented by large wavelet coefficients are assumed to be associated with outflows. In contrast, slow shocks generated by cloud-cloud collisions are scale-free and therefore, represented by small wavelet coefficients. Fig. 5.24 represents the result of power spectrum analysis of the peak intensity map of SiO. The wavelet and Fourier power spectrum are calculated using Eqs. 5.7 and 5.8, respectively for every scale denoted by diamond symbols in Fig. 5.24. As shown in the figure, the wavelet power spectrum closely matches the Fourier power spectrum except for small deviations due to the noise level. The consistency between the Fourier and wavelet power spectrum suggests that the Fourier power spectrum is sensitive to the mean variation of intensity as a function of spatial scale. However, the presence of a widespread diffuse emission with a smooth density distribution over all scales does not have a strong impact on the mean value of intensity distribution. This point emphasises on the need for using the wavelet transforms instead of Fourier transformation for decomposing the two types of shocked gas.

The extraction algorithm included in the `MnGSeg` package has been applied to the SiO peak intensity map. The two sets of wavelet coefficients are used to reconstruct the Gaussian and non-Gaussian segments of the map following Eqs. 5.13 and 5.14. The Gaussian and coherent reconstructed images are shown in Fig. 5.27. The reconstruction of the two sets of wavelet coefficients present structures that are significantly different. The Gaussian map shows smooth features dominated by large-scale intensity fluctuations. The coherent map is dominated by elongated structures which have higher intensities. The coherent map together with a large amount of non-Gaussinity seen in the intermittency PDFs suggest that most of the emission in the SiO peak intensity map is due to the presence of energetic outflows and slow shocks have a smaller contribution to the total intensity. Eqs. 5.7 and 5.8 are used to calculate the corresponding power spectra. As shown in Fig. 5.25, the two Gaussian and coherent components possess different power laws. The steeper slope of the Gaussian component suggests that it has less energy at small scales. The Gaussian power spectrum becomes flat for $k8$ arcmin^{-1}, which indicates that the smaller scales k are dominated by noise. However, the coherent component still has emission structures below these scales. No particular break is visible in the coherent power spectrum, which can be interpreted as no spatial scale is preferred for the non-Gaussianity. The two distinct behaviours seem to separate larger scales, >8 arcmin^{-1}, from smaller scales, < 8 arcmin^{-1}. The non-Gaussian features associated with outflows seem to dominate on all lower scales. The Gaussian part of the segmentation associated with slow shocks contributes to the intensity on large scales. Since each type of shock

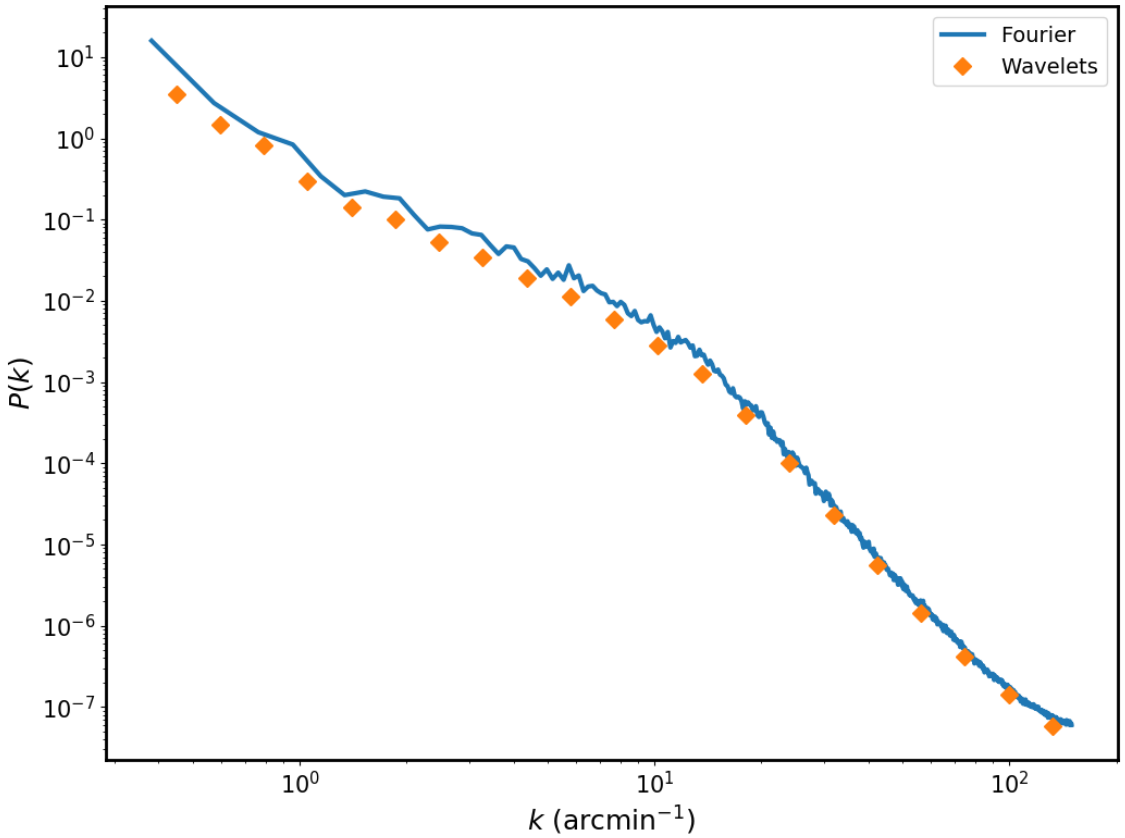

FIGURE 5.24: Fourier (solid lines) and wavelet (diamond symbols) power spectra of the SiO peak intensity map over the region observed with ALMA.

is dominated in a different scale, analysing the power distribution scale by scale gives a more accurate statistical description of intensity distribution throughout the map. For this, I take advantage of the local intermittency coefficient defined by Farge et al. (1990) as

$$I(l,x) = \frac{\mid \tilde{f}(l,x) \mid^2}{\langle \mid \tilde{f}(l,x) \mid^2 \rangle_x}, \tag{5.15}$$

where $\mid \tilde{f}(l,x) \mid^2$ is squared amplitude of wavelet coefficients and $\langle \rangle_x$ denotes the mean calculated over all positions. The intermittency PDFs for the Gaussian and coherent maps over a scale of 0.1 pc are shown in Fig. 5.26. The PDF associated to the Gaussian map shows that the segmentation algorithm successfully removed most of the coherent components compared to the original intermittency measure. After the segmentation, most of the intermittency values are in the range $0 < I(l,x) < 3$, and the distribution is almost symmetric and centred at 1. This suggests that all the regions in the map at this scale contribute equally to the average power spectrum.

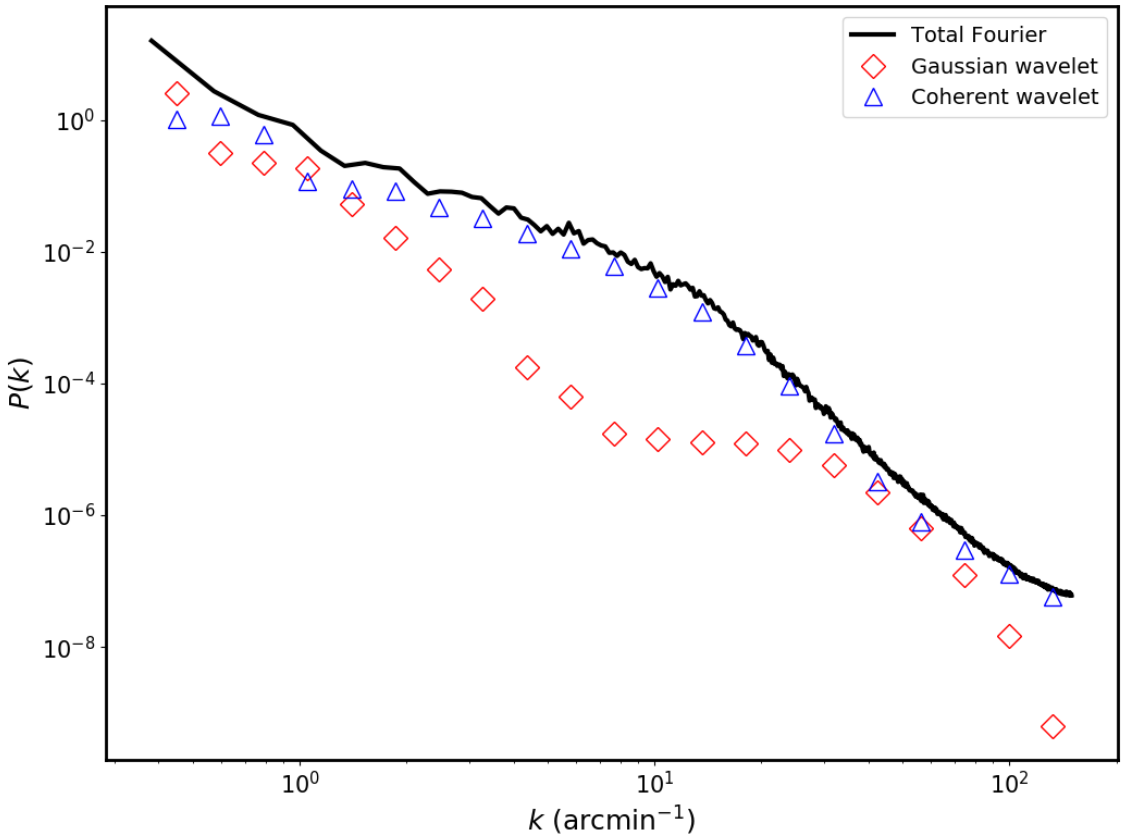

FIGURE 5.25: Decomposed power spectra for the SiO peak intensity map. The total Fourier power spectrum shown in Fig. 5.24 is represented by solid black line. The red diamonds show the power spectrum for the Gaussian part of the map. The blue triangles show the power spectrum for the non-Gaussian coherent part of the map.

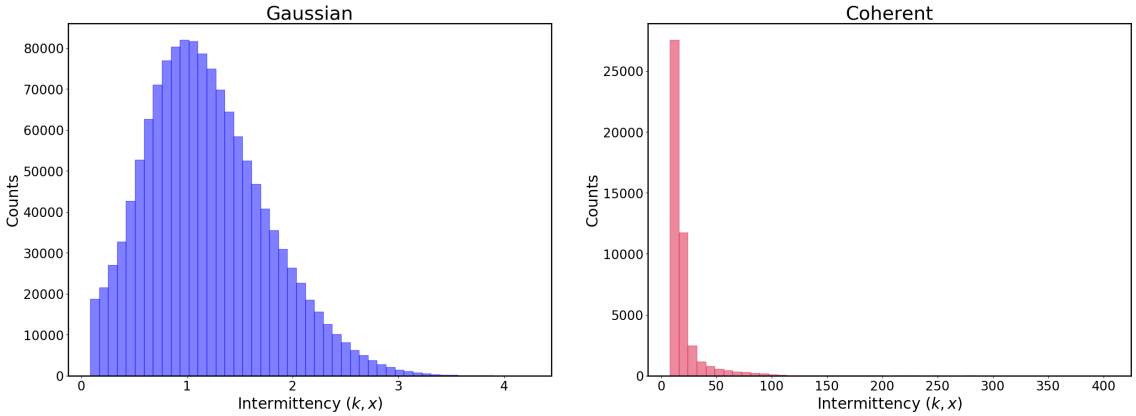

FIGURE 5.26: PDF of the wavelet coefficients for the Gaussian (*left*) and the coherent (*right*) components of the SiO peak intensity map at the scale of 0.1 pc.

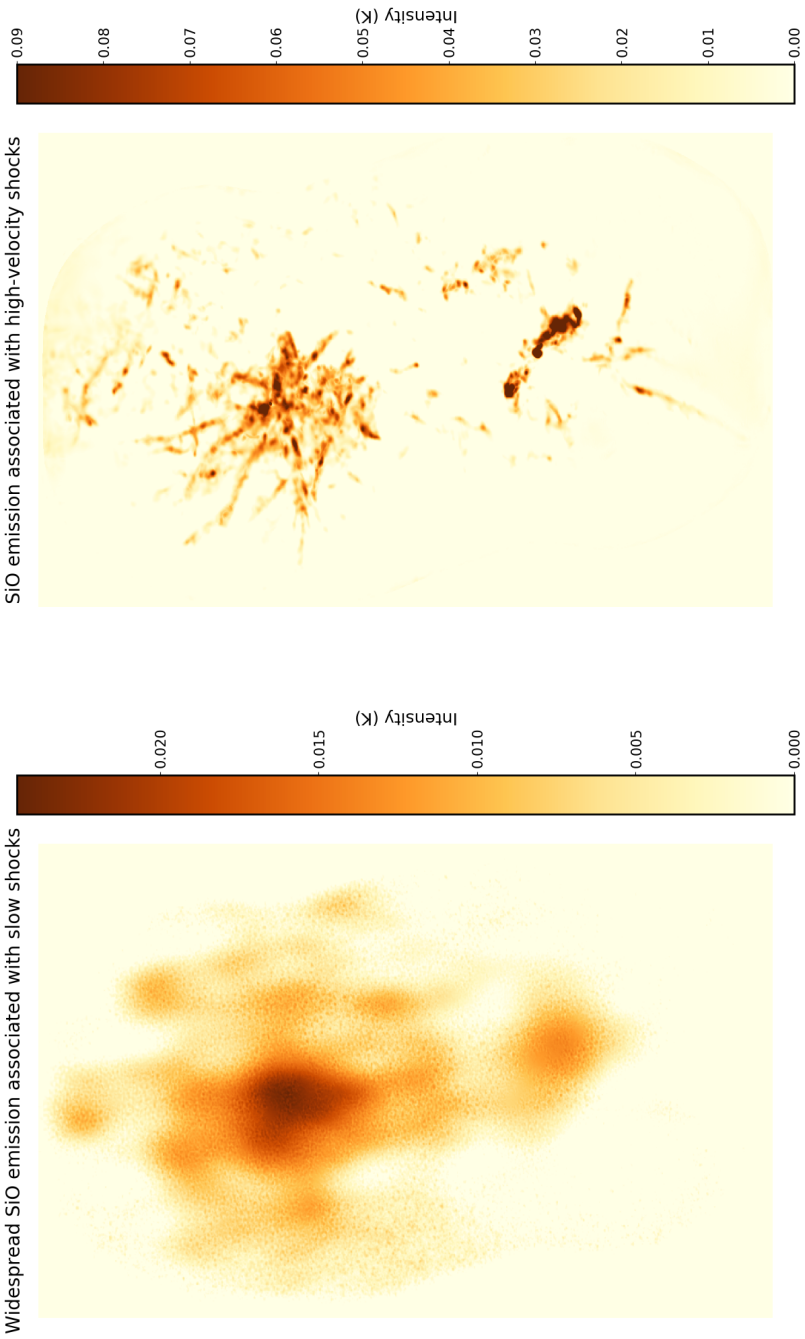

FIGURE 5.27: Gaussian (*left*) and coherent (*right*) reconstructed SiO peak intensity maps following Eqs. 5.13 and 5.14.

5.6 Discussion

I obtained a SiO (2-1) transition map with ALMA towards the massive protoclusters NGC 6334-I and NGC 6334-I(N). In the previous sections, I derived the statistical properties of the SiO emission in terms of line profiles, column density and dynamical parameters. Furthermore, I took advantage of two different methods to decompose the high-velocity shocks from the slow shocks. In this section, I discuss the origin of these two types of shock based on their driving mechanisms.

5.6.1 SiO as a probe of outflow shocks

This study confirms that SiO is a good indicator of outflows in massive star-forming regions. The spectral decomposition analysis (see § 5.5.1) indicates that ∼60% of the pixels of the SiO data cube are fitted with either one single broad Gaussian component or multiple components with at least one component exhibiting a broad profile. Finding of a high detection rate of the broad component in the SiO (2-1) line suggests the presence of high-velocity shocks associated with protostellar activity. Moreover, analysing the dynamical properties of the SiO emission (see § 5.4) suggests that ∼70% of the kinetic energy is associated with high-velocity shocks.

In § 5.3.2, I identified a total of 89 SiO emission structures using a dendrogram analysis. To investigate if the identified structures (see Table B.1) are associated with outflows, I divided the velocity range of the channels which include SiO emission (-60–20 km s^{-1}) into ten bins. The bins which are close to the systemic velocity (-5 km s^{-1}) have a width of 5 km s^{-1}, while the remaining bins have a width of 20 km s^{-1}. In the second step, I applied dendrogram to the peak intensity maps associated with each bin. Doing so makes it possible to trace the identified structures (see Table B.1) in different channels from red-shifted to blue-shifted velocities. The structures which only appear in the velocity bin close to the systemic velocities are likely outflows in the plane of sky or patches of shocked gas associated with low-velocity shocks. Out of the 89 SiO emission structures, ∼70% appear in the blue-shifted velocities ranging from -60 km s^{-1} to -10 km s^{-1} which are likely blue-shifted lobes of an outflow. Among the outflow candidates, 6 features seem to be associated with the compact sources detected in the ALMA 3 mm continuum map. The features which are not associated with ALMA sources are likely to be driven by either faint low-mass objects or more evolved YSOs (i.e., class II and class III objects) which are bright at IR wavelengths. The large population of dense cores found in NGC 6334-I(N) together with the large number of SiO emission features likely tracing outflows, suggest that we are witnessing a micro-burst of star formation with an efficiency of ∼15% in this cluster.

5.6.2 Origin of the narrow SiO emission

According to the results of spectral decomposition (see § 5.5.1), about 30% of the pixels of the SiO data cube are fitted with a single Gaussian component which has a width in the range 1.1–11.9 km s^{-1}. Such narrow emission could have various origins, and in the following I shall explore some of the possibilities.

One hypothesis is that it arises from the mixing of shocked gas and colder ambient gas along the wall of the outflow cavities (Duarte-Cabral et al., 2014). This type of gas can still form SiO, but with lower velocity dispersion (see e.g. Codella and Bachiller, 1999; Lefloch et al., 1998). This hypothesis is an alternative to explain the narrow emission in the central regions of NGC 6334-I and NGC 6334-I(N) (see left panels of Figs. 5.19 and

5.21). Another alternative scenario could be the mixing of the gas due to the interaction of different outflows driven by a population of low-mass cores which remain undetected in the ALMA 3 mm continuum map.

Although outflows are conspicuous because of their high-velocity emission, narrow SiO emission from outflows has been reported in recent studies. Csengeri et al. (2016) found a low-velocity component SiO emission towards a group of infrared-quite objects. Duarte-Cabral et al. (2014) studied several massive dense clumps in Cygnus-X which reveal the existence of narrow emission offset from the systemic velocities. According to the 1D shock models (Anderl et al., 2013; Gusdorf et al., 2008a), if the composition of the pre-shock gas is such that silicon is solely in the grain cores, sputtering by high-velocity shocks will produce SiO emission with narrow line profiles. For the case of emission close to systemic velocities, an alternative hypothesis is sputtering of the grain mantles which contain a small fraction of Si/SiO. These two alternative scenarios can explain the formation of collimated SiO emission structures, in the vicinity of high-velocity shocks towards the outer regions of NGC 6334-I and NGC 6334-I(N) (see Figs. 5.19 and 5.21).

Despite the existence of SiO narrow emission associated with outflows, I also detect some extended SiO emission towards NGC 6334-I and NGC 6334-I(N) using the wavelet decomposition method (see § 5.5.2). Although, the narrow low-velocity emission has a significant overlap/adjacency to outflow regions, its spatial distribution is similar to extended SiO emission observed towards the W43-MM1 ridge (Louvet et al., 2016), CygX-N3 and N48 massive clumps (Duarte-Cabral et al., 2014), and filamentary IRDC G035.39–00.33 (Jiménez-Serra et al., 2010). According to the dynamical scenarios of star formation, protoclusters are formed via slow and inter-mediate scale converging flows. These flows are the results of ongoing infall of material from beyond the protocluster scale (>0.5 pc) to the central regions (<0.1–0.3 pc), which leads to mass accumulation and formation of individual cores. As the NGC 6334-I(N) is less evolved compared to NGC 6334-I, there is a lot of SiO emission in outskirts likely tracing the shock from global collapse. In contrast, narrow SiO emission in NGC 6334-I is more confined and likely traces the post-shock material from the shocks of infalling material towards the densest cores in the central regions.

The question which arises when studying the SiO narrow emission is how low-velocity shocks can form SiO. Using 1D shock models, it is possible to constraint the Silicon chemistry and the physical conditions which lead to formation of SiO as a result of sputtering by low-velocity shocks. Louvet et al. (2016) took advantage of the Paris-Durham 1D shock model (Gusdorf et al., 2008a,b) to compare the theoretical and observational constraints. This model assumes that silicon-bearing material is locked up in the grain cores. However, up to 10% of Silicon is free and can belong either to the gas phase or grain mantles. This is consistent with Nguyen-Lu'o'ng et al. (2013) claiming that low-velocity shocks can form SiO if there is already some Si in the gas phase or in the ice mantles. To run the 1D shock model, Louvet et al. (2016) considered a preshock density of 10^4 cm^{-3}, shock velocity v_s from 4 to 20 km s^{-1} and the external radiation field $G_0 = 0, 1$. The assumed preshock density is in agreement with the H_2 volume density obtained for NGC 6334-I and NGC 6334-I(N) (see Table 3.4). The model runs for two different cases. In one case, the free preshock silicon is in the gas phase (SiG scenario) and in the other, silicon belongs to the grain mantles (SiM scenario).

The integrated intensity of SiO (2-1) transition predicted by the model against the shock velocity is shown in Fig. 5.28. The left panel represents the SiG models, while the right panel represents the SiM models. In order to constraint the physical conditions out of which narrow SiO emission is formed in NGC 6334, I compare the observed integrated

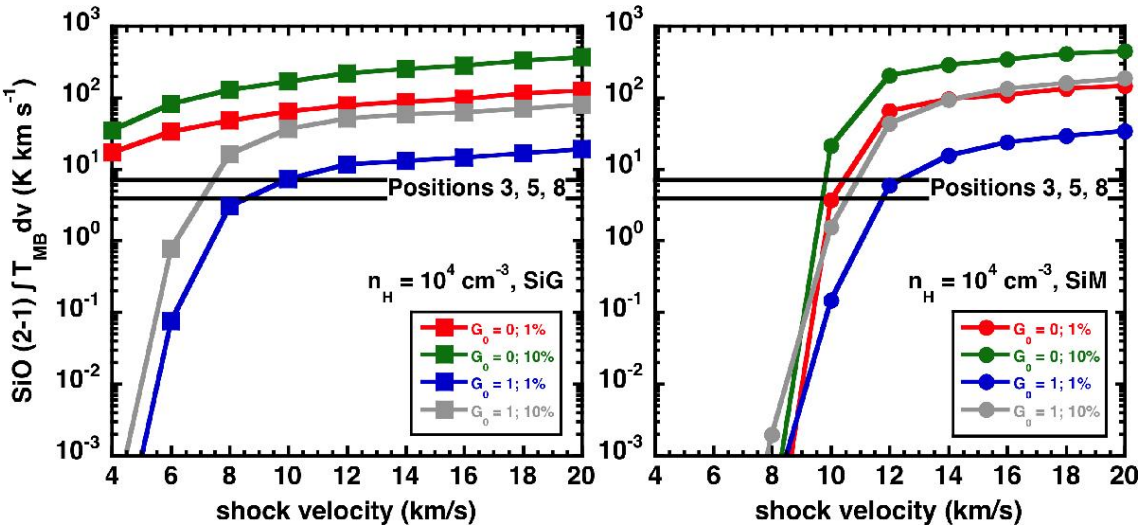

FIGURE 5.28: Integrated intensity of the SiO (2-1) transition against the shock velocity calculate by 1D Paris-Durham shock model (colored symbols), and compared to the observations of W43-MM1 ridge (thick, horizontal black lines). The left and the right panels correspond to the SiG and SiM scenarios (Louvet et al., 2016).

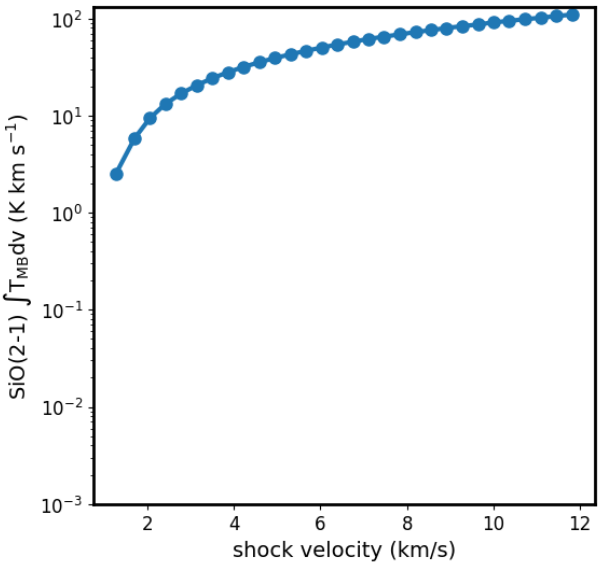

FIGURE 5.29: Integrated intensity of the SiO (2-1) transition against the shock velocity observed with ALMA towards NGC 6334.

SiO (2-1) intensity with the prediction of the model. For a better comparison, I divided the measured intensities and corresponding shock velocities into 30 bins and calculated the mean value of each bin. Fig. 5.29 shows the observed integrated intensity of SiO narrow component towards NGC 6334 against the shock velocity measured for each bin. As shown in the figure, the SiO (2-1) integrated intensity slightly increases with shock velocity. The comparison with the model indicates that the observed trend is more consistent with the SiG scenario with no external radiation field. In this case, the model predicts that

almost all the free silicon is in the form of SiO in the preshock phase. As the shock propagates, the SiO abundance will decrease in the postshock phase due to the adsorption onto grains when the temperature drops. According to the model, the maximum neutral temperature that can be reached with the shock velocity of 12 km s^{-1} is $\sim$600 K. The observed average intensities suggest that the fraction of free silicon in the gas phase is likely close to 10%. In the absence of external radiation fields, the SiO in the preshock phase can be due to shocks from earlier high-velocity outflows. This SiO could then be maintained in the gas phase by slow shocks. Therefore, low-velocity shocks could produce enough SiO to be detected.

Chapter 6

Summary & outlook

6.1 Summary

NGC 6334 is a nearby high-mass star-forming complex that has been the target of multiple studies at different wavelengths. This filamentary cloud contains several massive protoclusters at different stages of evolution which are likely pinpointing sites of high-mass star formation activity (Persi and Tapia, 2008; Russeil et al., 2013). The APEX observations of ^{13}CO molecular emission over the scale of the whole filament ($\sim$60 pc) revealed a large-scale velocity gradient which traces the original rotation of the cloud (Zernickel, 2015). Moreover, the HCO^+ observations towards the central part of the filament (12 pc) together with the radiative transfer modelling indicated a gravitational collapse along the main axis of the filament (Zernickel, Schilke, and Smith, 2013). In order to investigate the kinematics of the dense gas at the scales of the clusters ($<$1 pc), we conducted ALMA observations towards the two high-mass protoclusters NGC 6334-I and NGC 6334-I(N) embedded in the filamentary star-forming complex NGC 6334, as well as the gas connecting them to the large-scale filament. The observations cover the spatial scales from 1800 au to 0.25 pc and are sensitive to the 3 mm continuum emission and different molecular species. The moment maps of the dense gas tracers reveal elongated filamentary structures converging to the positions of the two massive clusters. The paths of the filaments observed in the ALMA maps are consistent with the filaments observed in the 350 μm continuum emission map of APEX. This finding confirms the existence of filamentary networks converging to a central hub and their role as accretion channels which transport material from the large-scale cloud to the clusters and finally to the cluster members. The analysis of the velocity structure of each filament reveals velocity gradients of about 10–32 km s^{-1} pc^{-1}. Based on the velocity gradient and mass obtained for the filaments, I calculate a total mass accretion rates of 4×10^{-3} $M_\odot$ yr^{-1} and 1.5×10^{-3} $M_\odot$ yr^{-1} for NGC 6334-I and NGC 6334-I(N), respectively. The similar mass accretion rate determined for both clusters and their proximity (0.5 pc between both clusters) suggest that they are competing for the mass reservoir contained in the whole filament.

The temperature and column density map of the region is obtained by fitting the K spectral line transitions of the CH_3CCH (6-5). The temperature map exhibits a gradient from the outskirts to the central parts of the region where NGC 6334-I and NGC 6334-I(N) are located. The local temperature minima in the central regions coincide with the density peaks, revealing the role of temperature fluctuations in the fragmentation of protoclusters and the formation of dense cores. Previous high-resolution observations revealed multiple cores with masses of a few $M_\odot$ in the clusters (Brogan et al., 2009, 2016; Hunter et al., 2006, 2014). In my new ALMA continuum map at 3 mm, the previously known sources are clearly appreciated. Additionally, I identified a large population of compact sources (a total of 142) distributed over the surveyed region of 9 arcmin^2. The ALMA compact sources seem to group in different structures. I used seven different machine learning

algorithms and identified four different clusters in the region: NGC 6334-E, NGC 6334-I, NGC 6334-I(N) and NGC 6334-I(NW). Among them, NGC 6334-I(N) is the most populated cluster with 80 cores. The ALMA observations provided me the possibility to study the physical properties of the identified protoclusters such as the CMF, the spatial distribution of cores as well as the mass segregation. I built the CMF of the identified cores towards the whole region as well as for each individual cluster. The CMF obtained for the complete sample of the dense cores is a top-heavy CMF, showing an apparent excess of high-mass cores compared to the canonical IMF. I evaluated the effect of the temperature and unresolved multiplicity on determination of the CMF. This study shows that wrong temperature values (necessary for mass determination) and limited angular resolution observations (unresolved fragments of the clusters) considerably affect the slope of the CMF explaining the difference with respect to the IMF. Therefore, excess of the high-mass cores might be spurious due to systematic uncertainties in the temperature measurements and/or resolution limitations of the observations. Based on the masses and relative positions of the cores inside the clusters, I searched for evidences of mass segregation using three different methods. Clusters NGC 6334-I and NGC 6334-I(N), both harboring massive cores, show clear hints of mass segregation with the most massive cores located towards the central regions of the clusters. The masses and separations of the cores in the clusters NGC 6334-E, NGC 6334-I and NGC 6334-I(N) are consistent with fragmentation of the original dense clump being regulated by turbulent motions. The cluster NGC 6334-I(NW), with no clear signs of massive cores or stars, has median masses of the cores consistent with thermal Jeans fragmentation. This may suggest that the fragmentation of the clusters in the NGC 6334 star forming complex may be dominated by turbulent motions in clusters forming high-mass stars, while it is mainly thermal dominated for low-/intermediate-mass star forming clusters. Combining information at different scales for the NGC 6334 region (from the large-scale filament of few a 10 pc, down to the core scales of few thousand au), I establish a hierarchical fragmentation picture of the region. Fragmentation in NGC 6334 seems to be governed by turbulent pressure at large scales, while the thermal pressure being more relevant at smaller scales.

As the last step of the analysis of the continuum emission, I investigated a possible correlation between the evolutionary stage of the studied clusters and their properties. The association of the identified clusters with HII regions and their content regarding infrared sources provide a simple diagnostic for their evolutionary stage. Based on these criteria, I classify three of the clusters from younger to more evolved: NGC 6334-I(N), NGC 6334-I and NGC 6334-E. I found that the median separation between the cluster members shifts to larger distances as the cluster evolves. This trend is consistent with the theoretical models where gas expulsion and stellar ejections determine the separations of the cluster members. I also found strong hints of mass segregation in NGC 6334-I and NGC 6334-I(N). The presence of filaments in NGC 6334-I(N) indicates that mass segregation in this cluster has a primordial origin, while for NGC 6334-I it is not possible to derive a firm conclusion, and dynamical segregation could have played a role. Finally, we found an excess of massive cores in clusters NGC 6334-I and NGC 6334-I(N), while NGC 6334-E lack high-mass dense cores. This finding likely suggests that in more evolved clusters the gas reservoir is already accreted. In contrast, younger clusters contain a larger amount of gas and dust reservoir in the form of massive dense cores.

The accretion process through the filamentary network and the presence of a large population of star-forming cores in the surveyed area provide a possibility for the formation of slow shock waves due to the accretion of material and high-velocity shocks due to outflows driven by young stellar objects. The SiO(2-1) emission is an ideal tracer of shocked gas and appears widespread with a complex morphology and a broad variety

of line profiles from very broad (35 km/s) blue-shifted lines to very narrow (1-3 km/s) lines peaking at the ambient velocity. In the region of NGC 6334-I, the SiO emission is dominated by a bipolar outflow associated with one of the hot cores in this cluster. The SiO emission towards NGC 6334-I(N) reveals a complex network of collimated structures extending up to a distance of ∼0.2 pc which are pointing in different directions. Both regions are surrounded with faint compact emission structures. In order to disentangle the distinct SiO emission structures in the regions of NGC 6334-I and NGC 6334-I(N), I applied the dendrogram technique to the 2D peak intensity map of SiO. A total of 89 SiO emission structures are found towards the whole surveyed area. The masses of the identified structures range from 0.03 $M_\odot$ to 80 $M_\odot$, their kinetic energy from 10^{43} erg to 10^{48} erg and the momentum from 0.15 $M_\odot$ km s^{-1} to 5300 $M_\odot$ km s^{-1}.

In order to decompose the widespread diffuse SiO emission that is associated with low-velocity shocks from the high-velocity shocks, I took advantage of two different methods. The first method is a decomposition based on the linewidth of the SiO line profile. The spectral information of the SiO data cube is obtained by Gaussian fitting. I adopt a threshold of 12 km s^{-1} for the linewidth to statistically disentangle the low- and high-velocity components. The spectral decomposition analysis indicated that 30% of the energetics of the shocked gas is associated with narrow components likely generated by colliding flows or mass accretion. As for the second method, I used the complex wavelet analysis (Robitaille, Joncas, and Miville-Deschênes, 2014; Robitaille et al., 2019) which isolates the slow shocks based on the PDF of their wavelet coefficients. In this method, the slow shocks are assumed to be widespread scale-free emission with a PDF that resembles a Gaussian function. In contrast, the SiO emission produced by energetic outflows is considered as a scale-dependent emission whose PDF looks pretty non-Gaussian. The complex wavelet analysis indicates that widespread scale-free emission is dominated over scales >0.1 pc, while the high-velocity shocks can be found found at scales of <0.1 pc. To investigate how low-velocity shocks are able to produce SiO, I compared the dependence of the integrated intensity of SiO on the shock velocity with the prediction of the 1D shock models (Gusdorf et al., 2008a). The comparison suggests that with a small fraction of free silicon in the gas phase (close to 10%), SiO could be maintained in the gas phase by slow shocks.

6.2 Outlook

In this work, I presented a comprehensive analysis of the physical properties of the two high-mass star forming protoclusters in the NGC 6334 complex, their connection with the main filament and the properties of the shocked gas in the cluster environment. However, as any scientific study, much progress remains to be made in further characterisation of the accretion process, physics and chemistry of the shocked gas and determination of the properties of embedded clusters. The next subsections point out different paths to be explored in the future.

Correlation between the time evolution and properties of a cluster

Our ALMA observations suggest that the physical properties change as the cluster evolves. However, we require a statistically larger sample of clusters to precisely address this question. One of the possible ways to investigate this topic is to conduct ALMA observations towards a large group of star-forming clumps in the NGC 6334 molecular cloud. By selecting regions with e.g., different masses, infrared properties, presence or lack of

evolved HII regions, we can compile a larger catalogue of clusters in different evolutionary stages, while at the same time ensuring that the dispersion of initial conditions is reduced because all of them formed within the same molecular cloud. Thus, we can investigate the time evolution of the physical properties of cluster-forming regions.

The critical role of magnetic field in the process of accretion

The large-scale APEX observations of ^{13}CO and intermediate-scale ALMA observations of HCN and HCO^+ isotopologues show evidence of mass flows, accretion and infall motions in NGC 6334. As investigated in MHD simulations, the presence of magnetic fields and its orientation with respect to the elongation of the filament affect the accretion process along the filament and its fragmentation into clusters forming stars (see e.g., Seifried and Walch, 2015). The analysis of mass accretion at different scales in NGC 6334 still has a missing ingredient: the magnetic field. Houde et al. (2008) proposed that turbulent eddies and the B-field should decouple from each other at damping scales, which will cause the linewidth of ionic species to be systematically narrower than neutral species. If this is true, the linewidth difference should positively correlate with B-field strength. Therefore, the next step is to take advantage of the observed line profiles of HCN and HCO^+ and their isotopologues to obtain the difference between the linewidth of the neutral and ionic species and consequently estimate the strength of the magnetic field. Complementary to the spectral line observations, we can take advantage of the APEX telescope to obtain a complete picture of the dust polarisation in NGC 6334. Previous observations towards the cluster NGC 6334-I and NGC 6334-I(N) show that the magnetic field seems to be perpendicular to the filament (Dotson et al., 2010; Novak, Dotson, and Li, 2009). As the next step, I plan to study the magnetic field orientation, not only toward the main cluster but along the filament that connects the different sites of star formation. These observations will nicely complement the spectral line observations to determine the magnetic field with two different methods, and to set important constraints to the effects of the magnetic field in the process of collapse and accretion of material along filaments. The result will be then compared to numerical simulations.

Accurate determination of CMF

As previously mentioned, the CMF obtained for the whole sample of compact sources over the observed region with ALMA shows an apparent excess of high-mass cores compared to the Kroupa IMF. I investigated the effect of temperature and resolution on the slope of the high-mass end of the CMF using Monte Carlo simulations. This study shows that the resolution limitations and systematic errors in temperature determination can bias the CMF towards flatter slopes. To overcome these biases and to determine the CMF accurately, high-resolution ALMA observations at 1 mm in continuum and lines are necessary. These observations provide the possibility to achieve the following goals:

- **Detection of the low-mass cores:** Due to the larger dust emissivity at shorter wavelengths, ALMA observations at 1 mm will be more sensitive to dust emission than the previous data. With 1σ mass sensitivity of 0.05 $M_\odot$ (20 times better than the previous observations, enough to detect that clumps produces brown dwarfs), a larger population of low-mass cores could be identified. This sensitivity would be enough to determine a CMF complete to 0.3 $M_\odot$ sufficient to reliably sample, e.g., the peak of the CMF in low-/intermediate-mass star-forming region like Aquila (Könyves et al., 2010, 2015).

- **Temperature determination:** Observations of molecular species such as CH_3CN and H_2CO would permit to derive the gas temperature for the cores where the lines are detected. CH_3CN is known to be an excellent probe of the gas temperature for the warm dense environments, thanks to the K-ladder structure of each rotational energy level, similar to the CH_3CCH K-ladder structure. By fitting the multiple transitions, we will derive the temperature for different cores. Similarly, different transitions of H_2CO will be used to estimate the temperature of the less dense cores with no detectable CH_3CN emission. A more accurate temperature measurement would allow to better estimate of the mass of the cores and consequently construct a more reliable CMF for each individual cluster.

- **Searching for multiplicity in the cores:** Combining information at different scales for the NGC 6334 region (from the large-scale filament of a few 10 pc, down to cores of few thousand au), I established a hierarchical picture of fragmentation. The smallest level of hierarchy which remains unresolved in our ALMA data is the further fragmentation of dense cores at a scales of a few hundred au. Higher angular resolution ($0.200''$ vs. $1.4''$) would allow to investigate the fragmentation process down to the scales of 250 au. High-resolution observations with ALMA provides the possibility to study the multiplicity level in the cores not only in the central parts of the clusters, but also in the outer regions. With this high resolution I could overcome the bias in determining the slope of the CMF, more accurately characterise the distribution of the cores in the clusters and constraint the mechanism that are responsible for the fragmentation at different scales (i.e., turbulent or thermal).

Investigating the origin of the complex SiO emission

The intensity map of the SiO (2-1) molecular emission towards NGC 6334-I and NGC 6334-I(N) exhibits a complex morphology with the overlapping of a large number of collimated structures. The actual catalog of SiO emission structures is obtained by applying the dendrogram technique to the SiO peak intensity map. The next step for an accurate automatic identification is to combine the intensity and spectral information and apply identification techniques to the 3D data cube.

Separation of widespread slow shocks from compact outflows is done using the two methods of wavelet analysis and spectral decomposition. While the first method takes advantage of the intensity variations, the second method is based on the widths of the SiO line profiles. In order to efficiently and accurately decompose different types of shocked gas, combining the spectral and spatial information is crucial. The current determination of the wavelet coefficients is based on the distribution of intensity over different scales. To further improve the wavelet analysis method, one possible alternative is to apply this method to each individual channel of a the SiO data cube and involve the information of intensity variations over a frequency range. Doing so, we will be able to fully characterise the observed emission and accurately decompose different types of emission based on their driving mechanisms. Moreover, observations of SiO (5-4) line enables us to study the differences in the excitation as a function of velocity, using non-LTE codes like `RADEX` (van der Tak et al., 2010). This will provide us with a first order estimate of the physical conditions at work in each cluster. The more sophisticated Paris-Durham shock model will better constrain these physical conditions, as well as the silicon chemistry and pre-shock distribution.

Local and global kinematics

^{13}CO APEX observations towards the NGC 6334 filament revealed a large-scale velocity gradient interpreted as the imprint of the original rotation of the molecular cloud. Moreover, velocity gradient towards the central 12-pc filament traces infall motions of diffuse gas towards the dense filament. On the other side, high-resolution ALMA observations over the scales of the clusters, revealed the presence of accretion channels connecting the two high-mass clusters NGC 6334-I and NGC 6334-I(N) to the main filament. In order to connect the large scales ($\sim$12 pc) to the scales of clusters ($\sim$0.5 pc), we need to take advantage of the ALMA ACA+TP observations to map the central part of the filament with a resolution of $\sim$0.1 pc. Covering different tracers of high-density gas (e.g., N_2H^+ and HC_3N) allows us to study the velocity field of the dense material leading to the formation of the individual clusters. Simultaneously, with ACA observations it is possible to investigate the relative motions within and between clusters using HNC as tracer of the low density material. Connecting the large and intermediate scales with proper resolution helps us to build a complete picture of the mass assembly process in the NGC 6334 region as a whole.

Accretion over the scales of a single core

In a simplified picture of accretion into a protocluster, it is assumed that the accretion is spherically symmetric. However, if the infalling matter has angular momentum, the accretion can be neither spherical nor direct. Instead, the infalling material first accumulates in a flattend, rotating structure (namely a disk) and only later spirals to the stellar surface. The disk-mediated accretion in nearby low- to intermediate-mass protostars have been studied to great extent and detail (see e.g., Dutrey, 2007; Mathieu et al., 2000; Simon, Dutrey, and Guilloteau, 2000). However, the question is whether B- and O-type stars also have circumstellar disks like those around the low-mass stars. In recent years, different theoretical studies have proposed the paradigm of disk-mediated accretion for stars of all masses (Krumholz, Klein, and McKee, 2007; Kuiper, Yorke, and Turner, 2015; Kuiper et al., 2010; Peters et al., 2011). As an attempt to search for circumstellar disks around high-mass stars, I investigated the velocity fields of disk tracers (e.g., CH_3CN, CH_3OCHO) towards hot cores in G29.960.02 as a high-mass star forming region (see Cesaroni et al., 2017, for a description of the project ad the ALMA observations). The dense gas traced by different complex molecules shows a velocity gradient corresponding to blue/red-shifted velocity features associated with the outflow. The existence of an outflow is an indirect evidence of the presence of a disk. However, the limited angular resolution prevents us from resolving the disk perpendicular to the current direction of the outflow. To characterise the disk around O-type protostars, we need to reach a spatial resolution of $\sim$100 au. Investigating the kinematics of disk tracers over this scale enables us to search for signatures of rotation as a clue to the presence of a disk.

Appendix A

Catalog of continuum sources in NGC 6334

TABLE A.1: Observed properties of the ALMA continuum sources in NGC 6334

	ALMA 87.6 GHz compact sources [a]				
#	R.A.	Dec.	$I_\circ$	$S_\circ$	θ_S, P.A.
(1)	(2)	(3)	(4)	(5)	(6)
1	17:20:46.680	−35:46:16.32	1.27	1.52 ± 0.25	1.70×1.42, 70
2	17:20:46.776	−35:46:17.76	1.64	2.71 ± 0.43	2.22×1.68, 25
3	17:20:47.184	−35:46:27.48	1.03	0.70 ± 0.11	1.70×1.20, 54
4	17:20:48.192	−35:45:44.28	0.70	0.92 ± 0.16	1.50×1.38, 309
5	17:20:48.288	−35:45:37.08	1.30	1.36 ± 0.22	1.50×1.38, 346
6	17:20:48.620	−35:48:26.69	0.54	0.37 ± 0.07	0.66×0.42, 25
7	17:20:48.720	−35:44:33.00	0.74	1.12 ± 0.18	1.94×1.26, 53
8	17:20:49.152	−35:44:59.64	1.48	3.78 ± 0.60	3.14×1.86, 2
9	17:20:49.296	−35:44:31.56	1.01	1.59 ± 0.26	2.00×1.46, 306
10	17:20:50.256	−35:44:19.68	0.51	0.34 ± 0.06	1.02×0.92, 343
11	17:20:50.520	−35:44:38.04	0.60	0.42 ± 0.07	1.26×0.88, 291
12	17:20:50.736	−35:45:07.56	0.59	3.38 ± 0.55	4.52×2.88, 312
13	17:20:50.784	−35:46:21.00	5.88	44.77 ± 6.79	8.04×5.90, 324
14	17:20:50.808	−35:46:28.92	2.13	6.51 ± 1.01	2.74×2.56, 31
15	17:20:50.904	−35:46:05.16	3.76	6.39 ± 0.99	2.64×1.84, 46
16	17:20:50.976	−35:44:14.64	4.80	6.10 ± 0.94	1.88×1.76, 301
17	17:20:51.000	−35:45:05.04	2.68	5.32 ± 0.83	3.12×1.82, 4
18	17:20:51.048	−35:47:25.80	1.55	1.97 ± 0.32	1.68×1.58, 69
19	17:20:51.072	−35:44:30.12	1.87	3.56 ± 0.56	2.30×1.92, 81
20	17:20:51.096	−35:44:22.20	0.50	0.29 ± 0.05	1.02×0.80, 345
21	17:20:51.120	−35:46:30.36	1.31	2.19 ± 0.35	3.14×1.22, 6
22	17:20:51.288	−35:45:07.56	1.89	5.05 ± 0.80	4.44×1.76, 2
23	17:20:51.672	−35:44:17.52	0.39	1.73 ± 0.29	4.48×1.54, 354
24	17:20:51.840	−35:46:12.36	1.57	3.63 ± 0.57	2.48×1.86, 73
25	17:20:51.888	−35:44:22.56	0.73	1.87 ± 0.30	2.38×1.52, 89
26	17:20:51.936	−35:44:19.32	1.09	4.27 ± 0.67	5.00×1.96, 69
27	17:20:52.032	−35:44:12.12	1.13	1.49 ± 0.24	1.82×1.34, 2
28	17:20:52.320	−35:44:21.12	3.40	3.65 ± 0.57	1.66×1.54, 2
29	17:20:52.512	−35:44:10.68	0.67	0.46 ± 0.08	1.22×0.82, 6
30	17:20:52.752	−35:43:58.44	1.02	0.99 ± 0.17	1.34×1.28, 52

TABLE A.1: Continued.

	ALMA 87.6 GHz compact sources [a]				
#	R.A.	Dec.	$I_\circ$	$S_\circ$	θ_S, P.A.
(1)	(2)	(3)	(4)	(5)	(6)
31	17:20:52.752	−35:47:04.92	0.76	2.85 ± 0.46	2.48×1.94, 350
32	17:20:52.752	−35:47:07.80	0.68	5.32 ± 0.84	3.66×2.70, 52
33	17:20:52.800	−35:43:51.24	1.15	1.15 ± 0.19	1.44×1.28, 14
34	17:20:52.848	−35:47:06.72	0.86	1.60 ± 0.26	1.98×1.58, 317
35	17:20:52.848	−35:47:04.56	0.99	1.86 ± 0.30	1.98×1.36, 59
36	17:20:52.992	−35:44:06.72	0.53	0.13 ± 0.03	0.60×0.56, 90
37	17:20:53.040	−35:44:23.64	2.31	4.19 ± 0.66	2.54×1.98, 358
38	17:20:53.088	−35:47:03.12	30.74	56.31 ± 8.50	3.24×3.06, 34
39	17:20:53.136	−35:44:24.00	1.41	1.55 ± 0.25	1.98×1.30, 11
40	17:20:53.160	−35:47:13.56	1.68	4.94 ± 0.77	3.14×2.3, 64
41	17:20:53.160	−35:47:29.04	1.61	1.99 ± 0.32	1.64×1.52, 388
42	17:20:53.160	−35:43:51.96	0.46	0.44 ± 0.08	1.28×1.14, 314
43	17:20:53.184	−35:46:59.16	21.42	102.6 ± 15.5	6.00×4.10, 276
44	17:20:53.424	−35:46:57.72	144.17	384.3 ± 57.7	3.72×2.48, 70
45	17:20:53.472	−35:45:08.64	0.93	1.49 ± 0.24	2.48×2.06, 355
46	17:20:53.500	−35:47:02.01	340.20	2073 ± 311	3.86×2.70, 31
47	17:20:53.616	−35:46:54.84	2.86	4.95 ± 0.77	2.84×1.76, 321
48	17:20:53.664	−35:45:38.16	0.65	0.85 ± 0.15	1.76×1.12, 2
49	17:20:53.784	−35:44:46.32	4.65	9.33 ± 1.44	2.90×2.28, 299
50	17:20:53.880	−35:46:59.16	2.89	5.10 ± 0.80	2.62×1.86, 307
51	17:20:53.904	−35:44:48.12	1.00	1.63 ± 0.26	1.90×1.52, 14
52	17:20:53.976	−35:45:47.52	2.78	3.55 ± 0.55	1.90×1.68, 29
53	17:20:54.048	−35:45:51.48	0.54	0.58 ± 0.11	1.98×0.94, 340
54	17:20:54.144	−35:44:38.76	2.11	4.18 ± 0.66	2.70×1.86, 53
55	17:20:54.168	−35:45:41.40	12.11	26.10 ± 3.98	4.86×2.56, 26
56	17:20:54.288	−35:45:09.36	0.79	3.78 ± 0.60	6.00×2.04, 52
57	17:20:54.360	−35:45:36.36	0.46	2.25 ± 0.37	3.72×2.00, 333
58	17:20:54.360	−35:47:09.96	2.20	2.69 ± 0.42	3.24×1.18, 12
59	17:20:54.384	−35:45:06.12	1.35	3.39 ± 0.54	2.50×2.04, 325
60	17:20:54.456	−35:45:20.88	1.30	0.39 ± 0.07	0.94×0.44, 321
61	17:20:54.480	−35:47:09.96	2.69	10.06 ± 1.55	4.88×2.36, 350
62	17:20:54.480	−35:45:42.48	0.82	4.42 ± 0.70	6.52×2.28, 319
63	17:20:54.552	−35:45:29.52	3.32	12.09 ± 1.86	3.34×2.46, 319
64	17:20:54.576	−35:45:18.00	20.23	53.91 ± 8.15	5.86×2.62, 300
65	17:20:54.576	−35:47:03.12	1.13	2.71 ± 0.43	2.82×1.72, 51
66	17:20:54.600	−35:45:35.64	0.57	0.87 ± 0.15	1.64×1.26, 346
67	17:20:54.648	−35:45:08.64	5.68	32.37 ± 4.92	6.48×4.10, 283
68	17:20:54.648	−35:45:51.48	1.28	0.95 ± 0.15	1.40×1.02, 355
69	17:20:54.648	−35:47:03.12	1.17	2.05 ± 0.33	2.36×1.32, 47
70	17:20:54.696	−35:45:26.28	1.04	4.43 ± 0.69	4.08×1.96, 297
71	17:20:54.720	−35:45:25.20	0.82	0.47 ± 0.08	1.52×0.62, 320
72	17:20:54.744	−35:45:20.16	3.70	20.23 ± 3.09	5.44×3.86, 328
73	17:20:54.792	−35:44:29.40	2.38	3.00 ± 0.47	1.82×1.60, 341
74	17:20:54.816	−35:46:51.24	1.00	2.80 ± 0.45	2.68×1.76, 331
75	17:20:54.840	−35:45:33.48	4.60	6.35 ± 0.98	2.08×1.98, 31

TABLE A.1: Continued.

	ALMA 87.6 GHz compact sources [a]				
#	R.A.	Dec.	$I_\circ$	$S_\circ$	θ_S, P.A.
(1)	(2)	(3)	(4)	(5)	(6)
76	17:20:54.888	−35:45:11.16	1.18	5.95 ± 0.93	3.18×2.66, 44
77	17:20:54.888	−35:45:01.80	1.53	3.12 ± 0.49	2.48×1.62, 46
78	17:20:54.888	−35:45:06.48	9.80	19.15 ± 2.90	2.60×2.18, 28
79	17:20:54.912	−35:45:16.56	7.34	18.01 ± 2.74	3.46×2.86, 87
80	17:20:54.912	−35:43:43.32	0.58	0.14 ± 0.03	0.74×0.42, 45
81	17:20:54.912	−35:45:03.24	1.55	1.26 ± 0.20	1.38×0.88, 270
82	17:20:54.960	−35:45:46.80	0.97	1.34 ± 0.22	2.16×1.22, 306
83	17:20:54.960	−35:47:11.04	0.84	1.89 ± 0.30	2.06×1.72, 25
84	17:20:54.984	−35:45:07.20	9.31	26.46 ± 4.01	7.34×3.84, 89
85	17:20:54.984	−35:44:57.84	1.61	8.35 ± 1.29	3.74×3.14, 24
86	17:20:55.056	−35:45:37.44	1.15	6.49 ± 1.02	5.76×2.92, 347
87	17:20:55.056	−35:45:01.44	8.47	30.40 ± 4.61	4.94×3.88, 29
88	17:20:55.080	−35:45:41.40	1.37	3.05 ± 0.49	3.2×1.82, 66
89	17:20:55.104	−35:45:16.20	2.20	9.29 ± 1.43	3.68×2.70, 87
90	17:20:55.104	−35:45:37.08	1.14	4.19 ± 0.66	3.74×2.18, 335
91	17:20:55.128	−35:45:05.76	13.80	24.31 ± 3.68	2.72×2.04, 293
92	17:20:55.152	−35:47:15.72	0.61	1.13 ± 0.19	1.94×1.46, 298
93	17:20:55.176	−35:44:25.80	0.97	4.64 ± 0.74	3.70×2.68, 330
94	17:20:55.200	−35:44:30.12	1.73	3.79 ± 0.60	2.34×2.18, 311
95	17:20:55.224	−35:45:03.60	33.16	144.2 ± 21.7	10.44×5.00, 305
96	17:20:55.296	−35:45:00.36	1.19	2.75 ± 0.43	2.20×1.80, 6
97	17:20:55.296	−35:46:50.52	0.70	2.91 ± 0.48	3.88×2.46, 70
98	17:20:55.320	−35:45:14.76	1.29	6.42 ± 1.00	3.46×2.74, 283
99	17:20:55.344	−35:44:31.20	1.15	2.45 ± 0.39	2.34×1.84, 30
100	17:20:55.368	−35:46:09.12	1.06	9.06 ± 1.41	5.16×3.10, 351
101	17:20:55.392	−35:46:13.08	1.01	2.51 ± 0.41	1.98×1.78, 320
102	17:20:55.392	−35:44:59.64	0.92	0.34 ± 0.06	0.96×0.56, 351
103	17:20:55.464	−35:45:32.04	2.85	7.00 ± 1.09	3.38×2.26, 310
104	17:20:55.488	−35:45:11.16	6.59	11.59 ± 1.78	4.62×1.84, 321
105	17:20:55.536	−35:45:24.48	0.53	1.69 ± 0.28	2.74×1.92, 332
106	17:20:55.536	−35:45:26.64	1.29	0.79 ± 0.13	1.26×0.86, 35
107	17:20:55.584	−35:44:56.40	3.63	40.86 ± 6.22	13.04×8.40, 334
108	17:20:55.608	−35:45:20.88	0.51	0.50 ± 0.08	1.42×0.82, 270
109	17:20:55.608	−35:45:27.00	1.47	11.45 ± 1.77	4.82×3.76, 50
110	17:20:55.680	−35:45:32.40	3.77	15.89 ± 2.43	4.86×3.08, 320
111	17:20:55.680	−35:45:51.12	0.83	1.56 ± 0.25	2.00×1.46, 64
112	17:20:55.680	−35:45:08.64	1.07	1.47 ± 0.24	1.72×1.34, 349
113	17:20:55.704	−35:45:23.76	0.67	0.66 ± 0.11	1.38×1.02, 78
114	17:20:55.800	−35:44:43.08	0.86	1.29 ± 0.21	1.84×1.36, 359
115	17:20:55.848	−35:45:27.00	2.94	5.11 ± 0.80	3.06×1.86, 284
116	17:20:55.848	−35:45:24.84	1.58	4.27 ± 0.67	3.08×2.20, 354
117	17:20:55.968	−35:45:23.40	1.50	2.57 ± 0.41	1.84×1.72, 87
118	17:20:55.992	−35:45:35.64	1.62	8.75 ± 1.35	3.32×3.04, 77
119	17:20:56.064	−35:45:32.76	3.57	6.97 ± 1.08	3.32×2.08, 88
120	17:20:56.088	−35:45:21.60	1.37	4.07 ± 0.64	3.60×2.32, 49

TABLE A.1: Continued.

	ALMA 87.6 GHz compact sources [a]				
#	R.A.	Dec.	$I_\circ$	$S_\circ$	θ_S, P.A.
(1)	(2)	(3)	(4)	(5)	(6)
121	17:20:56.088	−35:45:23.04	1.50	2.76 ± 0.43	2.32×1.64, 43
122	17:20:56.184	−35:45:19.80	0.94	2.50 ± 0.40	2.36×1.64, 307
123	17:20:56.304	−35:45:27.36	6.64	9.67 ± 1.48	2.98×1.72, 53
124	17:20:56.328	−35:45:30.96	1.29	3.83 ± 0.60	3.02×2.18, 307
125	17:20:56.328	−35:45:21.96	1.51	13.60 ± 2.09	5.92×4.04, 275
126	17:20:56.376	−35:45:28.80	0.94	0.76 ± 0.12	1.36×0.84, 87
127	17:20:56.400	−35:45:19.80	0.57	2.55 ± 0.41	4.06×1.92, 25
128	17:20:56.496	−35:45:37.08	1.51	1.38 ± 0.23	1.34×1.26, 344
129	17:20:56.544	−35:45:33.48	0.73	1.71 ± 0.28	2.16×1.60, 21
130	17:20:56.568	−35:45:26.64	0.59	1.20 ± 0.20	1.86×1.44, 28
131	17:20:56.568	−35:45:17.28	3.29	6.50 ± 1.00	2.68×2.02, 289
132	17:20:56.616	−35:45:10.08	3.33	5.18 ± 0.81	2.30×1.72, 306
133	17:20:56.640	−35:45:18.72	1.97	3.91 ± 0.62	2.40×1.86, 319
134	17:20:56.736	−35:45:23.40	0.63	1.42 ± 0.23	2.32×1.30, 287
135	17:20:56.736	−35:45:17.64	1.74	5.30 ± 0.82	3.02×2.16, 73
136	17:20:56.952	−35:45:18.00	1.76	3.09 ± 0.48	2.30×1.62, 355
137	17:20:56.976	−35:45:16.20	2.47	6.11 ± 0.95	3.38×2.04, 340
138	17:20:57.264	−35:45:17.28	0.59	0.53 ± 0.09	1.36×0.84, 325
139	17:20:57.336	−35:45:14.40	3.30	7.86 ± 1.22	3.54×2.22, 346
140	17:20:57.672	−35:45:12.24	1.96	4.22 ± 0.66	2.76×1.86, 308
141	17:20:58.656	−35:44:59.64	0.43	0.27 ± 0.05	1.14×0.86, 336
142	17:20:59.760	−35:45:30.96	0.85	0.56 ± 0.09	1.14×0.96, 347

[a] Observed parameters of the ALMA compact sources identified as explained in § 3.1.1. In each column we have: R.A. (right ascension, column 2) in $^{\rm h}$:$^{\rm m}$:$^{\rm s}$; Dec. (declination, column 3) in $^\circ$:′:″; I_ν (peak intensity at 87.6 GHz, column 4) in mJy beam^{-1}; S_ν (flux density, column 5) in mJy; $\theta_{\rm s}$ (observed sizes of the major and minor axis obtained from the `SExtractor`) and P.A. (position angle, column 6) in arcsec^2 and degrees.

TABLE A.2: Measured properties of the ALMA continuum sources in NGC 6334

	Counterparts [a]			Physical properties [b]					Membership [c]		
#	free-free	IR		T	M_{g+d}	n_{H_2}	N_{H_2}		Cluster	%	Others [d]
(1)	(2)	(3)		(4)	(5)	(6)	(7)		(8)	(9)	(10)
1	–	f*		50	0.82	2.34	1.78		E	86	
2	–		20	3.90	5.74	5.43		E	86		
3	–	–		20	1.01	7.78	4.24		E	86	
4	–	f*		50	0.50	1.81	1.27		E	86	
5	4–100	YSO I		50	0.73	2.63	1.85		E	86	
6	–	f*		50	0.2	1.84	0.95		–	–	
7	–	–		20	1.61	4.35	3.36		I(NW)	86	
8	–	–		20	5.44	4.11	4.86		I(NW)	86	
9	–	–		20	2.29	4.83	4.05		I(NW)	86	
10	–	–		20	0.49	5.63	2.68		I(NW)	86	
11	–	–		20	0.60	5.39	2.79		I(NW)	86	
12	–	–		20	4.86	1.11	1.96		I(NW)	86	
13	–	f*		50	24.14	0.80	2.67		E	86	
14	–	f*		50	3.51	2.05	2.64		E	86	
15	9–100	f*		50	3.45	3.46	3.72		E	86	
16	–	–		20	8.77	15.66	13.88		I(NW)	86	
17	–	–		20	7.65	5.98	6.98		I(NW)	86	
18	–	–		20	2.83	7.17	5.66		I	86	
19	–	–		20	5.12	6.01	6.13		I(NW)	86	
20	–	–		20	0.42	5.95	2.64		I(NW)	86	
21	–	–		20	3.15	4.67	4.41		E	86	
22	–	–		20	7.26	3.57	4.87		I(NW)	86	
23	–	–		20	2.49	1.51	1.92		I(NW)	86	
24	–	–		20	5.22	5.57	5.86		E	86	
25	–	–		20	2.69	4.15	3.86		I(NW)	86	
26	–	–		20	6.14	2.18	3.31		I(NW)	86	
27	–	–		20	2.14	5.81	4.48		I(NW)	86	
28	–	–		20	5.25	14.33	11.03		I(NW)	86	
29	–	–		20	0.66	7.18	3.48		I(NW)	86	
30	–	–		20	1.42	6.64	4.27		I(NW)	86	
31	–	–		20	4.10	3.46	3.94		I	100	
32	–	–		20	7.65	2.64	4.05		I	100	
33	–	–		20	1.65	7.08	4.69		I(NW)	86	
34	–	–		20	2.30	4.32	3.76		I	100	
35	–	–		20	2.68	6.62	5.27		I	100	
36	–	–		20	0.19	10.48	2.96		I(NW)	86	
37	–	–		20	6.03	5.76	6.29		I(NW)	86	
38	–	–		20	80.99	28.15	43.07		I	100	MM4
39	–	–		20	2.23	5.85	4.56		I(NW)	86	
40	–	f*		50	2.66	1.48	1.93		I	100	
41	–	–		20	2.86	7.81	6.01		I	100	
42	–	–		20	0.63	3.74	2.22		I(NW)	86	
43	–	–		100	27.07	2.37	5.74		I	100	MM2

TABLE A.2: Continued.

	Counterparts [a]		Physical properties [b]				Membership [c]		
#	free-free	IR	T	M_{g+d}	n_{H_2}	N_{H_2}	Cluster	%	Others [d]
(1)	(2)	(3)	(4)	(5)	(6)	(7)	(8)	(9)	(10)
44	0–35	–	100	101.40	38.88	57.57	I	100	MM1
45	–	–	20	2.14	5.29	4.21	I(N)	100	
46	100	f*	–	–	–	–	I	100	MM3
47	–	–	20	7.12	6.85	7.46	I	100	MM7
48	–	YSO II	50	0.46	1.79	1.22	I(N)	100	
49	–	–	20	13.42	8.39	10.56	I(NW)	71	SMA8
50	–	f*	50	2.75	2.73	2.95	I	100	
51	–	–	20	2.34	5.20	4.29	I(NW)	71	
52	–	YSO I	50	1.91	3.54	3.10	I(N)	100	
53	–	–	20	0.83	3.46	2.31	I(N)	100	
54	–	–	20	6.01	5.90	6.38	I(N)	71	
55	–	–	20	37.54	9.13	15.74	I(N)	100	SMA9
56	–	–	20	5.44	1.36	2.33	I(N)	100	
57	–	–	20	3.24	1.72	2.28	I(N)	100	
58	–	f*	50	1.45	2.14	2.02	I	100	SMA10
59	–	–	20	4.88	4.50	4.97	I(N)	100	
60	–	–	20	0.56	21.92	6.94	I(N)	100	
61	–	–	20	14.47	3.98	6.58	I	100	
62	–	–	20	6.36	1.19	2.24	I(N)	86	
63	–	–	20	17.39	3.90	6.90	I(N)	100	
64	–	–	95	14.99	2.63	5.06	I(N)	100	SMA6
65	–	f*	50	1.46	1.45	1.57	I	100	
66	–	–	20	1.25	4.42	3.12	I(N)	100	
67	1–100	–	208	4.06	0.32	0.80	I(N)	100	SMA4
68	–	–	20	1.37	8.38	4.93	I(N)	100	
69	–	f*	50	1.11	2.17	1.87	I	100	
70	–	–	20	6.37	3.03	4.17	I(N)	100	
71	–	–	20	0.68	8.39	3.91	I(N)	100	
72	–	–	20	29.10	3.27	7.30	I(N)	100	SMA11
73	–	–	20	4.31	9.17	7.67	I(NW)	71	
74	–	f*	50	1.51	1.58	1.68	I	100	
75	–	f*	50	3.42	4.46	4.39	I(N)	100	SMA12
76	–	–	20	8.56	3.82	5.37	I(N)	100	
77	–	–	20	4.49	5.88	5.78	I(N)	100	
78	–	–	20	27.54	22.23	25.69	I(N)	100	SMA2
79	–	–	20	25.90	8.92	13.69	I(N)	100	SMA13
80	–	f*	50	0.08	4.82	1.32	I(NW)	86	
81	–	–	20	1.81	14.22	7.70	I(N)	100	
82	–	–	20	1.93	4.73	3.77	I(N)	100	
83	–	–	20	2.72	4.32	3.98	I	100	
84	–	–	20	38.06	2.72	7.05	I(N)	100	SMA3
85	–	–	20	12.01	3.15	5.29	I(N)	100	
86	–	–	20	9.33	1.45	2.91	I(N)	100	
87	–	–	20	43.72	5.56	11.90	I(N)	100	SMA5
88	–	–	20	4.39	3.48	4.04	I(N)	100	

TABLE A.2: Continued.

	Counterparts [a]		Physical properties [b]				Membership [c]		
#	free-free	IR	T	$M_{\rm g+d}$	$n_{\rm H_2}$	$N_{\rm H_2}$	Cluster	%	Others [d]
(1)	(2)	(3)	(4)	(5)	(6)	(7)	(8)	(9)	(10)
89	–	–	20	13.36	4.53	6.99	I(N)	100	
90	–	–	20	6.03	2.77	3.86	I(N)	100	
91	–	–	20	34.97	28.75	33.01	I(N)	100	SMA1a
92	–	–	20	6.67	2.28	3.50	I(NW)	71	
94	–	f*	50	2.04	1.9	2.1	I(NW)	71	
95	0–52	–	143	26.44	0.76	2.67	I(N)	100	SMA1b/d
96	–	–	20	3.96	5.40	5.24	I(N)	100	
97	–	–	20	4.19	1.51	2.28	I	100	
98	–	–	20	9.23	3.39	5.09	I(N)	100	
99	–	–	20	3.52	4.18	4.25	I(NW)	71	
100	–	–	20	13.03	2.17	4.24	I(N)	100	
101	–	f*	50	1.35	2.12	1.96	I(N)	100	
102	–	–	20	0.49	13.36	4.77	I(N)	100	
103	–	–	20	10.07	5.24	7.01	I(N)	86	
104	–	–	20	16.67	7.27	10.32	I(N)	100	
105	–	–	72	0.62	0.56	0.62	I(N)	86	SMA15
106	–	–	20	1.14	10.75	5.47	I(N)	86	
107	–	–	20	58.77	0.55	2.82	I(N)	100	SMA17
108	–	–	20	0.72	6.07	3.21	I(N)	86	
109	–	–	20	16.47	2.31	4.78	I(N)	86	
110	–	–	139	3.00	0.56	1.05	I(N)	86	SMA18
111	–	f*	50	0.84	1.85	1.53	I(N)	100	
112	–	–	20	2.11	6.63	4.87	I(N)	100	
113	–	–	20	0.95	6.44	3.66	I(N)	86	
114	–	f*	50	0.70	1.90	1.47	I(N)	57	
115	–	–	20	7.35	5.67	6.65	I(N)	86	SMA19
116	–	–	20	6.14	3.74	4.75	I(N)	86	
117	–	–	20	3.70	7.06	6.12	I(N)	86	
118	–	–	20	12.59	4.22	6.53	I(N)	86	
119	–	–	20	10.03	5.94	7.61	I(N)	86	SMA20
120	–	–	20	5.85	2.60	3.67	I(N)	86	
121	–	f*	50	1.49	2.16	2.05	I(N)	86	
122	–	–	20	3.60	3.56	3.84	I(N)	86	
123	–	–	20	13.91	12.75	14.12	I(N)	86	SMA21
124	–	–	20	5.51	3.52	4.40	I(N)	86	
125	–	–	20	19.56	1.80	4.28	I(N)	86	
126	–	–	20	1.09	9.59	5.00	I(N)	86	
127	–	–	20	3.67	1.80	2.45	I(N)	86	
128	–	–	20	1.98	9.69	6.14	I(N)	86	
129	–	–	20	2.46	4.11	3.73	I(N)	86	
130	–	–	20	1.73	4.17	3.35	I(N)	86	
131	–	–	20	9.35	8.10	9.14	I(N)	86	SMA22
132	–	–	20	7.45	10.04	9.78	I(N)	86	SMA23
133	–	–	20	5.62	6.30	6.52	I(N)	86	
134	–	–	20	2.04	4.09	3.49	I(N)	86	

TABLE A.2: Continued.

	Counterparts [a]		Physical properties [b]				Membership [c]		
#	free-free	IR	T	M_{g+d}	n_{H_2}	N_{H_2}	Cluster	%	Others [d]
(1)	(2)	(3)	(4)	(5)	(6)	(7)	(8)	(9)	(10)
135	–	–	20	7.62	4.87	6.08	I(N)	86	
136	–	f*	50	1.67	2.51	2.36	I(N)	86	
137	–	–	20	8.79	5.17	6.64	I(N)	86	
138	–	–	20	0.76	6.69	3.48	I(N)	86	
139	–	–	20	11.31	5.40	7.43	I(N)	86	
140	–	–	20	6.07	5.70	6.26	I(N)	86	
141	–	–	20	0.39	4.59	2.17	I(N)	86	
142	–	YSO I	50	0.30	2.89	1.46	I(N)	86	

[a] Information on the counterparts at different wavelengths. Radio continuum contribution (free-free, column 2) to the ALMA 87.6 GHz continuum flux, determined from observations published in Hunter et al. (2014), Brogan et al. (2016), and Medina et al. (2018). Association with infrared source (IR, column 8) from Willis et al. (2013). f* denotes field stars.

[b] Physical properties of the ALMA compact sources. In each column we have: T (assumed temperature, column 4) in K; M_{g+d} (dust and gas mass, column 5) in $M_\odot$; n_{H_2} (volume density, column 6) in 10^8 cm^{-3}; N_{H_2} (column density, column 7) in 10^{24} cm^{-2}.

[c] Cluster membership for each ALMA compact sources: cluster to which the source is associated (column 8); and confidence level of membership in percentage (column 9, see § 3.2.1).

[d] Other names for each source, from Brogan et al. (2016), Hunter et al. (2014).

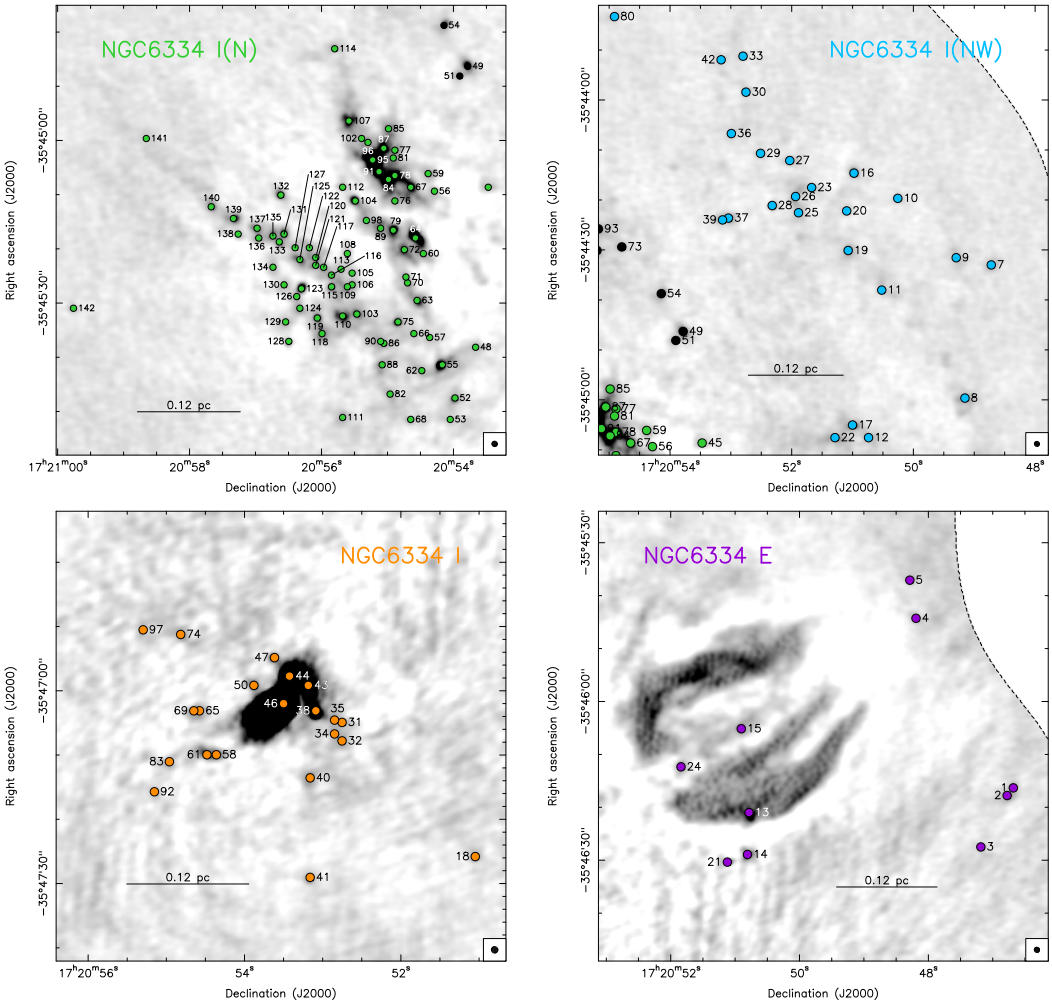

FIGURE A.1: Close-up view of the 4 different clusters identified towards the observed region with ALMA. The identifiers of each source are marked as listed in column 1 of Table A.1.

Appendix B

Catalog of SiO emission structures

TABLE B.1: Properties of the SiO emission structures in NGC 6334

#	R.A.	Dec.	θ_S, P.A.	$S_\circ$	Mass	P	E
(1)	(2)	(3)	(4)	(5)	(6)	(7)	(8)
1	17h20m47.99s	-35d45m30.45s	4.11×2.41, 122	7.37	0.86	18.37	4.82e+45
2	17h20m48.53s	-35d45m56.73s	4.53×1.03, 358	6.37	0.20	2.12	2.26e+44
3	17h20m49.17s	-35d45m19.99s	2.78×1.28, 127	4.84	0.30	3.61	4.47e+44
4	17h20m49.41s	-35d46m07.42s	2.76×1.44, 358	6.33	1.41	33.04	8.10e+45
5	17h20m49.85s	-35d44m58.50s	5.53×2.54, 358	8.87	0.09	0.66	5.53e+43
6	17h20m49.87s	-35d44m24.84s	4.12×1.88, 54	4.89	0.51	18.25	7.59e+45
7	17h20m49.95s	-35d46m46.67s	5.52×2.71, 90	15.85	16.09	936.18	5.88e+47
8	17h20m49.97s	-35d44m32.41s	2.69×2.33, 358	4.28	1.07	30.08	9.03e+45
9	17h20m50.28s	-35d46m39.51s	5.05×2.51, 358	21.63	6.87	251.53	9.74e+46
10	17h20m50.33s	-35d47m13.23s	3.06×2.46, 62	8.88	1.52	41.96	1.24e+46
11	17h20m50.36s	-35d44m43.98s	6.38×2.29, 51	10.85	0.45	6.79	1.12e+45
12	17h20m50.38s	-35d46m23.75s	2.5×1.85, 140	4.51	0.16	1.69	2.00e+44
13	17h20m50.40s	-35d46m33.75s	3.27×2.69, 88	21.07	10.41	421.18	1.84e+47
14	17h20m50.47s	-35d44m08.52s	4.4×2.52, 111	15.35	0.96	20.64	5.53e+45
15	17h20m50.66s	-35d46m46.84s	4.62×2.15, 79	7.48	0.52	17.64	7.48e+45
16	17h20m50.77s	-35d44m14.35s	3.69×2.83, 102	9.56	0.75	10.80	1.61e+45
17	17h20m50.99s	-35d44m24.63s	2.19×1.5, 171	8.82	0.81	17.34	4.30e+45
18	17h20m51.02s	-35d46m45.06s	2.93×1.41, 160	7.30	3.94	158.72	6.68e+46
19	17h20m51.07s	-35d46m22.50s	7.0×5.09, 103	60.68	2.94	65.35	1.84e+46
20	17h20m51.16s	-35d44m04.49s	4.34×1.35, 358	4.57	0.03	0.18	9.23e+42
21	17h20m51.28s	-35d45m56.84s	7.69×2.2, 68	34.98	3.54	81.51	1.92e+46
22	17h20m51.37s	-35d44m12.45s	5.03×3.11, 157	25.31	0.58	6.63	8.19e+44
23	17h20m51.43s	-35d46m50.87s	4.76×3.15, 358	9.29	0.22	2.04	1.95e+44
24	17h20m51.76s	-35d47m35.93s	10.74×1.91, 166	36.91	2.52	56.00	1.25e+46
25	17h20m51.82s	-35d44m36.67s	4.49×1.56, 118	5.85	2.24	127.22	8.23e+46
26	17h20m52.32s	-35d44m31.38s	6.39×3.19, 116	13.93	1.39	35.54	9.59e+45
27	17h20m52.46s	-35d47m08.46s	11.0×3.51, 122	232.89	7.86	147.77	4.10e+46
28	17h20m52.66s	-35d47m06.44s	15.97×7.5, 130	560.55	7.45	202.49	8.57e+46
29	17h20m52.98s	-35d47m32.31s	2.59×1.72, 84	13.77	3.52	96.87	2.93e+46
30	17h20m53.19s	-35d45m13.62s	5.67×0.88, 358	22.04	1.90	29.24	5.71e+45
31	17h20m53.41s	-35d47m39.64s	7.24×2.29, 105	22.47	0.33	2.66	2.22e+44
32	17h20m53.59s	-35d47m25.32s	7.29×4.32, 107	36.56	1.29	27.87	8.17e+45
33	17h20m53.64s	-35d45m22.02s	5.12×1.39, 140	27.34	1.34	23.71	6.47e+45
34	17h20m53.65s	-35d44m20.60s	4.39×1.24, 358	17.19	0.25	1.83	1.38e+44

TABLE B.1: Continued.

#	R.A.	Dec.	θ_S, P.A.	$S_\circ$	Mass	P	E
(1)	(2)	(3)	(4)	(5)	(6)	(7)	(8)
35	17h20m53.75s	-35d45m10.63s	5.99×2.74, 170	64.19	6.53	234.98	9.75e+46
36	17h20m53.83s	-35d45m36.69s	3.69×1.38, 139	15.73	1.32	18.62	2.77e+45
37	17h20m53.88s	-35d46m05.59s	2.83×1.56, 107	9.62	0.30	2.74	2.56e+44
38	17h20m54.06s	-35d45m58.13s	3.57×1.34, 95	6.17	0.29	3.27	3.80e+44
39	17h20m54.17s	-35d44m30.76s	3.58×2.19, 358	17.53	2.14	46.32	1.16e+46
40	17h20m54.21s	-35d45m15.41s	3.9×2.75, 158	33.50	14.16	557.04	2.53e+47
41	17h20m54.32s	-35d44m53.19s	5.17×1.44, 73	22.36	1.67	21.89	3.04e+45
42	17h20m54.33s	-35d45m27.87s	4.24×2.1, 137	33.84	6.75	159.51	4.00e+46
43	17h20m54.51s	-35d45m01.33s	2.39×2.13, 79	18.48	1.45	30.83	1.10e+46
44	17h20m54.60s	-35d46m48.45s	9.72×4.91, 161	174.79	80.81	5319.88	3.74e+48
45	17h20m54.61s	-35d45m07.03s	6.29×1.9, 179	65.60	12.86	556.98	3.08e+47
46	17h20m54.65s	-35d43m58.44s	3.54×1.77, 153	14.37	1.22	19.90	3.32e+45
47	17h20m53.61s	-35d44m03.71s	10.91×3.94, 163	23.22	0.50	10.74	2.51e+45
48	17h20m54.80s	-35d44m41.61s	4.49×3.13, 132	23.81	2.88	67.26	1.65e+46
49	17h20m54.80s	-35d45m18.11s	3.39×1.74, 132	27.39	14.83	724.38	4.37e+47
50	17h20m54.83s	-35d45m46.90s	3.34×1.16, 168	9.01	1.37	25.29	4.92e+45
51	17h20m54.92s	-35d45m33.50s	5.43×1.78, 358	24.38	10.43	441.38	2.32e+47
52	17h20m54.95s	-35d45m24.44s	3.32×2.7, 358	31.29	1.43	15.48	1.75e+45
53	17h20m54.96s	-35d46m12.84s	5.21×2.2, 150	14.23	0.05	0.18	7.56e+42
54	17h20m54.97s	-35d43m45.10s	6.93×1.54, 172	14.12	2.03	71.38	2.66e+46
55	17h20m54.97s	-35d47m50.10s	18.45×2.12, 69	55.83	0.77	11.39	1.70e+45
56	17h20m55.04s	-35d45m37.40s	3.26×1.25, 156	21.29	15.49	670.22	3.37e+47
57	17h20m55.13s	-35d44m29.21s	8.18×2.18, 153	19.88	1.84	66.78	2.88e+46
58	17h20m55.23s	-35d45m43.46s	3.4×1.41, 358	14.56	1.39	26.72	6.03e+45
59	17h20m55.27s	-35d45m11.71s	4.16×2.57, 71	50.73	2.96	41.77	7.39e+45
60	17h20m55.40s	-35d45m01.42s	4.32×3.93, 118	79.46	36.32	2014.28	1.27e+48
61	17h20m55.42s	-35d47m05.19s	5.58×1.62, 358	18.26	0.24	1.69	1.25e+44
62	17h20m55.43s	-35d43m38.28s	4.59×2.84, 177	14.16	1.81	54.59	1.88e+46
63	17h20m55.63s	-35d45m30.40s	5.34×3.82, 358	63.31	9.53	318.49	1.27e+47
64	17h20m55.75s	-35d46m07.42s	4.3×1.52, 53	9.29	0.11	0.62	3.61e+43
65	17h20m55.78s	-35d43m45.36s	4.72×2.6, 66	25.14	3.68	91.50	2.38e+46
66	17h20m55.79s	-35d44m55.58s	2.72×2.2, 157	20.59	5.11	169.24	6.33e+46
67	17h20m55.80s	-35d47m02.95s	2.86×1.36, 358	7.85	0.05	0.22	8.78e+42
68	17h20m55.83s	-35d46m26.12s	5.27×1.73, 61	12.05	0.32	3.44	3.91e+44
69	17h20m55.98s	-35d45m11.63s	4.01×2.02, 172	36.80	3.21	50.88	8.25e+45
70	17h20m56.05s	-35d45m44.60s	8.4×2.53, 358	61.35	1.21	13.85	1.69e+45
71	17h20m56.08s	-35d46m35.51s	3.77×2.29, 358	12.68	0.12	0.65	3.81e+43
72	17h20m56.16s	-35d44m34.15s	10.65×6.27, 123	68.19	2.09	44.06	1.05e+46
73	17h20m56.30s	-35d44m48.70s	6.26×1.31, 122	24.05	1.00	11.84	1.62e+45
74	17h20m56.39s	-35d46m25.62s	3.48×1.81, 118	5.27	0.03	0.15	9.30e+42
75	17h20m56.47s	-35d44m18.98s	3.99×1.51, 87	11.03	3.44	90.25	2.42e+46
76	17h20m56.68s	-35d45m01.51s	7.21×3.01, 129	46.28	3.42	103.40	3.71e+46
77	17h20m56.81s	-35d44m22.09s	2.77×1.35, 56	8.85	0.12	1.70	3.61e+44
78	17h20m56.81s	-35d45m10.44s	3.58×1.62, 358	17.66	7.52	362.39	2.28e+47
79	17h20m56.83s	-35d45m15.23s	7.65×1.44, 358	44.44	1.90	56.18	2.65e+46
80	17h20m56.90s	-35d44m50.49s	3.17×1.42, 95	8.94	0.46	6.00	1.09e+45

TABLE B.1: Continued.

#	R.A.	Dec.	θ_S, P.A.	$S_\circ$	Mass	P	E
(1)	(2)	(3)	(4)	(5)	(6)	(7)	(8)
81	17h20m57.10s	-35d45m25.95s	15.59×2.79, 167	87.76	25.05	1561.66	1.08e+48
82	17h20m57.65s	-35d44m37.84s	4.7×2.77, 94	31.17	1.63	22.13	3.14e+45
83	17h20m57.84s	-35d45m40.34s	4.03×1.5, 50	9.24	0.59	8.56	1.32e+45
84	17h20m57.85s	-35d44m31.22s	3.77×1.23, 157	7.49	0.63	9.13	1.44e+45
85	17h20m58.13s	-35d45m18.22s	5.65×2.1, 358	28.11	10.84	565.46	3.44e+47
86	17h20m58.14s	-35d45m07.52s	7.11×3.12, 155	19.30	0.16	1.01	6.25e+43
87	17h20m58.43s	-35d44m48.70s	17.53×2.47, 157	62.97	0.38	4.17	4.76e+44
88	17h20m58.80s	-35d44m59.63s	4.02×1.6, 167	6.99	0.10	0.66	4.84e+43
89	17h20m59.97s	-35d44m30.76s	3.98×2.28, 121	12.73	2.47	63.75	1.76e+46

Observed parameters of the SiO (2-1) emission structures identified as explained in § 5.3.2. In each column we have: R.A. (right ascension, column 2) in ^{h} :^{m}:^{s}; Dec. (declination, column 3) in $^\circ$:′:″; θ_s (observed sizes of the major and minor axis obtained from the `Astrodendro`) and P.A. (position angle, column 4) in arcsec^2 and degrees; S_ν (integrated flux, column 5) in Jy/beam; Mass in $M_\odot$ (column 6); P (momentum, in column 7) in $M_\odot$ km s^{-1}; E (kinetic energy, column 8) in erg.

Appendix C

Softwares and packages

C.1 Behind The Spectrum (BTS)

Behind The Spectrum (BTS)[1] is an automated multi-Gaussian fitting algorithm which can be applied to optically thin spectra (Clarke et al., 2018). The advantage of this Python module is that the number of Gaussian components in a spectrum is not assumed as an input. Instead, the BTS routine determine the number and the position of the velocity/frequency components based on the first, second and third derivatives of the spectrum. Once the number of components are determined, BTS applies a least-square fitting routine to determine the best fit parameters with the previously-determined number of components. Fig C.1 shows a perfect Gaussian with a mean of zero and standard deviation of one, together with its first, second and third derivatives. As indicated in the figure, the position of the Gaussian's maximum coincides with the minimum of the second derivative. Therefore, the second derivative is used as the indicator of a component. The first and the third derivatives can be used for additional checks.

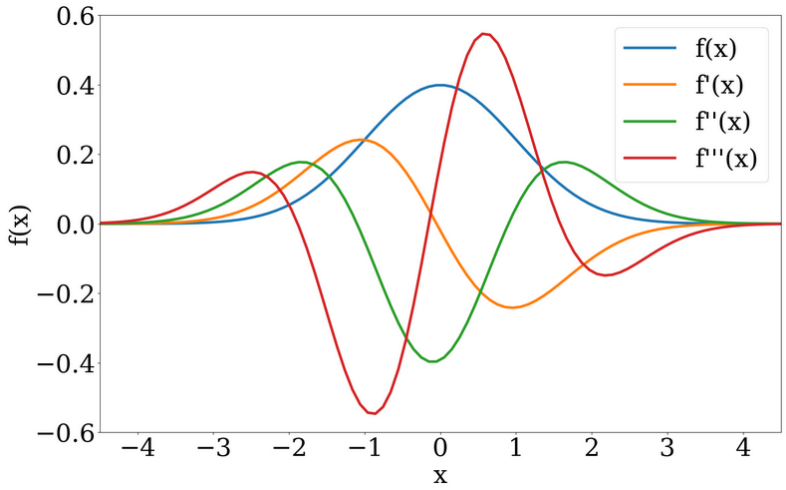

FIGURE C.1: A perfect Gaussian function with its first, second and third derivatives.

In case of observed spectra, the fitting routines have to deal with considerable amount of noise which makes the detection of the peak challenging. Fig. C.2 shows the same Gaussian as presented in Fig. C.1 but with noise added. As shown in Fig. C.2, the second derivative has no clear peak at the position of the maximum due to the high noise level.

[1] available at https://github.com/SeamusClarke/BTS

To be able to determine the derivatives accurately, it is necessary to smooth the noisy Gaussian with convolving it with a Gaussian kernel which has a smoothing length of h. However, after the convolution the second derivative may still remain noisy. Due to the high noise level, the second derivative exhibits numerous local minima which are not associated with the position of the Gaussian spectrum. To filter such minima, BTS takes advantage of a signal-to-noise threshold and ignores the velocity channels in which the intensity of the Gaussian spectrum is lower than the threshold. The locations of the local minima define the number and positions of the velocity components. These are the two of the necessary parameters that are used as initial guess for fitting a multi-component Gaussian to the spectrum.

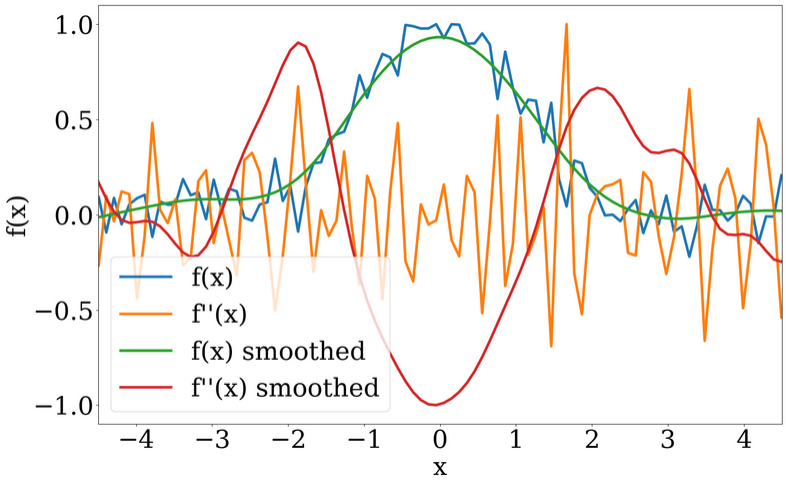

FIGURE C.2: A perfect Gaussian as seen in Fig. C.1, with noise added. The first derivative denoted by solid orange line exhibits pure noise, while the second derivative presented by solid red line shows local minima and maxima despite the noise.

For the amplitudes, the intensities of the spectrum at the minima of the second derivative are used as initial guess. To estimate a guess for the width, BTS uses the FWHM of the width. Then, the values of FWHM are converted into standard deviation. Once the number of components and initial guesses are determined, BTS applies the `curve_fit` routine in `Scipy` to the spectrum. The bounds used for the fitting parameters (i.e., amplitude, position and width) are as follows:

- $n\,\sigma_{\rm noise} < \mathrm{A} < 2 \times \max(\mathrm{spectrum})$,
- $v_{\rm min} < v_{\rm cent} < v_{\rm max}$,
- $\delta v < \sigma_{\rm width} < v_{\rm max} - v_{\rm min}$,

where n is the multiple of the noise level, $\max(\mathrm{spectrum})$ is the maximum intensity of the spectrum, $v_{\rm min}$ and $v_{\rm max}$ define velocity range of the spectrum, and δv is the spectral resolution. Once the fitting process is performed, the reduced χ^2 is calculated. If the value of reduced χ^2 is larger than the user-defined limit, the fitting will be repeated with one additional component. If the reduced χ^2 is below the limit, the fitting will be repeated with one fewer component. If the result of the fitting with fewer velocity component leads to a reduced χ^2 smaller than the limit, the new fitting parameters are saved. Otherwise, the old parameters are preserved. This extra step is implemented to avoid over-fitting.

User-defined parameters

BTS routine works based on 25 parameters regarding to the smoothing, noise level, input and output `FITS` files and the properties of the spectrum. In the following, I briefly explain the most important user-defined parameters:

- **chi_limit:** This is a threshold for the value of the χ^2 which determines the accuracy of the fit.
- **smoothing_length:** This is the smoothing length of the Gaussian kernel which smooths the noisy observed or synthetic spectrum.
- **signal_to_noise_ratio:** This is a threshold which determines if the components is significant enough to be fitted.
- **variable_noise:** This is a flag which determines if the noise level is constant across the observed map. For a varying noise level this parameter should be set to 1. For the case of constant level of noise the flag is set to 0.
- **noise_level:** This is the r.m.s noise level if a constant level of noise across the observed map is assumed.

In the actual work I took advantage of the BTS algorithm to obtain the velocity fields of the dense gas tracers (see § 4). Moreover, the output of this algorithm is used to better disentangle different types of shocks based on their leading mechanism (see § 5).

C.2 eXtended CASA Line Analysis Software Suite (XCLASS)

`XCLASS`[2] is a toolbox for `CASA` which provides the possibility of identifying, fitting and modelling the spectral line data using the queries of Cologne Database for Molecular Spectroscopy (CDMS), Virtual Atomic and Molecular Data Centre (VAMDC) and Jet Propulsion Laboratory (JPL) molecular databases (Möller, Endres, and Schilke, 2017; Möller et al., 2013). The toolbox includes several main functions: (i) `myXCLASS` which generates a synthetic spectrum, (ii) `myXCLASSFit` which fits the observed spectrum of a single pixel with a synthetic spectrum, (iii) `myXCLASSMapFit` which fits a complete data cube instead of a single spectrum ; and (iv) `LineIdentification` which identifies molecular transitions in a given spectrum. In order to optimize the best-fit parameters, `XCLASS` takes advantage of a model optimizer package `MAGIX` (Möller et al., 2013) which helps to find the best description of the data using a certain model. The model spectrum is obtained by solving the radiative transfer equation under the LTE assumption for an isothermal object in one dimension, called detection equation

$$\mathrm{T_{B0}} = \mathrm{T_0}[\mathrm{f(T_{ex})} - \mathrm{f(T_{bg})}[1 - e^{-\Delta\tau_0}], \tag{C.1}$$

where $\mathrm{T_{B0}} = \mathrm{T}$ is the received brightness temperature at $(\mathrm{v} = v_0)$, T_0 is the equivalent temperature of transition, $\Delta\tau_0$ is the cloud optical depth at the center of the line, and

$$\mathrm{f(T)} = [exp(\mathrm{T_0/T}) - 1]^{-1}. \tag{C.2}$$

For the actual work, I took advantage of the `myXCLASSMapFit` function and therefore, this section mainly concentrates on this function.

[2] available at https://xclass.astro.uni-koeln.de/

myXCLASSFit

This function uses the Levenberg-Marquardt algorithm to fit the experimental data. The user-defined parameters which need be given as input are as follows:

- The `molfit` file: using this file, the user defines which molecular transitions need to be fitted and specifies the number of components for each molecule. Additionally, the user has to define the source size (`size`) in arcsec, the excitation temperature (`T_ex`) in K, the column density (`N_tot`) in cm^{-2}, the velocity width (`V_width`) in km s^{-1}, the velocity offset (`V_off`) for each component, and finally the flag (`CFFlag`) indicating if a component is considered for core `c` or foreground `f`. For each parameter in the `molfit` file, a range and an initial guess needs to defined. The initial guess has to be optimized and not to be significantly different from the best-fit result.

```
% Number of molecules = 2
% size:    T_ex:     N_tot:   V_width:    V_off:   CFFlag:
CS;v=0;    3
 48.470   300.00   3.91E+17       2.86   -20.564         c
 21.804   320.00   6.96E+17       8.07    30.687         c
 81.700   208.00   1.46E+17       5.16   -10.124         c
HCS+;v=0;    2
% size:    T_ex:     N_tot:   V_width:    V_off:   CFFlag:
          150.00   1.10E+18       5.00    -0.154         f
          200.00   2.20E+17       3.10    -2.154         f
```

FIGURE C.3: An example of a `molfit` file.

- `NumberIteration`: maximum number of iterations (default: 50)
- `experimentalData`: the path and name of an ASCII file which includes the frequencies (in MHz) and intensities (in K) of the spectrum.
- `TelescopeSize`: size of the telescope (in m) for single-dish observations and the beam FWHM for the interferometric observations
- `tBack` and `tslope`: contribution of the continuum emission
- `beta_dust`: spectral index for dust
- `N_H`: hydrogen column density

The settings for minimum and maximum frequency as well as for the step size is taken from the experimental data. As the output, `myXCLASSFit` function returns a `molfit` file which contains the best-fit parameters. Moreover, the modelled intensities are restored in an ASCII file together with the velocities and frequencies of the spectrum.

Appendix D

Additional figures

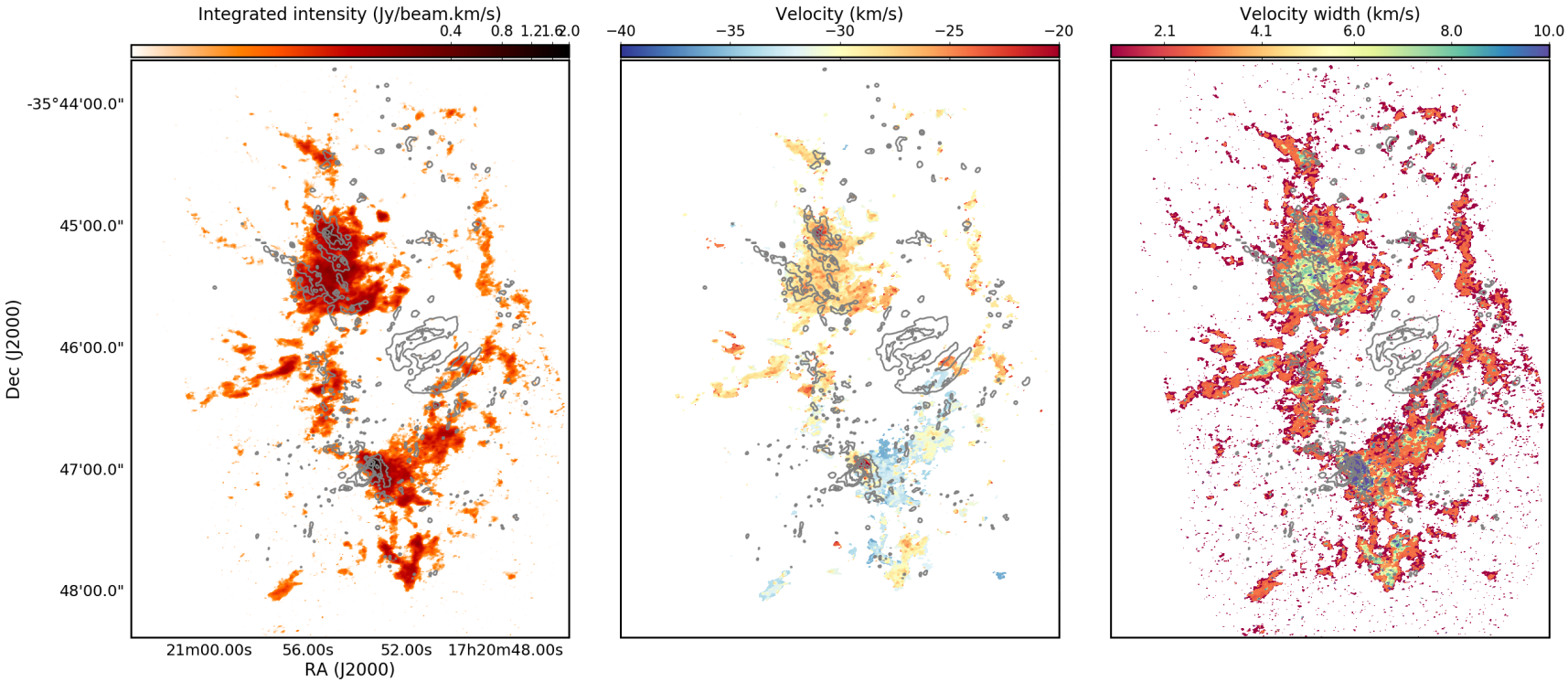

FIGURE D.1: Spectral moments of CH_3CCH molecule in NGC 6334. *Left:* Integrated intensity in units of Jy beam^{-1} kms^{-1}. *Middle:* Centroid velocity in km s^{-1}. *Right:* FWHM of central line in km s^{-1}. ALMA continuum map at 88 GHz is shown in gray contours.

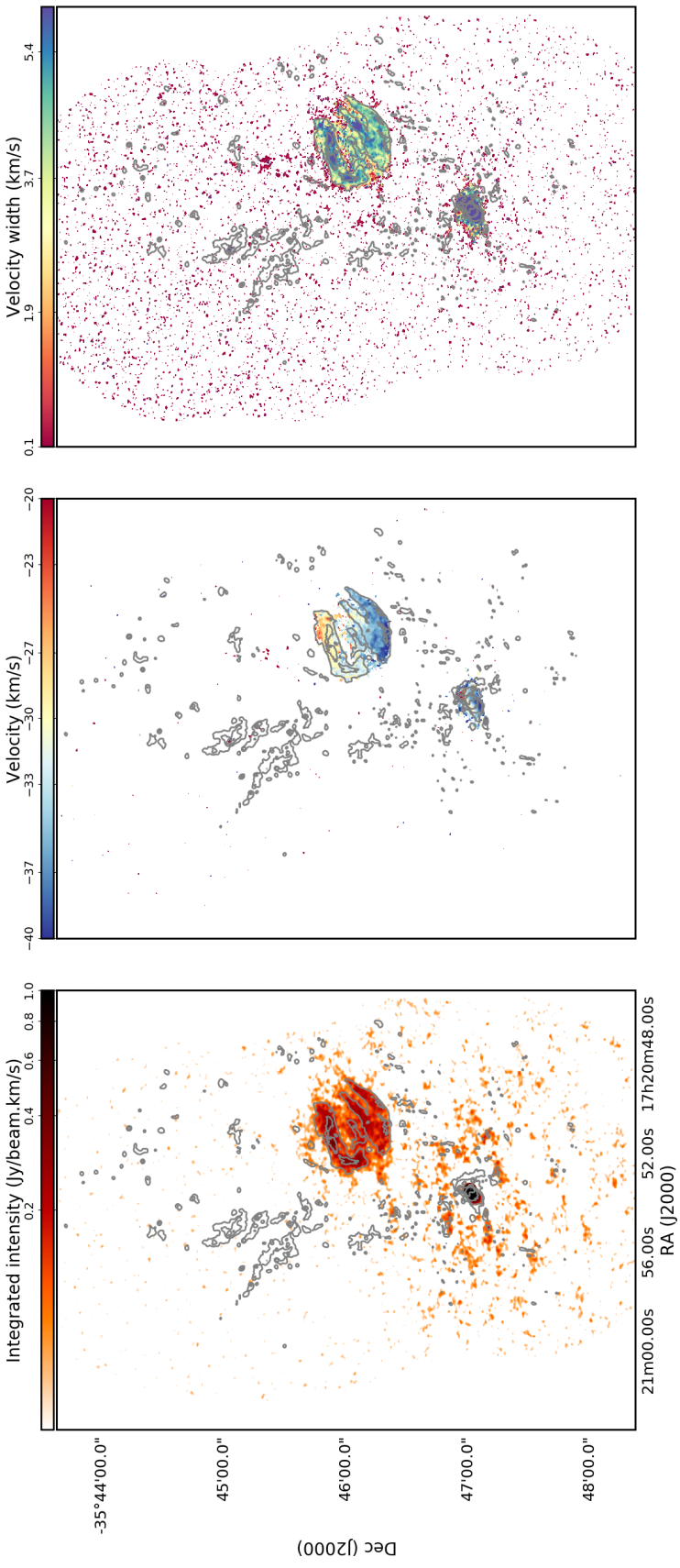

FIGURE D.2: Spectral moments of H^{42}ff molecule in NGC 6334. *Left:* Integrated intensity in units of Jy beam^{-1} kms^{-1}. *Middle:* Centroid velocity in km s^{-1}. *Right:* FWHM of central line in km s^{-1}. ALMA continuum map at 88 GHz is shown in gray contours.

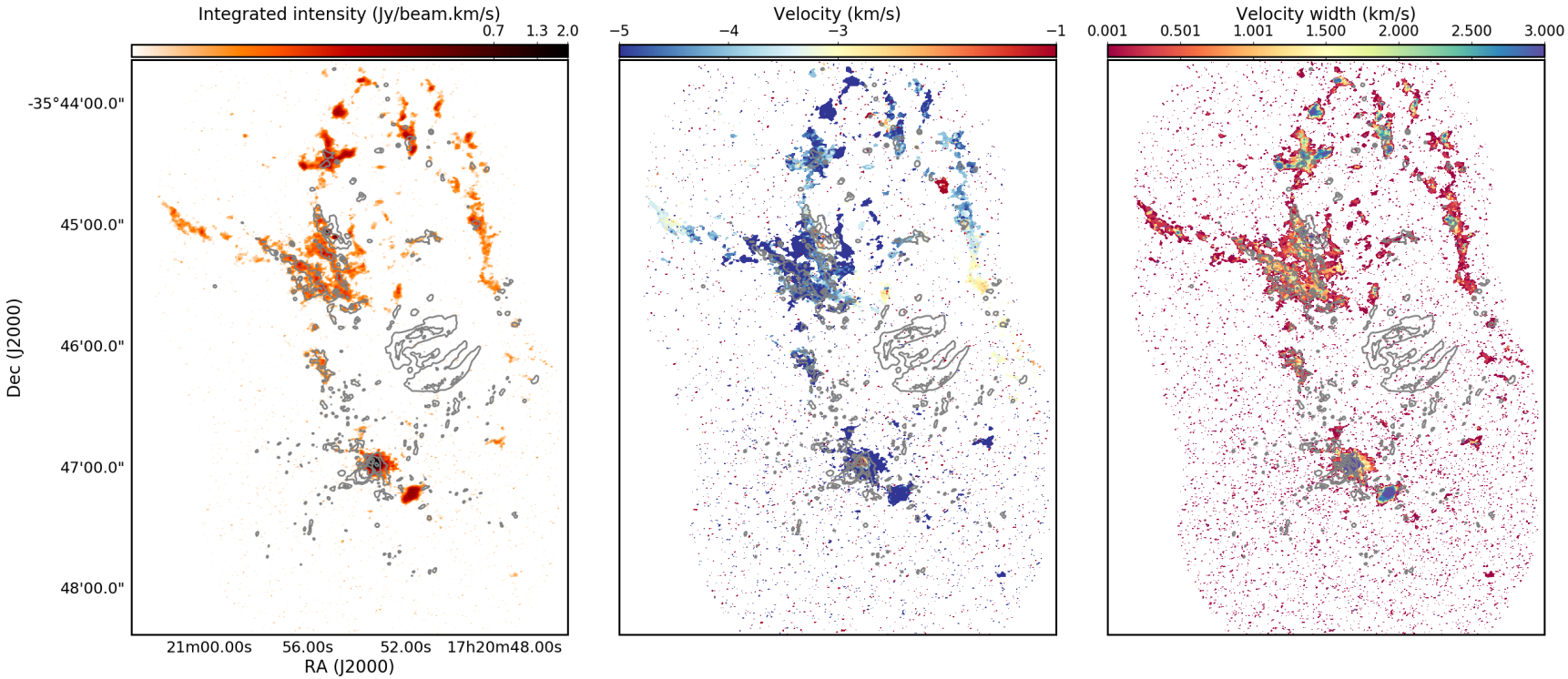

FIGURE D.3: Spectral moments of NH_2D molecule in NGC 6334. *Left:* Integrated intensity in units of Jy beam^{-1} kms^{-1}. *Middle:* Centroid velocity in km s^{-1}. *Right:* FWHM of central line in km s^{-1}. ALMA continuum map at 88 GHz is shown in gray contours.

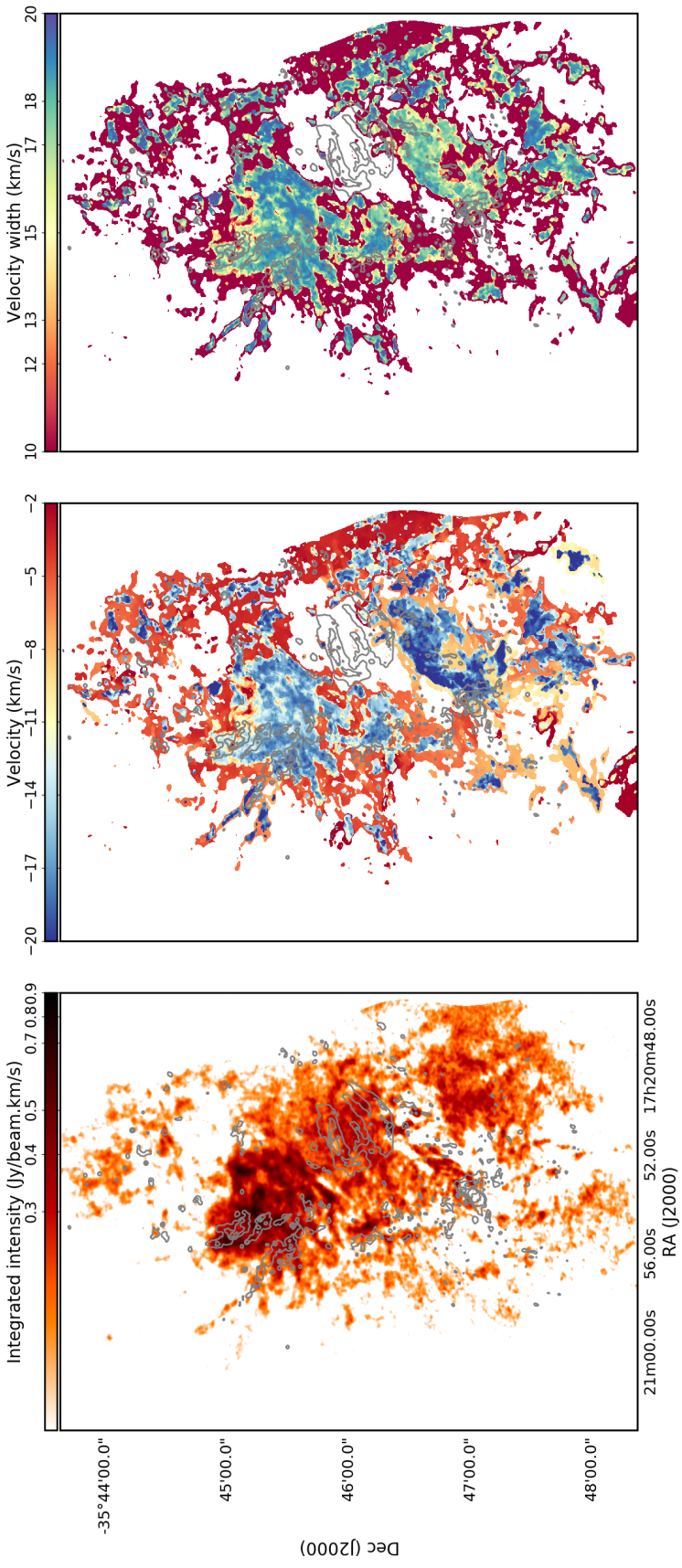

FIGURE D.4: Spectral moments of CCH molecule in NGC 6334. *Left:* Integrated intensity in units of Jy beam^{-1} kms^{-1}. *Middle:* Centroid velocity in km s^{-1}. *Right:* FWHM of central line in km s^{-1}. ALMA continuum map at 88 GHz is shown in gray contours.

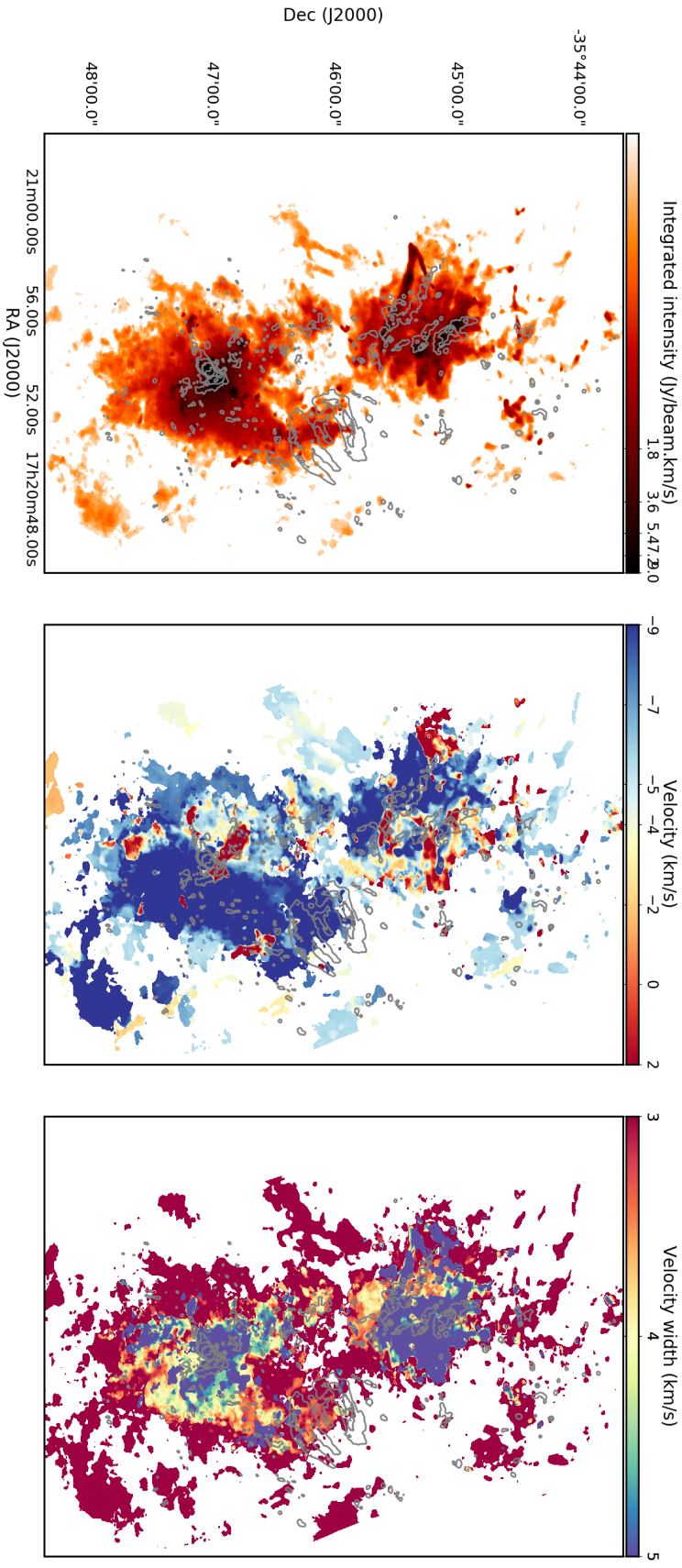

FIGURE D.5: Spectral moments of HCN molecule in NGC 6334. *Left:* Integrated intensity in units of Jy beam^{-1} kms^{-1}. *Middle:* Centroid velocity in km s^{-1}. *Right:* FWHM of central line in km s^{-1}. ALMA continuum map at 88 GHz is shown in gray contours.

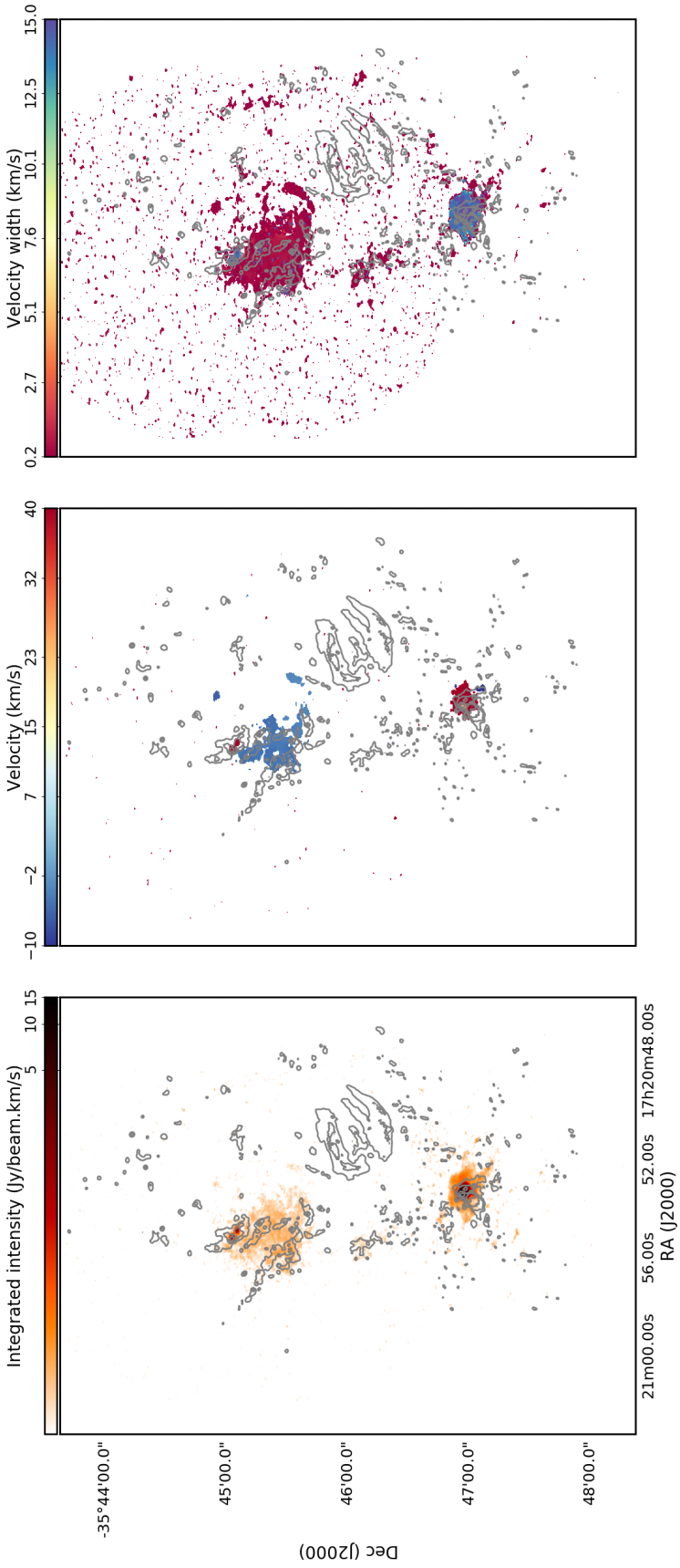

FIGURE D.6: Spectral moments of $H^{15}NC$ molecule in NGC 6334. *Left:* Integrated intensity in units of Jy beam^{-1} kms^{-1}. *Middle:* Centroid velocity in km s^{-1}. *Right:* FWHM of central line in km s^{-1}. ALMA continuum map at 88 GHz is shown in gray contours.

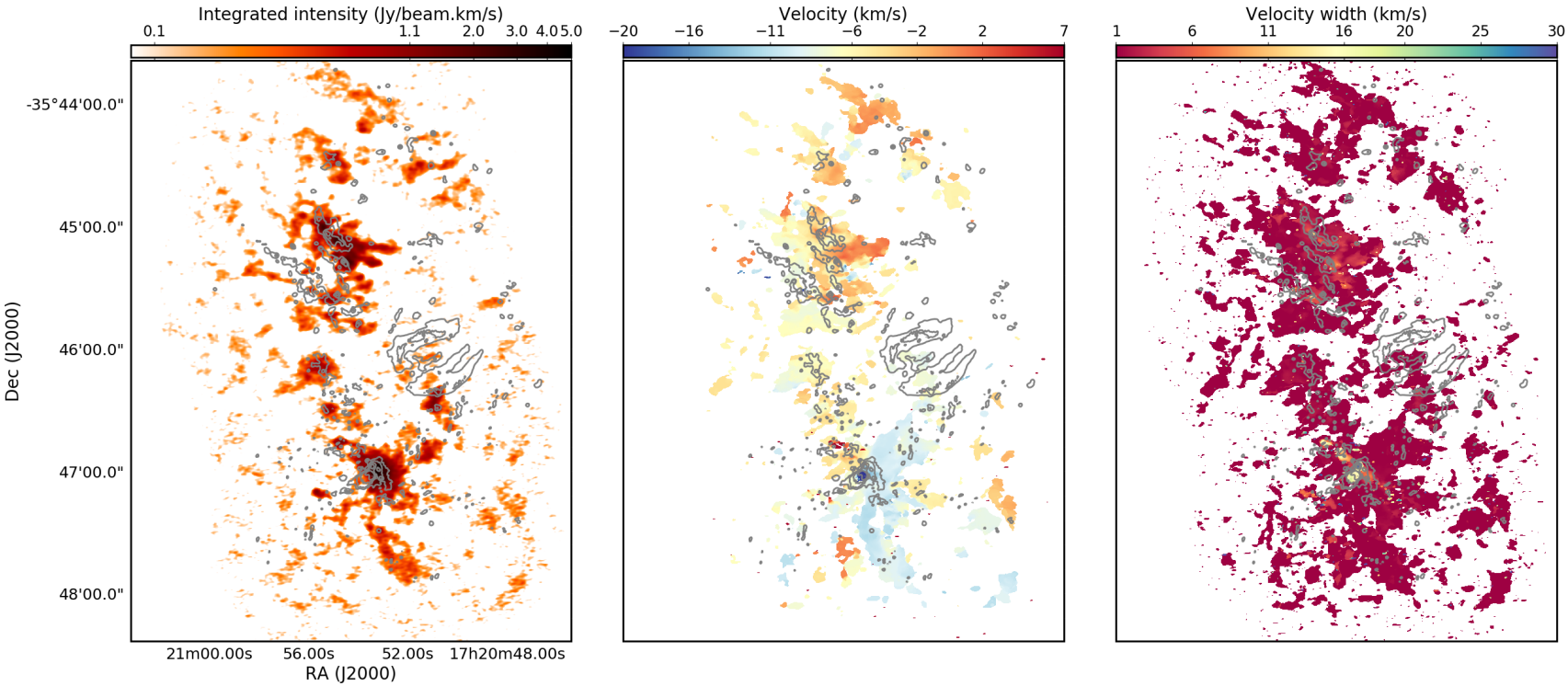

FIGURE D.7: Spectral moments of HCO^+ molecule in NGC 6334. *Left:* Integrated intensity in units of Jy beam^{-1} kms^{-1}. *Middle:* Centroid velocity in km s^{-1}. *Right:* FWHM of central line in km s^{-1}. ALMA continuum map at 88 GHz is shown in gray contours.

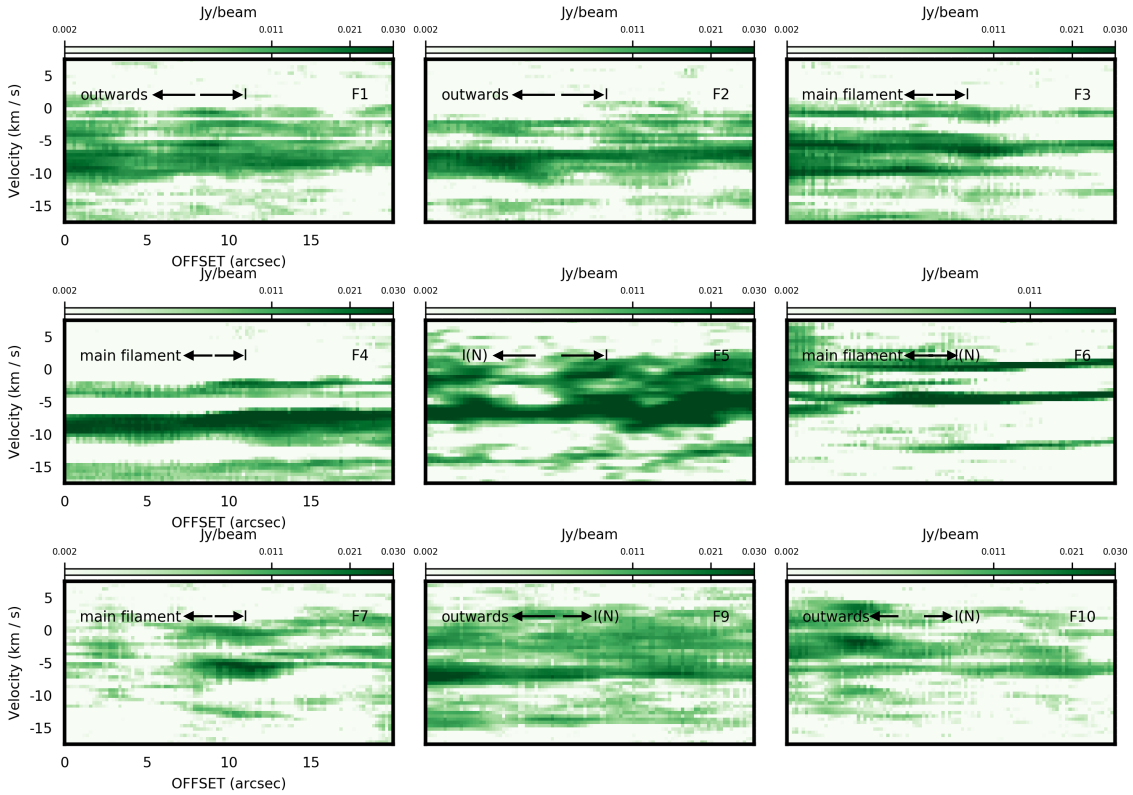

FIGURE D.8: Position velocity cut along each identified filament in $H^{13}CN$ (see Fig. 4.11). The arrows show the paths of the filaments.

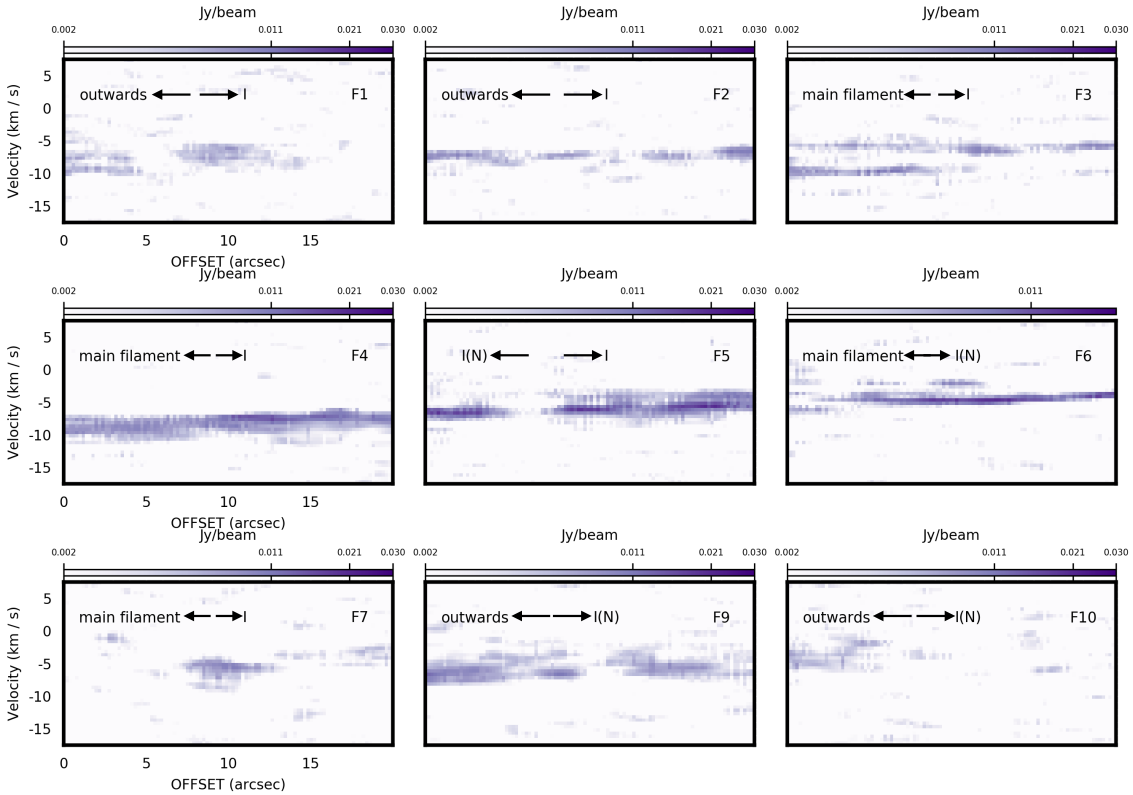

FIGURE D.9: Position velocity cut along each identified filament in $HC^{15}N$ (see Fig. 4.11). The arrows show the paths of the filaments.

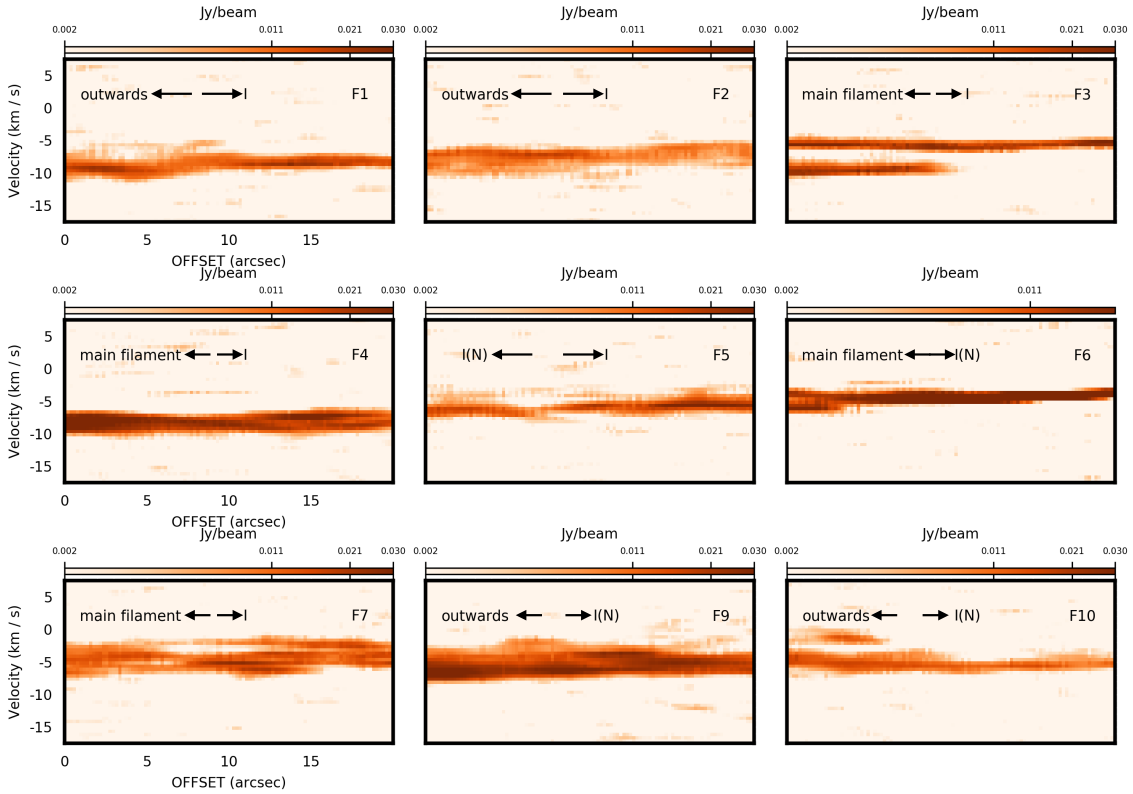

FIGURE D.10: Position velocity cut along each identified filament in $HN^{13}C$ (see Fig. 4.11). The arrows show the paths of the filaments.

Bibliography

(2005). Vol. 227. IAU Symposium.

Allison, Richard J. et al. (2009a). "Dynamical Mass Segregation on a Very Short Timescale". In: 700.2, pp. L99–L103. DOI: 10.1088/0004-637X/700/2/L99. arXiv: 0906.4806 [astro-ph.GA].

Allison, Richard J. et al. (2009b). "Using the minimum spanning tree to trace mass segregation". In: 395.3, pp. 1449–1454. DOI: 10.1111/j.1365-2966.2009.14508.x. arXiv: 0901.2047 [astro-ph.GA].

Alves, Joao, Marco Lombardi, and Charles Lada (2007). "The Origin of the Initial Mass Function is in the Cloud Structure". In: *Astrophysics and Space Science Proceedings* 3, p. 417. DOI: 10.1007/978-1-4020-5573-7_72.

Anderl, S. et al. (2013). "Shocks in dense clouds. IV. Effects of grain-grain processing on molecular line emission". In: 556, A69, A69. DOI: 10.1051/0004-6361/201321399. arXiv: 1408.0140 [astro-ph.GA].

André, Ph. et al. (2007). "The initial conditions of star formation in the Ophiuchus main cloud: Kinematics of the protocluster condensations". In: 472.2, pp. 519–535. DOI: 10.1051/0004-6361:20077422. arXiv: 0706.1535 [astro-ph].

André, Ph. et al. (2010). "From filamentary clouds to prestellar cores to the stellar IMF: Initial highlights from the Herschel Gould Belt Survey". In: 518, L102, p. L102. DOI: 10.1051/0004-6361/201014666. arXiv: 1005.2618 [astro-ph.GA].

André, Ph. et al. (2016). "Characterizing filaments in regions of high-mass star formation: High-resolution submilimeter imaging of the massive star-forming complex NGC 6334 with ArTéMiS". In: 592, A54, A54. DOI: 10.1051/0004-6361/201628378. arXiv: 1605.07434 [astro-ph.GA].

André, Philippe (1994). "Observations of protostars and protostellar stages". In: *The Cold Universe*. Ed. by Thierry Montmerle et al., p. 179.

Andre, Philippe, Derek Ward-Thompson, and Mary Barsony (1993). "Submillimeter Continuum Observations of rho Ophiuchi A: The Candidate Protostar VLA 1623 and Prestellar Clumps". In: 406, p. 122. DOI: 10.1086/172425.

Anglada, Guillem, Luis F. Rodríguez, and Carlos Carrasco-González (2018). "Radio jets from young stellar objects". In: 26.1, 3, p. 3. DOI: 10.1007/s00159-018-0107-z. arXiv: 1806.06444 [astro-ph.SR].

Arnold, Steven (2014). "The History of Radio Astronomy". In: *Getting Started in Radio Astronomy: Beginner Projects for the Amateur*. New York, NY: Springer New York, pp. 1–32. ISBN: 978-1-4614-8157-7. DOI: 10.1007/978-1-4614-8157-7_1. URL: https://doi.org/10.1007/978-1-4614-8157-7_1.

Arzoumanian, D. et al. (2011). "Characterizing interstellar filaments with Herschel in IC 5146". In: 529, L6, p. L6. DOI: 10.1051/0004-6361/201116596. arXiv: 1103.0201 [astro-ph.GA].

Arzoumanian, Doris et al. (2018). "Molecular filament formation and filament-cloud interaction: Hints from Nobeyama 45 m telescope observations". In: 70.5, 96, p. 96. DOI: 10.1093/pasj/psy095. arXiv: 1807.08968 [astro-ph.GA].

Audit, E. and P. Hennebelle (2005). "Thermal condensation in a turbulent atomic hydrogen flow". In: 433.1, pp. 1–13. DOI: 10.1051/0004-6361:20041474. arXiv: astro-ph/0410062 [astro-ph].

Bachiller, R. and M. Pérez Gutiérrez (1997). "Shock Chemistry in the Young Bipolar Outflow L1157". In: 487.1, pp. L93–L96. DOI: 10.1086/310877.

Bania, T. M. and J. G. Lyon (1980). "OB stars and the structure of the interstellar medium - Cloud formation and effects of different equations of state". In: 239, pp. 173–192. DOI: 10.1086/158099.

Bate, Matthew R. (2009). "Stellar, brown dwarf and multiple star properties from hydrodynamical simulations of star cluster formation". In: 392.2, pp. 590–616. DOI: 10.1111/j.1365-2966.2008.14106.x. arXiv: 0811.0163 [astro-ph].

Beltrán, M. T. and W. J. de Wit (2016). "Accretion disks in luminous young stellar objects". In: 24, 6, p. 6. DOI: 10.1007/s00159-015-0089-z. arXiv: 1509.08335 [astro-ph.GA].

Bertin, E. and S. Arnouts (1996). "SExtractor: Software for source extraction." In: 117, pp. 393–404. DOI: 10.1051/aas:1996164.

Beuther, H. et al. (2018). "Fragmentation and disk formation during high-mass star formation. IRAM NOEMA (Northern Extended Millimeter Array) large program CORE". In: 617, A100, A100. DOI: 10.1051/0004-6361/201833021. arXiv: 1805.01191 [astro-ph.GA].

Blitz, L. and F. H. Shu (1980). "The origin and lifetime of giant molecular cloud complexes". In: 238, pp. 148–157. DOI: 10.1086/157968.

Blitz, Leo (1993). "Giant Molecular Clouds". In: *Protostars and Planets III*. Ed. by Eugene H. Levy and Jonathan I. Lunine, p. 125.

Bonnell, I. A. et al. (2001). "Accretion in stellar clusters and the initial mass function". In: 324.3, pp. 573–579. DOI: 10.1046/j.1365-8711.2001.04311.x. arXiv: astro-ph/0102121 [astro-ph].

Bonnell, Ian A. and Matthew R. Bate (2002). "Accretion in stellar clusters and the collisional formation of massive stars". In: 336.2, pp. 659–669. DOI: 10.1046/j.1365-8711.2002.05794.x.

— (2006). "Star formation through gravitational collapse and competitive accretion". In: 370.1, pp. 488–494. DOI: 10.1111/j.1365-2966.2006.10495.x. arXiv: astro-ph/0604615 [astro-ph].

Bonnell, Ian A. and Melvyn B. Davies (1998). "Mass segregation in young stellar clusters". In: 295.3, pp. 691–698. DOI: 10.1046/j.1365-8711.1998.01372.x.

Bontemps, S. et al. (2010). "Fragmentation and mass segregation in the massive dense cores of Cygnus X". In: 524, A18, A18. DOI: 10.1051/0004-6361/200913286. arXiv: 0909.2315 [astro-ph.GA].

Bressert, E. et al. (2012). "How to Find Young Massive Cluster Progenitors". In: 758.2, L28, p. L28. DOI: 10.1088/2041-8205/758/2/L28. arXiv: 1208.3472 [astro-ph.GA].

Brogan, C. L. et al. (2009). "Digging Into NGC 6334 I(N): Multiwavelength Imaging of a Massive Protostellar Cluster". In: 707.1, pp. 1–23. DOI: 10.1088/0004-637X/707/1/1. arXiv: 0909.5256 [astro-ph.GA].

Brogan, C. L. et al. (2016). "The Massive Protostellar Cluster NGC 6334I at 220 au Resolution: Discovery of Further Multiplicity, Diversity, and a Hot Multi-core". In: 832.2, 187, p. 187. DOI: 10.3847/0004-637X/832/2/187. arXiv: 1609.07470 [astro-ph.GA].

Burkert, Andreas and Lee Hartmann (2004). "Collapse and Fragmentation in Finite Sheets". In: 616.1, pp. 288–300. DOI: 10.1086/424895. arXiv: astro-ph/0409680 [astro-ph].

Busquet, G. et al. (2019). "Unveiling a cluster of protostellar disks around the massive protostar GGD 27 MM1". In: 623, L8, p. L8. DOI: 10.1051/0004-6361/201833687. arXiv: 1902.07581 [astro-ph.SR].

Carey, Sean J. et al. (1998). "The Physical Properties of the Midcourse Space Experiment Galactic Infrared-dark Clouds". In: 508.2, pp. 721–728. DOI: 10.1086/306438.

Carral, Patricia et al. (2002). "Detection of the Winds from the Exciting Sources of Shell H II Regions in NGC 6334". In: 123.5, pp. 2574–2582. DOI: 10.1086/339701.

Cartwright, Annabel and Anthony P. Whitworth (2004). "The statistical analysis of star clusters". In: 348.2, pp. 589–598. DOI: 10.1111/j.1365-2966.2004.07360.x. arXiv: astro-ph/0403474 [astro-ph].

Ceccarelli, C. et al. (2007). "Extreme Deuteration and Hot Corinos: The Earliest Chemical Signatures of Low-Mass Star Formation". In: *Protostars and Planets V*. Ed. by Bo Reipurth, David Jewitt, and Klaus Keil, p. 47. arXiv: astro-ph/0603018 [astro-ph].

Cesaroni, R. et al. (2017). "Chasing discs around O-type (proto)stars: Evidence from ALMA observations". In: 602, A59, A59. DOI: 10.1051/0004-6361/201630184.

Chandrasekhar, S. (1953). "Problems of stability in hydrodynamics and hydromagnetics (George Darwin Lecture)". In: 113, p. 667. DOI: 10.1093/mnras/113.6.667.

Chandrasekhar, Subrahmanyan (1942). *Principles of stellar dynamics*.

Charrad, Malika et al. (2014). "NbClust: An R Package for Determining the Relevant Number of Clusters in a Data Set". In: *Journal of Statistical Software, Articles* 61.6, pp. 1–36. ISSN: 1548-7660. DOI: 10.18637/jss.v061.i06. URL: https://www.jstatsoft.org/v061/i06.

Chen, L. J. et al. (2014). "Effects of ion dynamics on kinetic structures of the diffusion region during magnetic reconnection". In: *AGU Fall Meeting Abstracts*. Vol. 2014, SM13C-4171, SM13C–4171.

Cheung, L. et al. (1978). "1.0 millimeter continuum map of cool sources in the NGC 6334 complex." In: 226, pp. L149–L152. DOI: 10.1086/182852.

Chibueze, James O. et al. (2014). "Astrometry and Spatio-kinematics of H_2O Masers in the Massive Star-forming Region NGC 6334I(North) with VERA". In: 784.2, 114, p. 114. DOI: 10.1088/0004-637X/784/2/114.

Chira, R. A. et al. (2013). "Characterization of infrared dark clouds. NH_3 observations of an absorption-contrast selected IRDC sample". In: 552, A40, A40. DOI: 10.1051/0004-6361/201219567. arXiv: 1302.6774 [astro-ph.SR].

Churchwell, E. (2002). "The Formation and Early Evolution of Massive Stars". In: *Hot Star Workshop III: The Earliest Stages of Massive Star Birth. ASP Conference Proceedings, Vol. 267. Edited by Paul A. Crowther. ISBN: 1-58381-107-9. San Francisco, Astronomical Society of the Pacific, 2002, p.3*. Ed. by P. Crowther. Vol. 267. Astronomical Society of the Pacific Conference Series, p. 3.

Clark, Paul C. and Ian A. Bonnell (2006). "Clumpy shocks and the clump mass function". In: 368.4, pp. 1787–1795. DOI: 10.1111/j.1365-2966.2006.10251.x. arXiv: astro-ph/0603578 [astro-ph].

Clark, Paul C. and Simon C. O. Glover (2014). "On column density thresholds and the star formation rate". In: 444.3, pp. 2396–2414. DOI: 10.1093/mnras/stu1589. arXiv: 1306.5714 [astro-ph.GA].

Clarke, C. J., I. A. Bonnell, and L. A. Hillenbrand (2000). "The Formation of Stellar Clusters". In: *Protostars and Planets IV*. Ed. by V. Mannings, A. P. Boss, and S. S. Russell, p. 151. arXiv: astro-ph/9903323 [astro-ph].

Clarke, S. D. et al. (2017). "Filamentary fragmentation in a turbulent medium". In: 468.2, pp. 2489–2505. DOI: 10.1093/mnras/stx637. arXiv: 1703.04473 [astro-ph.GA].

Clarke, S. D. et al. (2018). "Synthetic $C^{18}O$ observations of fibrous filaments: the problems of mapping from PPV to PPP". In: 479.2, pp. 1722–1746. DOI: 10.1093/mnras/sty1675. arXiv: 1806.08564 [astro-ph.GA].

Clarke, S. D. et al. (2019). "Determining the presence of characteristic fragmentation length-scales in filaments". In: 484.3, pp. 4024–4045. DOI: 10.1093/mnras/stz248. arXiv: 1901.06205 [astro-ph.GA].

Codella, C. and R. Bachiller (1999). "Molecular outflows in intermediate-mass star forming regions: the case of CB3". In: 350, pp. 659–671.

Codella, C. et al. (2005). "Chemical differentiation along the CepA-East outflows". In: 361.1, pp. 244–258. DOI: 10.1111/j.1365-2966.2005.09165.x. arXiv: astro-ph/0505168 [astro-ph].

Colombo, D. et al. (2015). "Graph-based interpretation of the molecular interstellar medium segmentation". In: 454.2, pp. 2067–2091. DOI: 10.1093/mnras/stv2063. arXiv: 1510.04253 [astro-ph.GA].

Crovisier, J. and J. M. Dickey (1983). "The spatial power spectrum of galactic neutral hydrogen from observations of the 21-cm emission line." In: 122, pp. 282–296.

Csengeri, T. et al. (2016). "ATLASGAL-selected massive clumps in the inner Galaxy. II. Characterisation of different evolutionary stages and their SiO emission". In: 586, A149, A149. DOI: 10.1051/0004-6361/201425404. arXiv: 1511.05138 [astro-ph.GA].

de Pree, C. G. et al. (1995). "Rotation and Outflow in Compact H II Regions: VLA Observations of the Molecular and Ionized Gas in NGC 6334A and NGC 6334F". In: 447, p. 220. DOI: 10.1086/175868.

de Vita, Ruggero, Michele Trenti, and Morgan MacLeod (2019). "Correlation between mass segregation and structural concentration in relaxed stellar clusters". In: 485.4, pp. 5752–5760. DOI: 10.1093/mnras/stz815. arXiv: 1903.07619 [astro-ph.GA].

Dobbs, C. L., A. Burkert, and J. E. Pringle (2011). "Why are most molecular clouds not gravitationally bound?" In: 413.4, pp. 2935–2942. DOI: 10.1111/j.1365-2966.2011.18371.x. arXiv: 1101.3414 [astro-ph.GA].

Dobbs, C. L. et al. (2008). "The ISM in spiral galaxies: can cooling in spiral shocks produce molecular clouds?" In: 389.3, pp. 1097–1110. DOI: 10.1111/j.1365-2966.2008.13646.x. arXiv: 0806.4312 [astro-ph].

Dobbs, Clare L., Ian A. Bonnell, and Paul C. Clark (2005). "Centrally condensed turbulent cores: massive stars or fragmentation?" In: 360.1, pp. 2–8. DOI: 10.1111/j.1365-2966.2005.08941.x. arXiv: astro-ph/0502479 [astro-ph].

Dopita, M. A., D. S. Mathewson, and V. L. Ford (1977). "Optical emission from shock waves. III. Abundances in supernova remnants." In: 214, pp. 179–188. DOI: 10.1086/155242.

Dotson, Jessie L. et al. (2010). "350 μm Polarimetry from the Caltech Submillimeter Observatory". In: 186.2, pp. 406–426. DOI: 10.1088/0067-0049/186/2/406. arXiv: 1001.2790 [astro-ph.GA].

Draine, B. T. (1980). "Interstellar shock waves with magnetic precursors". In: 241, pp. 1021–1038. DOI: 10.1086/158416.

Draine, Bruce T (2010). *Physics of the interstellar and intergalactic medium*. Princeton series in astrophysics. Princeton, NJ: Princeton University Press. URL: https://cds.cern.ch/record/2317527.

Duarte-Cabral, A. et al. (2014). "SiO emission from low- and high-velocity shocks in Cygnus-X massive dense clumps". In: 570, A1, A1. DOI: 10.1051/0004-6361/201423677. arXiv: 1407.6400 [astro-ph.GA].

Dutrey, A. (2007). "Circumstellar disks around young low-mass stars: Observed properties and lifetime". In: *Comptes Rendus Geoscience* 339.14-15, pp. 862–871. DOI: 10.1016/j.crte.2007.09.010.

Edelsbrunner, Herbert, David Letscher, and Afra Zomorodian (Feb. 2000). "Topological persistence and simplification". In: vol. 28, pp. 454 –463. ISBN: 0-7695-0850-2. DOI: 10.1109/SFCS.2000.892133.

Egan, M. P. et al. (1998). "A Population of Cold Cores in the Galactic Plane". In: 494.2, pp. L199–L202. DOI: 10.1086/311198.

Farge, M. et al. (1990). "Continuous wavelet analysis of coherent structures". In: *Studying Turbulence Using Numerical Simulation Databases. 3: Proceedings of the 1990 Summer Program*, pp. 331–348.

Federrath, Christoph et al. (2010). "Modeling Collapse and Accretion in Turbulent Gas Clouds: Implementation and Comparison of Sink Particles in AMR and SPH". In: 713.1, pp. 269–290. DOI: 10.1088/0004-637X/713/1/269. arXiv: 1001.4456 [astro-ph.SR].

Feigelson, Eric D. et al. (2009). "Stellar Clusters in the NGC 6334 Star-Forming Complex". In: 138.1, pp. 227–239. DOI: 10.1088/0004-6256/138/1/227. arXiv: 0905.0716 [astro-ph.GA].

Fiege, Jason D. and Ralph E. Pudritz (2000). "Prolate Cores in Filamentary Molecular Clouds". In: 534.1, pp. 291–308. DOI: 10.1086/308734. arXiv: astro-ph/9909356 [astro-ph].

Field, G. B. (1969). "The Physics of the Interstellar and Intergalactic Medium". In: *Astrophysics and General Relativity, Volume 1*. Vol. 1, p. 59.

Fischera, J. and P. G. Martin (2012). "Estimating distance, pressure, and dust opacity using submillimeter observations of self-gravitating filaments". In: 547, A86, A86. DOI: 10.1051/0004-6361/201219728. arXiv: 1209.4111 [astro-ph.GA].

Flower, D. R. and G. Pineau des Forêts (2003). "The influence of grains on the propagation and structure of C-type shock waves in interstellar molecular clouds". In: 343.2, pp. 390–400. DOI: 10.1046/j.1365-8711.2003.06716.x.

Forman, Robin (2002). "Discrete Morse Theory and the Cohomology Ring". In: *Transactions of the American Mathematical Society* 354.12, pp. 5063–5085. ISSN: 00029947. URL: http://www.jstor.org/stable/3072980.

Frey, Sándor and László Mosoni (2009). "A short introduction to radio interferometric image reconstruction". In: 53.11-12, pp. 307–311. DOI: 10.1016/j.newar.2010.07.005.

Galván-Madrid, R. et al. (2013). "MUSCLE W49: A Multi-Scale Continuum and Line Exploration of the Most Luminous Star Formation Region in the Milky Way. I. Data and the Mass Structure of the Giant Molecular Cloud". In: 779.2, 121, p. 121. DOI: 10.1088/0004-637X/779/2/121. arXiv: 1309.4129 [astro-ph.GA].

Garay, Guido et al. (1998). "Molecular Abundance Enhancements in the Highly Collimated Bipolar Outflow BHR 71". In: 509.2, pp. 768–784. DOI: 10.1086/306534.

Gerner, T. et al. (2014). "Chemical evolution in the early phases of massive star formation. I". In: 563, A97, A97. DOI: 10.1051/0004-6361/201322541. arXiv: 1401.6382 [astro-ph.SR].

Gezari, D. Y. (1982). "The remarkable 400micron source NGC 6334/I(North)." In: 259, pp. L29–L33. DOI: 10.1086/183842.

Gibb, A. G., F. Wyrowski, and L. G. Mundy (2004). "High-Velocity Gas toward Hot Molecular Cores: Evidence for Collimated Outflows from Embedded Sources". In: 616.1, pp. 301–318. DOI: 10.1086/424810. arXiv: astro-ph/0407276 [astro-ph].

Girart, J. M. et al. (2013). "DR 21(OH): A Highly Fragmented, Magnetized, Turbulent Dense Core". In: 772.1, 69, p. 69. DOI: 10.1088/0004-637X/772/1/69. arXiv: 1305.6509 [astro-ph.GA].

Gómez, Gilberto C. and Enrique Vázquez-Semadeni (2014). "Filaments in Simulations of Molecular Cloud Formation". In: 791.2, 124, p. 124. DOI: 10.1088/0004-637X/791/2/124. arXiv: 1308.6298 [astro-ph.GA].

Goodman, Alyssa A. et al. (2009). "A role for self-gravity at multiple length scales in the process of star formation". In: 457.7225, pp. 63–66. DOI: 10.1038/nature07609.

Green, D. A. (1993). "A power spectrum analysis of the angular scale of Galactic neutral hydrogen emission towards L = 140 deg, B = 0 deg". In: 262.2, pp. 327–342. DOI: 10.1093/mnras/262.2.327.

Gusdorf, A. et al. (2008a). "SiO line emission from C-type shock waves: interstellar jets and outflows". In: 482.3, pp. 809–829. DOI: 10.1051/0004-6361:20078900. arXiv: 0803.2791 [astro-ph].

Gusdorf, A. et al. (2008b). "SiO line emission from interstellar jets and outflows: silicon-containing mantles and non-stationary shock waves". In: 490.2, pp. 695–706. DOI: 10.1051/0004-6361:200810443.

Gutermuth, R. A. et al. (2009). "A Spitzer Survey of Young Stellar Clusters Within One Kiloparsec of the Sun: Cluster Core Extraction and Basic Structural Analysis". In: 184.1, pp. 18–83. DOI: 10.1088/0067-0049/184/1/18. arXiv: 0906.0201 [astro-ph.SR].

Hacar, A., M. Tafalla, and J. Alves (2017). "Fibers in the NGC 1333 proto-cluster". In: 606, A123, A123. DOI: 10.1051/0004-6361/201630348. arXiv: 1703.07029 [astro-ph.GA].

Hacar, A. et al. (2013). "Cores, filaments, and bundles: hierarchical core formation in the L1495/B213 Taurus region". In: 554, A55, A55. DOI: 10.1051/0004-6361/201220090. arXiv: 1303.2118 [astro-ph.GA].

Hacar, A. et al. (2017). "Gravitational collapse of the OMC-1 region". In: 602, L2, p. L2. DOI: 10.1051/0004-6361/201730732. arXiv: 1703.03464 [astro-ph.GA].

Hartmann, Lee, Javier Ballesteros-Paredes, and Fabian Heitsch (2012). "Rapid star formation and global gravitational collapse". In: 420.2, pp. 1457–1461. DOI: 10.1111/j.1365-2966.2011.20131.x. arXiv: 1111.2582 [astro-ph.SR].

Heitsch, F. and L. Hartmann (2008). "Flow-Driven Formation of Massive Cores: Rapid & Efficient?" In: *Massive Star Formation: Observations Confront Theory ASP Conference Series, Vol. 387, proceedings of the conference held 10-14 September 2007 at Heidelberg Convention Center, Heidelberg, Germany. Edited by Henrik Beuther, Hendrik Linz, and Thomas Henning. San Francisco: Astronomical Society of the Pacific, 2008., p.15*. Ed. by H. Beuther, H. Linz, and Th. Henning. Vol. 387. Astronomical Society of the Pacific Conference Series, p. 15.

Hennemann, M. et al. (2012). "The spine of the swan: a Herschel study of the DR21 ridge and filaments in Cygnus X". In: 543, L3, p. L3. DOI: 10.1051/0004-6361/201219429. arXiv: 1206.1243 [astro-ph.GA].

Hill, T. et al. (2010). "Physical characterization of southern massive star-forming regions using Parkes NH_3 observations". In: 402.4, pp. 2682–2702. DOI: 10.1111/j.1365-2966.2009.16101.x. arXiv: 0911.4479 [astro-ph.SR].

Hill, T. et al. (2011). "Filaments and ridges in Vela C revealed by Herschel: from low-mass to high-mass star-forming sites". In: 533, A94, A94. DOI: 10.1051/0004-6361/201117315. arXiv: 1108.0941 [astro-ph.GA].

Hosking, J. G. and A. P. Whitworth (2004). "Fragmentation of magnetized cloud cores". In: 347.3, pp. 1001–1010. DOI: 10.1111/j.1365-2966.2004.07274.x.

Houde, Martin et al. (2008). "B strengths in molecular clouds from ion and neutral line width differences". In: *Cosmic Agitator: Magnetic Fields in the Galaxy*, 39, p. 39.

Houlahan, Padraig and John Scalo (1992). "Recognition and Characterization of Hierarchical Interstellar Structure. II. Structure Tree Statistics". In: 393, p. 172. DOI: 10.1086/171495.

Hunter, T. R. et al. (2006). "Millimeter Multiplicity in NGC 6334 I and I(N)". In: 649.2, pp. 888–893. DOI: 10.1086/505965. arXiv: astro-ph/0605468 [astro-ph].

Hunter, T. R. et al. (2014). "Subarcsecond Imaging of the NGC 6334 I(N) Protocluster: Two Dozen Compact Sources and a Massive Disk Candidate". In: 788.2, 187, p. 187. DOI: 10.1088/0004-637X/788/2/187. arXiv: 1405.0496 [astro-ph.SR].

Inutsuka, Shu-Ichiro and Shoken M. Miyama (1992). "Self-similar Solutions and the Stability of Collapsing Isothermal Filaments". In: 388, p. 392. DOI: 10.1086/171162.

Inutsuka, Shu-ichiro and Shoken M. Miyama (1997). "A Production Mechanism for Clusters of Dense Cores". In: 480.2, pp. 681–693. DOI: 10.1086/303982.

Ivezić, Ž. et al. (2014). *Statistics, Data Mining, and Machine Learning in Astronomy: A Practical Python Guide for the Analysis of Survey Data*. Princeton Series in Modern Observational Astronomy. Princeton University Press. ISBN: 9780691151687. URL: https://books.google.de/books?id=AvE3YgEACAAJ.

Jiménez-Serra, I. et al. (2010). "Parsec-scale SiO emission in an infrared dark cloud". In: 406.1, pp. 187–196. DOI: 10.1111/j.1365-2966.2010.16698.x. arXiv: 1003.3463 [astro-ph.SR].

Johnstone, D. and J. Bally (1999). "JCMT/SCUBA sub-millimetre wavelength imaging of star formation in the Orion A molecular cloud." In: 93.4, pp. 179–180.

Johnstone, Doug and John Bally (2006). "Large-Area Mapping at 850 μm. V. Analysis of the Clump Distribution in the Orion A South Molecular Cloud". In: 653.1, pp. 383–397. DOI: 10.1086/508852. arXiv: astro-ph/0609171 [astro-ph].

Juárez, Carmen et al. (2017). "Magnetized Converging Flows toward the Hot Core in the Intermediate/High-mass Star-forming Region NGC 6334 V". In: 844.1, 44, p. 44. DOI: 10.3847/1538-4357/aa78a6. arXiv: 1706.03534 [astro-ph.SR].

Kalberla, P. M. W. et al. (2016). "Cold Milky Way HI Gas in Filaments". In: 821.2, 117, p. 117. DOI: 10.3847/0004-637X/821/2/117. arXiv: 1602.07604 [astro-ph.GA].

Kaufman, Leonard and Peter J. Rousseeuw (1990). *Finding Groups in Data: An Introduction to Cluster Analysis*. John Wiley. ISBN: 978-0-47031680-1.

Keto, Eric and Kenneth Wood (2006). "Observations on the Formation of Massive Stars by Accretion". In: 637.2, pp. 850–859. DOI: 10.1086/498611. arXiv: astro-ph/0510176 [astro-ph].

Kirby, J. F. (2005). "Which wavelet best reproduces the Fourier power spectrum?" In: *Computers Geosciences* 31, pp. 846–864.

Kirk, Helen et al. (2013a). "Filamentary Accretion Flows in the Embedded Serpens South Protocluster". In: 766.2, 115, p. 115. DOI: 10.1088/0004-637X/766/2/115. arXiv: 1301.6792 [astro-ph.GA].

— (2013b). "Filamentary Accretion Flows in the Embedded Serpens South Protocluster". In: 766.2, 115, p. 115. DOI: 10.1088/0004-637X/766/2/115. arXiv: 1301.6792 [astro-ph.GA].

Klessen, R. S. et al. (2004). "Gravoturbulent Star Cluster Formation". In: *The Formation and Evolution of Massive Young Star Clusters, ASP Conference Series, Vol. 322. Edited by H.J.G.L.M. Lamers, L.J. Smith, and A. Nota. San Francisco: Astronomical Society of the Pacific, 2004., p.299-308*. Ed. by Henry J. G. L. M. Lamers, Linda J. Smith, and Antonella Nota. Vol. 322. Astronomical Society of the Pacific Conference Series, pp. 299–308.

Klessen, Ralf S. and Simon C. O. Glover (2016). "Physical Processes in the Interstellar Medium". In: *Saas-Fee Advanced Course* 43, p. 85. DOI: 10.1007/978-3-662-47890-5_2. arXiv: 1412.5182 [astro-ph.GA].

Koch, Eric W. and Erik W. Rosolowsky (2015). "Filament identification through mathematical morphology". In: 452.4, pp. 3435–3450. DOI: 10.1093/mnras/stv1521. arXiv: 1507.02289 [astro-ph.GA].

Könyves, V. et al. (2010). "The Aquila prestellar core population revealed by Herschel". In: 518, L106, p. L106. DOI: 10.1051/0004-6361/201014689. arXiv: 1005.2981 [astro-ph.SR].

Könyves, V. et al. (2015). "A census of dense cores in the Aquila cloud complex: SPIRE/PACS observations from the Herschel Gould Belt survey". In: 584, A91, A91. DOI: 10.1051/0004-6361/201525861. arXiv: 1507.05926 [astro-ph.GA].

Kroupa, P. (2001). "The Local Stellar Initial Mass Function". In: *Dynamics of Star Clusters and the Milky Way, ASP Conference Series, Vol. 228. Edited by S. Deiters, B. Fuchs, R. Spurzem, A. Just, and R. Wielen. San Francisco: Astronomical Society of the Pacific. ISBN: 1-58381-060-9, 2001., p.187*. Ed. by S. Deiters et al. Vol. 228. Astronomical Society of the Pacific Conference Series, p. 187.

Krumholz, Mark R., Richard I. Klein, and Christopher F. McKee (2007). "Molecular Line Emission from Massive Protostellar Disks: Predictions for ALMA and EVLA". In: 665.1, pp. 478–491. DOI: 10.1086/519305. arXiv: 0705.0536 [astro-ph].

Krumholz, Mark R. and Christopher F. McKee (2005). "A General Theory of Turbulence-regulated Star Formation, from Spirals to Ultraluminous Infrared Galaxies". In: 630.1, pp. 250–268. DOI: 10.1086/431734. arXiv: astro-ph/0505177 [astro-ph].

Krumholz, Mark R. et al. (2009). "The Formation of Massive Star Systems by Accretion". In: *Science* 323.5915, p. 754. DOI: 10.1126/science.1165857. arXiv: 0901.3157 [astro-ph.SR].

Krumholz, Mark R. et al. (2010). "Radiation Feedback, Fragmentation, and the Environmental Dependence of the Initial Mass Function". In: 713.2, pp. 1120–1133. DOI: 10.1088/0004-637X/713/2/1120. arXiv: 1001.0971 [astro-ph.GA].

Kruskal Jr., Joseph B. (1956). "On the shortest spanning subtree of a graph and the traveling salesman problem". In: *Proc. Amer. Math. Soc.* 7, pp. 48–50. ISSN: 0002-9939. DOI: 10.2307/2033241. URL: https://doi.org/10.2307/2033241.

Kuiper, Rolf, Harold W. Yorke, and Neal J. Turner (2015). "Protostellar Outflows and Radiative Feedback from Massive Stars". In: 800.2, 86, p. 86. DOI: 10.1088/0004-637X/800/2/86. arXiv: 1412.6528 [astro-ph.SR].

Kuiper, Rolf et al. (2010). "Circumventing the Radiation Pressure Barrier in the Formation of Massive Stars via Disk Accretion". In: 722.2, pp. 1556–1576. DOI: 10.1088/0004-637X/722/2/1556. arXiv: 1008.4516 [astro-ph.SR].

Kurtz, S., E. Churchwell, and D. O. S. Wood (1994). "Ultracompact H II Regions. II. New High-Resolution Radio Images". In: 91, p. 659. DOI: 10.1086/191952.

Kurtz, S. and P. Hofner (2005). "Water Masers Toward Ultracompact H II Regions". In: 130.2, pp. 711–720. DOI: 10.1086/431546. arXiv: astro-ph/0507039 [astro-ph].

Kurtz, S. E. (2000). "Ultracompact H II Regions: New Challenges". In: *Revista Mexicana de Astronomia y Astrofisica Conference Series*. Ed. by S. J. Arthur, N. S. Brickhouse, and J. Franco. Vol. 9. Revista Mexicana de Astronomia y Astrofisica Conference Series, pp. 169–176.

Kwan, J. and F. Valdes (1983). "Spiral gravitational potentials and the mass growth of molecular clouds". In: 271, pp. 604–610. DOI: 10.1086/161227.

Lada, Charles J. (1987). "Star formation: from OB associations to protostars." In: *Star Forming Regions*. Ed. by Manuel Peimbert and Jun Jugaku. Vol. 115. IAU Symposium, p. 1.

Lada, Charles J. and Elizabeth A. Lada (2003). "Embedded Clusters in Molecular Clouds". In: 41, pp. 57–115. DOI: 10.1146/annurev.astro.41.011802.094844. arXiv: astro-ph/0301540 [astro-ph].

Landy, Stephen D. and Alexander S. Szalay (1993). "Bias and Variance of Angular Correlation Functions". In: 412, p. 64. DOI: 10.1086/172900.

Larson, R. B. (1981). "Turbulence and star formation in molecular clouds." In: 194, pp. 809–826. DOI: 10.1093/mnras/194.4.809.

— (1984). "Gravitational torques and star formation". In: 206, pp. 197–207. DOI: 10.1093/mnras/206.1.197.

Lee, Y. N. and P. Hennebelle (2016). "The gaseous proto-cluster as a product of gravo-turbulent interaction: modified local environment for stellar cluster formation?" In: *SF2A-2016: Proceedings of the Annual meeting of the French Society of Astronomy and Astrophysics*, pp. 189–197.

Lefloch, B. et al. (1998). "Widespread SiO Emission in NGC 1333". In: 504.2, pp. L109–L112. DOI: 10.1086/311581.

Li, H. et al. (2006). "Results of SPARO 2003: Mapping Magnetic Fields in Giant Molecular Clouds". In: 648.1, pp. 340–354. DOI: 10.1086/505858. arXiv: astro-ph/0602455 [astro-ph].

Li, Hua-bai et al. (2015). "Self-similar fragmentation regulated by magnetic fields in a region forming massive stars". In: *Nature* 520.7548, 518–521. ISSN: 1476-4687. DOI: 10.1038/nature14291. URL: http://dx.doi.org/10.1038/nature14291.

Liu, Hauyu Baobab (2019). "The Anomalously Low (Sub)Millimeter Spectral Indices of Some Protoplanetary Disks May Be Explained By Dust Self-scattering". In: 877.2, L22, p. L22. DOI: 10.3847/2041-8213/ab1f8e. arXiv: 1904.00333 [astro-ph.SR].

Liu, Hauyu Baobab et al. (2015). "ALMA Resolves the Spiraling Accretion Flow in the Luminous OB Cluster-forming Region G33.92+0.11". In: 804.1, 37, p. 37. DOI: 10.1088/0004-637X/804/1/37. arXiv: 1505.04255 [astro-ph.SR].

Louvet, F. et al. (2016). "Tracing extended low-velocity shocks through SiO emission. Case study of the W43-MM1 ridge". In: 595, A122, A122. DOI: 10.1051/0004-6361/201629077. arXiv: 1607.08668 [astro-ph.GA].

Lu, Xing et al. (2018). "Filamentary Fragmentation and Accretion in High-mass Star-forming Molecular Clouds". In: 855.1, 9, p. 9. DOI: 10.3847/1538-4357/aaad11. arXiv: 1801.05955 [astro-ph.GA].

MacKay, David J. C. (2002). *Information Theory, Inference & Learning Algorithms*. New York, NY, USA: Cambridge University Press. ISBN: 0521642981.

MacQueen, J. (1967). "Some methods for classification and analysis of multivariate observations". In: pp. 281–297. URL: https://projecteuclid.org/euclid.bsmsp/1200512992.

Maddalena, R. J. et al. (1986). "The Large System of Molecular Clouds in Orion and Monoceros". In: 303, p. 375. DOI: 10.1086/164083.

Marr, J.M., R.L. Snell, and S.E. Kurtz (2015). *Fundamentals of Radio Astronomy: Observational Methods*. Series in Astronomy and Astrophysics. CRC Press. ISBN: 9781498770194. URL: https://books.google.de/books?id=T54oCwAAQBAJ.

Martin-Pintado, J., R. Bachiller, and A. Fuente (1992). "SiO emission as a tracer of shocked gas in molecular outflows." In: 254, pp. 315–326.

Maschberger, Th. et al. (2010). "Properties of hierarchically forming star clusters". In: 404.2, pp. 1061–1080. DOI: 10.1111/j.1365-2966.2010.16346.x. arXiv: 1002.4401 [astro-ph.GA].

Mathieu, R. D. et al. (2000). "Young Binary Stars and Associated Disks". In: *Protostars and Planets IV*. Ed. by V. Mannings, A. P. Boss, and S. S. Russell, p. 703. arXiv: astro-ph/9909424 [astro-ph].

May, P. W. et al. (2000). "Sputtering of grains in C-type shocks". In: 318.3, pp. 809–816. DOI: 10.1046/j.1365-8711.2000.03796.x.

McCray, R. (1975). "Gas flows in binary X-ray systems". In: *X-Rays in Space - Cosmic, Solar, and Auroral X-Rays, Volume 1*. Vol. 1, pp. 547–564.

McKee, C. F. (2004). "Massive Star Formation: Now and Then". In: *Star Formation in the Interstellar Medium: In Honor of David Hollenbach, Chris McKee and Frank Shu, ASP Conference Proceedings, Vol. 323. Edited by D. Johnstone, F.C. Adams, D.N.C. Lin, D.A. Neufeld, and E.C. Ostriker. San Francisco: Astronomical Society of the Pacific, 2004., p.21*. Ed. by D. Johnstone et al. Vol. 323. Astronomical Society of the Pacific Conference Series, p. 21.

McKee, C. F. and J. P. Ostriker (1977). "A theory of the interstellar medium: three components regulated by supernova explosions in an inhomogeneous substrate." In: 218, pp. 148–169. DOI: 10.1086/155667.

McKee, Christopher F. and Eve C. Ostriker (2007). "Theory of Star Formation". In: 45.1, pp. 565–687. DOI: 10.1146/annurev.astro.45.051806.110602. arXiv: 0707.3514 [astro-ph].

McKee, Christopher F. and Jonathan C. Tan (2002). "Massive star formation in 100,000 years from turbulent and pressurized molecular clouds". In: 416.6876, pp. 59–61. DOI: 10.1038/416059a. arXiv: astro-ph/0203071 [astro-ph].

McNamara, Bernard J. and Kazuhiro Sekiguchi (1986). "An Internal Motion Analysis of the Open Cluster M35". In: 310, p. 613. DOI: 10.1086/164714.

Medina, S. N. X. et al. (2018). "Richness of compact radio sources in NGC 6334D to F". In: 610, A27, A27. DOI: 10.1051/0004-6361/201731774. arXiv: 1711.02934 [astro-ph.GA].

Men'shchikov, A. (2013). "A multi-scale filament extraction method: getfilaments". In: 560, A63, A63. DOI: 10.1051/0004-6361/201321885. arXiv: 1309.2170 [astro-ph.GA].

Men'shchikov, A. et al. (2010). "Filamentary structures and compact objects in the Aquila and Polaris clouds observed by Herschel". In: 518, L103, p. L103. DOI: 10.1051/0004-6361/201014668. arXiv: 1005.3115 [astro-ph.GA].

Miville-Deschênes, M. A. et al. (2003). "High resolution 21 cm mapping of the Ursa Major Galactic cirrus: Power spectra of the high-latitude H I gas". In: 411, pp. 109–121. DOI: 10.1051/0004-6361:20031297. arXiv: astro-ph/0306570 [astro-ph].

Molinari, S. et al. (2010). "Clouds, filaments, and protostars: The Herschel Hi-GAL Milky Way". In: 518, L100, p. L100. DOI: 10.1051/0004-6361/201014659. arXiv: 1005.3317 [astro-ph.GA].

Möller, T., C. Endres, and P. Schilke (2017). "eXtended CASA Line Analysis Software Suite (XCLASS)". In: 598, A7, A7. DOI: 10.1051/0004-6361/201527203. arXiv: 1508.04114 [astro-ph.IM].

Möller, T. et al. (2013). "Modeling and Analysis Generic Interface for eXternal numerical codes (MAGIX)". In: 549, A21, A21. DOI: 10.1051/0004-6361/201220063. arXiv: 1210.6466 [astro-ph.IM].

Motte, F. and P. André (2001). "Wide-field (Sub)millimeter Continuum Surveys of Protoclusters: Clues to the Origin of the IMF". In: *From Darkness to Light: Origin and Evolution of Young Stellar Clusters, ASP Conference Proceedings, Vol. 243. Edited by Thierry Montmerle and Philippe André. San Francisco: Astronomical Society of the Pacific, ISBN: 1-58381-081-1, 2001, p.301*. Ed. by Thierry Montmerle and Philippe André. Vol. 243. Astronomical Society of the Pacific Conference Series, p. 301.

Motte, F., P. Andre, and R. Neri (1998). "The initial conditions of star formation in the rho Ophiuchi main cloud: wide-field millimeter continuum mapping". In: 336, pp. 150–172.

Motte, Frédérique, Sylvain Bontemps, and Fabien Louvet (2018). "High-Mass Star and Massive Cluster Formation in the Milky Way". In: 56, pp. 41–82. DOI: 10.1146/annurev-astro-091916-055235. arXiv: 1706.00118 [astro-ph.GA].

Myers, Philip C. (2009). "Filamentary Structure of Star-forming Complexes". In: 700.2, pp. 1609–1625. DOI: 10.1088/0004-637X/700/2/1609. arXiv: 0906.2005 [astro-ph.GA].

— (2012). "Mass and Luminosity Evolution of Young Stellar Objects". In: 752.1, 9, p. 9. DOI: 10.1088/0004-637X/752/1/9. arXiv: 1204.1032 [astro-ph.GA].

Nguyen Luong, Q. et al. (2011). "W43: the closest molecular complex of the Galactic bar?" In: 529, A41, A41. DOI: 10.1051/0004-6361/201016271. arXiv: 1102.3460 [astro-ph.SR].

Nguyen-Lu'o'ng, Q. et al. (2013). "Low-velocity Shocks Traced by Extended SiO Emission along the W43 Ridges: Witnessing the Formation of Young Massive Clusters". In: 775.2, 88, p. 88. DOI: 10.1088/0004-637X/775/2/88. arXiv: 1306.0547 [astro-ph.GA].

Nisini, B. et al. (2007). "Warm SiO gas in molecular bullets associated with protostellar outflows". In: 462.1, pp. 163–172. DOI: 10.1051/0004-6361:20065621. arXiv: astro-ph/0610037 [astro-ph].

Novak, G., J. L. Dotson, and H. Li (2009). "Dispersion of Observed Position Angles of Submillimeter Polarization in Molecular Clouds". In: 695.2, pp. 1362–1369. DOI: 10.1088/0004-637X/695/2/1362. arXiv: 0707.2818 [astro-ph].

Offner, S. S. R. et al. (2014). "The Origin and Universality of the Stellar Initial Mass Function". In: *Protostars and Planets VI*. DOI: 10.2458/azu_uapress_9780816531240-ch003. URL: http://dx.doi.org/10.2458/azu_uapress_9780816531240-ch003.

Offner, Stella S. R. et al. (2010). "The Formation of Low-mass Binary Star Systems Via Turbulent Fragmentation". In: 725.2, pp. 1485–1494. DOI: 10.1088/0004-637X/725/2/1485. arXiv: 1010.3702 [astro-ph.SR].

Offringa, A. R. and O. Smirnov (2017). "An optimized algorithm for multiscale wideband deconvolution of radio astronomical images". In: 471.1, pp. 301–316. DOI: 10.1093/mnras/stx1547. arXiv: 1706.06786 [astro-ph.IM].

Onishi, Toshikazu et al. (2002). "A Complete Search for Dense Cloud Cores in Taurus". In: 575.2, pp. 950–973. DOI: 10.1086/341347.

Ossenkopf, V. and Th. Henning (1994). "Dust opacities for protostellar cores." In: 291, pp. 943–959.

Ostriker, J. (1964). "On the Oscillations and the Stability of a Homogeneous Compressible Cylinder." In: 140, p. 1529. DOI: 10.1086/148057.

Padoan, Paolo and Åke Nordlund (2002). "The Stellar Initial Mass Function from Turbulent Fragmentation". In: 576.2, pp. 870–879. DOI: 10.1086/341790. arXiv: astro-ph/0011465 [astro-ph].

Padoan, Paolo et al. (1999). "Supersonic Turbulence in the Perseus Molecular Cloud". In: 525.1, pp. 318–329. DOI: 10.1086/307864. arXiv: astro-ph/9905383 [astro-ph].

Padoan, Paolo et al. (2001). "Theoretical Models of Polarized Dust Emission from Protostellar Cores". In: 559.2, pp. 1005–1018. DOI: 10.1086/322504. arXiv: astro-ph/0104231 [astro-ph].

Palau, Aina et al. (2013). "Early Stages of Cluster Formation: Fragmentation of Massive Dense Cores down to <~1000 AU". In: 762.2, 120, p. 120. DOI: 10.1088/0004-637X/762/2/120. arXiv: 1211.2666 [astro-ph.GA].

Palau, Aina et al. (2015). "Gravity or turbulence? - III. Evidence of pure thermal Jeans fragmentation at 0.1 pc scale". In: 453.4, pp. 3785–3797. DOI: 10.1093/mnras/stv1834. arXiv: 1504.07644 [astro-ph.GA].

Palau, Aina et al. (2018). "Thermal Jeans Fragmentation within 1000 au in OMC-1S". In: 855.1, 24, p. 24. DOI: 10.3847/1538-4357/aaad03. arXiv: 1706.04623 [astro-ph.GA].

Palla, F., S. W. Stahler, and G. Parigi (1993). "New evolutionary tracks of pre-main-sequence stars". In: *Inside the stars; Proceedings of the 137th IAU Colloquium, Univ. of Vienna, Austria, Apr. 13-18, 1992. Astronomical Society of the Pacific (ASP Conference Series. Vol. 40), Edited by Werner W. Weiss and Annie Baglin, 1993, p.437*. Ed. by Werner W. Weiss and Annie Baglin. Vol. 40. Astronomical Society of the Pacific Conference Series, p. 437.

Palmeirim, P. et al. (2013). "Herschel view of the Taurus B211/3 filament and striations: evidence of filamentary growth?" In: 550, A38, A38. DOI: 10.1051/0004-6361/201220500. arXiv: 1211.6360 [astro-ph.SR].

Panagia, N. and M. Felli (1975). "The spectrum of the free-free radiation from extended envelopes." In: 39, pp. 1–5.

Parker, Richard J. and Simon P. Goodwin (2015). "Comparisons between different techniques for measuring mass segregation". In: 449.4, pp. 3381–3392. DOI: 10.1093/mnras/stv539. arXiv: 1503.02692 [astro-ph.GA].

Peebles, P. J. E. (1980). "Statistics of the distribution of galaxies". In: *Ninth Texas Symposium on Relativistic Astrophysics*. Vol. 336, pp. 161–171. DOI: 10.1111/j.1749-6632.1980.tb15927.x.

Perault, M. et al. (1996). "First ISOCAM images of the Milky Way." In: 315, pp. L165–L168.

Peretto, N. and G. A. Fuller (2010). "A Statistical Study of the Mass and Density Structure of Infrared Dark Clouds". In: 723.1, pp. 555–562. DOI: 10.1088/0004-637X/723/1/555. arXiv: 1009.0716 [astro-ph.GA].

Peretto, N., P. Hennebelle, and P. André (2007). "Probing the formation of intermediate- to high-mass stars in protoclusters. II. Comparison between millimeter interferometric observations of NGC 2264-C and SPH simulations of a collapsing clump". In: 464.3, pp. 983–994. DOI: 10.1051/0004-6361:20065653. arXiv: astro-ph/0611277 [astro-ph].

Peretto, N. et al. (2013). "Global collapse of molecular clouds as a formation mechanism for the most massive stars". In: 555, A112, A112. DOI: 10.1051/0004-6361/201321318. arXiv: 1307.2590 [astro-ph.GA].

Peretto, N. et al. (2014). "SDC13 infrared dark clouds: Longitudinally collapsing filaments?" In: 561, A83, A83. DOI: 10.1051/0004-6361/201322172. arXiv: 1311.0203 [astro-ph.GA].

Perley, R.A. et al. (1989). *Synthesis imaging in radio astronomy: a collection of lectures from the third NRAO synthesis imaging summer school*. Astronomical Society of the Pacific conference series. Astronomical Society of the Pacific. ISBN: 9780937707234.

Persi, P. and M. Tapia (2008). "Star Formation in NGC 6334". In: *Handbook of Star Forming Regions, Volume II: The Southern Sky ASP Monograph Publications, Vol. 5. Edited by Bo Reipurth, p.456*. Ed. by B. Reipurth. Vol. 5, p. 456.

Peters, T. et al. (2011). "Radiative Feedback in Massive Star and Cluster Formation". In: *Stellar Clusters & Associations: A RIA Workshop on Gaia*, pp. 229–234. arXiv: 1110.2892 [astro-ph.SR].

Pfalzner, Susanne and Thomas Kaczmarek (2013). "The expansion of massive young star clusters - observation meets theory". In: 559, A38, A38. DOI: 10.1051/0004-6361/201322134. arXiv: 1309.0315 [astro-ph.GA].

Pillai, T. et al. (2011). "Probing the initial conditions of high-mass star formation. II. Fragmentation, stability, and chemistry towards high-mass star-forming regions G29.96-0.02 and G35.20-1.74". In: 530, A118, A118. DOI: 10.1051/0004-6361/201015899. arXiv: 1105.0004 [astro-ph.GA].

Planck Collaboration (2016). "Planck intermediate results - XXXII. The relative orientation between the magnetic field and structures traced by interstellar dust". In: *A&A* 586, A135. DOI: 10.1051/0004-6361/201425044. URL: https://doi.org/10.1051/0004-6361/201425044.

Plunkett, Adele L. et al. (2018). "Distribution of Serpens South protostars revealed with ALMA". In: 615, A9, A9. DOI: 10.1051/0004-6361/201732372. arXiv: 1804.02405 [astro-ph.SR].

Pokhrel, Riwaj et al. (2018). "Hierarchical Fragmentation in the Perseus Molecular Cloud: From the Cloud Scale to Protostellar Objects". In: 853.1, 5, p. 5. DOI: 10.3847/1538-4357/aaa240. arXiv: 1712.04960 [astro-ph.GA].

Pudritz, R. E. and N. K. R. Kevlahan (2013). "Shock interactions, turbulence and the origin of the stellar mass spectrum". In: *Philosophical Transactions of the Royal Society of London Series A* 371.2003, pp. 20120248–20120248. DOI: 10.1098/rsta.2012.0248. arXiv: 1201.2650 [astro-ph.GA].

Rathborne, J. M. et al. (2015). "A Cluster in the Making: ALMA Reveals the Initial Conditions for High-mass Cluster Formation". In: 802.2, 125, p. 125. DOI: 10.1088/0004-637X/802/2/125. arXiv: 1501.07368 [astro-ph.GA].

Robitaille, J. F., G. Joncas, and M. A. Miville-Deschênes (2014). "Multiscale analysis of Galactic dust emission using complex wavelet transforms - I. Separation of Gaussian and non-Gaussian fluctuations in Herschel observations". In: 440.3, pp. 2726–2741. DOI: 10.1093/mnras/stu375.

Robitaille, J. F. et al. (2019). "Exposing the plural nature of molecular clouds. Extracting filaments and the cosmic infrared background against the true scale-free interstellar medium". In: 628, A33, A33. DOI: 10.1051/0004-6361/201935545. arXiv: 1905.11492 [astro-ph.GA].

Rodríguez, L. F. et al. (2003). "Radio Detection of the Exciting Sources of Shell H II Regions in NGC 6334". In: *Revista Mexicana de Astronomia y Astrofisica Conference Series*. Ed. by Jane Arthur and William J. Henney. Vol. 15. Revista Mexicana de Astronomia y Astrofisica Conference Series, pp. 194–196.

Rosolowsky, E. W. et al. (2008). "Structural Analysis of Molecular Clouds: Dendrograms". In: 679.2, pp. 1338–1351. DOI: 10.1086/587685. arXiv: 0802.2944 [astro-ph].

Rousseeuw, Peter (Nov. 1987). "Silhouettes: A Graphical Aid to the Interpretation and Validation of Cluster Analysis". In: *Journal of Computational and Applied Mathematics* 20.1, pp. 53–65. ISSN: 0377-0427. DOI: 10.1016/0377-0427(87)90125-7. URL: http://svn.donarmstrong.com/don/trunk/projects/research/papers_to_read/statistics/silhouettes_a_graphical_aid_to_the_interpretation_and_validation_of_cluster_analysis_rousseeuw_j_comp_app_math_20_53_1987.pdf.

Russeil, D. et al. (2010). "The earliest phases of high-mass star formation: the NGC 6334-NGC 6357 complex". In: 515, A55, A55. DOI: 10.1051/0004-6361/200913632.

Russeil, D. et al. (2013). "The Herschel view of the massive star-forming region NGC 6334". In: 554, A42, A42. DOI: 10.1051/0004-6361/201219971.

Rybicki, George B. and Alan P. Lightman (1986). *Radiative Processes in Astrophysics*.

Sadaghiani, M. et al. (Mar. 2020). "Physical properties of the star-forming clusters in NGC 6334. A study of the continuum dust emission with ALMA". In: 635, A2, A2. DOI: 10.1051/0004-6361/201935699. arXiv: 1911.06579 [astro-ph.SR].

Salji, C. J. et al. (2015). "The JCMT Gould Belt Survey: properties of star-forming filaments in Orion A North". In: 449.2, pp. 1782–1796. DOI: 10.1093/mnras/stv369.

Salpeter, Edwin E. (1955). "The Luminosity Function and Stellar Evolution." In: 121, p. 161. DOI: 10.1086/145971.

Sánchez, N. and E. J. Alfaro (2010). "The fractal spatial distribution of stars in open clusters and stellar associations". In: *Lecture Notes and Essays in Astrophysics, vol. 4, Name of the proceedings book: Lecture Notes and Essays in Proceedings of the conference held 7-11 September, 2009 at Ciudad Real (Spain). Edited by A. Ulla and M. Manteiga. Tórculo Press (Vigo, Spain). ISBN: 978-84-936098-8-7, p. 1-11.* Vol. 4, pp. 1–11.

Sánchez-Monge, Á. et al. (2013a). "Evolution and excitation conditions of outflows in high-mass star-forming regions". In: 557, A94, A94. DOI: 10.1051/0004-6361/201321589. arXiv: 1305.3471 [astro-ph.GA].

Sánchez-Monge, Á. et al. (2015). "Mass accretion flows in the high-mass star forming complex NGC 6334". In: *EAS Publications Series*. Vol. 75-76. EAS Publications Series, pp. 269–272. DOI: 10.1051/eas/1575053.

Sánchez-Monge, Á. et al. (2017). "The physical and chemical structure of Sagittarius B2. II. Continuum millimeter emission of Sgr B2(M) and Sgr B2(N) with ALMA". In: 604, A6, A6. DOI: 10.1051/0004-6361/201730426. arXiv: 1704.01805 [astro-ph.GA].

Sánchez-Monge, Álvaro et al. (2013b). "Deciphering the Ionized Gas Content in the Massive Star-forming Complex G75.78+0.34". In: 766.2, 114, p. 114. DOI: 10.1088/0004-637X/766/2/114. arXiv: 1302.3018 [astro-ph.GA].

Sánchez-Monge, Álvaro et al. (2013c). "Properties of dense cores in clustered massive star-forming regions at high angular resolution". In: 432.4, pp. 3288–3319. DOI: 10.1093/mnras/stt679. arXiv: 1304.5136 [astro-ph.GA].

Sanders, D. B., N. Z. Scoville, and P. M. Solomon (1985). "Giant molecular clouds in the galaxy. II. Characteristics of discretefeatures." In: 289, pp. 373–387. DOI: 10.1086/162897.

Sanhueza, Patricio et al. (2013). "Distinct Chemical Regions in the "Prestellar" Infrared Dark Cloud G028.23-00.19". In: 773.2, 123, p. 123. DOI: 10.1088/0004-637X/773/2/123. arXiv: 1307.1474 [astro-ph.GA].

Schilke, P. et al. (1997). "SiO production in interstellar shocks." In: 321, pp. 293–304.

Schneider, N. et al. (2010). "Dynamic star formation in the massive DR21 filament". In: 520, A49, A49. DOI: 10.1051/0004-6361/201014481. arXiv: 1003.4198 [astro-ph.GA].

Schneider, N. et al. (2012). "Cluster-formation in the Rosette molecular cloud at the junctions of filaments". In: 540, L11, p. L11. DOI: 10.1051/0004-6361/201118566. arXiv: 1203.6472 [astro-ph.GA].

Schneider, S. and B. G. Elmegreen (1979). "A catalog of dark globular filaments." In: 41, pp. 87–95. DOI: 10.1086/190609.

Schwörer, A. et al. (2019). "The physical and chemical structure of Sagittarius B2. IV. Converging filaments in the high-mass cluster forming region Sgr B2(N)". In: 628, A6, A6. DOI: 10.1051/0004-6361/201935200. arXiv: 1906.10979 [astro-ph.GA].

Seifahrt, Andreas et al. (2008). "Synergy of multi-frequency studies from observations of NGC 6334I". In: *Journal of Physics Conference Series*. Vol. 131. Journal of Physics Conference Series, 012030, p. 012030. DOI: 10.1088/1742-6596/131/1/012030. arXiv: 0811.2495 [astro-ph].

Seifried, D. and S. Walch (2015). "The impact of turbulence and magnetic field orientation on star-forming filaments". In: 452.3, pp. 2410–2422. DOI: 10.1093/mnras/stv1458. arXiv: 1503.01659 [astro-ph.GA].

Shandarin, S. F. and Ya. B. Zeldovich (1989). "The large-scale structure of the universe: Turbulence, intermittency, structures in a self-gravitating medium". In: *Reviews of Modern Physics* 61.2, pp. 185–220. DOI: 10.1103/RevModPhys.61.185.

Shetty, Rahul and Eve C. Ostriker (2008). "Cloud and Star Formation in Disk Galaxy Models with Feedback". In: 684.2, pp. 978–995. DOI: 10.1086/590383. arXiv: 0805.3996 [astro-ph].

Shirley, Yancy L. et al. (2011). "Mustang 3.3 mm Continuum Observations of Class 0 Protostars". In: 141.2, 39, p. 39. DOI: 10.1088/0004-6256/141/2/39. arXiv: 1011.3817 [astro-ph.GA].

Shu, Frank H., Fred C. Adams, and Susana Lizano (1987). "Star formation in molecular clouds: observation and theory." In: 25, pp. 23–81. DOI: 10.1146/annurev.aa.25.090187.000323.

Simon, M., A. Dutrey, and S. Guilloteau (2000). "Dynamical Masses of T Tauri Stars and Calibration of Pre-Main-Sequence Evolution". In: 545.2, pp. 1034–1043. DOI: 10.1086/317838. arXiv: astro-ph/0008370 [astro-ph].

Smith, Rowan et al. (2013). "Signatures of Dynamical Collapse during High-Mass Star Formation". In: *Protostars and Planets VI Posters*.

Smith, Rowan J., Steven Longmore, and Ian Bonnell (2009a). "The simultaneous formation of massive stars and stellar clusters". In: 400.4, pp. 1775–1784. DOI: 10.1111/j.1365-2966.2009.15621.x. arXiv: 0908.3910 [astro-ph.SR].

— (2009b). "The simultaneous formation of massive stars and stellar clusters". In: 400.4, pp. 1775–1784. DOI: 10.1111/j.1365-2966.2009.15621.x. arXiv: 0908.3910 [astro-ph.SR].

Sousbie, T., C. Pichon, and H. Kawahara (2011). "The persistent cosmic web and its filamentary structure - II. Illustrations". In: 414.1, pp. 384–403. DOI: 10.1111/j.1365-2966.2011.18395.x. arXiv: 1009.4014 [astro-ph.CO].

Spera, Mario and Roberto Capuzzo-Dolcetta (2017). "Rapid mass segregation in small stellar clusters". In: 362.12, 233, p. 233. DOI: 10.1007/s10509-017-3209-6. arXiv: 1501.01040 [astro-ph.GA].

Spitzer Lyman, Jr. (1969). "Equipartition and the Formation of Compact Nuclei in Spherical Stellar Systems". In: 158, p. L139. DOI: 10.1086/180451.

Storm, Shaye et al. (2014). "Dendrogram Analysis of Large-Area CARMA Images in Perseus: the Dense Gas in NGC 1333, Barnard 1, and L1451". In: *American Astronomical Society Meeting Abstracts #223*. Vol. 223. American Astronomical Society Meeting Abstracts, 214.06, p. 214.06.

Suri, Sümeyye et al. (2019). "The CARMA-NRO Orion Survey. Filamentary structure as seen in $C^{18}O$ emission". In: 623, A142, A142. DOI: 10.1051/0004-6361/201834049. arXiv: 1901.00176 [astro-ph.GA].

Tan, J. C. et al. (2014). "Massive Star Formation". In: *Protostars and Planets VI*. Ed. by Henrik Beuther et al., p. 149. DOI: 10.2458/azu_uapress_9780816531240-ch007. arXiv: 1402.0919 [astro-ph.GA].

Tapia, M., P. Persi, and M. Roth (1996). "The embedded stellar population in northern NGC 6334." In: 316, pp. 102–110.

Tatematsu, Ken'ichi et al. (1993). "Molecular Cloud Cores in the Orion A Cloud. I. Nobeyama CS (1–0) Survey". In: 404, p. 643. DOI: 10.1086/172318.

Tielens, A.G.G.M. (2005). *The Physics and Chemistry of the Interstellar Medium*. Cambridge University Press. ISBN: 9781139445658. URL: https://books.google.de/books?id=o7KDfwkoXa0C.

Treviño-Morales, S. P. et al. (2019). "Dynamics of cluster-forming hub-filament systems. The case of the high-mass star-forming complex Monoceros R2". In: 629, A81, A81. DOI: 10.1051/0004-6361/201935260. arXiv: 1907.03524 [astro-ph.GA].

van der Tak, F. F. S. et al. (2010). *Radex: Fast Non-LTE Analysis of Interstellar Line Spectra*. ascl: 1010.075.

Vazquez-Semadeni, E., T. Passot, and A. Pouquet (1995). "MHD Turbulence, Cloud Formation, and Star Formation in the ISM (Invited paper)". In: *Revista Mexicana de Astronomia y Astrofisica Conference Series*. Ed. by M. Pena and S. Kurtz. Vol. 3. Revista Mexicana de Astronomia y Astrofisica Conference Series, p. 61. arXiv: astro-ph/9602004 [astro-ph].

Vázquez-Semadeni, E. et al. (2005). "Initial Stages of Molecular Cloud Evolution". In: *Protostars and Planets V Posters*, p. 8471.

Wada, Keiichi, Marco Spaans, and Sungeun Kim (2000). "Formation of Cavities, Filaments, and Clumps by the Nonlinear Development of Thermal and Gravitational

Instabilities in the Interstellar Medium under Stellar Feedback". In: 540.2, pp. 797–807. DOI: 10.1086/309347. arXiv: astro-ph/0005330 [astro-ph].

Walsh, A. J. et al. (1998). "Studies of ultracompact HII regions - II. High-resolution radio continuum and methanol maser survey". In: 301.3, pp. 640–698. DOI: 10.1046/j.1365-8711.1998.02014.x.

Wang, Ke et al. (2011). "Hierarchical Fragmentation and Jet-like Outflows in IRDC G28.34+0.06: A Growing Massive Protostar Cluster". In: 735.1, 64, p. 64. DOI: 10.1088/0004-637X/735/1/64. arXiv: 1105.4559 [astro-ph.GA].

Ward-Thompson, D. and A.P. Whitworth (2011). *An Introduction to Star Formation*. Cambridge University Press. ISBN: 9781139494472. URL: https://books.google.de/books?id=3tFAR3UmHJkC.

Williams, David A. and Serena Viti (2013). *Observational Molecular Astronomy: Exploring the Universe Using Molecular Line Emissions*. Cambridge Observing Handbooks for Research Astronomers. Cambridge University Press. DOI: 10.1017/CBO9781139087445.

Willis, Sarah et al. (2013). "A Wide-Field Census of Young Stars in NGC 6334". In: *American Astronomical Society Meeting Abstracts*. Vol. 222. American Astronomical Society Meeting Abstracts, 310.01, p. 310.01.

Wilson, Thomas L., Kristen. Rohlfs, and Susanne. Huettemeister (2009). *Tools of Radio Astronomy*. Berlin, Heidelberg : Springer Berlin Heidelberg,

Yorke, Harold W. and Cordula Sonnhalter (2002). "On the Formation of Massive Stars". In: 569.2, pp. 846–862. DOI: 10.1086/339264. arXiv: astro-ph/0201041 [astro-ph].

Yu, Jincheng et al. (2017). "Simulations of Fractal Star Cluster Formation. I. New Insights for Measuring Mass Segregation of Star Clusters with Substructure". In: 840.2, 91, p. 91. DOI: 10.3847/1538-4357/aa6ea5. arXiv: 1704.07962 [astro-ph.GA].

Zernickel, A., P. Schilke, and R. J. Smith (2013). "The global velocity field of the filament in NGC 6334". In: 554, L2, p. L2. DOI: 10.1051/0004-6361/201321425.

Zernickel, Alexander (2015). "Submm Observations of Massive Star Formation in the Giant Molecular Cloud NGC 6334 : Gas Kinematics with Radiative Transfer Models". PhD thesis. Universität zu Köln. URL: https://kups.ub.uni-koeln.de/6138/.

Zhang, Qizhou et al. (2014). "Magnetic Fields and Massive Star Formation". In: 792.2, 116, p. 116. DOI: 10.1088/0004-637X/792/2/116. arXiv: 1407.3984 [astro-ph.GA].

Zhang, Qizhou et al. (2015). "Fragmentation of Molecular Clumps and Formation of a Protocluster". In: 804.2, 141, p. 141. DOI: 10.1088/0004-637X/804/2/141. arXiv: 1503.03017 [astro-ph.SR].

Zinnecker, Hans, Mark J. McCaughrean, and Bruce A. Wilking (1993). "The Initial Stellar Population". In: *Protostars and Planets III*. Ed. by Eugene H. Levy and Jonathan I. Lunine, p. 429.

Zinnecker, Hans and Harold W. Yorke (2007). "Toward Understanding Massive Star Formation". In: 45.1, pp. 481–563. DOI: 10.1146/annurev.astro.44.051905.092549. arXiv: 0707.1279 [astro-ph].

List of Figures

List of Tables

List of Abbreviations

ACA	Atacama Compact Array
ALMA	Atacama Large Millimeter/submillimeter Array
APEX	Atacama Pathfinder Experiment
ATCA	Australia Telescope Compact Array
ATLASGAL	APEX Telescope Large Area Survey of the Galaxy
BTS	Behind The Spectrum
CASA	Common Astronomical Software Application
CDMS	Cologne Database of Molecular Spectroscopy
CMF	Core Mass Function
CNM	Cold Neutral Medium
DisPerSE	Discrete Persistent Structures Extractor
FWHM	Full Width at Half-Maximum
GBT	Green Bank Telescope
GILDAS	Grenoble Image and Line Data Analysis Software
GMC	Giant Molecular Cloud
HIM	Hot Ionised Medium
HMC	Hot Molecular Core
IMF	Initial Mass Function
IRAC	Infrared Array Camera
IRAM	Institut de Radioastronomie Millimétrique
IRDC	Infrared Dark Cloud
ISM	Interstellar Medium
KDE	Kernel Density Estimation
LTE	Local Thermodynamic Equilibrium
MSC	Morse-Sample Complex
NOEMA	NOrthern Extended Millimeter Array
PDF	Probability Density Function
SED	Spectral Energy Distribution
SMA	Submillimeter Array
SN	supernova
SNR	Signal-to-Noise Ratio
SPW	Spectral Window
UV	Ultraviolet
VLA	Very Long Array
VLBA	Very Long Baseline Array
WNM	Warm Neutral Medium
WIM	Warm Ionised Medium
WTTS	Weak-lined T-Tauri Star
XCLASS	eXtended CASA Line Analysis Software Suite
YSO	Young Stellar Object

Acknowledgements

This work is carried out within the Collaborative Research Centre 956 "Conditions and Impact of Star Formation - Astrophysics, Instrumentation and Laboratory Research", subproject "A6: High-Mass Star formation", funded by the Deutsche Forschungsgemeinschaft (DFG).

Publication of this thesis marks the end of my 22 years of formal education. I have been extremely fortunate to have fantastic teachers and mentors helping me to pursue my dream in astrophysics. First and foremost, I would like to thank my advisers, Prof. Dr. Peter Schilke and Dr. Álvaro Sánchez-Monge, for wonderful guidance in my graduate study. With their incredible amount of energy and patience, they taught me, among many other things, how to think like a researcher, see beyond the results and be critical in my research. Talking to them, always makes me feel inspired and encouraged. I am really grateful for all the resources with which they have provided me, including a highly supportive research group and lively weekly topical meetings, many opportunities to attend the conferences and workshops and the possibilities for collaboration with the experts of the field. I am also thankful for their courage and enthusiasm in hitting new goals and applying innovative methods, which taught me to think out of box.
I would like to extend my gratitude to Dr. Seamus Clarke for very valuable discussions on statistical analysis. I am also grateful to Dr. Josep Miquel Girart, Dr. Qizhou Zhang, Dr. Baobab Liu, Dr. Daniel Seifried and all my collaborators in the NGC 6334 project for their useful comments and feedback on my first publication.

I would like to thank Dr. Jean-Francois Robitaille for instructing me in wavelet analysis and being always open to discussions and questions. In addition, I am thankful to Dr. Antoine Gusdorf for sharing his insight in the physics of shocks and shock models.

My sincerest gratitude to Dr. Friedrich Wyrowski for accepting to be part of the supervision committee, and to Dr. Markus Röllig and Prof. Dr. Joachim Saur for serving in my dissertation committee.

I cannot thank enough to Álvaro and Veena for their valuable comments on this manuscript and Andreas for translating the abstract and finding right German words. In addition, special thanks goes to all amazing members of our research group for being always supportive, communicative, helpful and friendly. My office mates: Álvaro, Fanyi, Andreas and Sümeyye. Thank you Andreas for all your helps in coding and analysis, encouragements and supports. Thanks Álvaro for all the helps and supports in each single step of this project. Thanks Fanyi, Andreas, Sümeyye and Álvaro for all the useful discussions and suggestions which helped me to make progress, for the very nice office atmosphere, all the laughs and inside jokes. A big big thanks to Mitra for all the fun we had while working together, all the wonderful moments we had while traveling, tea times, nice chats and all the supports. Many many thanks to Roya for being always there to listen and help, and for many inspirational conversations. Many thanks to Veena, Nassim, Flavia, Niraj, Liem, Tianwei, Thomas, Wiebke, Kai, Stephan, Dirk, Claudia, Gwendoline and Anika.

A big thanks goes to Elaheh who is the source of all good feelings and nice thoughts.

Many many thanks to Dr. Petra Neubauer-Guenther, Dr. Susanne Herbst, Mariia Soloviova, Bettina Krause and Steffi Simon for all their helps throughout these years.

I am grateful to Pejman Norouzi and Babak A. Tafreshi, my first astronomy teachers, who generated an enthusiasm toward astronomy in my mind and made me familiar with the beauty and peacefulness of the night sky when I was ten years old. All the nights I spent in the desserts and mountains of Iran observing the night sky, made me more and

more motivated to follow my dream to become an astrophysicist.

I would like to take moment and cordially thank the official members of the Persian Gang (PG :D): Elaheh, Samaneh, Nafiseh, Mitra, Mehdi, Iman, Roya, Sajjad, Zahra and our little princess Dana. Thanks for all the gatherings, surprise birthdays, photography sessions, hikings and campings, movie nights and endless good time accompanied with so much fun, joy and laugh. Without you guys Cologne couldn't feel like home.

From the bottom of heart, I would like to thank the dearest friends Shadi and Afsaneh for standing by my side in all ups and downs I have been through. You guys have been like a second family to me within the years that I have been far away from home.

Last but not least, my deepest and most sincere gratitude to my parents for their infinite capacity of love. Without their tremendous support, patience, love and kindness no dream in my life could come true. Their strength and faith enlightened my life and encouraged me to continue. Although I have been far away from home in the last few years, I spent every moment with them in mind. This thesis is dedicated to them.

Erklärung

Ich versichere, dass ich die von mir vorgelegte Dissertation selbständig angefertigt,die benutzten Quellen und Hilfsmittel vollständig angegeben und die Stellen derArbeit – einschließlich Tabellen, Karten und Abbildungen –, die anderen Werken im Wortlaut oder dem Sinn nach entnommen sind, in jedem Einzelfall als Entlehnungkenntlich gemacht habe; dass diese Dissertation noch keiner anderen Fakultät oder Universität zur Prüfung vorgelegen hat; dass sie – abgesehen von unten angegebenen Teilpublikationen – noch nicht veröffentlich worden ist, sowie, dass ich eine solche Veröffentlichung vor Abschluss des Promotionsverfahrens nicht vornehmen werde.Die Bestimmungen der Promotionsordnung sind mir bekannt. Die von mir vorgelegte Dissertation ist von Prof. Dr. Peter Schilke betreut worden.

Teilpublikationen:

Phyiscal properties of the star-forming clusters in NGC 6334

M.sadaghiani, Á. Sánchez-Monge, P. Schilke, H. B. Liu, S. D. Clarke, Q. Zhang, J. M. Girart, D. Seifried, A. Aghababaei, H. Li, C. Júarez, and K. S. Tang
2019, accepted for publication in Astronomy & Astrophysics

Ich versichere, dass ich alle Angaben wahrheitsgemäss nach bestem Wissen und Gewissen gemacht habe und verpflichte mich, jedmögliche, die obigen Angaben betreffenden Veränderungen, dem Dekanat unverzüglich mitzuteilen.

Unterschrift: _____

Datum: _____